Surface dynamics of inversion tectonics systems through analogue modelling

Meije Sibbel, February 2017

A BSc. Thesis by: Meije Sibbel

Supervisors: Prof. Dr. Dimitrios Sokoutis & Dr. Ernst Willingshöfer

Faculty of Geosciences, department of Earth Sciences

Utrecht University

1 General introduction

1.1 Abstract

High resolution 4D monitoring using dynamic-photogrammetry was deployed to monitor the surface deformation of a series of analogue modelling experiments with variable angles of inversion (0 ° < α < 75°) in both the brittle and brittle-ductile regimes. This technique allowed for the compilation of a magnitude of valuable datasets to accurately extrapolate both timing and magnitude of the model deformation. This monitoring techniques was coupled with advanced 3D and 4D observational techniques that include fully textured 3D model web-rendering, modern room-scale Virtual reality (VR) which was used to inspect fully textured 3D models including cross section, and finally 3D color printing was used to print the surface topography including cross-sections.
It was found that reactivation in the form of reverse dip-slip is a selective process and occurs at both low and high angle normal faults. High angle normal faults are mostly reactivated during the initial steps of inversion. This reactivation is paired with rotation of the fault towards the vertical axis, which puts the fault close to an oblique angel to the principal stress axis, which locks the faults from being further reactivated. Moderate to high angel normal faults are reactivated in the purely brittle environment when faults are very steep or if enough confining pressure is present to prevent the fault plane from locking due to brittle decay. This decay can be attributed to the low cohesion of the sediments under low pressure conditions which causes the sediments making up the fault plane to fracture, rotate and slip in irregular ways, greatly increasing the coefficient of internal friction of the fault. The reactivation occurs manly within the graben infill where the sediment cover is thick and the confining pressure is highest. No low-angle normal fault reactivation occurred in the purely brittle experiments. Most of the low-angle normal fault reactivation occurred in the brittle-ductile models at the rift basin border normal faults that were decoupled from the basement and pushed upwards by the convex flowing ductile layer towards the graben borders that led to the formation of salt walls and minor diapirism. Reactivation in the form of strike-slip deformation occurred in the brittle models mainly at the rift basin border fault in the hanging-wall, however, significant reactivation also occurred in the rotated blocks within the graben. PIV analysis showed that strike-slip reactivation is progressively filtered out and converted to oblique displacement towards the footwall due to the principal stress axis rotation and the lack of instantaneous differential stress necessary for the reactivation to initiate. Hard-linked rift border faults in the ductile regime are the main absorbers of strike-slip displacement followed by the soft-linked opposing listric border fault. It was found that the highest magnitude of vertical reverse slip occurred at a 75° inversion angle for the brittle regime experiments and at a 45° in the ductile regime experiments.

Table of Contents

1.2 Introduction

Scaled analogue models have been widely used to investigate the structural styles and mechanisms of basin extension and inversion as well as the factors controlling fault reactivation (e.g. Brun and Nalpas, 1996; Nalpas et al., 1994; Bonini et al., 2012). Positive inversion involves a change in tectonic style from extension to contraction, resulting in shortening and uplift of a rift basin above its regional elevation to form a positive structural feature (Bally, 1984; Williams et al., 1989; Jagger and McClay, 2016; Buchanan and Buchanan, 1995; Cooper and Williams, 1989; Harding, 1985; Ziegler, 1982, 1987). Basin inversion is accommodated by (e.g. Cooper et al., 1989; Turner & Williams, 2004): (1) contraction in the form of thrust fault formation; (2) reversal of slip on pre-existing extensional faults; (3) strike-slip movement along strike. Inversion of purely brittle domino-style extensional fault systems formed during rifting involves back-rotation of the basement fault blocks when sufficient confining pressure is present (e.g. Coward, 1994, 1996; Nalpas et al., 1994). Reverse reactivation along the pre-existing fault planes proceeds until the dips of the basement faults reach a critical value to inhibit reactivation (Coward, 1996). Petroleum prospects for sedimentary basins are intimately related to positive fault inversion, which can potentially control the thermal history of basins (e.g. by favoring uplift, erosion and exhumation of sedimentary basin), as well as the formation of trapping structures, or the breaching and destruction of layers sealing Petroleum reservoirs (e.g. Bonini et al., 2011; Turner and Williams, 2004; Ziegler, 1987). Basin inversion and fault reactivation have been the focus of an extensive amount of analytical- (e.g. Etheridge, 1986; Nielsen and Hansen, 2000; Ranalli and Yin, 1990; Sandiford, 1999; Sibson, 1985, 1995; Tong and Yin, 2011; Yin and Ranalli, 1992), and analogue modelling studies (e.g. Bonini, 1998; Brun and Nalpas, 1996; Ziegler et al., 1995; Nalpas, 1996; Nalpas et al., 1995; Marques and Nogueira, 2008; Sassi et al., 1993). This work focuses on integrating advanced 4D monitoring (e.g. 4D Photogrammetry) and observational techniques (e.g. 2D DIC, textured 3D model visualization, modern room scale virtual reality (VR), color 3D printing and Dynamic DEM's) to obtain better understanding on the timing and mechanisms involved in basin inversion tectonics and the origin of associated structured, including thrust fault formation and the compressional reactivation of normal faults inherited from pre-orogenic rifting phases. Application of advanced surface observation techniques allows to obtain a better grasp on the evolution and timing of graben extension and inversion by the detailed study of the dynamic surface evolution. This experimental method aims to get insights into the complex natural geological processes by analyzing the mechanical response of analogue materials which display simplified rheological properties of rocks existing in nature (e.g. Bonini et al., 2011; Gabrielsen et al., 2015). The obtained experimental results can give insight in the mechanisms and factors controlling graben inversion and more specifically fault reactivation.

1.3 Analogue Modelling

Laboratory analogue experiments are a tool to study the mechanisms of tectonic deformation by testing hypotheses concerning the link between deformation, rheology and boundary conditions (Hubbert, 1937; Ramberg, 1981). Analogue experiments involve drastic simplification in rheology and geometry relatively to natural conditions to keep experimental results interpretable. A major simplification in analogue models is the homogeneous rheology of analogue materials, whereas in nature rocks show variable rheological properties at different depths and geographic locations (e.g. Ranalli, 1995, 1997). An equilibrium must be found between the complexity and simplicity of the model to prevent results from being extremely difficult to interpret or oversimplified and meaningless. Finding equilibrium between the necessary simplification of the experiments and the complexity of the natural conditions is a continuing challenge. It should be noted that the aim of analogue modelling is not to rebuild nature, only the systematic variation of model input parameters can provide closer insight in the mechanics, kinematics and geometry of tectonic processes. Therefore, a series of analogue model experiments with different input parameters were performed and examined to analyze the influence of the parameter changes. Different input parameter will undoubtedly change to the resemblance with natural conditions and must be carefully analyzed for their linkage to natural processes, as some input parameters might not have any resemblance to natural conditions.

1.3.1 Modelling setup and Procedures

Modelling was performed in the Tectonic Laboratory (TecLab) at the Department of Earth Sciences at Utrecht University, The Netherlands. The goal of the experiments is to investigate the surface dynamics of inversion of rift basins subject to various angles of convergence in brittle and brittle-ductile regimes. Two types of models were deployed: (1) purely brittle models, representing the upper brittle crust; (2) Brittle-ductile models with a single ductile layer, representing the upper crust with a weak sedimentary layer (e.g. salt, shales).
The experiments were carried out in two phases: (1) extension (rifting); (2) shortening (inversion). Each experiment was carried out with different angles of inversion relative to the extension direction (Figure 1.3.2; Table 1 and 2). To be able to determine the impact of variable inversion angles on the system, a reference must exist to which the results of the inversion experiments can be compared to. This can be accomplished by running an experiment with solely the rifting phase.

Inversion Angles	15°	45°	75°	0°	No Inversion
Brittle	2x	1x	1x	1x	1x
Brittle - Ductile	1x	1x	1x	1x	0x

Table 1 - Inversion angles for each type of the experiment and the number of experiments carried out.

The model setup (Figures 1.3.1 and 1.3.2), was built as follows: 2 plastic sheets *(sheet 1 and 2)* of ca. *2 mm* thick were put on top of each other at only half the distance (*20 cm*) of the model's shortest axis (*y-axis*). This created *20 cm,* where the plates overlap and *20 cm* where only the bottom plate used for the inversion is present. The line running perpendicular to the y-axis of the model where the latter of the two sheets overlap represents the *velocity discontinuity (VD)*. The term (VD) was used for the first time in French (discontinuité de vitesse DV) by Ballard et al. (1987).
Microsphere (GM) particles were spread between the different sheets and between the sheets and the table beneath to ensure frictionless sliding since the friction coefficient between the plastic plates is nonexistent in nature and will blur the modelling results. Metal bars with thicknesses of *0.2 cm*, *0.4 cm* and *0.8 cm* were placed along the borders of the sheets to guide their movement and to prevent unwanted rotation of the system. First the bottom sheet (*sheet 2)* used for the inversion was fixed so that it does not move during the rifting phase. Then in the case of the brittle-ductile models, the top plate *(sheet 1)* was attached to the engine that pulls the sheet at a set velocity and distance. This represents the rifting phase. After the rifting phase the bottom plate (*Sheet 2*) was attached to the engine for the inversion phase. Since purely brittle models are strain independent, the extension was performed by manually pulling the straps attached to the sheets in steps of *0.5 cm*. The metal bars were stacked on top of each other, allowing the model to be built with the set dimensions of *40x 60 x 4 cm*.
The setup and dimensions of the models are shown in figure 1.3.1.

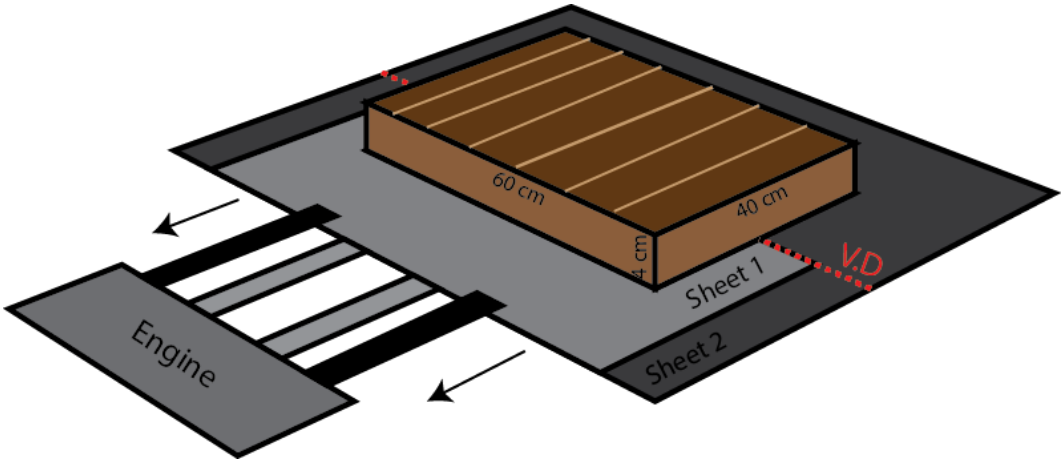

Figure 1.3.1. Perspective-view of the model setup and dimensions. X-axis: 60 cm (length); Y-axis: 40 cm (width); Z-axis: 4 cm (height). The V.D. represent the velocity discontinuity where the two plates cease to overlap. The plates are pulled with the straps by a stepper motor engine with gears.

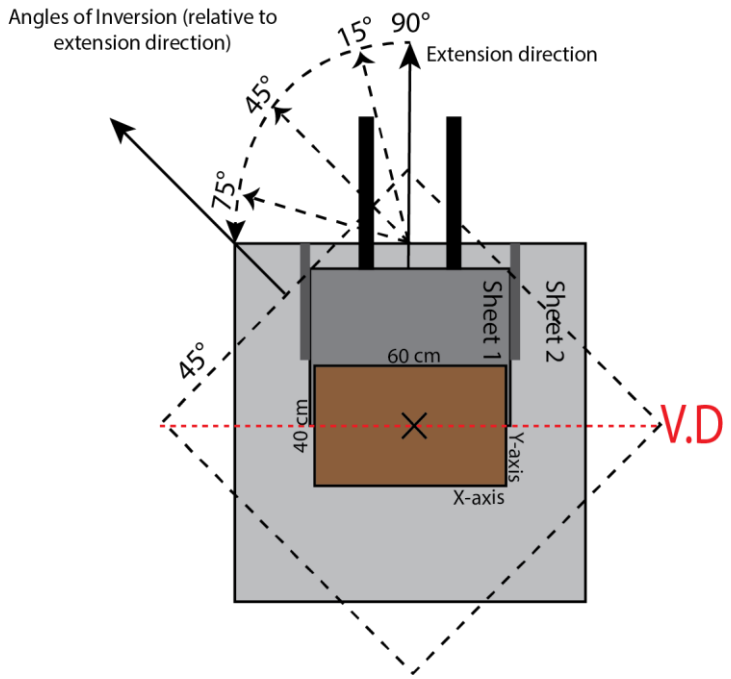

Figure 1.3.2. Top View of the model setup. The figure displays the angles of inversion relative to the extension direction.

Different bars with variable thicknesses were used to be able to build a model in a modular manner and with different colored sand layers. This creates the necessary contrast between the layers that helps to better visualize the cross-sections and the surface deformation of the models. The order in which these bars were used varies only between the brittle and brittle-ductile models due to the presence of the *0.8 cm* thick ductile silicon layer in the brittle-ductile models (Figure 1.3.3). The placed silicon layer has a dimension of *30 cm x 50 cm x 0.8 cm* and was placed in the central-top part of the model to ensure that the silicon was covered with enough sediment so that it does not reach the surface during the deformation process. Parallel to the y-axis of the model grid-lines were added with black-and purple (central line) colored quartz sand. These grid lines will also help to visualize the surface deformation of the models (Sokoutis et al., 2005). Small scale black-colored coffee particles were spread over the surface of the models to create the necessary contrast from the uniform surface layer. These particles were used for the particle tracing discussed later and for the 3D reconstruction software since these particles are used as trace-points during the reconstruction.

After the model build process was completed *2 x 0.8 mm* thick bars were added containing 12-bit Agisoft markers. These markers are used for scaling and orienting the model during the 3D reconstruction of the models (Figure 1.4.3).

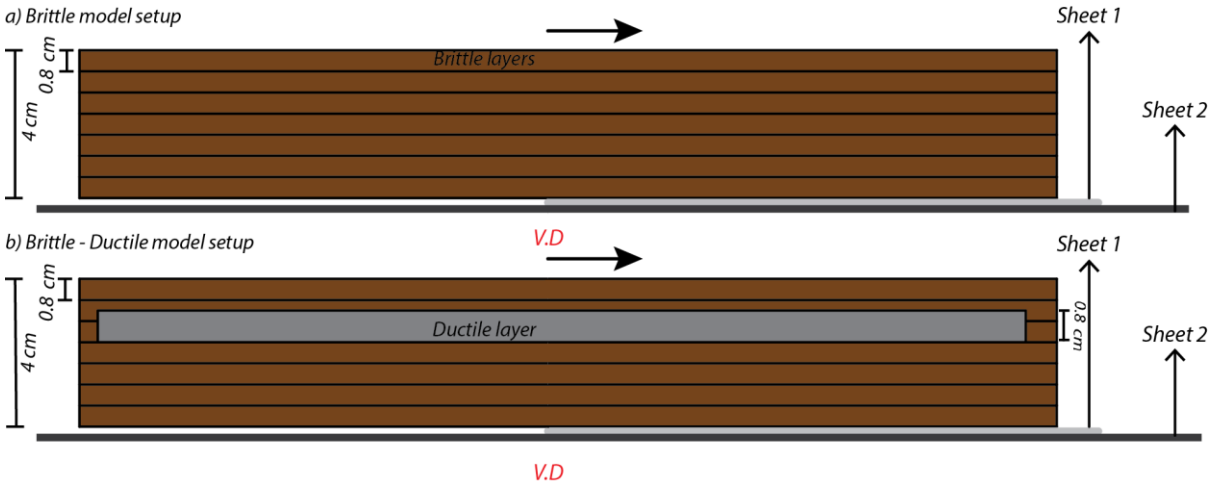

Figure 1.3.3. Schematic cross-sections illustration of each of the setups, including booth plates and the velocity discontinuity. (a) Cross-section view of the pure-brittle system. b) Cross-section view of the brittle-ductile system. Both models are 4.0 cm thick.

To be able to deform the *brittle-ductile (BD)* model the stepping motor was put at the correct PWM frequency *(127 Hz)* determined by the required velocity. For both extension and shortening of the model the same velocity was applied (*v = 6.0 cm/h*), for a total displacement of *5.0 cm* for the extension phase and *6.0 cm* for the inversion phase. As described above the purely brittle models were extended and shortened with steps of *0.5 cm* at a time for a total of *5.0 cm* during the extension phase and *6.0 cm* during the inversion phase. For both types of models syn-tectonic sedimentation was carried out only during the extension phase to simulate natural conditions of filling up of the formed rift basin with sediments. Only a small amount of sediment was added each time to solely cover the newly formed structures within the lowest parts of the rift basin. Different feldspar sand colors were also used for sedimentation to produce the necessary layer contrast. Extra coffee particles are added after the extension phase was completed. At the end of the extension phase the top sheet was fixed in place and the bottom plate was released to allow it to move freely. As shown in figure 1.3.2, the bottom plate was rotated with an angle (α) relative to the top plate for different angles of inversion, this required the supporting side bars that support the sheet to be moved before the inversion phase can be initiated. This also implied that in the case of the brittle-ductile models the engine also had to be moved and rotated an amount equivalent to the inversion angle (α). No syn-tectonic sedimentation or erosion was carried out during the inversion. Photographs were taken during the experiments in time steps of *7 seconds* with the photogrammetry setup as explained in the photogrammetry section below, consisting of between 9x and 11x DSLR canon 1100D and 700D cameras. During the sedimentation process of the extension phase the photography process was paused for the shortest time interval possible, usually between *30-60 seconds*. After the inversion phase the engine was stopped and the models were soaked in water to create the necessary cohesion between the sand particles to allow easier cutting of the cross-sections which exposes the internal structures of the models (e.g. Sokoutis et al., 2005).
A series of photographs are then taken parallel to the cross-sections for analysis.

Experiments	**Velocity**	**Type**	**Inversion Angle (degrees)**	**Extension (cm)**	**Inversion (cm)**	**Thickness (cm)**
GS-B-Ext	-	Brittle	-	6 cm	-	4 cm
GS-B15	-	Brittle	15°	6 cm	7 cm	6 cm
Gs-B15-v2	-	Brittle	15°	5cm	6 cm	4 cm
GS-B45	-	Brittle	45°	5 cm	6 cm	4 cm
GS-B75	-	Brittle	75°	5 cm	6 cm	4 cm
GS-B90	-	Brittle	*0*°	5 cm	6 cm	4 cm
GS-D15	6cm/h	Brittle-Ductile	75 °	5 cm	6 cm	4 cm
GS-D45	6 cm/h	Brittle-Ductile	45°	5 cm	6 cm	4 cm
GS-D75	6 cm/h	Brittle-Ductile	15°	5 cm	6 cm	4 cm
GS-D90	6cm/h	Brittle-Ductile	0°	5 cm	6 cm	4 cm

Table 2 - summary of the models and their characteristics.

1.3.2 Materials

Analogue materials were employed to construct the brittle and brittle-ductile systems (Table 3). The brittle and ductile layering of the continental lithosphere refers to geophysical data and extrapolation of laboratory experiments (e.g. Sokoutis et al., 2005; Kirby, 1983, 1985; Carter and Tsenn, 1987; Ranalli, 1995, 1997; Elisa et al., 2016). Care must be taken since the extrapolation of these results is less valid for the oceanic lithosphere, where intensive deformation is absent, fortunately this study only involves continental lithosphere.
Dry K-Feldspar sand, a Mohr-Coulomb material (Sokoutis et al., 2005) composed the brittle layer and represents the brittle upper crust. The silicon layer was implemented as a ductile material to simulate weak sedimentary layers (e.g. evaporites and shales). The density ratio of both materials for the upper crust is 0.83. In nature, this ratio is approximately 0.9 (Hubbert, 1951), this value thus is in good agreement with natural conditions. Schellart (2003) showed that these mechanical property values are slightly different in each model. He found that well-rounded and spherical material is the best suited to model brittle behavior of rocks since it has a smaller cohesion and coefficient of internal friction. It is for this reason that the feldspar sand was sieved to the correct grain size of 100-300 µm to assure the maximum rounding, as larger grains are normally more angular and thus less suited for these experiments.

Material	Density, ρ (g/cm3)	Grain size (μm)	Viscosity (Pa)	Coefficient of internal friction	Cohesion
Silicon Putty	1.06	-	1.98x10^ 4	-	-
Feldspar Sand	1.28	100-300	-	0.6 (ϕ = 37.2º)	15

Table 3 - Parameters of model materials.

1.3.3 Model Scaling

Tectonic structures that form in analogue models are typically smaller, develop in a much shorter time window, and require much less stresses than structures forming in the natural prototype (Bonini et al., 2011).
For a small-scale model to be representative for natural examples, the models must be scaled in terms of distribution of stresses, rheologies and densities (J.-P. Brun, 1999; Davy and Cobbold, 1991; Hubbert, 1937, 1951; Ramberg, 1981; Weijermars and Schmeling, 1986; Weijermars et al., 1993).
The models were scaled following the principles of geometric and dynamic -rheological similarity (e.g. Hubbert, 1937; Ramberg, 1981; Weijermars and Schmeling, 1986), this was expanded to lithosphere scale experiments by Davy (1986) and Cobbold and Davy (1991).
In analogue modelling, scaling relationships between natural conditions and the analogue model are obtained by keeping the average strength of brittle layers correctly scaled with respect to the strength of the ductile layers and the gravitational stresses in the equation of dynamics:

$$\left(\frac{\partial \sigma ij}{\partial Xij}\right) + \rho\,(g - (d^2 * \frac{\varepsilon ij}{dt2})) = 0 \;\; (i,j = 1,2,3) \qquad (1.0)$$

Where σ_{ij} are the components of stress, ε_{ij} the components of deformation, Xij space coordinates, (ρ) density of the material, (g) acceleration of gravity and (t*) for time.
The gravitational stress (σ*) under this condition is related to the ratio of density (ρ*), acceleration (*g**) and the length (L*) as follows:

$$\sigma^* = \rho^* g^* L^* \qquad (1.1)$$
$$\varepsilon * = g^* (t^*)^2 \qquad (1.2)$$

Where the exponent (*) refer to the ratio between the analogue model and the natural prototype, e.g. $\sigma^* = \frac{\sigma m}{\sigma p}$ (Brun, 1999). Inertial forces can be neglected in geological processes (Hubbert, 1937; Ramberg 1981). Under normal gravity conditions, g* ≈ 1, most densities of the modelling materials range from *0.96 - 1.6* Kg/m^{-3}, and rocks from *2.3 -*

3.0 Kg/m^{-3}. Since the model and the natural conditions are correctly scaled and in the same order of magnitude, the ratio of density (ρ*) is close to *1*. Which means the equation can be simplified to:

$$\sigma * = \ L *$$ (1.3)

This shows that the stresses ratio is almost equal to the length ratio (Brun, 1999).
A more detailed analysis is given by Davy & Cobbold (1991). Strength profiles must be calculated to assure that the profiles between the analogue model and natural conditions are similar (Figure 1.3.4). The following two sections describe the way to calculate stresses in the model in both ductile and brittle layers, allowing the stress ratio to be determined. It is important to note that cohesion of the brittle material should scale down in a similar way to how stress scales down (Horsfield, 1977; Davy and Cobbold, 1988; Cobbold and Jackson, 1992).
When analogue experiments are carried out in a normal gravity field, stresses should be scaled down as the product of density and length vectors scale down (Schellart., 2003):

$$\frac{C^a}{C^n} = (\frac{\sigma^a ij}{\sigma^n ij}) \ = (\frac{\rho^a * x^a j}{\rho^n * x^n j})$$ (1.4)

Where superscript *(a)* denotes the analogue model and superscript *(n)* the natural prototype; (*C)* is the cohesion; (σ_{ij}) are the stresses; *ρ* is the density; and (*x_{ij})* is the length vector.

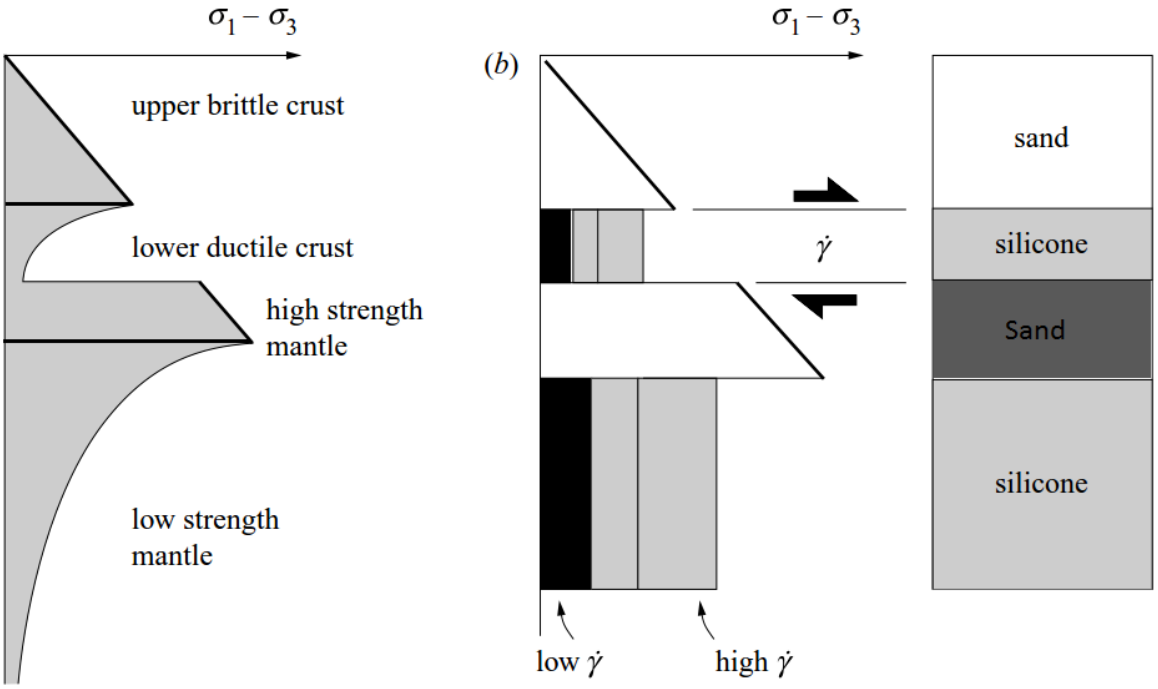

Figure 1.3.4. Strength profile for the natural lithosphere and the corresponding sand-silicon model strength profile for different strain rates (from Brun, 1999).

1.3.4 Brittle Behavior

Based on rock deformation experiments, Byerlee (1978) proposed that brittle rocks in the crust deform per the Mohr-Coulomb criterion:

$$\tau = C + (tan\,\Phi) * \sigma \quad (1.5)$$

Where (τ) is shear stress, (*C*) the cohesion, (Φ) the angle of internal friction and (σ) the normal stress. From the Mohr Coulomb criterion, it follows that the maximum differential stress in brittle layers increases linearly with depth and is independent on strain rate (Byerlee, 1978). According to Byerlee (1978), Φ = 31° for most crustal rocks and the cohesion (C) of natural rocks is in the order of *50 MPa*. A length-scale ratio between model and nature ($L^* \approx 10^{-6}$) requires a modeling material with very small cohesion compared to the differential stress in the models. Dry Feldspar sand was used and has a mean density of ρ = 1300 kg^{-3}, very small cohesion and a coefficient of internal friction of ϕ ≈ 0.6, and is thus suitable to represent natural brittle rocks. The cohesion of natural rocks will probably be even lower due to the large number of joints, faults and fractures in them.
From the Mohr circle the following relations can be obtained:

$$\sigma n = (\frac{\sigma_1+\sigma_2}{2}) + (\frac{\sigma_1-\sigma_3}{2}) * cos(2\alpha) \quad (1.6)$$

$$\sigma s = (\frac{\sigma_1-\sigma_3}{2}) * sin(2\alpha) \quad (1.7)$$

Where (σ_1) and (σ_3) are the maximum and minimum principal stresses, (σ_n) the normal stress and (σ_s) the shear stress on the structural discontinuity.
By the Andersonian fault classification, the following equations are applicable on the brittle part of the model:

In *compression*, where σ = σ_3, the maximum differential stress is:

$$\sigma_1 - \sigma_3 = 2\rho g h_b \quad (1.8)$$

In *extension*, where σ = σ_1, the maximum differential stress is:

$$\sigma_1 - \sigma_3 = (\frac{2}{3})\rho g h_b \quad (1.9)$$

In *strike-slip*, where σ = σ_2, the maximum differential stress is:

$$\sigma_1 - \sigma_3 = \rho g h_b \quad (1.10)$$

Where (σ_1) are the minimum principle stress, (σ_3) the maximum principle stress, (ρ) the density, (g) the gravitational constant and (h_b) the thickness of the brittle layer (Fossen H., 2010).

For a two-dimensional case of an existing fault containing the (σ_2) axis, optimal reactivation occurs when the differential stress required for shear is minimum, which is when:

$$\theta r = 0.5\ tan - 1(\frac{1}{\mu s}) \quad (1.11)$$

Frictional lockup ($\frac{\sigma' 1}{\sigma' 3} = \infty$) takes place when (Collettini and Sibson, 2001; Sibson, 1985, 1995):

$$\Theta r = 2\theta * r = tan - 1\ (\frac{1}{\mu s}) \quad (1.12)$$

1.3.5 Ductile Behavior

Goetze and Evans (1979) expressed the mechanisms of the ductile flow of rock (e.g. olivine, evaporites) analytically in the following flow law:

$$\varepsilon\ =\ A\ exp\ (-\frac{Q}{RT})\ (\sigma 1\ -\ \sigma 2)^n \quad (1.13)$$

Where (ε) is the deviatoric strain rate, (Q) the activation energy, ® the universal gas constant, (T) the absolute temperature, (A) the material constant and (n) the stress exponent. The ductile layer in this study is represented as a silicone-putty.
Silicon is a Newtonian viscous fluid, *it's resistance to flow is linearly dependent on strain rate (n±1)*.
Experimental data indicates that most natural ductile rocks display a strain rate range of *1-4*. Ductile lower-crust rocks with a stress exponent of *±1* are nearly Newtonian. Silicone-putties with higher stress exponents are normally too difficult to deform and are thus not commonly used in analogue model experiments (Davy and Cobbold, 1991).

The *shear strain rate* (*ẏ)* in the ductile part of the model is given by:

$$\dot{y}\ =\ (\frac{V}{h_d}) \quad (1.14)$$

Where (*V*) is the displacement rate and (h_d) the thickness of the ductile layer. Therefore, the shear stress in the ductile layer can be written as:

$$\tau\ =\ (\frac{\eta V}{h_d}) \quad (1.15)$$

or:

$$\tau\ =\ \eta\varepsilon \quad (1.16)$$

Where (τ) is the shear stress, (η) the viscosity and (ε) the shear strain rate. In terms of strength:

$$\sigma_1 - \sigma_3 = 2\tau \quad (1.17)$$

Thus, for a given thickness, the strength of a ductile layer is twice the product of the displacement rate. A ductile layer with a given thickness (h_d) and viscosity (η) can result in a wide range of shear stresses, and ductile strengths are easily obtained from the variations of the displacement rate (*V*).
The calibration of the analogue model based on the natural ductile strength conditions in the crust is no easy task due to the fact that most of the parameters of these natural conditions are not precisely known, this can give rise to a large range of experimental results with an unknown deviation from the natural conditions, this is one of the large limitations of analogue modelling.
Selected analogue materials allow the exploration of a large variety of natural rock properties. Particularly, the dependence of strength of Newtonian and non-Newtonian materials on the applied strain rate allows investigating a wide range of strength profiles by varying the strain rate (as well as other parameters, such as (η), (*A*) and (*n*) (Davy and Cobbold, 1991; Bonini et al., 2011).

1.3.6 Limitations

As explained in the sections above the purpose is not to completely rebuild nature, but only to model parts of its complex behavior. Although changing input parameters can give clear insight into the impact of these parameters, the signal to noise ration of analogue models can be substantial which makes it difficult to interpret the results.
Even when the input parameters remain constant in different experiments, the kinematics and therefore the results be different since every experiment is unique and cannot be reproduced to the full extent due to the change is material properties in every experiment (e.g. Lohrmann et al., 2003; Schreurs., et al., 2016). Parameters such as porosity of the layers, small-scale strain hardening and softening, grain shape/size/rounding and sphericity, grain size distribution and sieving vs pouring of the materials will all change the cohesion and coefficient of internal friction of the sediment body (Schellart., 1999). These factors will change the mechanical properties in every different experiment, and will thus change the way the model behaves during the deformation process (e.g. Krantz., 1991; Schellart, 2000; Lohrmann et al., 2003; Panien et al., 2006; Gomes, 2013; Maillot., 2013). Other factors such as temperature variations, flexural and isostatic variations, erosion, denudation are all variables that interact very differently in analogue models and in the natural prototypes. This induced noise into the system that can be so substantial that care must be taken when analyzing and making conclusions when it comes to relating the analogue experiments to natural prototypes as the results may well not apply to nature or be only a version of the truth. The rheological stratification of sand–silicone models necessarily approximate the complex thermo-dynamic deformation to a purely mechanical process (Bonini et al., 2011).

1.4 Existing monitoring techniques

Many methods exist to create 2D and 3D datasets that allow archiving, analyzing and visualization of subjects. These methods include *laser scanners* (e.g. Sokoutis and Willingshofer, 2011), *reflective light scanners* (e.g. Brèque et al., 2004), *Photogrammetry* (e.g. Galland et al., 2016), computation from tomographic datasets, e.g. *computed tomography* (CT) scans (e.g. Schreurs et al.,2016). Below these methods used to qualitatively and quantitatively monitor analogue models are listed and briefly reviewed, including their advantages, disadvantages and what data they produce.

1.4.1 Laser Scanning

Laser scanners have widely been used to obtain topography measurements in e.g. geomorphology (Lague et al., 2003) and tectonic experiments (Martinod and Davy, 1994; Sokoutis and Willingshofer, 2011; Farzipour-Saein et al., 2013; Luth et al., 2009; Elisa et al., 2016).
For laser scanning techniques, the characteristics of the equipment define the maximum level of detail that can be acquired (Viana et al., 2016). Two types of resolution determine the end resolution of the obtained dataset; (1) Range resolution, which determines if the scanner can differentiate between two objects on the same optical axis. (2) Angular resolution, which determines the ability to distinguish two objects on adjacent optical axis (e.g. Pesci et al., 2011).
Laser scanning methods produce precise point clouds that can be converted to digital elevation models (DEM's). Unfortunately, the acquisition time can be lengthy and laser scanners cannot handle fast dynamic models due to the *line-by-line* scanning method of the laser instead of instantaneous framing of an entire analogue model (Figure 1.4.1). This line-by-line scanning of the surface will induce time-and-space warping due to the different time and deformation instances on which the scans were taken, producing a low temporal and spatial resolution model. Therefore, the faster the model is moving the lower the quality and resolution of the resulting scans will become. For a static or semi-static models these inaccuracies will be small, however, for fast moving analogue models this is a very big issue.

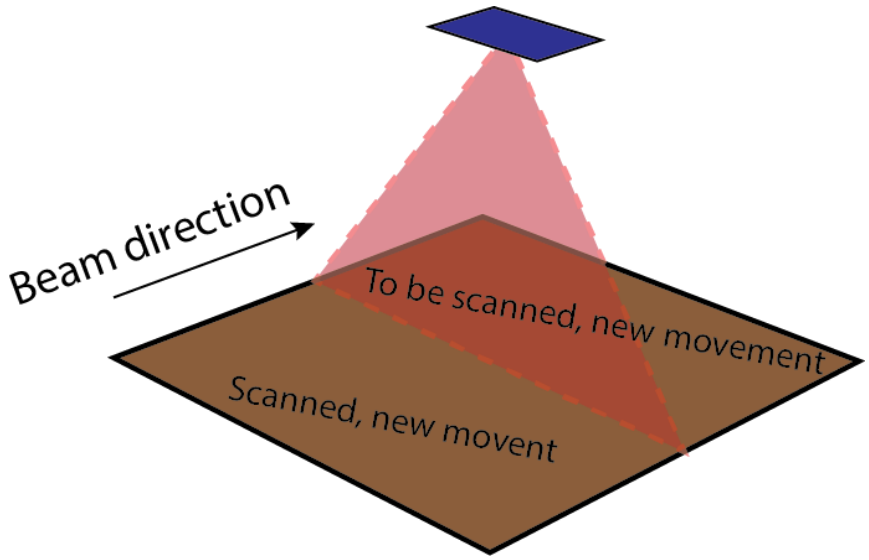

Figure 1.4.1. Schematic illustration of a laser scanner in the process of scanning a moving analogue model.

Another downside to laser scanners is that almost none produce textured models. Each laser scanner is made to scan an object of a specific size, a laser scanner used for centimeter scale models can normally not be used for meter-scale models and requires a different scanner. More recently a combination of laser scanner with an integrated photo-camera sensor for texture generation methods was developed (David Hodgetts, 2013), this method is mainly used in the oil and gas industry to study large surface areas (e.g. outcrops) but have rarely been used in deformation experiments in the laboratory as these setups are very expensive. The advantage of this technique over photogrammetry is that it is much less computer intensive as meshes are generated automatically by the scanner and the scanning is less influenced by the degree and type of lighting needed to carry out the data capture (Thielemann et al., 2013). On the other hand, the spatial resolution of very expensive scanners is normally higher than that of photogrammetry. One of the main downsides of laser scanners is that it also requires expensive proprietary software with limited post-processing capabilities. Laser Telemetric System (Metrology) have been applied to laboratory experiment by Lague et al. (2003), they achieved high spatial resolution by using multiple telemetric lasers to scan a surface, unfortunately the temporal resolution was still very low (6 minutes for a single scan).

1.4.2 Structural Lights (Moiré projection, 3D)

The principle of this technique is to project a pattern (e.g. fringes) onto the surface of the experiment that will be monitored. The monitored fringe pattern is then digitally analyzed and processed to build a DEM of the surface. This method has been used extensively in geomorphology laboratory experiments (Babault et al., 2005; Babault et al., 2007) and tectonics (Grujic et al., 2002; Graveleau and Dominguez, 2008; Graveleau et al., 2012). This Technique provides a good temporal resolution; however, the spatial resolution is limited to

the width of the fringes. The spatial resolution of this technique is normally much lower than that of laser scanning techniques.
More recently the Microsoft Kinect system that combines structural lights with two classic computer vision techniques (depth from focus, and depth from stereo) was used by Tortini et al., (2014) to measure the surface topography of models. Although the spatial resolution of this system is very low compared to laser-scanning techniques, this system can be optimized with better and more expensive sensors that can possibly make this system a good middle-ground between laser scanning and the current Moiré projection technique used in geoscience experiments.

1.4.3 In-plane displacement (2D)

Two-dimensional (2D) in-plane displacement, also called Particle Imaging Velocimetry (PIV) is an non-destructive quantitative and qualitative analysis technique that implies modelling parallel to the surface of the analogue model and has been widely used to study geologic processes, in particular where horizontal displacement is larger compared to topographic changes (e.g. Adam et al., 2005; Leever et al., 2011; Carbonell et al., 2016; Boutelier., 2016; Krezsek et al., 2007; van Gent et al., 2010; Bonini et al., 2015) . A simple method to quantify such in-plane displacements is *digital image correlation* (DIC) using a vertically fixed inexpensive DSLR camera above the model (Donnadieu et al., 2003; Delcamp et al., 2008; Abdelmalak et al., 2012). DIC compares known points with subpixel size (e.g. grains, 10-200 microns) across interrogation areas inside the images taken at different time steps. The correlations yield the most probable displacement for a group of particles. The size of the interrogation area and the number of interrogation passes determines the sampling resolution. Care must be taken with interrogation areas that are too small, as very small interrogation areas will largely increase the noise floor. DIC gives mainly insight into 2D surface geometry and displacement development through time, which in the case of strike-slip, transtensional and transpressional deformation experiments can yield very useful results (e.g. Leever et al., 2011). One of the main negative aspects of DIC software is that most software packages that exist such as LaVision are very expensive, (e.g. Burchardt and Walter, 2010; Jagger and McClay, 2016), fortunately several DIC programs are free, such as MatPIV and PIVlab for MATLAB® (Sveen, 2004; William and Eize, 2014). The advantage of PIVlab over MatPIV is that PIVlab has a user-friendly GUI (graphical user interface) and has a broader toolkit with more features, such as the ability to do pre-and-post processing, image evaluation and the ability to choose different algorithms for DIC (Figure 1.4.2).

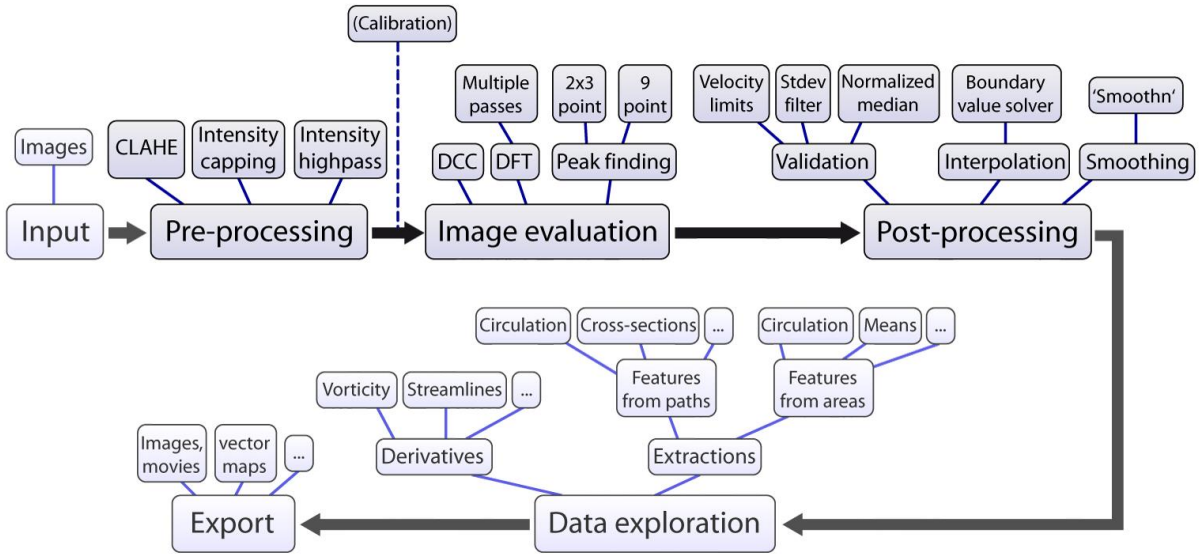

Figure 1.4.2. DIC analyses in PIVlab. Overview of the workflow and the implemented features (from William and Eize, 2014).

DIC has also been used in 3D experiments composed of transparent materials containing tracers lighted up by a laser sheet (Kavanagh et al., 2015), this technique is useful to measure displacement at different depths in the model, although the displacement can only be measured in the 2D plane parallel to the camera and out-of-plane movements are not measured or corrected, the results are also 2D only. The temporal and spatial resolution of DIC results depends mainly on the resolution of the camera sensor, lens distortion, the number of software recognizable points on the surface of the analogue model and the frame-rate. Optical distortion due to low quality lenses or very low focal-lengths leads to fish-eye in the images that will cause the displacement distance in the images to deviate from the true displacements. Large topography can also cause significant distortion in images due to the creation of shadows and the change of the *depth-of-field* that will change the camera focus at different topographic levels.

1.4.4 Three-Dimensional (3D) surface displacement

Adam et al., (2015) produced 3D displacement maps of analogue models using the commercial package (LaVision). This package produced good results, unfortunately the price is prohibitive for most laboratories.
Combining laser scanning methods and DIC was used by (Trippanera et al., 2014) to compute topography change and horizontal displacement. Although such combination produces 3D displacement maps of the surface of the subject, the inherent limitation of each separate methods persists. Linking laser and DIC data sets is no easy task.

1.4.5 XCT scanner (2D and 3D)

XCT scanners have been used to monitor the internal deformation of analogue models both in 2D (e.g. Schreurs and Colletta, 1998) and recently also as the basis of 3D image correlation (Adam et al., 2013). Although very useful 3D displacement fields can be generated, there are some very crucial limitations. (1) Their spatial and temporal resolution are usually quite low compared to optical methods (Adam et al., 2013), (2) The size of the subject that can be scanned depends on the size of the scanner, (3) the datasets of the scans are very large and requires significant storage space and advanced expensive software.

1.4.6 Photogrammetry (3D)

Over the last few years, Photogrammetry has revolutionized the digitizing process of surface topography. Photogrammetry has proven to be an affordable alternative to laser or structured light scanners and is widely used in many different fields, including topographic mapping with small UAVs, e.g. small drones (Lejot et al., 2007), architecture (Yilmaz et al., 2007), archeology (e.g. De Reu et al. 2013) as well as many fields in geosciences such as planetary sciences (Albertz, 2005; Haruyama et al., 2012), paleontology (Mallison and wings, 2014), geomorphology (Javernick et al., 2014), Physical geography (Smith et al., 2016; Vautier et al., 2016) and tectonics laboratory experiments (Galland et al., 2016). Done correctly, it does not only yield highly resolution textured models, it is also very user-friendly, relatively fast and inexpensive and extremely scalable.
The method of Photogrammetry involves taking a series of photographs of an object from many different angles around the object (N-view) to computationally generate a 3D model by comparing known features across the photographs. It was the automation of this process through what is known as *Structure from Motion (SfM)* that made this application so popular in a wide range of fields and applications. The main concepts were laid out by Koenderink and van Doorn (1991) that was later shaped into a highly efficient and easy to use software by Snavely et al., (2006, 2008). The process of creating 3D models from photographs involves a multi-step process (Figure 1.4.5) that starts with:

(1) A program that finds specific tie points on each image (Figure. 1.4.4) using, e.g. the SIFT algorithm (Lowe, 1999; Lowe, 2004), or more recently SURF (Bay et al., 2006) or ASIFT (Morel and Yu, 2009). A tie point is defined as a negative or positive peak in brightness intensity: continuous gradients or small amplitude peaks will not yield any tie points (Rosu et al., 2015a).
(2) The next step involves comparing the tie points from all images to find corresponding image parts and mathematical relations between the parts using, e.g. the RANSAC algorithm (Fischler and Bolles, 1980). In this step tie points are used to compute booth the camera positions and viewing angles and the distortion of the camera optics. The output of this step is a sparse point cloud consisting of three dimensional coordinates of some of the extracted data points that were used for the image alignment.
(3) The sparse cloud is now manually cleaned and optimized to improve resolution, accuracy and precision of the 3D model. This is achieved by changing the tolerances in the following

camera alignment parameters: (1) Reprojection error; (2) Projection Accuracy; (3) reconstruction uncertainty; (4) The number of cameras used to determine each point.

(4) The cameras are now realigned and will yield a better qualitative model with less spatial error.

(5) The printed 12-bit markers (Figure 1.4.3) visible on the photographs are automatically detected by the software and are used to scale and orientate the model by running python scripts (Photoscan Python Reference, 2016). A minimum of three markers on at least three images should be detected for accurate geo-referencing. Due to the 90° angle of the markers and their known distance, an x-y (z = 0) reference plane can be calculated using the scripts to correctly orientate the model in 3D space. The markers are placed as far from each other as possible as it reduces the relative measuring error (Mallison and Wings, 2014).

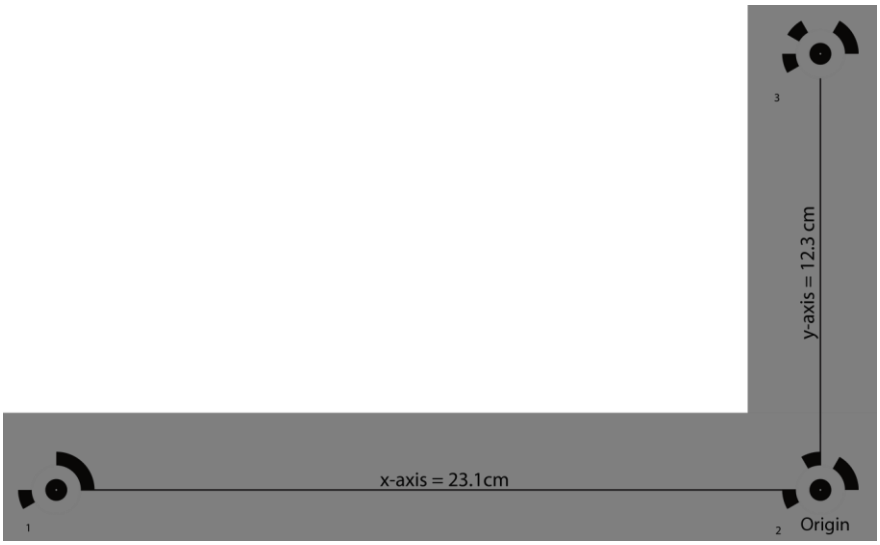

Figure 1.4.3. Schematic illustration of the marker setup used in the experiments.

(6) Next, all remaining points are used to construct a high-density point cloud that is a very close representation of the real 3D subject. At this point, accurate DEM's can be extracted from the dense point cloud.

(7) The dense cloud can be turned into a polygon mesh which consists of triangles that connect the points.

(8) A texture map can be computed from the photographs by assigning (U, V) coordinates to each triangle vertex that represents a point in the texture map. These coordinates allow to crop a triangle in the texture map and project it onto the corresponding triangle of the mesh (Tavani et al., 2014).

(9) Based on camera positions and angles an ortho-rectified image can be produced that is geometrically corrected photograph that can be used to measure true horizontal distances. A ortho-rectified photo has been adjusted for topographic relief, lens distortion and camera tilt (Gwinner et al., 2016).

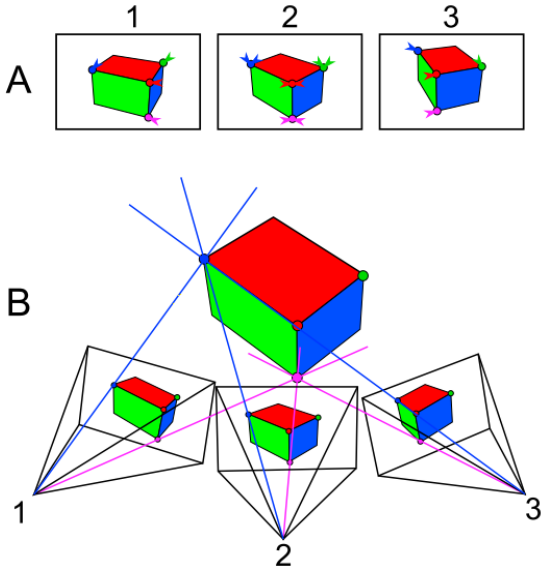

Figure 1.4.4. Schematic drawing of the two main image processing steps in SfM. (a) - An algorithm finds specific known points across all images taken from different viewpoints. (b) The algorithm compares the points obtained in step (a) from all images to find corresponding image parts and mathematical relations between the parts (from Galland et al., 2016).

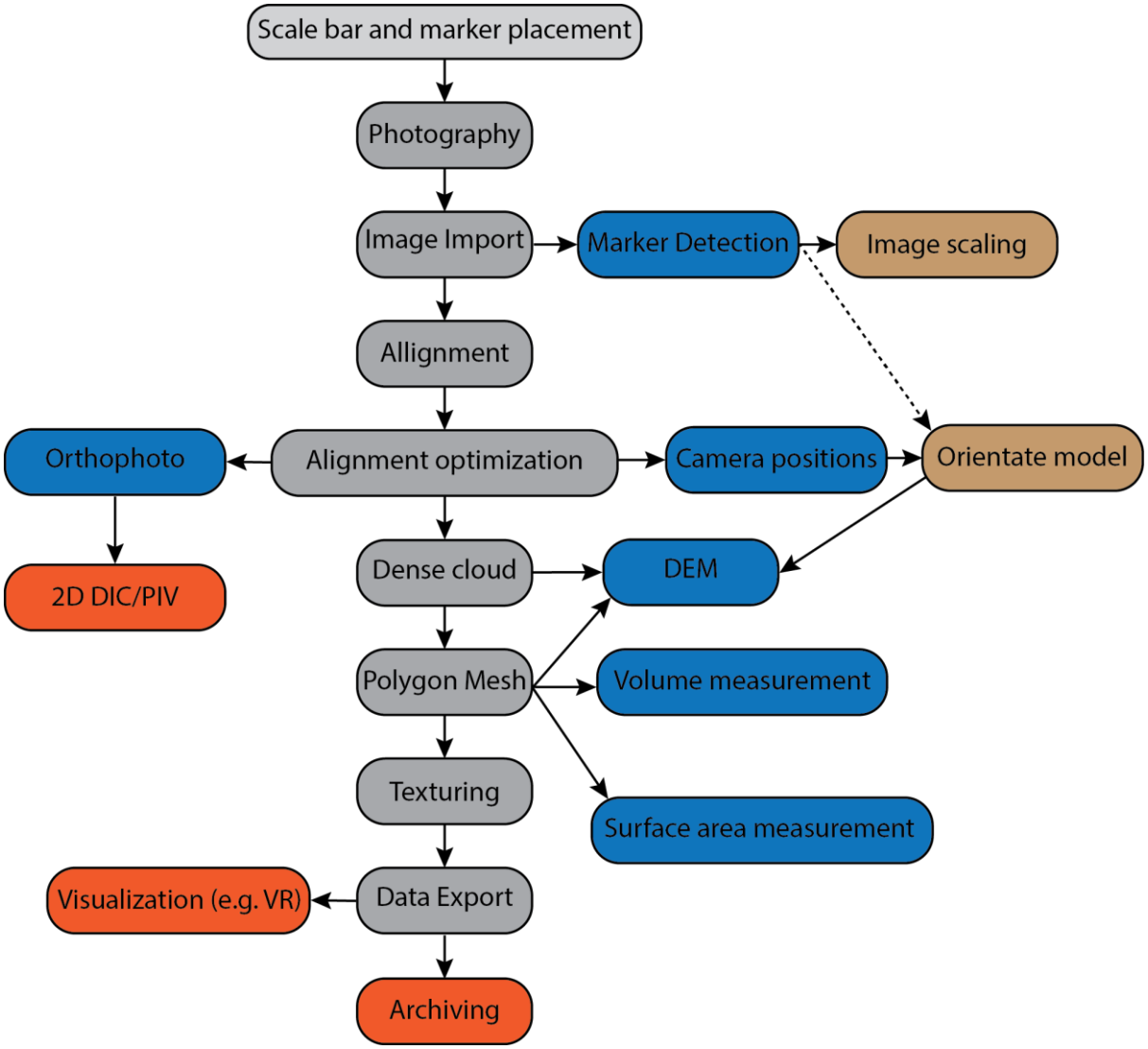

Figure 1.4.5. Standard photogrammetry workflow diagram

The potential maximum resolution of photogrammetry varies considerably. At the extreme, 3D models generated by photographs taken with scanning Electron microscopes (SEM) can show nanometer resolution (e.g. Piazzesi.,1973; Kearsley et al., 2007). Models generated from e.g. old analogue satellite photographs cover the lower part of the spectrum. The quality of models constructed with photogrammetry is dependent on many factors such as: (1) Camera resolution; (2) Camera calibration; (3) Angles between photos; (4) photo redundancy; (5) Photo orientation and quality; (6) Data processing accuracy; (7) Distance to subject. The maximum resolution of a model depends on the resolution of the camera sensor, focal length and the distance between the sensor and the object. High-megapixel consumer grade DSLR cameras allow the creation of models with resolution measured in the tens to hundreds of micrometers. The resolution of the 2D photographs and that of the reconstructed 3D model are not equal. In 2D-photographs the resolution is a measure of the ratio between the size of a pixel on the image sensor and the size of a pixel on the object:

$$Pixel\ Size\ (_{ground}) = \left(\frac{d}{f}\right) * \ Pixel\ Size\ (_{image\ sensor}) \quad (1.18)$$

Where, *Pixel Size (ground)* is the size of a pixel on the surface of the model, (*d)* the distance between the focal point and the object, (*f*) the focal length and *Pixel Size (image sensor)* the size of a pixel on the camera sensor, this can be found by dividing the size of the sensor by the maximum resolution of the camera.

With 3D models the resolution depends on the number of known points in the reconstructed model, this is tied to the smallest known features in the photographs used for the reconstruction and is thus tied to *equation 1.18*. Quantitative deformation monitoring of analogue models in the laboratory can be carried out using photogrammetry techniques to measure: (1) topography; (2) topography changes; (3) horizontal and vertical displacements; (4) volume and volume changes; (6) surface area and surface area changes. This technique can be used to monitor the surface evolution of the analogue models and to image internal structures of the model at the end of the experiment. The ortho-rectified images produced can be used for very high-quality 2D DIC (Rosu et al., 2015 b).

1.4.7 Implementation in the laboratory and experimental setup

The implementation of Photogrammetry in the laboratory involves three successive steps: (1) image acquisition, (2) image processing, and (3) data analysis.

Image acquisition

To produce DEMs, orthorectified images, point clouds, meshes and texture maps of the surveyed analogue model surface, it is necessary to have several images of it. To be able to produce high spatial and temporal resolution models of the dynamic surface, it is necessary to acquire images from multiple synchronized cameras (e.g. Galland et al., 2016). Synchronized cameras have the advantage of being able to take a snapshot of an exact point in time during the deformation process. The synchronized triggering was achieved by using a digital remote/timer switch connected to the remote-control terminal on each of the cameras via stereo cable splitters for all the cameras, the remaining connections can be used in case more cameras are desired. The camera settings are computer controlled using 'Smart Shooter 3 PRO®' by connecting a USB 2.0 cable to each of the cameras going to a central powered USB-hub, then the main cable from the hub goes to the computer. The large advantage of this is that most camera settings can be easily monitored, changed and controlled (e.g. shutter speed, clock, f-stop, ISO and file naming), simply by changing the necessary parameters in the software. Manually changing and adjusting camera parameters would be very tedious and risky as cameras can accidentally be put out of focus or changed its spatial position. The other advantage is that it allows to directly download the images to the computer instead of having to remove each of the SD-cards. USB triggering is possible but not desired due to the 100ms latency of USB 2.0 per camera, amounting to a total of 900ms (9x cameras) between the first and last camera triggered. Care should be taken though when controlling the cameras from both the USB and remote trigger switch as signal

interference can cause the cameras to lose synchronization and fire their shutters at different times or not at all, which can be a disaster if it happens in the middle of the experiment as filtering thousands of photographs across all cameras is not a desired task. The following workflow was found to work best with our cameras: (1) Connecting the cameras through USB for changing settings, (2) disconnecting USB and connecting the remote triggers, (3) shooting. Depending on the cameras and triggering mechanisms used this might or might not be a problem. In our laboratory, we used between 9-11 standard DSLR (digital single-lens reflex) cameras with the standard 18-55mm kit-lenses (Table 4). Each of the cables going to a specific camera are sticker labeled with a fixed number that simplifies to distinguish between the cameras and is very handy for troubleshooting purposes. Inside the software, the cameras are also labeled with the same numbers. As the number of cameras increases, so does the spatial resolution due to the extra view-angles and the spatial error decreases.

Camera	Number of Cameras	Focal length	Resolution (Megapixels)	ISO	Aperture	Crop factor
Canon EOS 1100D	8x	35mm	12.2	200	f/16	1.6x
Canon EOS 700D	3x	35mm	18.1	200	f/16	1.6x

Table 4 - Cameras used in the setup, including most important camera parameters.

The focal length and camera settings on all cameras are identical to ensure that all photos taken have the same properties to avoid heterogeneities (e.g. over-under exposed sections) in the SfM models (Mikolajczyk et al., 2005). By having homogeneous camera settings, the overall error of the produced datasets is lowered. 35mm focal length was used due to: (1) The limited amount of space, (2) small amount of lens distortion. *Agisoft Photoscan*® recommends to use a focal length from *20 to 80 mm* interval in *35mm* film equivalent (Agisoft Photoscan User Manual, 2016). The focal length with the lowest amount of distortion for Photogrammetry has proven to be *50mm on 35mm* equivalent. As the APS-C sensors in canon cameras have a crop factor of 1.6x it is necessary to multiply the focal length by the crop factor to obtain the *35mm* equivalent focal length:

Crop factor x focal length = 35mm focal length equivalent,
1.6 x 35mm = 56mm.

This means that our *35mm* lens has an equivalent field of view/focal length of a *56mm* lens on *35mm* equivalent, which is very close to the ideal 50mm.

High aperture values *(f/8 - f/16)* were used to ensure the maximum *depth-of-field* that will produce sharp images of the entire surface of the analogue model. This is required because most of the cameras are positioned at an angle of 45° to the center of the analogue model. Care should be taken not to go beyond *f-stops* of *(f/16)* as this will induce diffraction and

lower the overall sharpness of the images (Mallison and Wings, 2014). A balance must be found between *f-stops*, *angle of the cameras relative to the center of the subject* and *distance to the subject*, as to shallow angles places the foreground and background of the model further apart and requires higher *f-stops* that induces more *diffraction*. It was found that angles between *20-60°* yielded the best results. To shallow angles (*<20°*) will produce less accurate 3D reconstructions as not enough view-angles are present for full 3D reconstruction. On the other hand, higher than *60°* angles requires the cameras to be positioned further away from the models, that will lower the spatial resolution, or higher f-*stops* must be used (higher than *f/16*), this in turn produces lower resolution 3D reconstructions due to the decay in sharpness of the photographs induced by *diffraction*. The cameras are mounted on a custom-made photogrammetry rig (Figure 1.4.6).

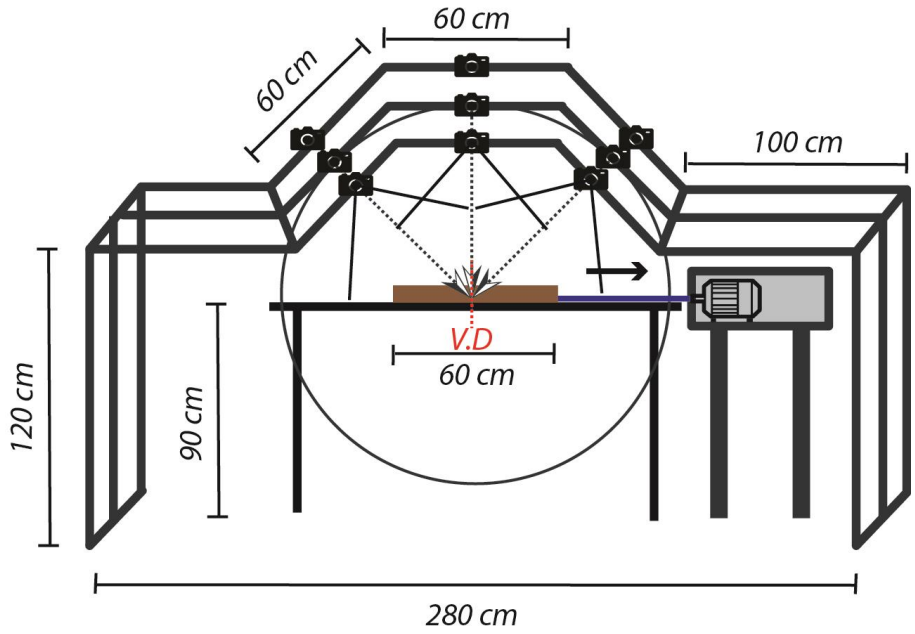

Figure 1.4.6. Schematic drawing of the photogrammetry rig setup used to monitor the experiments. The cameras are mounted at a regular spaced distance from each other.

The camera frame is composed of three longitudinal bars that can be adjusted vertically to the correct height. On each of these bars 3x cameras are mounted, that gives a total of 9x cameras mounted on the rig.
To be able to position the cameras uniformly in 3D space (Figure 1.4.7), the following parameters should be obeyed:

(1) The distance between a camera and each of its direct neighbors is the same.
(2) The difference in angle on the x-y-z axis between each camera and its direct neighbors is 45°.
(3) The distance from the lens of the camera to the center of the analogue model is the same for all cameras.

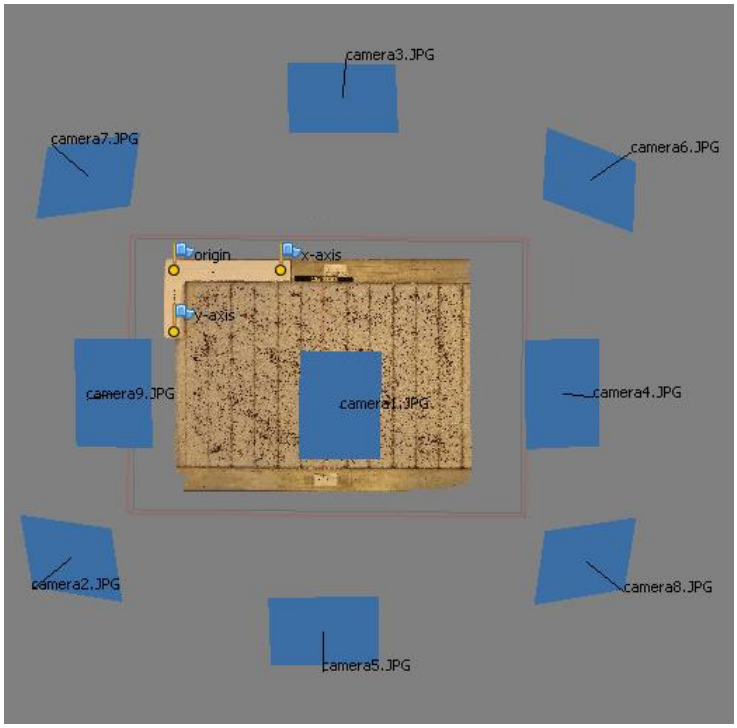

Figure 1.4.7. Top view of the cleaned 3D reconstructed textured polygon mesh from nine photographs including camera positions for the initial time step of the Brittle-Ductile analogue model deformation with 15° inversion.

This implies that the frame should have the shape of an imaginary sphere with a fixed radius (r), where the center of the sphere is the center of the analogue model and the lenses sit on the surface of the sphere. The central camera of the frame represents the z-axis direction and is thus positioned with the lens straight down (Figure 1.4.8). The height to which each of the three bars should be positioned and the distance between them is calculated to comply with the necessary parameters described above. The number of photographs taken in the interval *(Δt)* depends on the following factors: (1) size of the camera storage or USB transfer speed, (2) computational power available, (3) storage capability, (4) data transfer speed. It was found that taking a photographs every *7 seconds* during a *3-4-hour* experiment would yield *80-90GB* of image data. This yields *≈1200* fully reconstructed 3D model frames (incl. DEM's, ortho-photos, point clouds, polygon meshes). This amount was within our computational power and storage capability. Higher resolution cameras will produce larger photographs that require more storage capabilities and require more computation during processing.

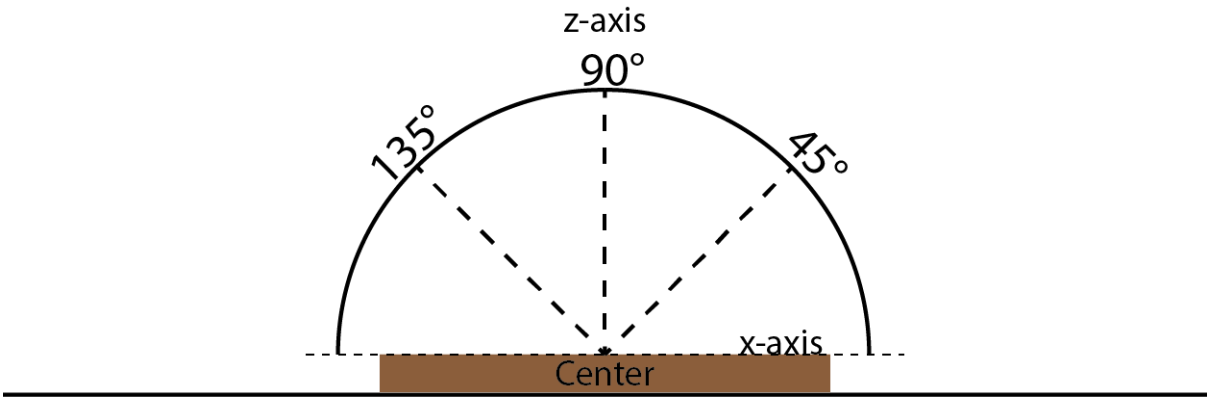

Figure 1.4.8. Schematic front-view (Z-X plane) of the cameras mounted on the central longitudinal bar of the rig, showing the positions and angles of the cameras relative to the center of the analogue model.

Image processing

For the 3D reconstruction, a simple consumer-grade desktop PC was used. To be able to see 3D deformation through time, dynamic 4D reconstruction is required, where each 3D model produced represents a single 3D frame in the 4D sequence, and thus *≈1200* 3D models must be reconstructed and rendered. To reconstruct and render large number of 3D models, hardware capabilities should be used that are well beyond the hardware specs a simple laptop, and depending on the reconstruction quality level could require supercomputer architectures or computer clusters.
Agisoft Photoscan professional is a very advanced photogrammetry software that offers advanced tools in an easy to understand and used GUI. It offers the possibility to automate photogrammetry workflows and the ability to run self-build python scripts. For each camera, a folder is created with the camera label and the photos are copied via the USB hub to each of the folders. Then the cameras are sorted manually and each folder is checked to ensure the number of frames in each of the folders is the same, if not, extra filtering is necessary. This part in the workflow is essential as carrying out 3D reconstruction of different photographs taken at different times will produce very inaccurate 3D models. In the case of photographs taken at the initial or final time steps when the model is static, many photographs are taken (500-100) for ultra-high quality reconstruction, the photographs are loaded as ‘camera from each file’ into the Agisoft file structure. In the case of the dynamic models, each of the labeled folders containing the photographs of a single camera are loaded into Agisoft the Agisoft file structure as multi-frame cameras from folders as cameras’, this structure is then loaded into the Agisoft 4D timeline tools for further processing. For all models the camera positions and tie-points during the camera alignment process can be manually optimized to ensure the best quality models using the ‘gradual selections’ option in the ‘Edit’ toolbar. The products of each time step are: (1) a gray-scale DEM in tagged image file format (TIFF), (2) Ortho-rectified image in TIFF, (3) a high-density point cloud in polygon (PLY) format, (4) surface area and volume measurements, and (5) A polygon-mesh including texture maps (e.g. Tavani et al., 2014).

Data analysis

The DEM's files in TIFF format are exported and can be loaded into many different data analysis programs such as Python, MATLAB®, Surfer®, and ENVI for quantitative analysis of the model surface evolution (Galland et al., 2016). In this study the DEM's were imported into ArcMap® for the following spatial analysis: (1) Slope, slope gradient, Hillshade, Aspect, contours, curvature and height-length profiles. The DEM processing for the Dynamic 4D sequence was automated using ArcPy for ArcMap, of which the results were compiled into time-lapses. Manual maps were produced in ArcMap for the final frames of each deformation phase.
PIV analysis of the inversion phase was carried out with PIVlab in MATLAB® (William and Eize, 2014), which includes vector analysis and vector magnitude analysis. As the extension phase is similar in all brittle models, the PIV analysis was only carried out once. The same applies for the Brittle-Ductile analogue models. PIV analysis was carried out of the inversion phase of each individual model.

1.4.8 Videogrammetry and Dynamic-photogrammetry

The Method of videogrammetry (e.g. Armin Gruen, 1997; Bio et al., 2015) involves almost the same process as Photogrammetry except for the fact that video frames are taken instead of photographs. For videogrammetry, video cameras must be synchronized with each other, and preferentially with a static position to produce an accurate temporal resolution. The upside of videogrammetry is that the temporal resolution compared to dynamic-photogrammetry with photo cameras is much higher, the downside is that the spatial resolution is much lower, most 1080p HD video cameras only offer an image resolution of 2.1 megapixels that is very low compared to most DSLR cameras. Although high resolution video cameras 4k (8.3 megapixels) and 8K cameras (33.1 megapixels) exits, the cost of such cameras, that also offer high frame rates (30-60 fps) is currently too high for most laboratories.
Alternatively, more modern DSLR cameras can take high resolution photographs at very fast rates, e.g. 3-8 fps that allows for the implementation of high speed Dynamic-photogrammetry when needed (e.g. Olivier Galland et al., 2016). For most laboratory experiments such high frame-rates are not necessary. As most tectonic and geomorphology laboratory experiments do not require cinematic frame rates for 3D model temporal analysis, this technique is a suitable alternative to videogrammetry. Surprisingly these techniques have rarely been used in geological laboratory experiments. The upper boundary limiting factor in the creation of dynamic models with video-and-Dynamic Photogrammetry techniques are the computer resources available. To be able to create a decent time lapse with dynamic models very powerful multicore computers are necessary and sometimes it is even favorable to do the computation on computer clusters that will decrease the calculation time dramatically and allow the generation of dynamic models with higher spatial and temporal resolution.

1.5 Visualization Techniques

In Geosciences, most of the spatial datasets are 2D, 3D or 4D. Before the age of modern computers, 3D visualization in geology mostly required manual or mechanical work to produce a physical topography, of which the results were subjected to large inaccuracies, high fragility and difficulty to transfer or transport the models. For this reason, the visualization of 3D datasets was preferentially carried out in 2D in the form of maps and cross-sections that would represent the 3D geometry. After the appearance of computer graphics in the 1980's both 2D and 3D datasets could now be digitized and visualized graphically, which removed the need to transfer physical datasets from one place to another. Visualization of 3D datasets on a 2D surface quickly became much more popular in the academic world as the cognitive burden of extrapolating a 3D surface from a 2D image was removed, which allowed much better understanding of spatial information, scale and depth. More recently 3D datasets can be visualized in true 3D (not on a 2D screen) by using virtual reality projectors or headsets and even augmented reality which increases our spatial perception and perception of depth even further. Currently the fabrication of digital 3D models of geological objects is very inexpensive, and with the internet these models can be shared for visualization and archived all around the world. This gives the science and non-science community access to otherwise inaccessible datasets which ultimately allows for better education and better science. In universities around the world 3D scanned fossils and Rocks (e.g. De Paor, 2015) are used for education and research purposes using the visualization techniques ranging from 2D projection to full virtual reality immersion to 3D printing. Below the observational techniques used in this study will be discussed.

1.5.1 Virtual and augmented reality (3D)

Our brains are constantly calculating distances, volumes and sizes to understand the world around us. As Geosciences advances, the complexity and amount of data obtained also increases, which makes it increasingly difficult to describe 3D spatial patterns in 2D with words or numbers (Vitek et al., 1995).
Computer-based visualization is increasingly more important in Geosciences. New visualization techniques permit new ways of viewing and interpreting data that provide researchers with different perspectives to the same dataset (Thurmond et al., 2005). Visualization of complex surface and subsurface dataset has been an area of significant research and development, particularly within the physical geography and petroleum industry (e.g. Tinker, 1996). Recent studies carried out by Chunyan Deng et al., (2016) and Wood et al., (2016) showed that applying Virtual reality (VR) and augmented reality (AR) to field geology, teaching of topographic maps and surficial processes studies, greatly helps to develop 3D thinking, reduce teaching cost, improve students learning efficiency and enhance learning interest. What sets apart Virtual reality from 3D visualization on a 2D surface (e.g. compute screen or projector surface) is that modern VR provides us with full immersion, which greatly enhances our perception of the 3D space and scale. Through sensitive head and eye tracking, stereoscopic rendering for each individual eye, the accuracy of depth perception is much more significant with VR than with traditional 3D

visualization techniques, which is very important to be able to grasp the true scale and geometry of geologic. The generated textured 3D polygon meshes in this study are analyzed in a room scale Virtual reality environment using the HTC-vive® headset. The static environments including cross-sections are constructed with the source 2.0 engine using the destinations tools®. For the observation of only the top-view 3D models constructed at the end of each deformation phase, all models can be visualized with a variety of different VR headsets using the *Sketchfab*® application that can be downloaded in SteamVR®, these models can be found here: https://sketchfab.com/TecLab/
Recently Google Inc. has made *Google Earth* compatible with Virtual Reality, this has particular interest not only for Geoscience professionals but also for students, as one of the main scouting tools for fieldwork locations in modern times is *Google Earth*. To be able to view the 3D surface of the Earth in a fully immersive environment allows much better perception of depth, scale and distance, which has large advantages over traditional *Google Earth* observations on a 2D computer screen. Hopefully in the near future professionals and students that are preparing for fieldwork will be able to use this tool to deepen their spatial knowledge of the future fieldwork location.

1.5.2 3D and 4D printing

Geoscientist are some of the most prolific producers of 3D data. The fundamental problem in geology is scale, booth temporal and spatial scales are hard to grasp as sometimes not enough cognitive sensor information is present to understand a geologic process or setting in 3D and 4D. Complex aspects of topography and internal geometry are easier to understand when using 3D models than using traditional contour maps because our brains do not have to create a 3D model from 2D data. The power of 3D printing lies in the hands-on interactivity, portability and the lack of necessity of electronic devices for 3D visualization. 3D printed models causes' haptic feedback, one of the most powerful sensor inputs used in geosciences, which immediately gives a sense of geologic scale and significance (Declan G. De Paor, 2015). A 3D printed model can be 'inferred' as a virtual reality system (Franciszek and Chris, 2016; Declan G. De Paor, 2015) that offers the most natural form of direct vision and touch, as topographic macro and microelements changes can be explored by the finger's skin sensors and by direct visualization. 3D printed models are cheap, tough, infinitely customizable and easy to produce. The workflow of 3D printing involves a multistage process:

(1) Importing point cloud, polygon-meshes or a textured mesh into CAD software.
(2) Creating a solid 'watertight' model with a volume.
(3) Extra cleaning or adding features to the model.
(4) Insuring sufficient model-wall thickness for the desired type of 3D printing material.
(5) Exporting to a desired 3D printing service or to an owned printer.
(6) Printing.

The combination of 3D printing with any of the multitude of 3D scanning technologies, e.g. computed tomography (e.g. Knecht et al., 2012), laser scanning or photogrammetry, creates a 3D photocopier (e.g. Rengier et al., 2010). Geoscientist have used this technique to print

(1) CT scans (Otten et al., 2012), (2) LiDAR and seismic data to understand morphology and stratigraphy (Reyes et al., 2008), (3) extra-terrestrial topography (Horowitz and Schultz, 2012) (4) earthquake distribution maps (Lindqvist et al., 2012), (5) river cobbles, which have been used to investigate weathering processes (Bourke et al., 2008), (6) Rocks and fossils (Declan G. De Paor., 2015).
By printing in multiple colors, geological attributes can be printed over elevation data that can turn 3D topography printing into 4D printing that lowers the cognitive burden to a level where only the temporal dimension remains as a cognitive burden. This is already much better than 2D topographic maps and by using dynamic-photogrammetry to print a sequence of 4D models, the temporal dimension can be easily represented. 4D printing of dynamic-photogrammetry sequences allows a high spatial and temporal resolution, it allows the observation of the surface evolution and internal structures when combined with cross-section photographs or 3D models of the cross sections, or even with CT scans. 3D printing can be used for fast prototyping for geological purposes, such as: (1) reconstruct geologic settings on which laboratory experiments can be carried out; (2) print laboratory equipment; (3) Educational purposes; (4) The utilization of the physical models in a variety of geologic experiments, e.g. volcanic system reconstruction, tectonic modelling, geomorphology modelling, basin filling reconstruction, fault system reconstruction and many more. What makes 3D printing such a powerful prototyping method in recent years is the fact that there are a large variety of different materials that can be printed for different purposes such as: Platinum, gold, Sterling silver, Plated metal, Strong and flexible plastic (PA 2200), Frosted Detail plastic (UV curable acrylic plastic), Acrylic Plastic (Acrylic based photopolymer), Metallic Plastic (Alumide®), Brass, Bronze, Steel, Full Color Sandstone, Porcelain, Castable Wax, Elasto Plastic (off-white elastomer), Aluminium, High Definition UV curable Acrylate, PLA. This list was taken from the 3D printing service *Shapeways*® based in the Netherlands. With a multitude of industries jumping on 3D printing techniques such as Aerospace industries, Healthcare sector, Food industries and many more, it is just a matter of time before every Geology department starts extensively using 3D printing techniques, whether it is for the printing of lab equipment, fast prototyping of the usage of 3D printed parts in experiments.

2 Results

All results of the analogue models are given in the following format: (1) top views, (2) 2D-DIC, (3) Ortho-photos, (4) DEM's, (5) Extracted datasets from the DEM's, (6) Top view of the textured polygon-mesh, (7) A full virtual reality environment and (8) Relevant cross sections. Due to the ground-up development process of the photogrammetry system already during the experiments it was not possible to capture the deformation of the early brittle models using this setup. In the sections where a specific dataset was not presented, the dataset does not exist for that specific experiment. An overview of the experimental parameters is given in the table below (Table 5). Sedimentation was carried out for each of the models only during the extensional phase for every *0.5 cm* of displacement. During the sedimentation process the photogrammetry process was paused momentarily, it was immediately resumed after sedimentation was completed. The average sedimentation time was ***≈30 seconds***, this represents a gap of 4 photographs if photographs are taken each *7 seconds*, leading to a gap in the spatial deformation monitoring of *0.5 mm*. The numbering of the faults is based on the formation history, lower numbers are formed first. Relative formation timing is unknown. 'Fixed plate' and 'mobile plate' terminology is used in every top view and cross section. Black colored faults represent normal faults, while red faults represent thrust faults. Forethrust and backthrust terms are used and based on the mobile plate in the system. The rift basin formed in extension models with a ductile layer are defined by flanks and its shoulders. The width of the deformation zone represents the distance between the two outermost faults found in the top views and cross sections.

Experiments	**Syn-tectonic Sedimentation (Extension only)**	**Type**	**Inversion Angle (degrees)**	**Extension (cm)**	**Inversion (cm)**	**Thickness (cm)**
GS-B-Ext	yes	Brittle	-	6 cm	-	4 cm
GS-B15	yes	Brittle	15°	6 cm	7 cm	6 cm
Gs-B15-v2	yes	Brittle	15°	5cm	6 cm	4 cm
GS-B45	yes	Brittle	45°	5 cm	6 cm	4 cm
GS-B75	yes	Brittle	75°	5 cm	6 cm	4 cm
GS-B90	yes	Brittle	0°	5 cm	6 cm	4 cm
GS-D15	yes	Brittle-Ductile	15 °	5 cm	6 cm	4 cm
GS-D45	yes	Brittle-Ductile	45°	5 cm	6 cm	4 cm
GS-D75	Yes	Brittle-Ductile	75°	5 cm	6 cm	4 cm

GS-D90	Yes	Brittle-Ductile	0°	5 cm	6 cm	4 cm

Table 5 - Overview of all the models and their parameters. The velocity for all the ductile models are the same (6 cm/h). The velocity for the brittle models is variable as these models are largely strain rate independent at this scale.

2.1 Brittle models

In the next sections the results are presented of the deformation of the purely brittle models.

2.1.1 GS-B-EXT: Brittle, extension only and sedimentation

To be able to compare the effect of the variability of inversion angles on the system, a reference model is required to which the results can be compared to. The understanding of the geometry and kinetics of normal faulting is essential in the study of the effect of variable inversion angles.
During the initial rifting phase (Figure 2.1.1), a rift graben developed as the results of the growth and movement of the two-large offset rift border faults (F1). The formed graben is asymmetrical along strike. Progressive extension of the analogue model led to the formation of faults F2 and F3 in the hanging wall (Figure 2.1.2). The in-sequence faulting above the immobile plate tends to move towards the center of the graben (V.D). After applying the rifting phase to the model the faults at the graben surface are not clearly visible due to the syntectonic sedimentation that covers the newly formed faults in the graben infill. Faults that developed within the graben can only be visualized using cross-sections or inferred using DEM's or PIV analysis.

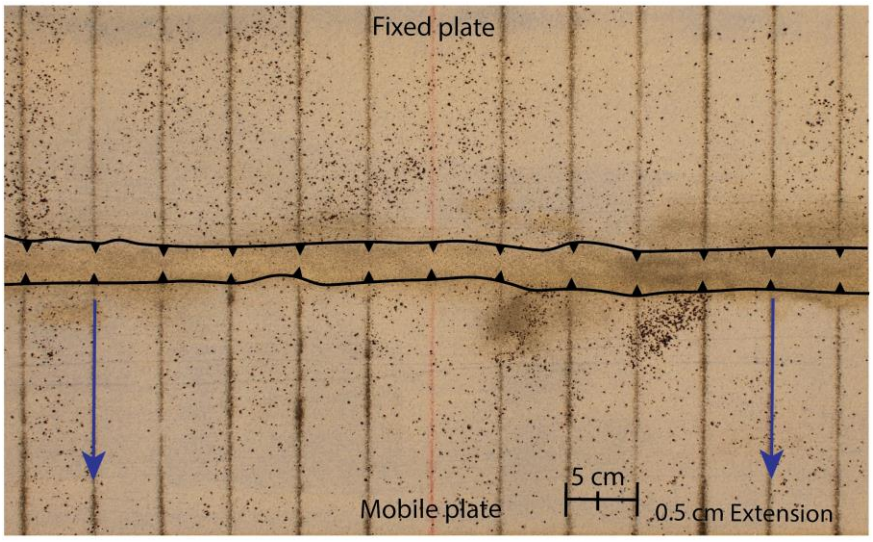

Figure 2.1.1. Top view (ortho-photo) of the experiment at 0.5 cm of displacement. Two opposing faults formed at the graben borders (F1). The Blue arrows represent the direction of extension.

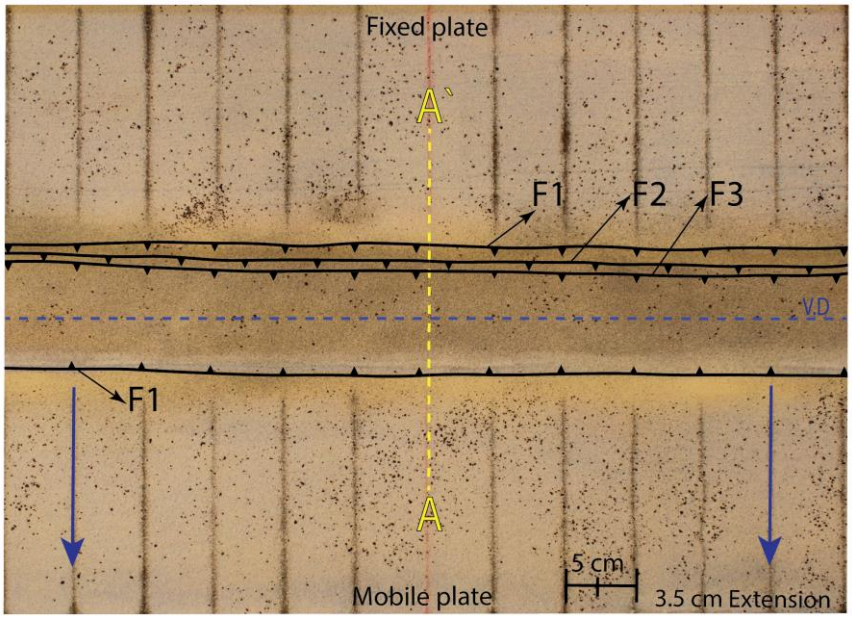

Figure 2.1.2. Top view (orthophoto) of the experiment at 3.5 cm of displacement. Two new faults form in the hanging wall of the moving plate. Two new normal faults formed in the footwall (F2 and F3).

Photograph sequences from 4x cameras were imported into Agisoft Photoscan® for processing. The following results were produced in this software package: (1) Individual textured 3D models, (2) A 4D textured dynamic model of the 3D model sequence, (3) Ortho-photos for PIV and top-view analysis, (4) DEM's that were exported into ArcMap® for further post-processing.

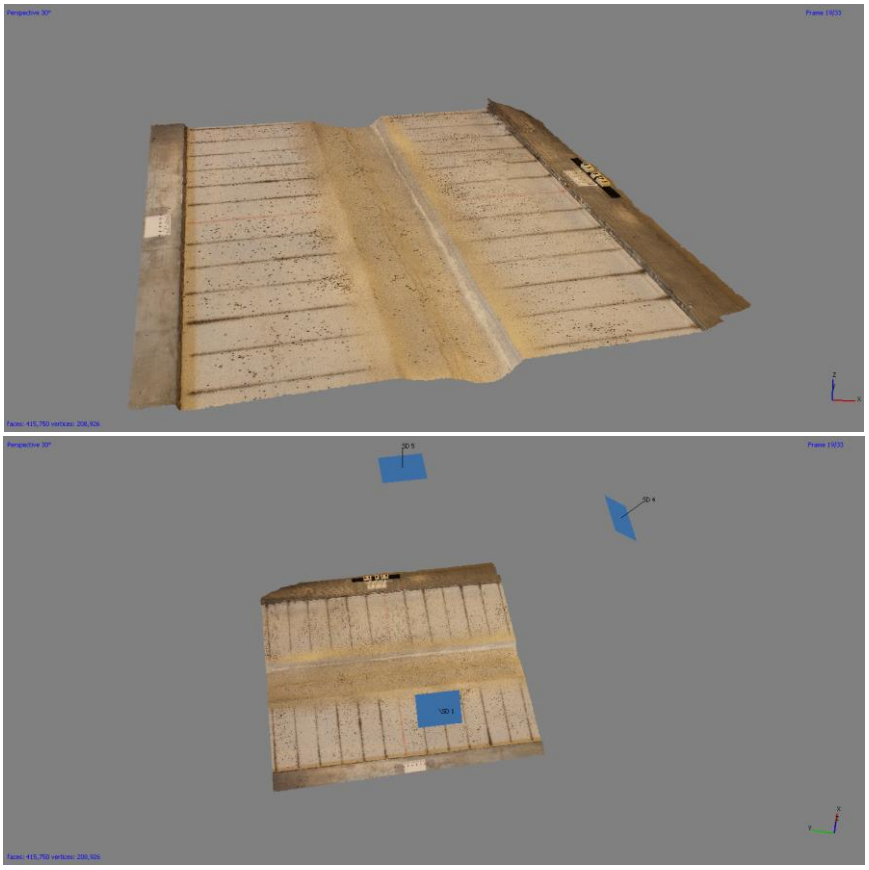

Figure 2.1.3. Screenshot of the 3D model in Agisoft Photoscan at 5.0 cm of extension. Sparse cloud (18.439 points), Dense cloud (2,690,246 points), 3D model (415,750 faces), DEM (1397x1829, 0.0995 mm/pix). The space between each two gridlines is 5.0 cm.

Using the 3D model, the asymmetry of the graben topography is clearly visible. Two main topographic zones are present inside of the graben that are separated by a small ridge right in the middle of the graben (Figure 2.1.3). From the DEM sequences illustrated below the asymmetry of the graben along strike and the difference in topography of the graben infill are clearly visible, the largest depression and slopes are produced above the moving plate (Figures 2.1.4, 2.1.5 and 2.1.6). The interface between the topographic low and high zones are separated by the ridge mentioned above, which runs above the V.D. It has a wave-like pattern, which is clearly visible in the slope analysis diagram (Figure 2.1.5). No calibration for distance was used due to the lack of accurate markers, so all data is based on pixel distance.

DEM analysis

In the figures below digital elevation models (DEM's) of the inversion phase are presented. Three analysis techniques were applied: Color ramp, Slope analysis and color ramp + Hillshade.

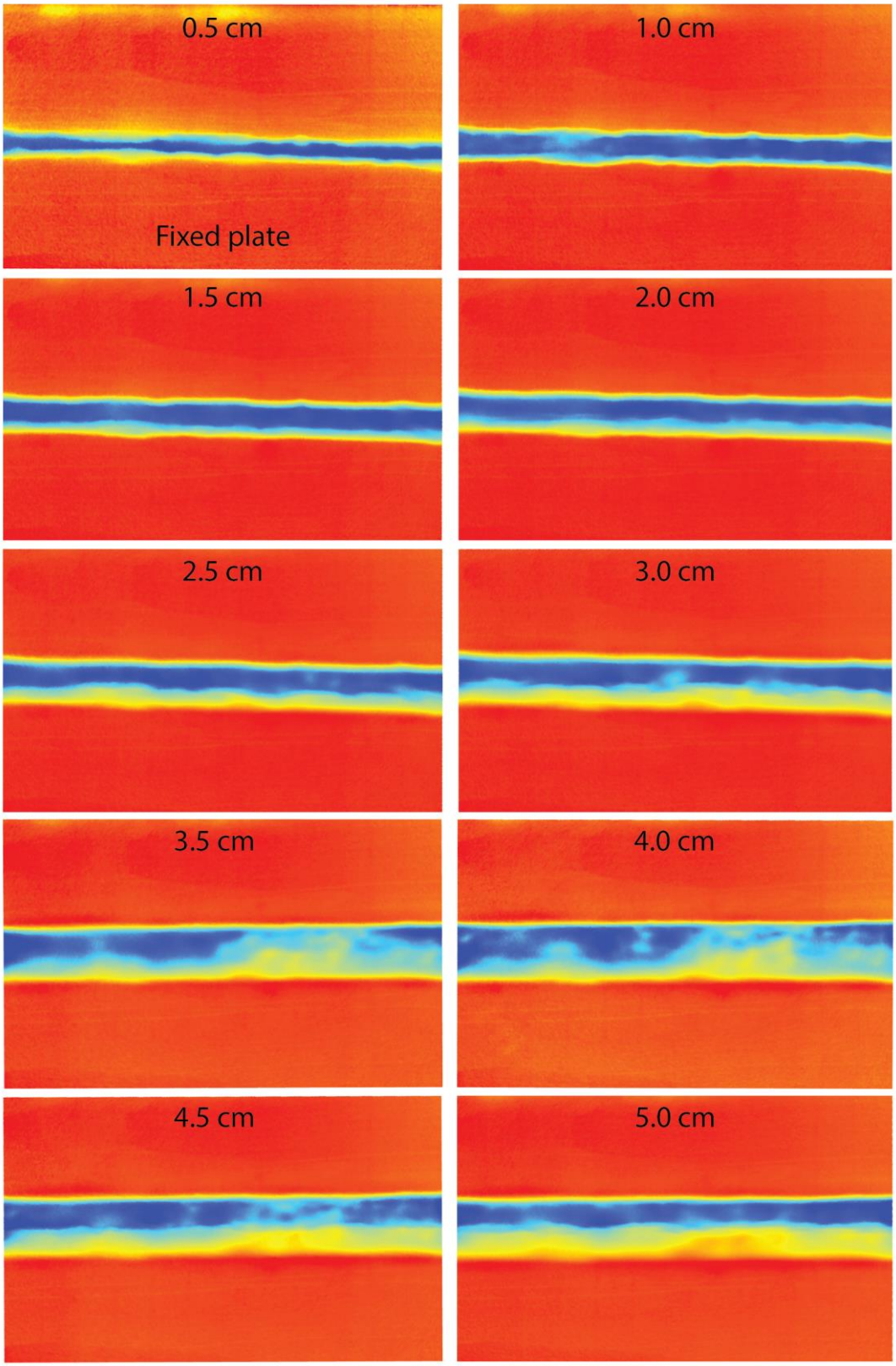

Figure 2.1.4. Rifting phase DEM's as frames (0.5 cm steps), no Hillshade. The Red color represents the surface of the model. The formed depression is characterized by the blue and yellow colors. The deepest zones are represented by the dark-blue color.

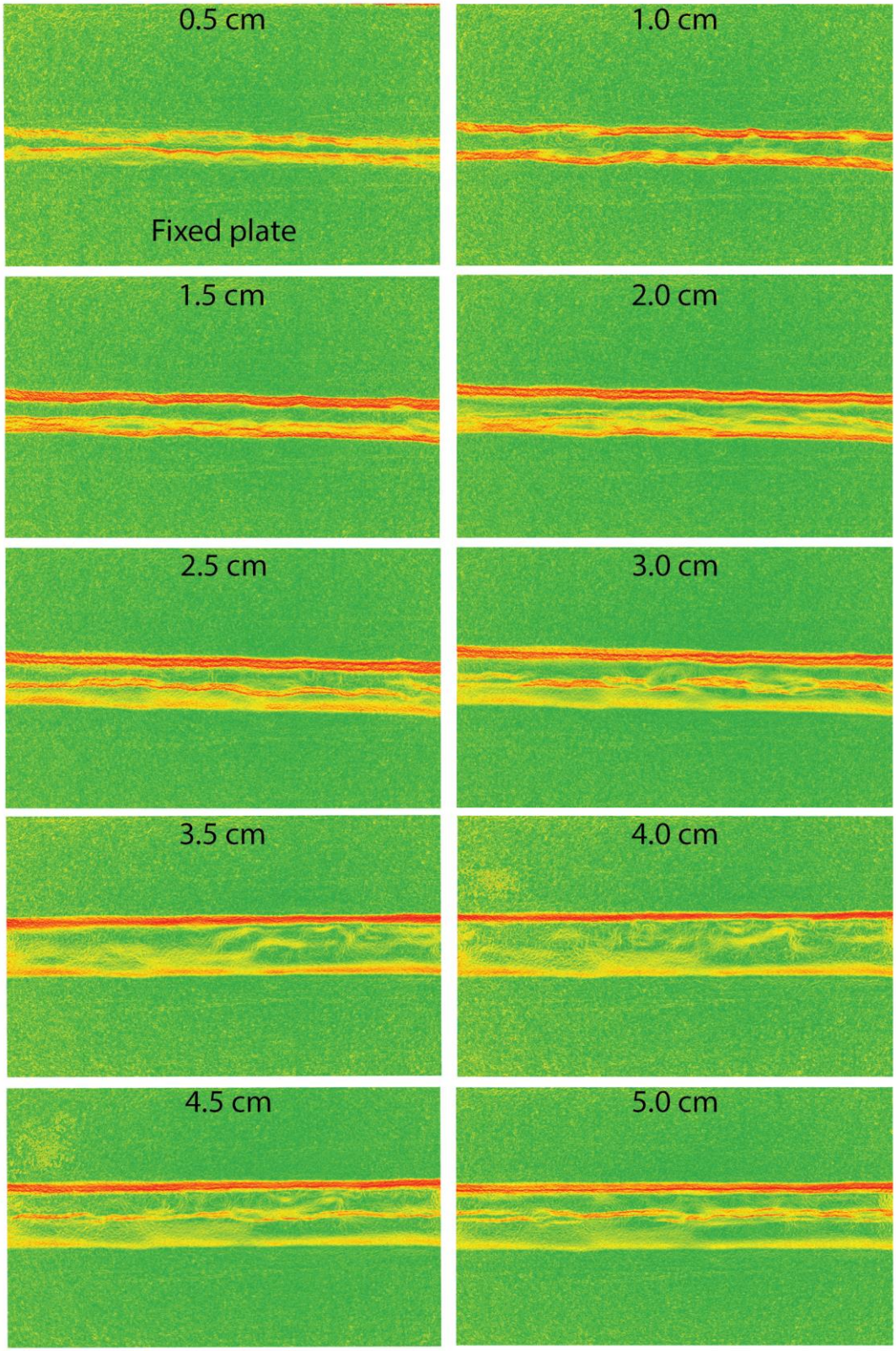

Figure 2.1.5. Spatial slope analysis of the DEM's in ArcMap of each frame of the rifting phase (0.5 cm steps). The ridges with the steepest slopes are red.

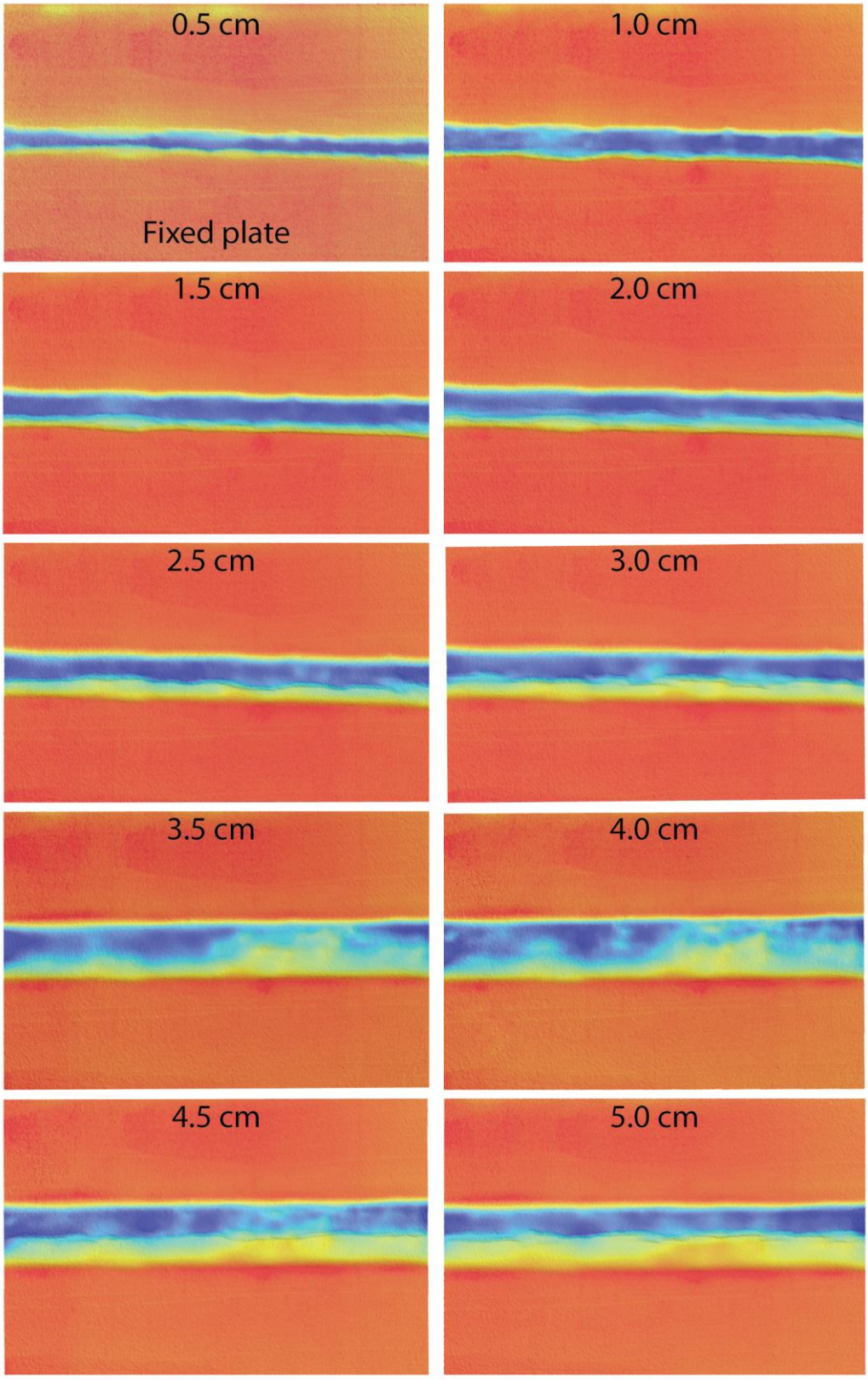

Figure 2.1.6. Spatial Hillshade and color ramp analysis of the DEM's in ArcMap of each frame of the rifting phase (0.5 cm steps). The Red color represents the surface of the model. The formed depression is characterized by the blue and yellow colors. The deepest zones are represented by the dark-blue color.

PIV analysis

PIV vector and vector magnitude analysis of the extension phase was carried out using PIVlab (William and Eize, 2014). Each frame represents a deformation step of 0.5 cm. Below in figures 2.1.7 and 2.1.8 two diagrams with 10x frames of the extension steps are illustrated. The following can be observed in the these diagrams: (1) The vector field starts at the V.D and most vectors point towards the mobile plate, indicating the displacement direction. (2) After the formation of the rift basin border faults (F1) the graben displacement magnitude in the direction of the mobile plate decreases, which indicated that there is growth and slip along these border faults. (3) The vectors at the graben infill flanks point towards the center of the model, which points to some movement parallel to the V.D., the exact meaning of this is not known. (4) Four main rows of vectors are visible in the PIV diagrams, this could represent the individual movement of the 4x fault blocks that developed (F1, F2, F3 and F4). The quality of the PIV analysis of the extension phase was influenced by the following: (1) DIC analysis is very sensitive to 3D non-planar displacement (e.g. steep slopes), resulting in less accurate analysis, which can be observed in the random vector orientation in the graben flanks where the highest amount of vertical displacement occurs. (2) Sedimentation in general and especially sedimentation of sand with the same color throughout the extension phase corrupts the DIC analysis as this causes sampling interference between the different frames, leading to large vector discrepancies (e.g. 1.0cm, 4.5cm and 5.0cm extension visible in the figures below), for this reason PIV analysis is not recommended when syn-tectonic sedimentation is involved. (3) The lack of high contrast surface features greatly lowers the quality of the results as the sampling size of the individual sand grains is normally too low for software recognition.

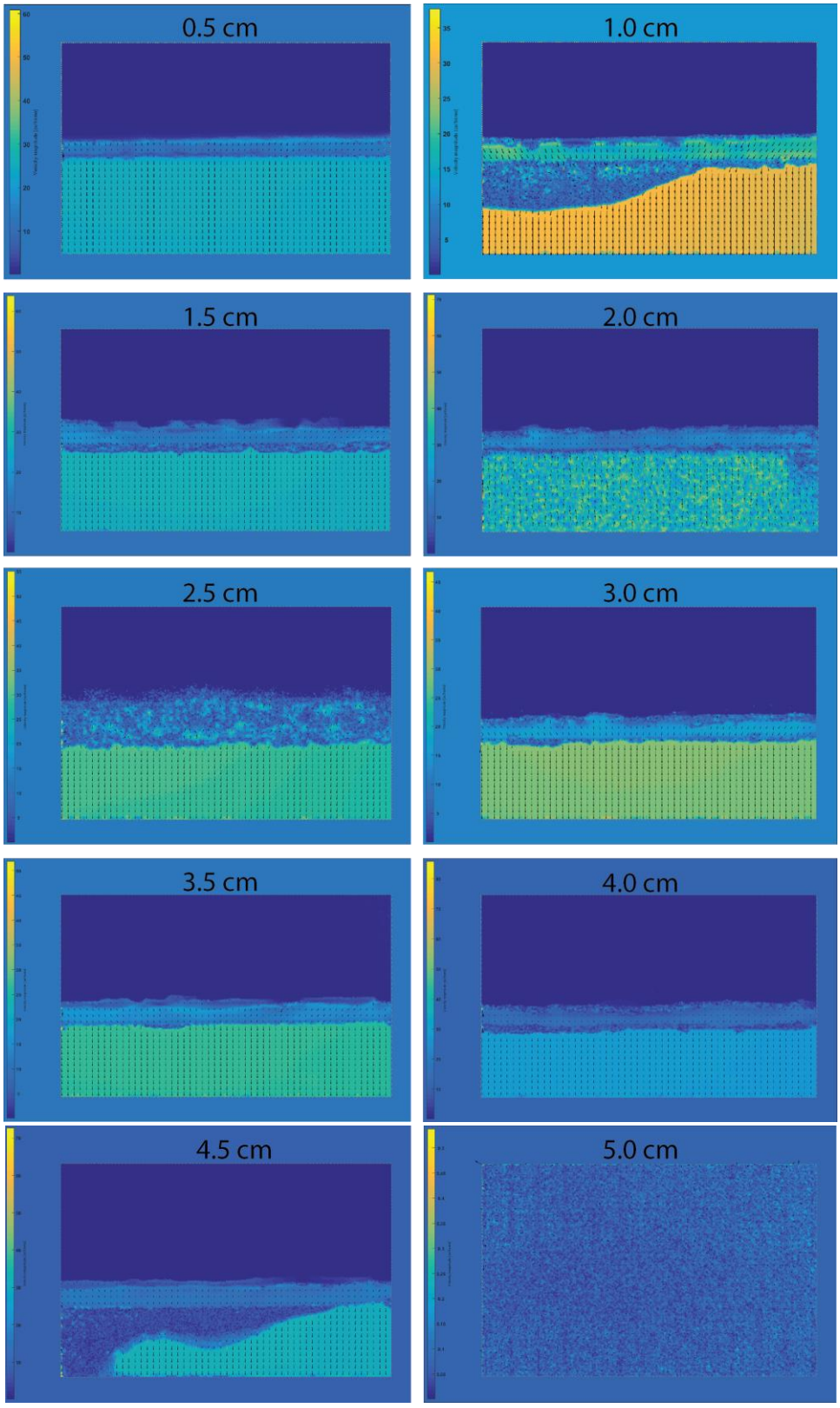

Figure 2.1.7. PIV analysis of the vector magnitude (pixels/frame) of the rifting phase, each diagram represents a step in the extension process. The irregular disturbance zones are the result of inaccurate software vector calculations.

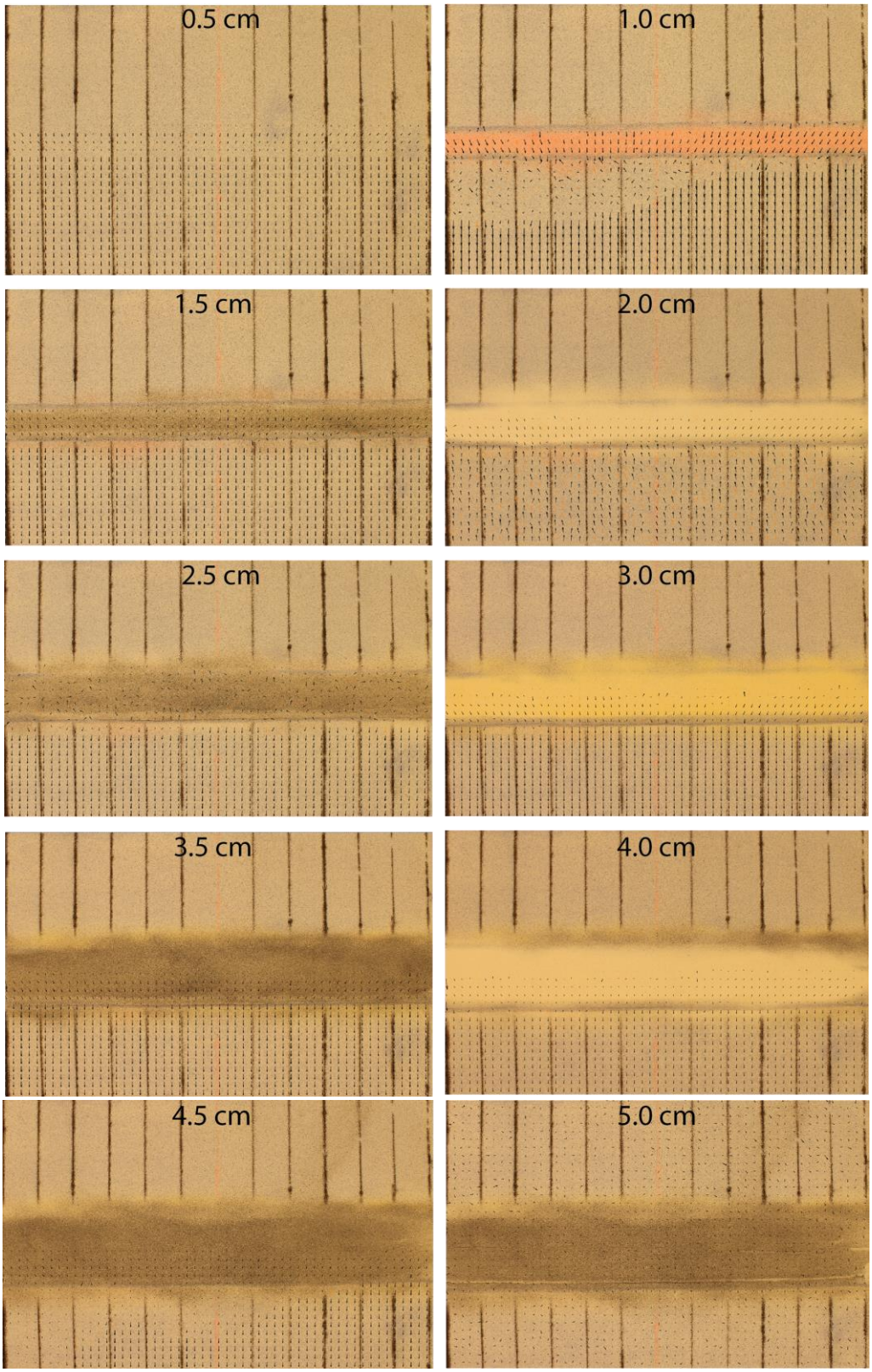

Figure 2.1.8. PIV vector analysis of the rifting phase, each diagram represents a 0.5 cm step in the extension phase. The irregular disturbance zones (e.g. missing vectors) are the result of inaccurate software vector calculations.

Cross-section analysis

In the cross section below (Figures 2.1.9 and 2.1.10) rotated fault blocks formed because of the in-sequence normal faulting of the system is clearly visible. Compared to the top-views, one extra fault is visible in the cross-section (F5). This fault did not extrude to the surface of the analogue model and is thus not visible from the top views. This fault system is characteristic of a soft block/domino style rift system with block rotation/internal. The internal 'wave' pattern inside of the blocks formed due to shear strain interaction with the adjacent blocks. The faults are listric and dip towards the hinterland (V.D). Master border fault (F1) in the footwall has a synthetic relation with the younger faults (F2, F3, F4, F5 and F6). Master fault (F1) in the hanging-wall has an antithetic relation to the graben infill faults. Although not clearly visible one can assume that F2, F3, F4 and F5 are located on the listric master fault F1 above the immobile plate. The fault planes are curved for all normal faults, steepening towards the surface and flattening towards the basement for the graben infill faults. The master normal faults tend to flatten towards the surface and flatten towards the basement. The formed graben is asymmetrical and has maximum thickness at above the V.D. The extruded blocks demonstrate a ramp-flat-ramp structure. All faults are steeper than 50°. The steepness of the faults increases inward towards the V.D. All faults formed along-strike propagation.

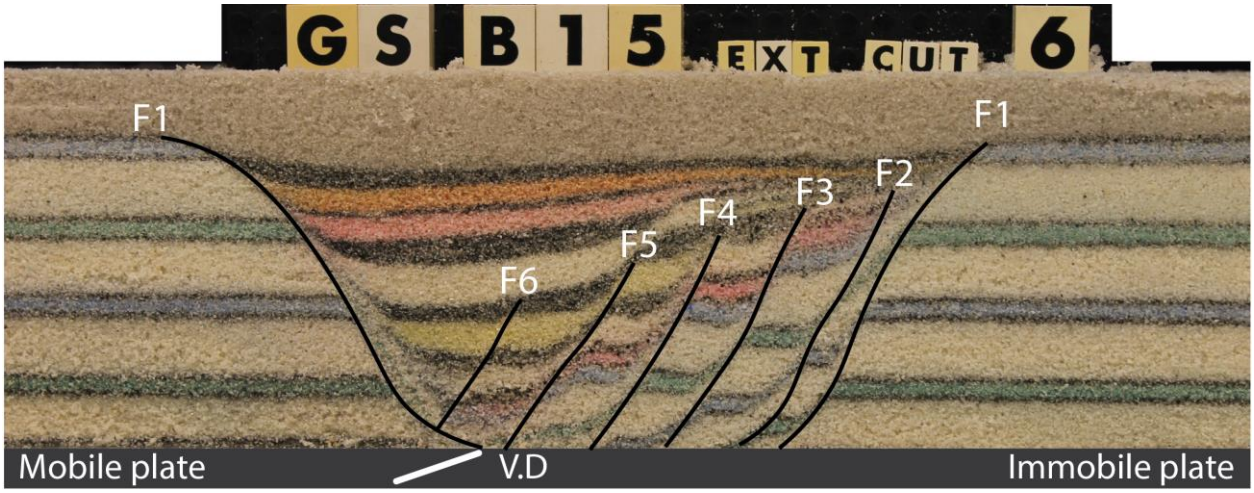

Figure 2.1.9. Cross section of the resulting analogue model of the experiment. This section was taken parallel to the y-axis in the center of mass of the model. All faults in this section are extensional (2x F1, F3, F4, F5 and F6).

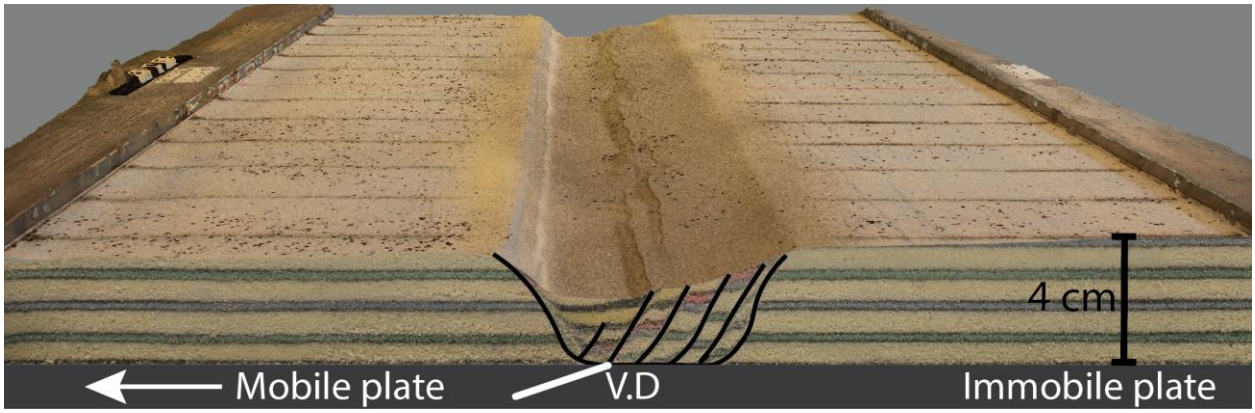

Figure 2.1.10. Combination between the cross-section in figure 2.1.9 and the 3D surface model in figure 2.1.3.

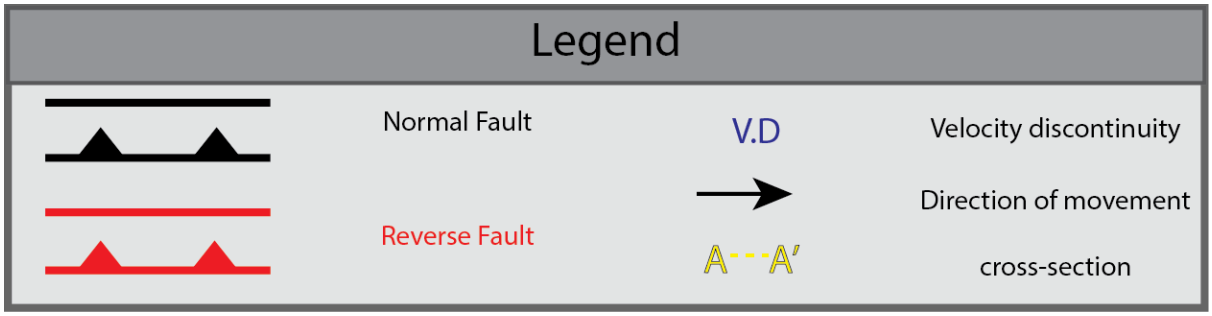

Figure 2.1.11. Legend used in the experiments.

2.1.2 GS-B90: Brittle, Extension and sedimentation followed by oblique inversion

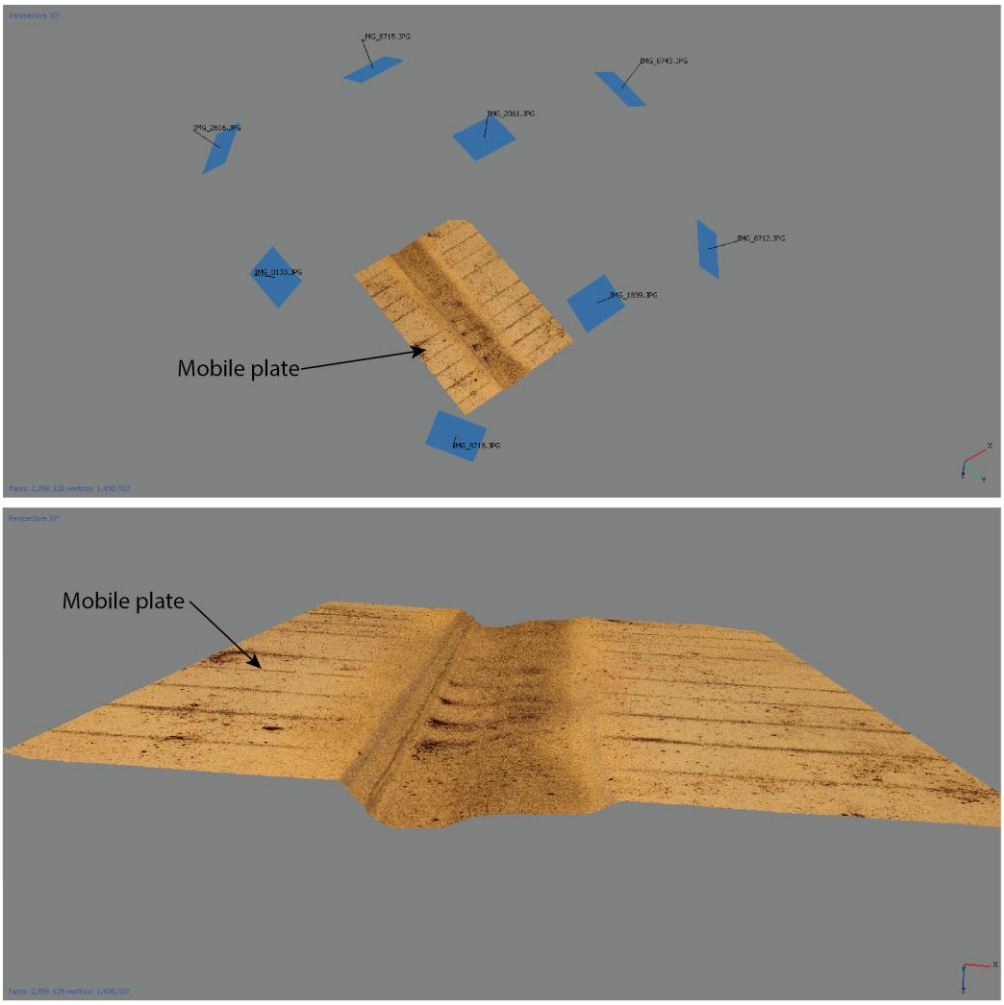

Figure 2.1.12. Screenshot of the 3D model in Agisoft Photoscan at 5.0 cm of extension (8x cameras). Sparse cloud (65,972 points), Dense cloud (20,245,288 points), Mesh (2,856,128 faces). The distance between each two gridlines is 5.0 cm.

The textured 3D model compiled at the end of the rifting phase can be visualized here: https://sketchfab.com/models/9e8558daff3c4193b552e2ae6a8b84b4
The following can be said after analyzing the top-view photographs and 3D model at 5.0 cm of extension: (1) Graben topography and morphology are asymmetrical along strike (Figures 2.1.12 and 2.1.13). (2) There are two main zones inside of the graben that are separated by a small ridge right in the middle of the graben infill. (3) The depth of the graben is maximum below the footwall. During the initial rifting phase a rift basin developed as the results of the growth and slip of two large offset border master faults (F1). Progressive extension of the analogue model led to the formation of faults F2 and F3 in the hanging wall above the immobile plate. After The completion of the extension phase the faults at the surface of the graben are not clearly visible due to the syn-tectonic sedimentation and collapse of the fault topography. Other faults and structures that may have developed can only be identified using cross-sections, DEM's or PIV analysis.

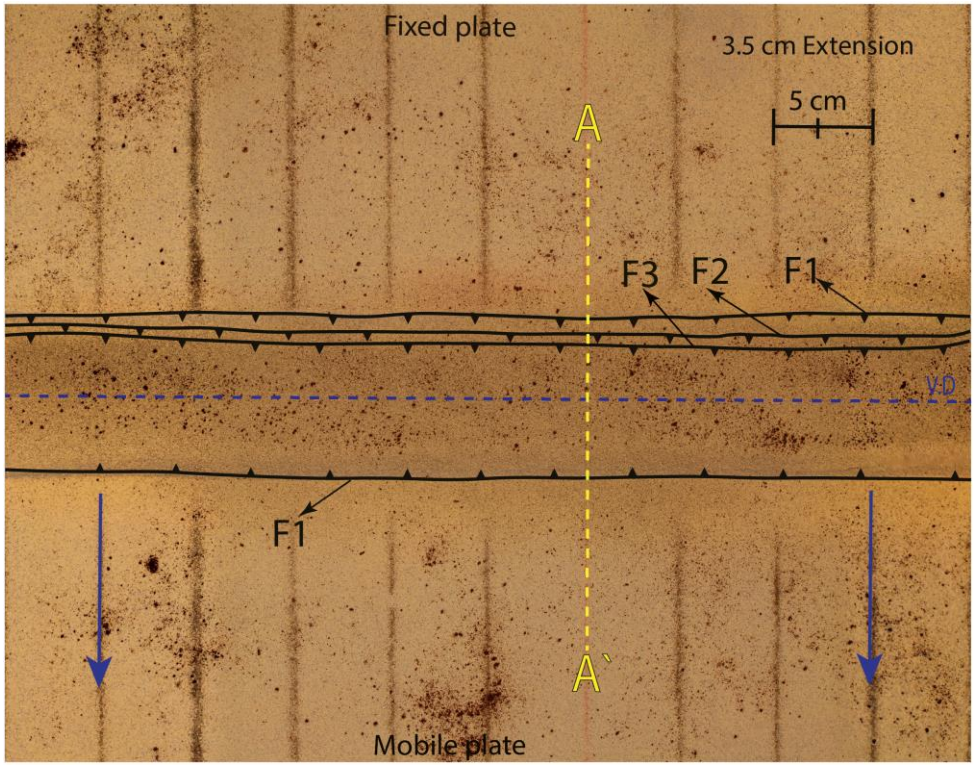

Figure 2.1.13. Top-view of the experiment at 3.5cm of extension (Ortho-mosaic image from Photoscan). Two new faults form in the hanging wall (F2 and F3). The blue arrows indicate the extension direction. A-A' represent the location and orientation where the cross-section was taken.

After the extensional phase, inversion is applied to the system (Figures 2.1.14 and 2.1.15). The textured 3D model compiled at the end of the inversion phase can be visualized here: https://sketchfab.com/models/5a32a19eec624b649e486c8cd881a8c2

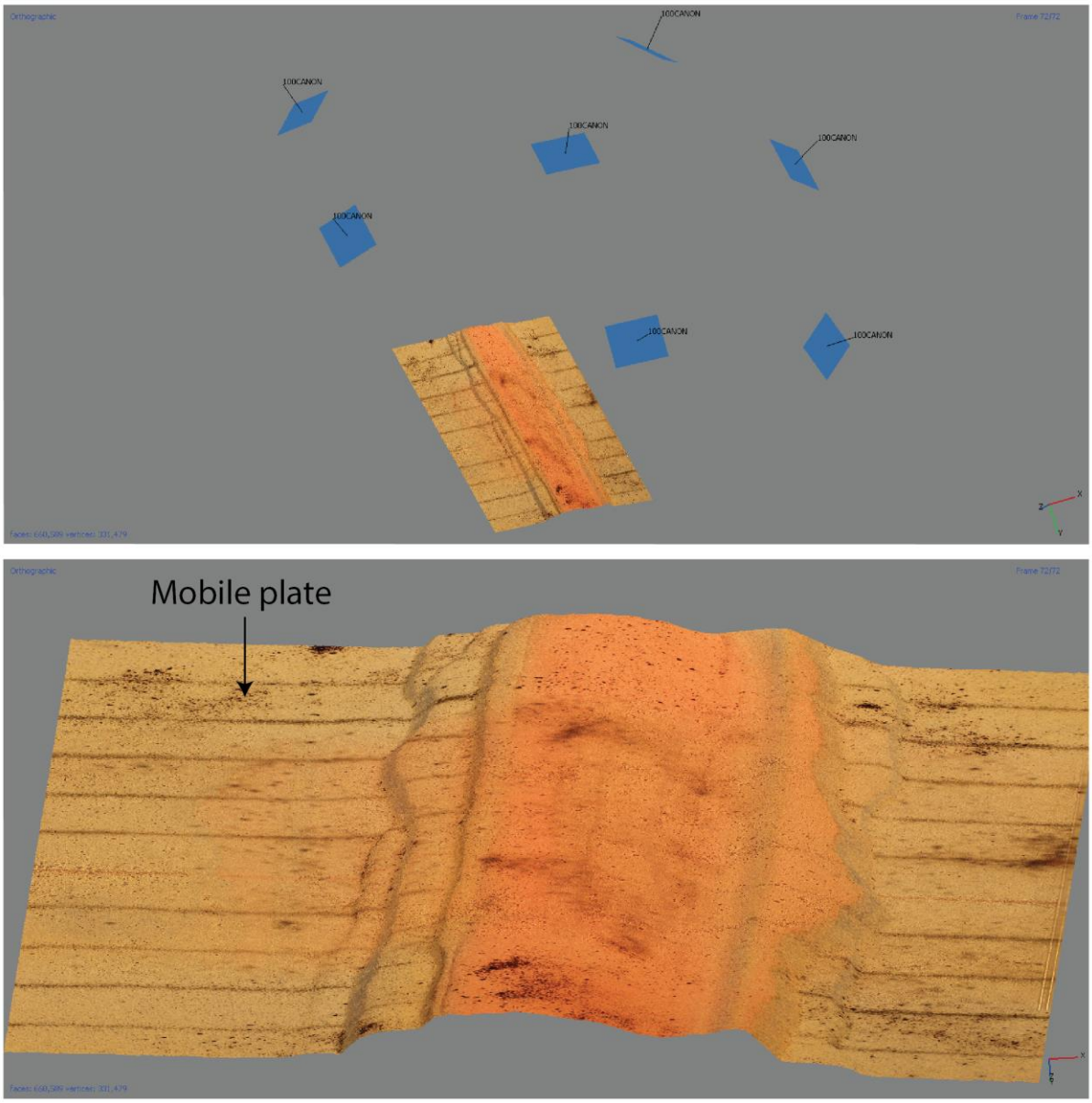

Figure 2.1.14. Screenshot of the 3D model in Agisoft Photoscan at 6.0 cm of inversion. (7x cameras), Sparse cloud (13,885), Dense cloud (3,673,233), Mesh (660,589 faces).

The following can be observed in the figure below: (1) An extensive number of thrust faults formed in both the footwall (R1 and R2) and hanging wall (R2, R3 and R4). (2) From deformation observations and PIV analysis in the next section it was found that thrust fault R1 was first to form, following by shortcut fault (small cover thrust) R2 and R2-(c) which is visible in cross-section (c) at CUT 4, followed R3 and R4. (3) There is no displacement of the line running through the center of the model which suggest that almost no strike-slip components was present in the system during inversion, in turn the movement was

accommodated by the formation of the thrust faults that elevated the graben vertically. (4) The asymmetry of the thrust faults is significant compared to the normal faults. (5) The thrust faults display a branch structure and not all of these faults are continuous along strike (e.g. R2-(c), R4), which disappear by linking to another thrust fault. (6) Small ridges are present between the thrust faults and the normal faults which indicate that reactivation occurred of the border master faults (F1). (7) The magnitude of movement of the graben in the direction of the foreland decreases as the result of the formation of the thrust faults which convert the purely horizontal displacement component of the graben into a horizontal and vertical component**.**

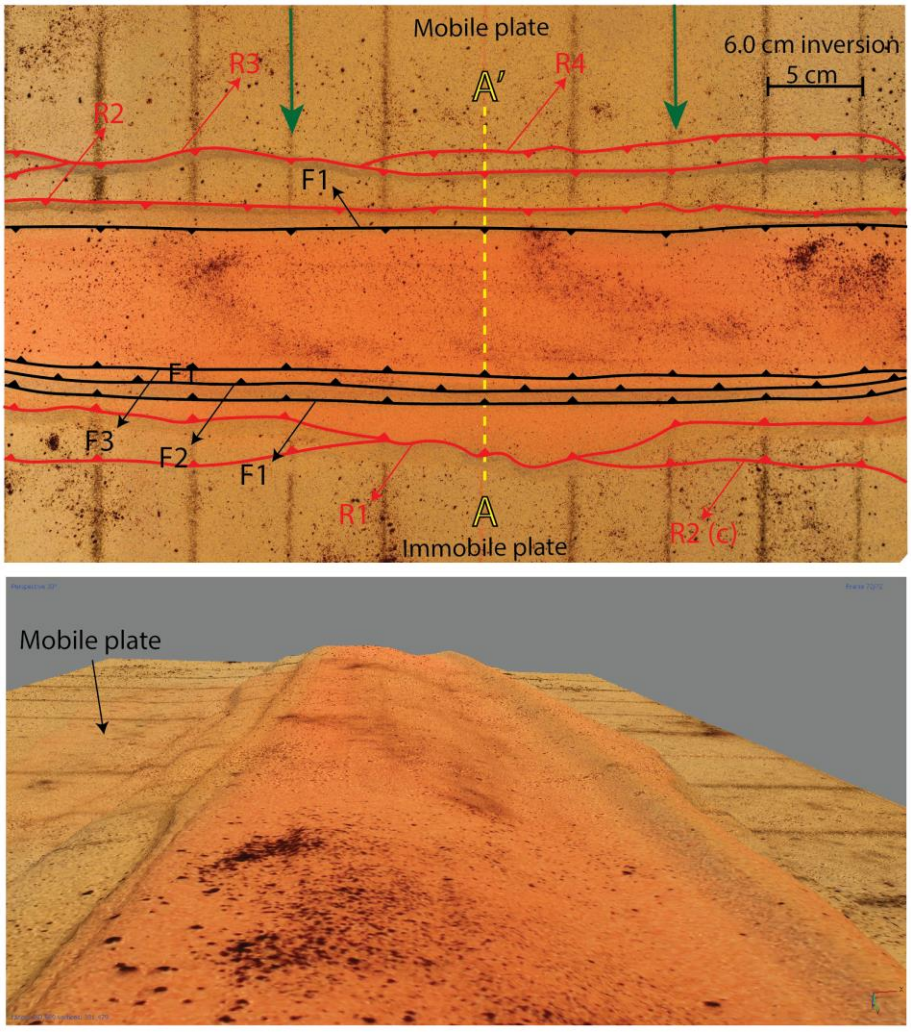

Figure 2.1.15. 3D view of the model at 6.0 cm of inversion (Bottom image) and Ortho-mosaic top-view of the experiment at 6.0 cm of inversion (Top image). The red lines represent thrust faults (R1, R2, R3 and R4). The sediment infill has a distinct color to the rest of the model.

PIV analysis

PIV vector and vector magnitude analysis was carried out using undistorted images exported from Agisoft Photoscan, the PIV analysis using these photographs yielded much higher quality results due to the correction for lens distortion and camera tilt. Due to the large number of frames captured and processed the images exported from PIV lab were compiled into a time-lapse of the individual frames at 1 FPS. The time-lapse of the vector analysis can be found here: https://www.youtube.com/watch?v=eTG-FmZkBw4 , and the vector magnitude analysis can be found here: https://www.youtube.com/watch?v=zR2XiX7TrnU .The figure below illustrates both PIV analysis methods at 3.0 cm (a) and 6.0 cm of inversion (b). The following can be observed in both the time lapses and diagram below: (1) The displacement velocity and magnitude decreases from the hinterland to the foreland. (2) Almost all displacement is perpendicular to the graben and no strike-slip component is visible, which leads to a more circular vector u & v distribution scatter (Figure 2.1.17). (3) The first thrust fault formed above the mobile plate (R1), after which shortcut thrust fault (R2) formed followed by thrust fault (R3) and (R4). (4) The foreland transport movement of the graben ceased after the formation of the second graben border thrust fault R3. The formation of these border thrust faults elevate the graben infill and thus lower the in planar horizontal velocity which led to smaller sized vectors. (6) Thrust fault (R4) is located on the mobile plate and originates from the branching of fault (R3) at the center of the model (parallel to grid lines) and migrates towards the sides of the graben along strike as inversion progresses. (7) Vector magnitude analysis showed that the basement rooted border thrust faults with the largest offset produced a pop-up structure during inversion (Figure 2.1.16). In the histogram in figure 2.1.17, three main zones with peaks of highest vector magnitudes can be observed at 2-4 pixels/frame (‘immobile’ plate), 8-9 pixels/frame (graben) and 12-13 pixels/frame (mobile plate). In this plot, it can be observed that the there is a large velocity decoupling between the graben and both plates, which suggest that there is extensive displacement along the graben border thrust faults. This decoupling decreases as the angle of inversion increases. The scatter-plot illustrates the orientation of the vectors at 6.0 cm of inversion, this pattern stands in contrast relative to other scatter plots of experiments with shallower angles of inversion where the scatter cloud has a (s) shape. This suggests that most vectors have the same orientation and thus there is almost no strike-slip component present in the system.

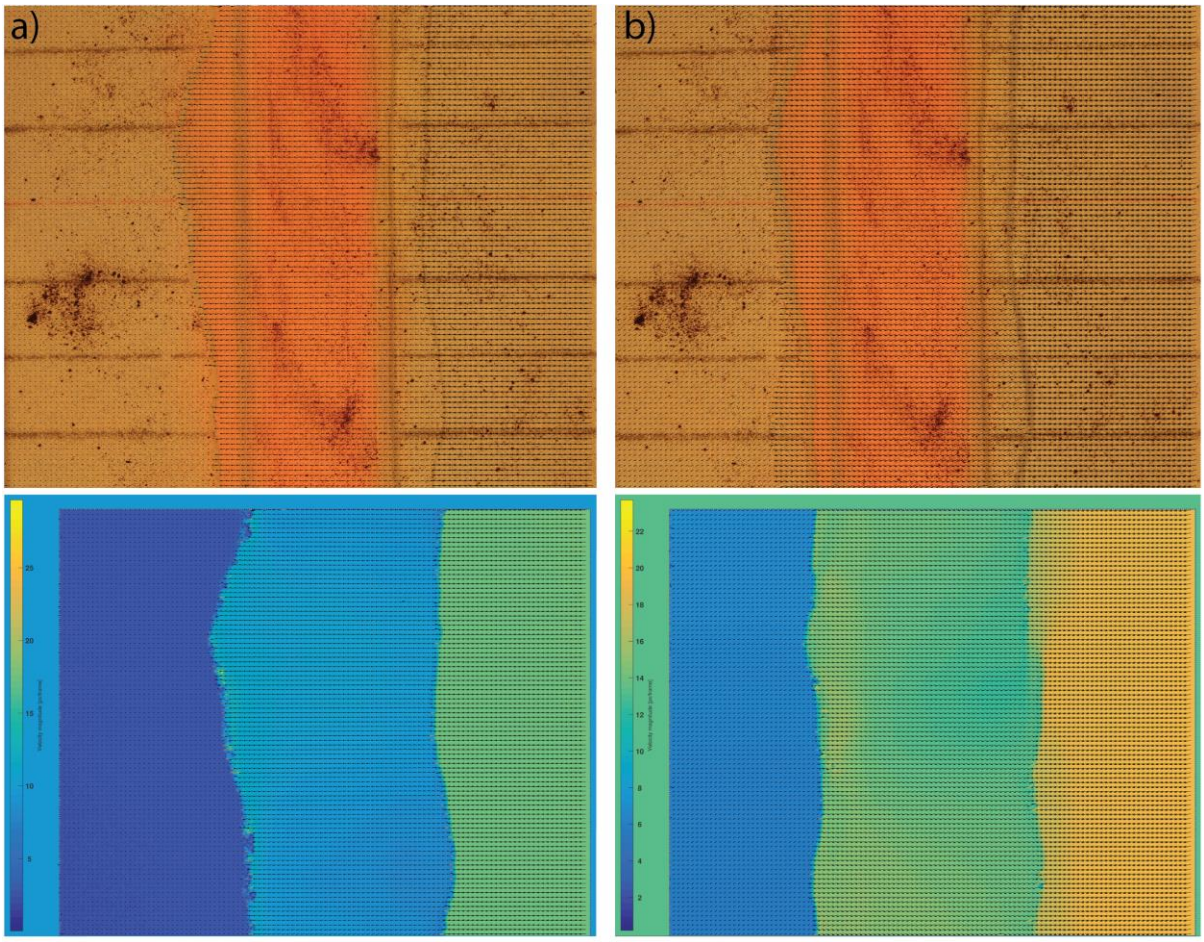

Figure 2.1.16. PIV Vector and Vector magnitude analysis (pixels/frame) at 3.0 cm - (a) and 6.0 cm - (b) of inversion.

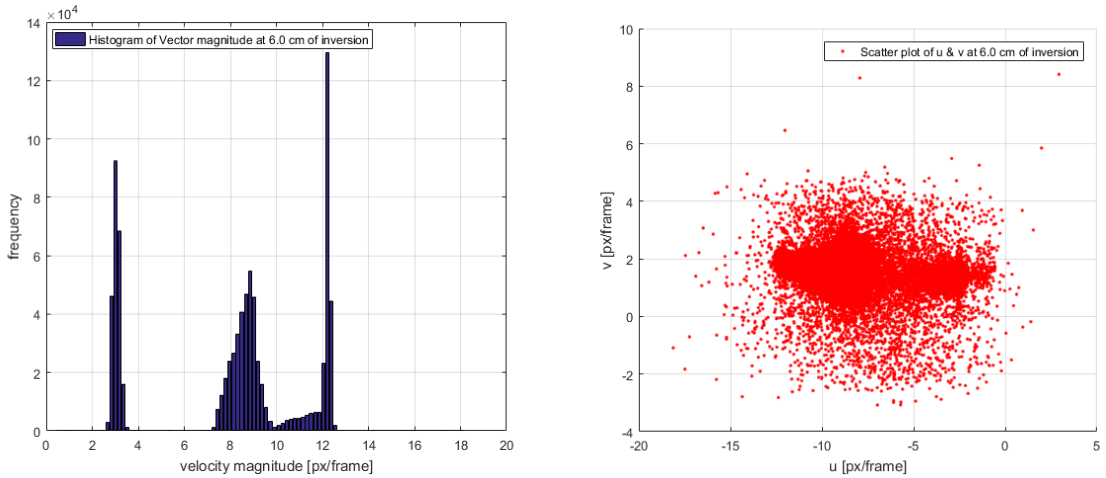

Figure 2.1.17. Histogram and scatter plots of the PIV analysis at 6.0 cm of inversion.

Due to the lack of visible 12-bit Agisoft target markers, it was not possible to carry out DEM analysis.

Cross-section analysis

The cross sections illustrated below in figures 2.1.18 and 2.1.19 are taken at the end of the experiment after 6.0 cm of inversion in the center of the model (CUT 5 - (a) and (b)) and close to it (CUT 4 - (c)). All cross-sections contain 7x normal faults (2xF1, F2, F3, F4, F5 and F6). Section (b) contains 3 forethrusts (R2, R3 and R4) and 1 backthrust (R1). Section (c) contains one extra backthrust. The following can be observed in these sections: (1) All Faults are steeper than 60°. (2) The normal faults formed at a higher angle than the thrust faults. (3) The angle of the thrust faults decreases towards the cover, while the angle of the normal faults increases towards the cover. (4) The largest number of faults formed above the mobile plate in the hanging wall as forethrusts. (5) The largest thrust fault with the largest throw formed above the immobile plate in the footwall in (b) - backthrust R1. (6) Small shortcut faults are present in both sections (b) and (c). (7) Little reverse faulting occurred, only the border master normal faults show slight reactivation. (8) Due to the formation of the large forethrust and backthrusts to accommodate the displacement, no major internal strain and rotation is present inside of the graben infill, however, it does appear that the entire graben was slightly rotated clockwise. (9) The graben infill is uplifted due to the displacement along the thrust border faults. (10) The sudden disappearance of an extra backthrust in section (b) is due to the linkage to the main pre-existing thrust fault. (11) The rifting phase produced a well-formed domino block system with a small increase in block size towards the immobile plate (mobile plate during inversion). (12) The normal faults inside of the graben are synthetic to (F1) in the hanging wall and antithetic to F1 in the footwall. (13) All normal faults link to the border faults (F1). (14) Only the two-main bounding thrust faults (R4 and R1 for (b), R5 and R2 for (c)) are basement rooted.

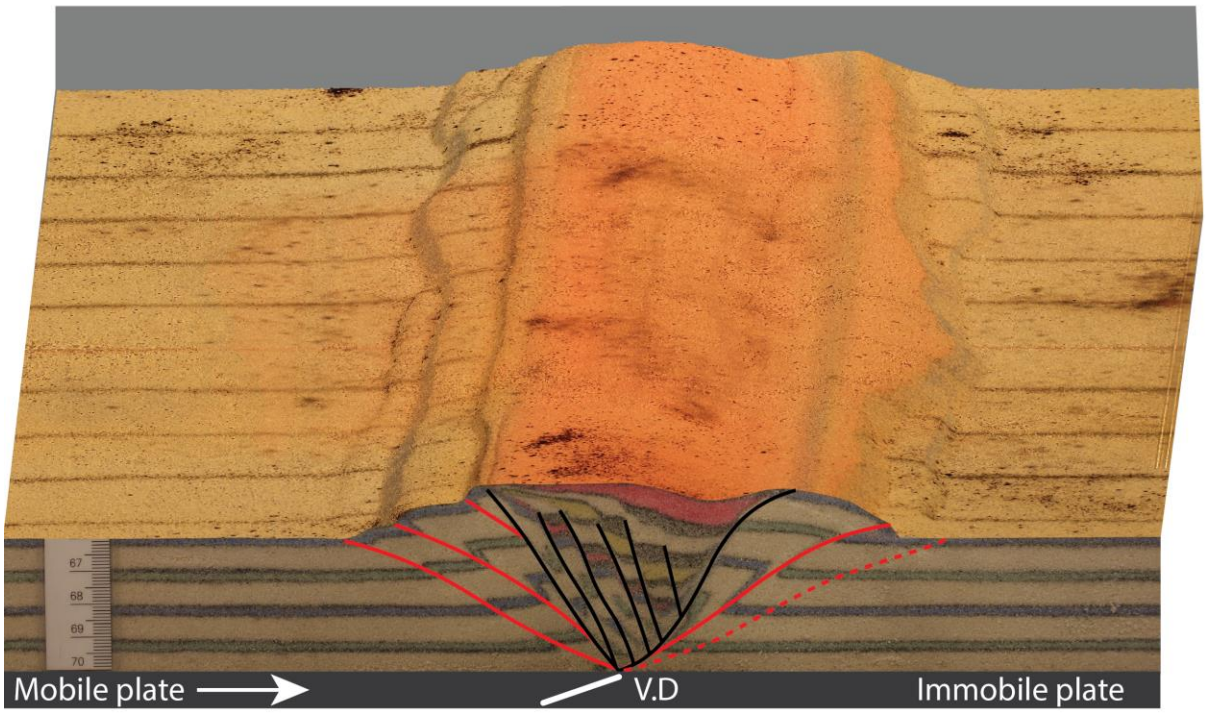

Figure 2.1.18. Combination between the cross-sections in figure 2.1.19 and the 3D surface model in figure 2.1.14.

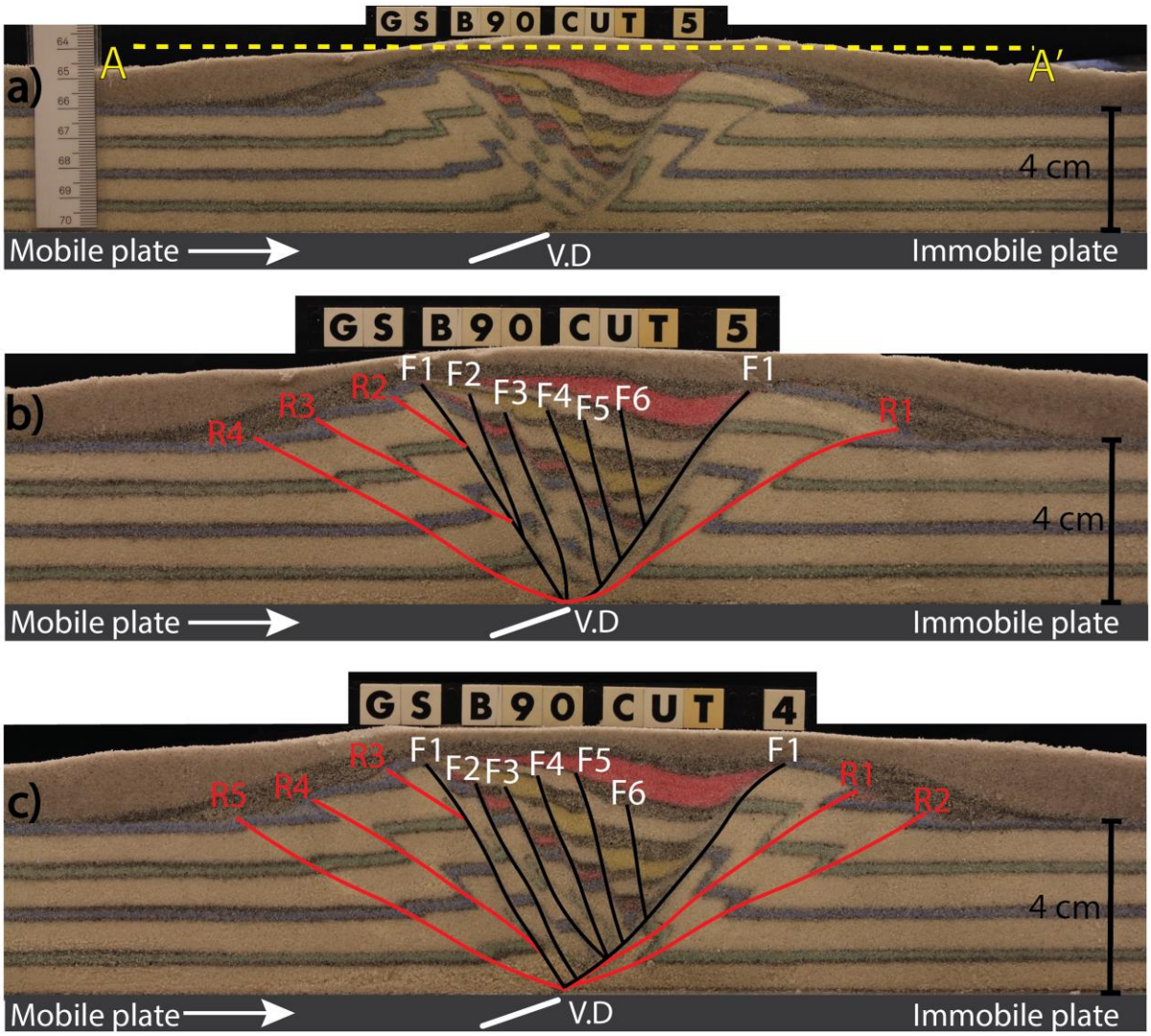

Figure 2.1.19. Cross sections taken at the end of the experiment after 6.0 cm of inversion. Many normal faults (2xF1, F2, F3, F4, F5 and F6) and thrust faults (R1, R2, R3, R4 and R5) formed.

Virtual Reality (VR) model

A virtual Reality (VR) environment was constructed using the final 3D model (6.0 cm inversion) from the 4D sequence and from the cross-section photographs. The textures and polygon mesh of the model were exported from Agisoft Photoscan and pre-processed using 3D modelling software (*3ds max*© and *Blender* ©). After the pre-processing the model was exported from the modelling software and imported into the *Destinations VR workshop tools* ®, where the VR environment was constructed, this includes mesh positioning, lighting, teleportation meshes, the addition of a sky and much more. Screenshots of the VR environment during rendering are illustrated below in figure 2.1.20. The VR environment can be found here (Figure 2.1.21):
http://steamcommunity.com/sharedfiles/filedetails/?id=818131814

It is possible to teleport not only around the model to see the cross sections but also on-top and inside of the model to analyze the surface and to be able to get a geologic overview of the 3D model. Although both the player and the model are scaled, both are scaled uniformly to preserve the true dimension ratios, this was done to ensure that the environment is as realistic as possible. In The screenshots below the HTC-vive controllers are visible including the beam that points towards the direction the user wants to teleport. To be able to scale the player and see the entire analogue model in a fully immersive VR environment is a transcending experience and permits the understanding of both the surface and internal geometry of the model at a pace that has never been observed before, as it allows the direct 3D visual correlation of surface and interior, which is one of the main challenges in geology.

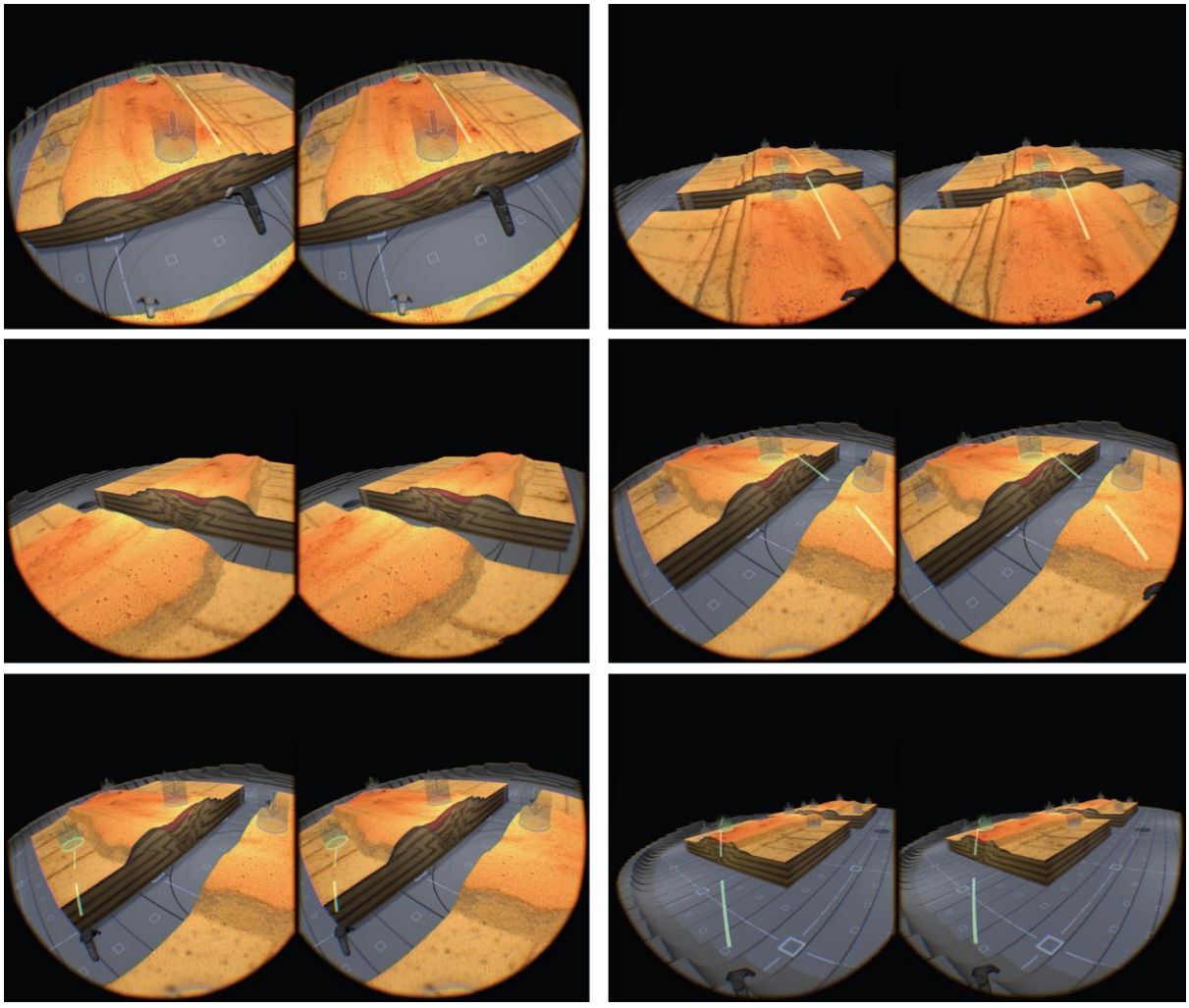

Figure 2.1.20. Screenshots of the VR model in Destinations© during rendering.

Figure 2.1.21. The VR environment can be found in the Destinations library on the Steam website.

Furthermore, the same model that was used for the creation of the VR environment was processed for 3D printing, this includes remapping textures and adding wall thickness. The model was 3D-printed in full color coated sandstone using *Shapeways*® 3D printing service. The model was printed in two separate shells to maximize the printing resolution, as printing the models together would require lowering the resolution of the meshes and textures. The bottom of the two halves was left hollow to minimize the material necessary, which lowers the price of the printed model significantly. This scaled model allows direct visualization of both the cross-sections and surface topography in a scaled and manageable manner without the necessity of a computer. Photographs of the final 3D printed model are illustrated below in figure 2.1.22.

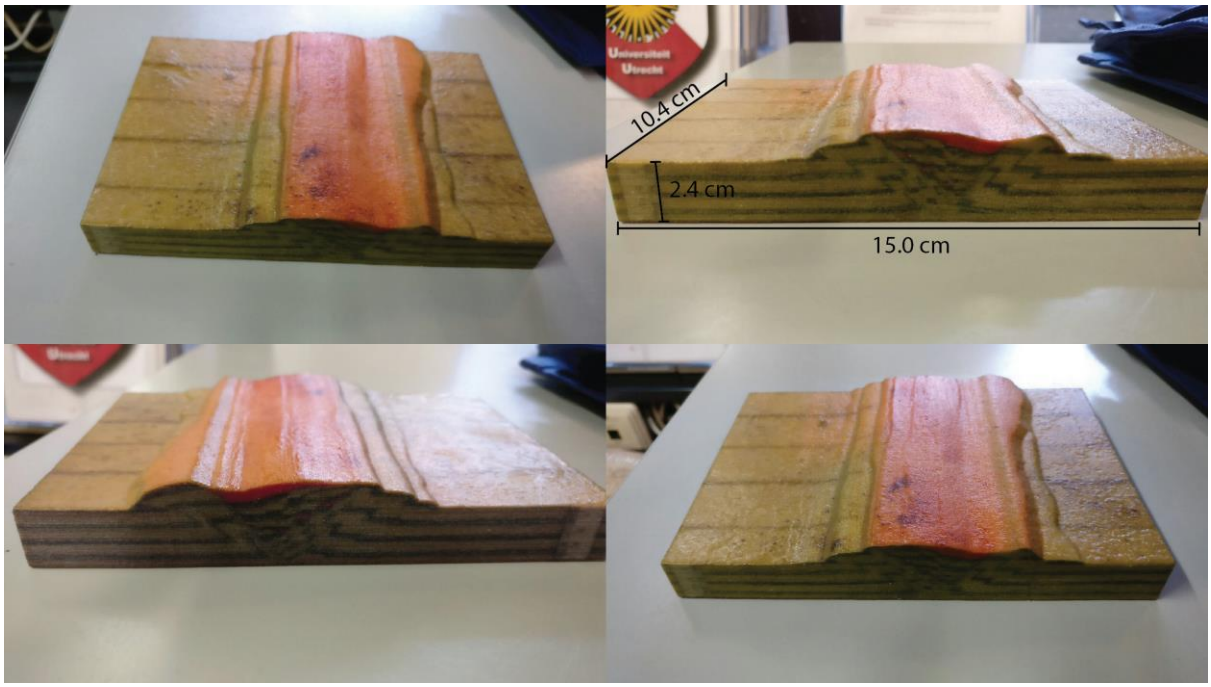

Figure 2.1.22. Photographs of a color 3D printed scaled section (15.0 x 10.4 x 2.4 cm) of the original analogue model. Thank you Lucas for taking the photographs.

2.1.3 GS-B15: Brittle, Extension and sedimentation followed by 15° inversion

Two experiments were carried out with the only difference being the thickness of the model (4.0 and 6.0 cm). During the initial rifting phase a rift basin developed because of the growth and slip of two large offset border master faults (F1), which become visible at the surface after 0.5 cm of displacement (Figure 2.1.23). As in the previous experiments, the formed graben is also asymmetrical along strike. Progressive extension of the analogue model led to the formation of fault (F2) in the hanging wall above the immobile plate. After the completion of the rifting phase the faults at the surface of the graben are not clearly visible due to the syn-tectonic sedimentation and collapse of the faults topography. Other faults that may develop within the graben can only be identified using cross-section or inferred using PIV analysis.

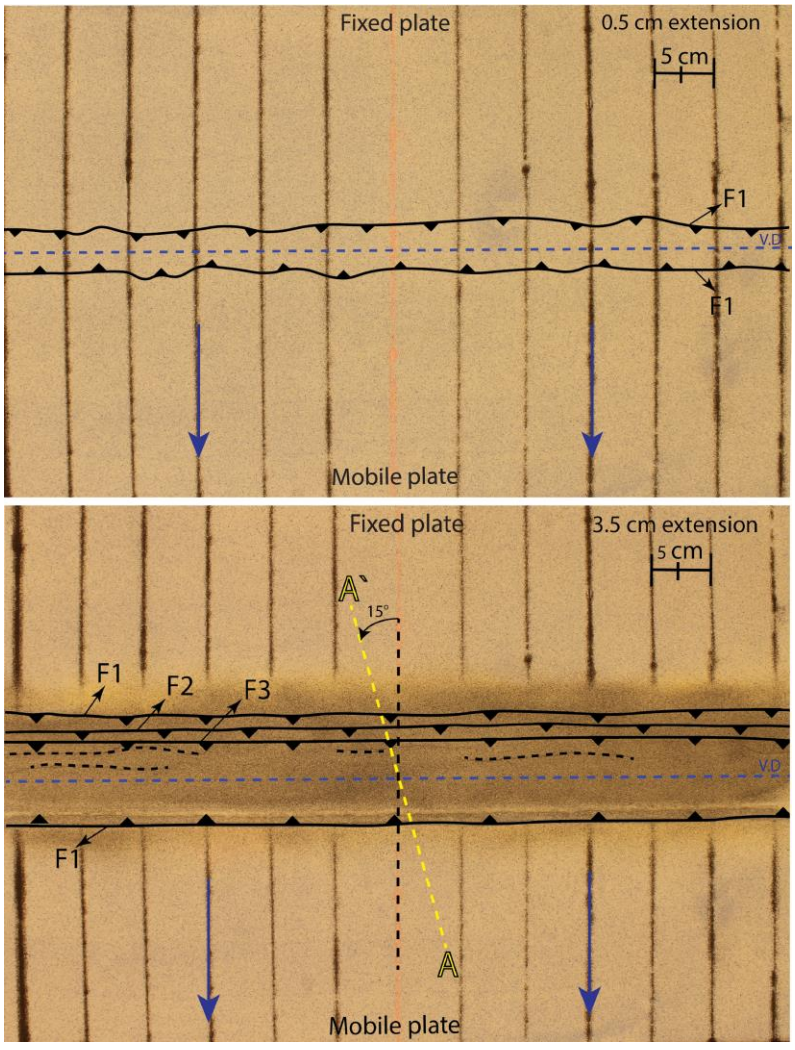

Figure 2.1.23. Top views of the experiment at 0.5 cm and 3.5 cm of extension. The blue arrows indicate the direction of extension. At 3.5 cm of extension two extra normal faults are present (F2 and F3). A-A' represent the location and orientation where the cross-section was taken.

After the completion of the extension phase, inversion is applied to the system. The following can be observed in figure 2.1.24 below: (1) The first thrust fault (R1) formed in the footwall above the static plate, subsequent inversion led to the formation of thrust fault (R2) and (R3) in the hanging-wall above the mobile plate. (2) As the inversion displacement increases, the asymmetry of the graben also tends to increase. (3) At the end of the experiment it appears that a large displacement component was accommodated by strike-slip, since the grid lines do not align on both sides of the V.D. The total magnitude of strike-slip displacement visible from the displacement of grid lines equates to 2.3 cm, which is 38.3% of the total displacement magnitude. (4) The graben underwent a slight clockwise rotation throughout the inversion phase. (5) The asymmetry of the thrust faults is greater than that of the normal faults. (6) No evidence for the reactivation of the normal faults is visible in the top-views. (7) The movement of the graben in the direction of the foreland decreases as the result of the formation of thrust fault (R1) which convert the purely horizontal displacement component of the graben into a horizontal and vertical component.

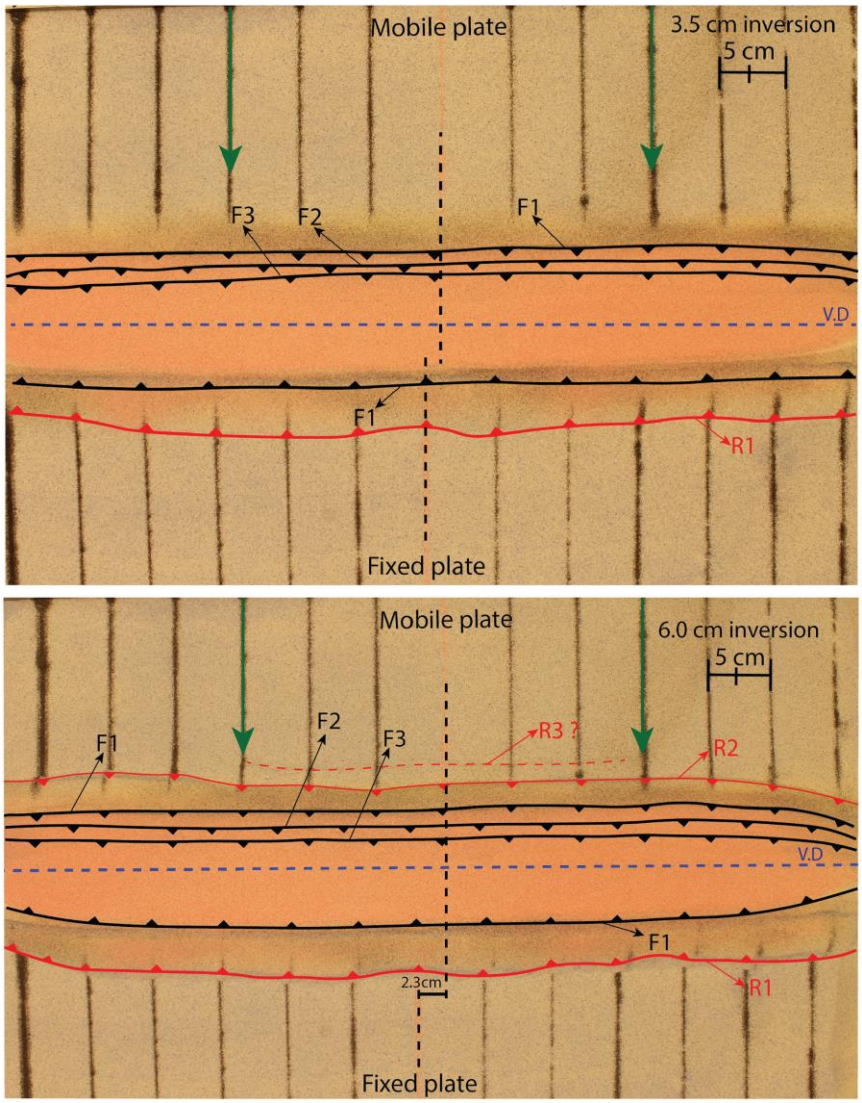

Figure 2.1.24. Top view of the experiment at 3.5 cm and 6.0 cm of inversion. The green arrows indicate the direction of shortening. The red lines represent the formation of thrust faults (R1, R2 and R3). The sediment infill has a distinct color to the rest of the model.

PIV analysis

PIV vector and vector magnitude analysis was carried using the top-view photographs taken during the inversion phase. The results of the analysis are illustrated below in figures 2.1.26 and 2.1.27 containing 12x frames for each of the analysis techniques for each 0.5 cm inversion. The following can be observed in the these figures: (1) The displacement velocity and magnitude decrease from the hinterland to the foreland. (2) The vectors diverge outwards from the graben, pointing to lateral spreading of the rift basin infill. (3) New vector fields form after the formation of the thrust faults above the static plate (e.g. formation of thrust fault (R1) after 2.5 cm of inversion), also, the formation of new thrust faults prevents the incremental straining and movement of the foreland as the displacement is accommodated by slip along the faults. (4) After the formation of the graben border thrust faults (R1) and (R2) the vector magnitudes inside the graben decreases due to the increased vertical displacement, so the movement transforms from a purely horizontal component to a vertical and horizontal component. (5) The inversion produces a vector field not only above the entire moving plate, but also above the entire graben, which stands in contrast with the extension phase PIV analysis, where most of the movement occurred only above the moving plate separated by the V.D, in which the displacement occurred fully along the normal faults. This indicates that the entire graben is displaced horizontally during inversion. This would not be the case if the normal faults inside of the graben accommodated all the displacement, which implies that there must have been other ways to accommodate the displacement (e.g. formation of thrust faults). Due to the absence of sedimentation interference, the results are of higher quality than the extension PIV analysis. From the Histogram (Figure 2.1.25), three main zones with peaks of highest vector magnitudes can be observed at 2-4 pixels/frame (‘immobile plate’), 16-20 pixels/frame (graben) and 30-34 pixels/frame (mobile plate). From the histogram plot it can observed that there is a large velocity decoupling between the graben and both plates, which suggests that there is extensive displacement along the graben border thrust faults. This decoupling decreases as the inversion angle increases. The scatterplot illustrates the orientation of the vectors at 3.0 cm of inversion. It is clearly visible that there is a large variation in shape of the data cloud compared to the previous experiment (GS-B90), the change in shape of the cloud could be related to the strike-slip movement that changes the orientation of the vectors. This asymmetry is expected to increase as the inversion angle increases and respectively the increase of the strike-slip component of the system.

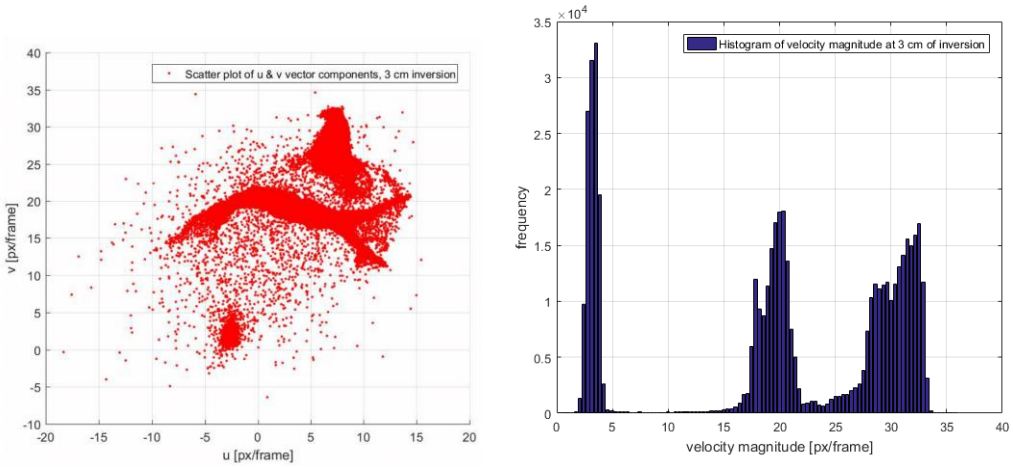

Figure 2.1.25. Histogram and scatter plots of the PIV analysis at 3.0 cm of inversion.

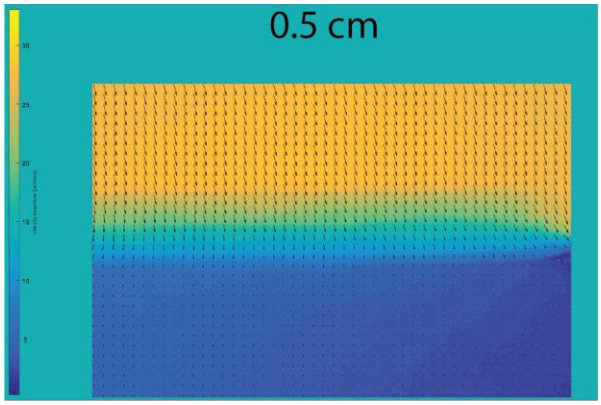
0.5 cm

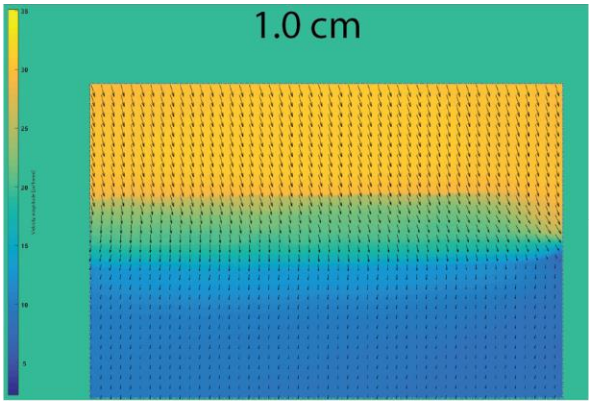
1.0 cm

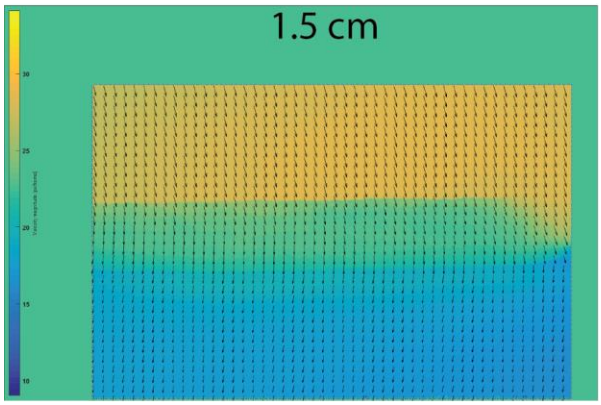
1.5 cm

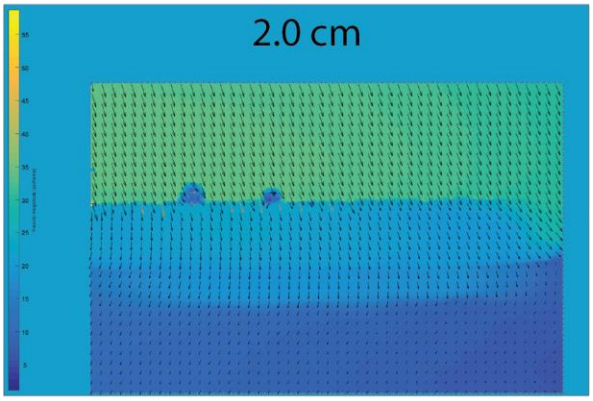
2.0 cm

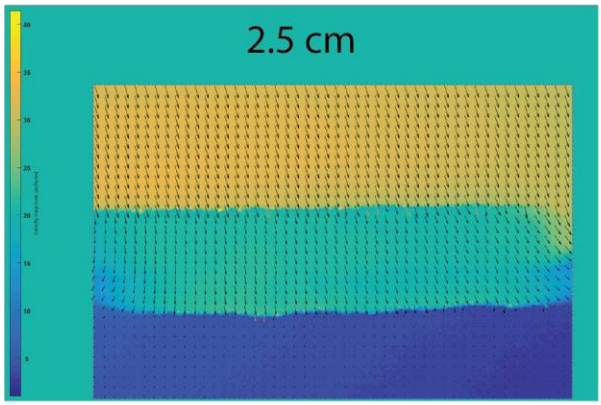
2.5 cm

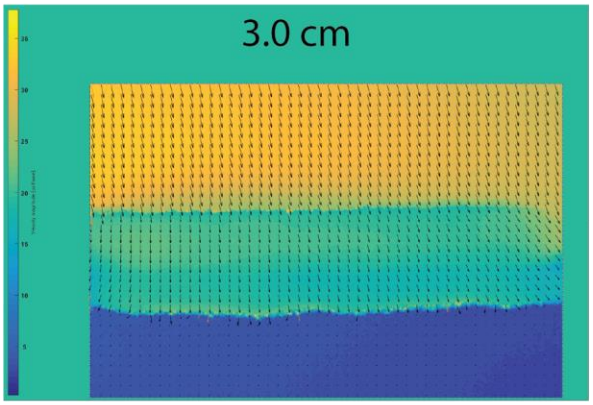
3.0 cm

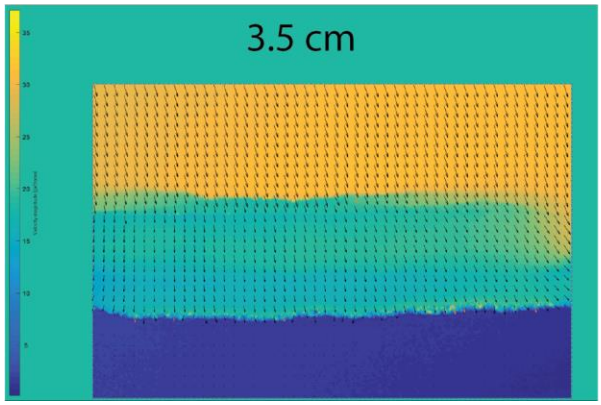
3.5 cm

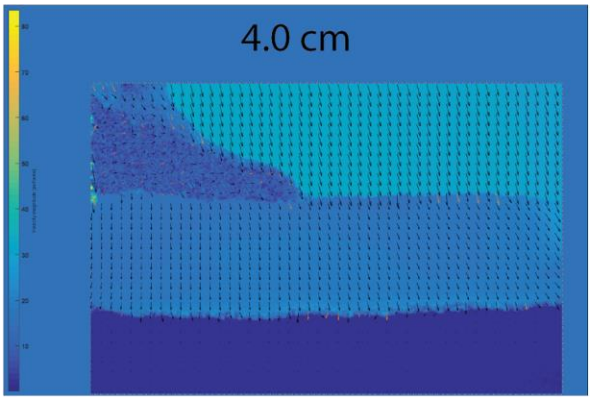
4.0 cm

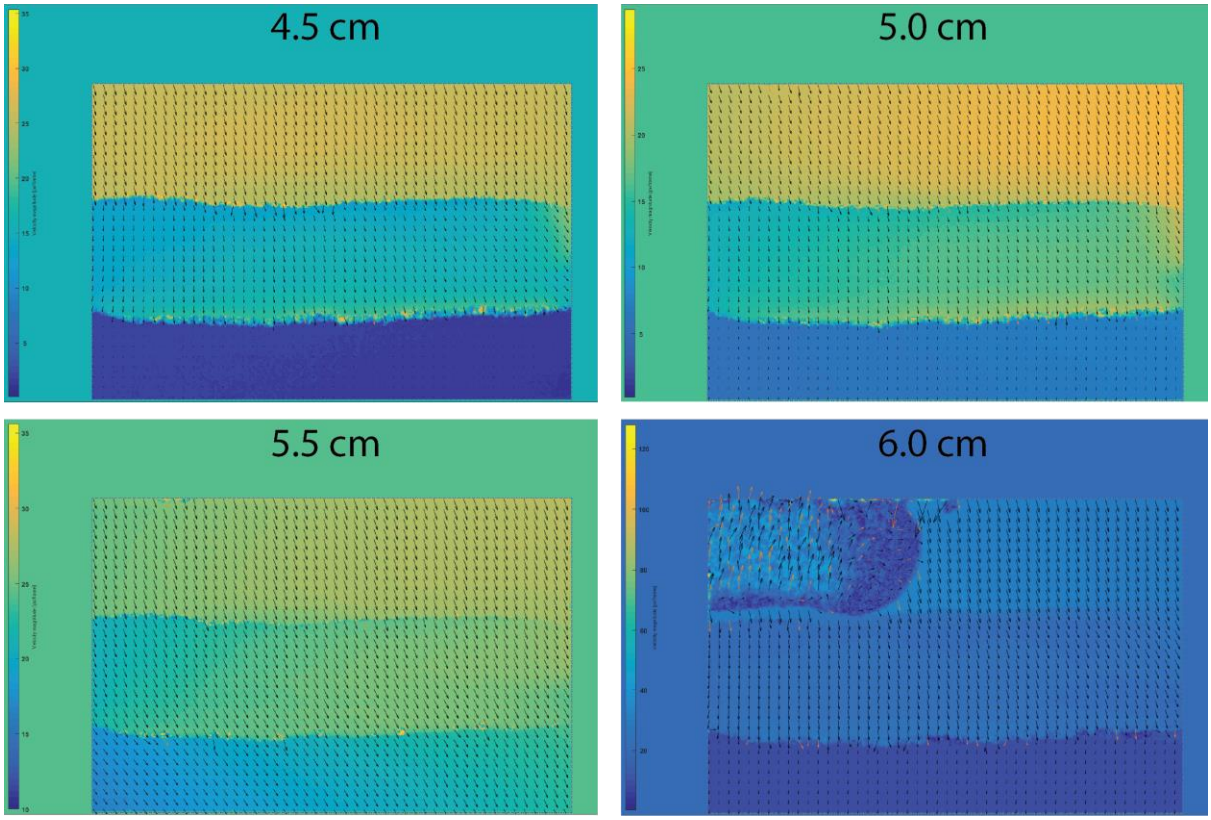

Figure 2.1.26. PIV analysis of the vector magnitude (pixels/frame) of the inversion phase, each diagram represents a 0.5 displacement step. There is some vector filed disturbance present in the frames at 4.0 and 6.0 cm of inversion.

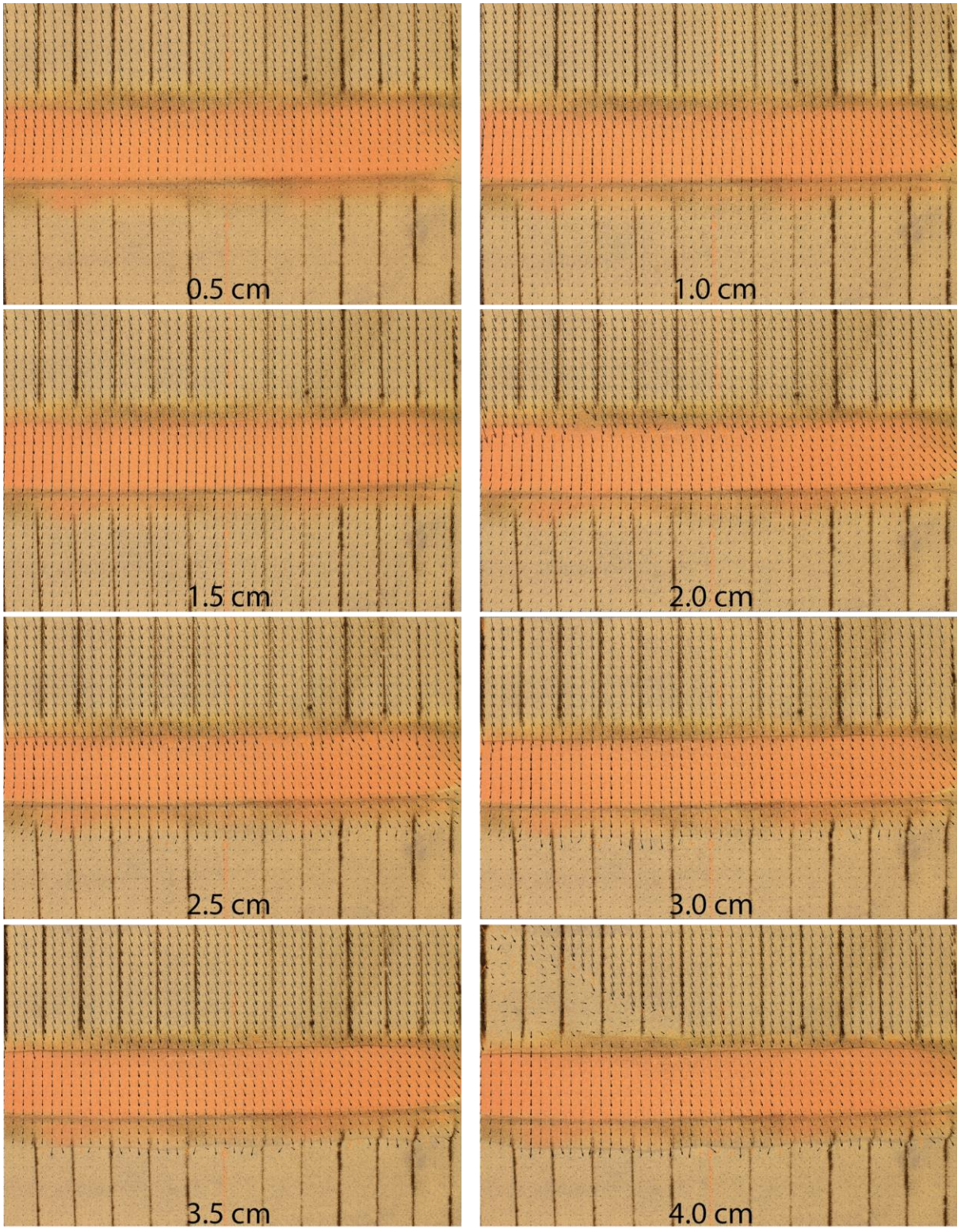
0.5 cm
1.0 cm
1.5 cm
2.0 cm
2.5 cm
3.0 cm
3.5 cm
4.0 cm

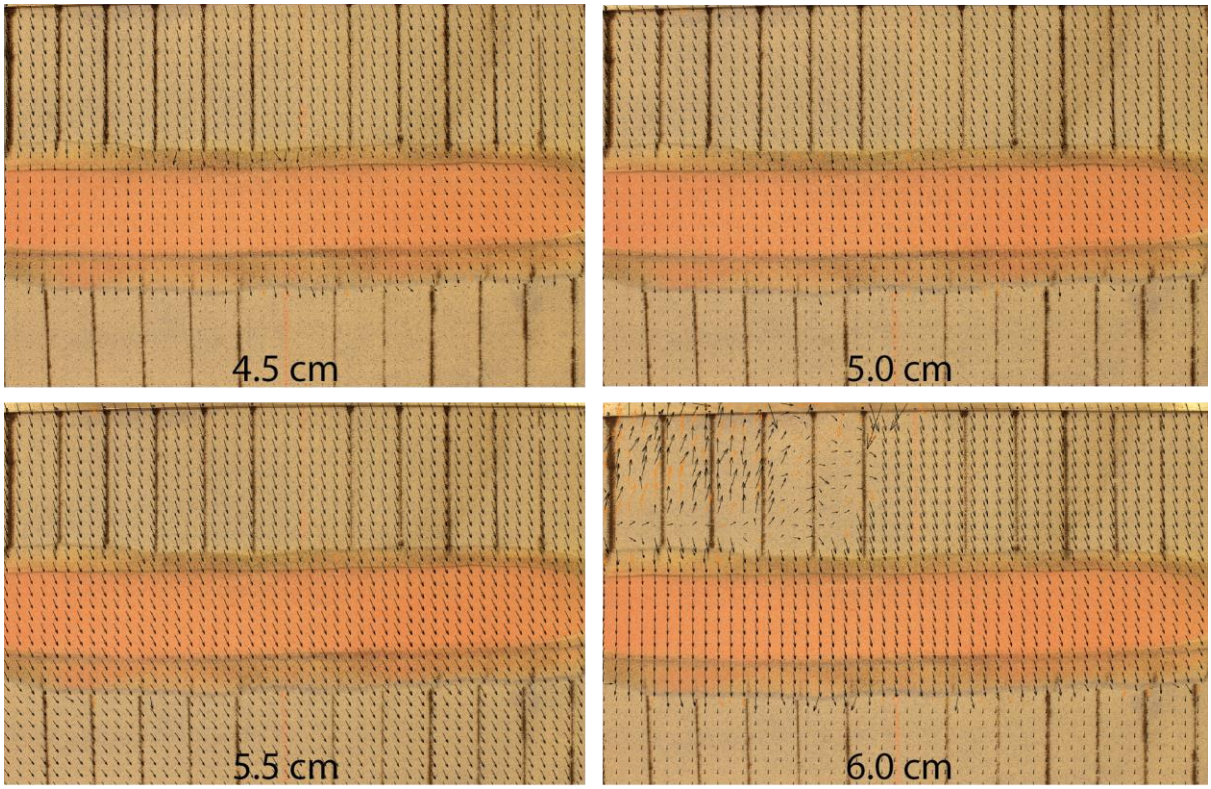

Figure 2.1.27. PIV vector analysis of the inversion phase, each diagram represents a 0.5 cm displacement frame of the inversion phase. There is some vector filed disturbance present in the frames at 4.0 and 6.0 cm of inversion.

Figure 2.1.28. Cross-section numbering of the analogue model and their relative positions and orientation.

Cross-section analysis

The cross section illustrated below in figure 2.1.29 is taken at the end of the experiment after 6.0 cm of inversion in the center of the model at a 15-degree angle to the V.D. The cross section contains six normal faults (2x F1, F2, F3, F4 and F5), two forethrusts (R2 and R3) and one backthrust (R1). The following can be observed in this section: (1) All faults are steeper than 60°. (2) The largest number of thrust faults formed above the mobile plate in the hanging wall as forethrusts. (3) The normal faults formed at a higher angle than the thrust faults. (4) The angle of the thrust faults decreases towards the cover, while the angle of the normal faults increases towards the cover (except for normal fault (F1) in the footwall). (5) The largest thrust fault with the largest throw formed above the immobile plate in the footwall as backthrust (R1). (6) The displacement along thrust faults (R1) and (R2) caused vertical uplift of the graben. (7) No shortcut thrust faults formed during the inversion phase. (8) There is no visual indication of the formation of reverse faults. (9) Due to the formation of the large forethrust and backthrusts to accommodate the displacement, no major internal strain and rotation is present inside of the graben infill, however, it does appear that the entire graben suffered a slight clockwise rotation. (10) The rifting phase produced a well-developed domino block system with a small increase in block size towards the immobile plate during rifting. (11) The normal faults inside of the graben are synthetic to (F1) in the hanging wall and antithetic to (F1) in the footwall. (13) All normal faults inside of the rift basin infill link to the master normal faults (F1), so none of these faults are directly linked to the basement or to the V.D. (14) Al thrust faults are basement rooted. (15) The throw of the thrust faults is smaller compared to that of experiments with shallower angles of inversion.

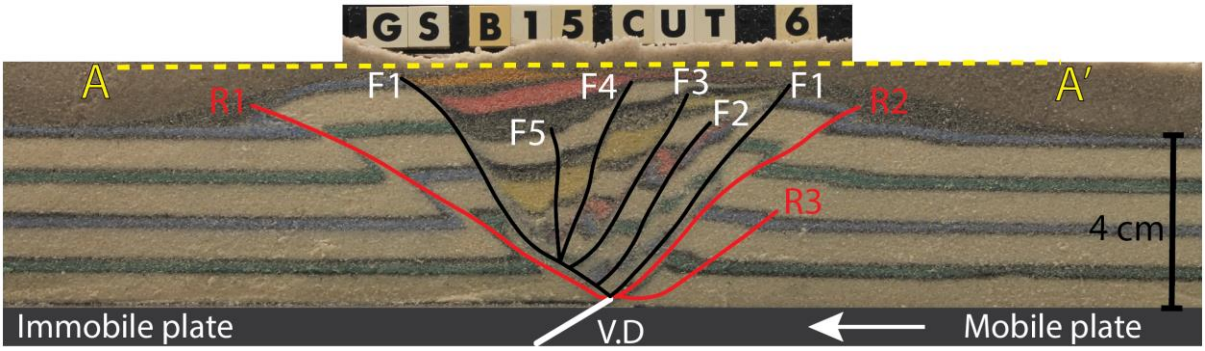

Figure 2.1.29. Cross section taken after 6.0 cm of inversion of the model GS-B15°. The section contains six normal faults (2x F1, F2, F3, F4 and F5) and three thrust faults (R1, R2 and R3).

The cross section illustrated below in figure 2.1.30 displays some subtle differences to the previous cross-section. One of the main differences is the formation of a shortcut thrust (R1), this thrust did not form in the 4.0 cm thick analogue model. This model also appears to have suffered less internal rotation and strain, which could be attributed to the increased confining pressure due to a higher amount of overburden.

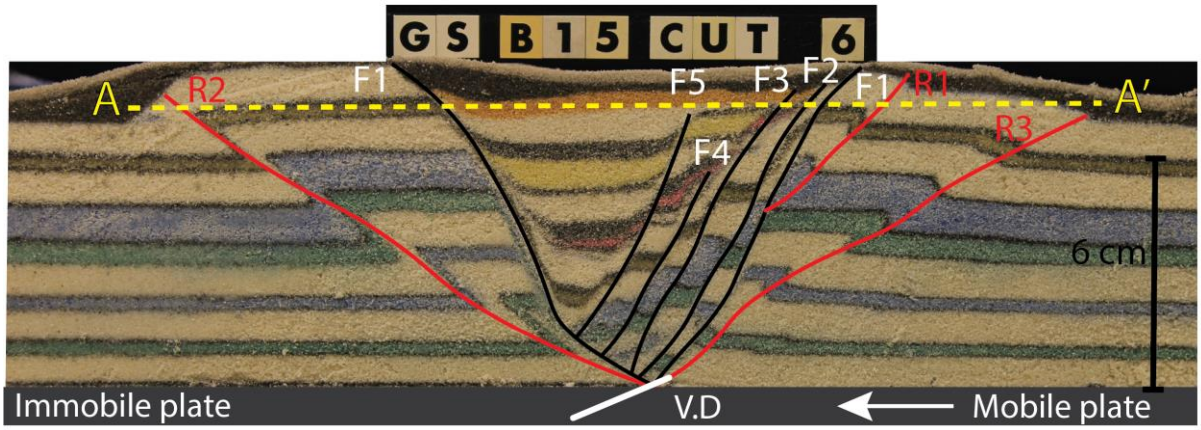

Figure 2.1.30. Cross section taken of the 6.0 cm thick analogue model after 6.0 cm of inversion. It contains six normal faults (2x F1, F2, F3, F4 and F5) and three thrust faults (R1, R2 and R3).

2.1.4 GS-B45: Brittle, Extension and sedimentation followed by 45° inversion

During the initial rifting phase a graben developed as the result of the formation of two large offset master rift border faults (F1). The formed graben is asymmetrical along strike. Progressive extension led to the development of faults (F2) and (F3) in the hanging-wall above the immobile plate (Figure 2.1.31). After The completion of the extension phase the faults at the surface of the graben are not clearly visible due to the syn-tectonic sedimentation and collapse of the fault topography. Other faults that may develop within the graben can only be observed or identified using cross-sections or by PIV analysis.

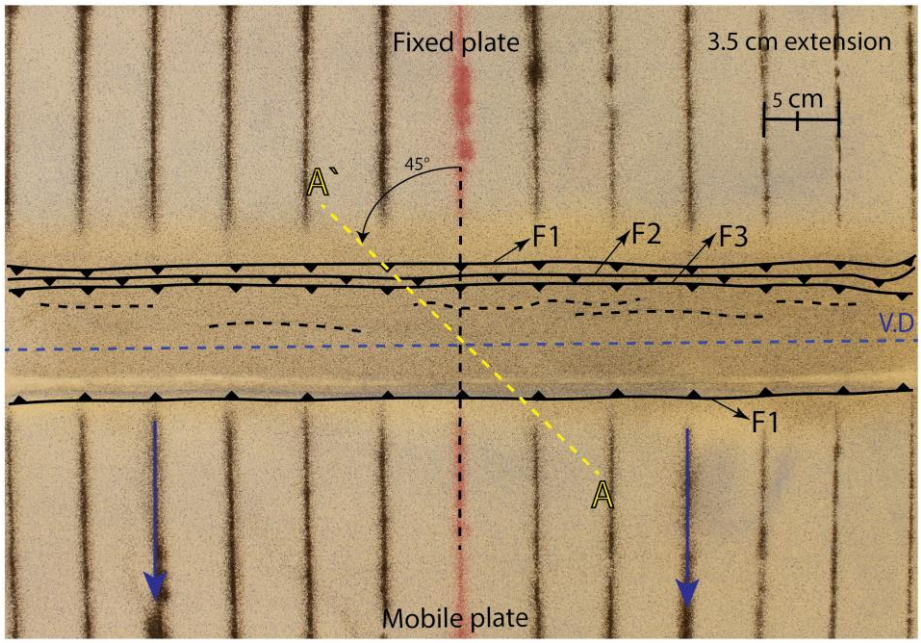

Figure 2.1.31. Top-view of the experiment at 3.5cm of extension. Two new faults form in the hanging wall above the static plate. The blue arrows indicate the direction of extension.

After the completion of the extensional phase, inversion is applied to the system (Figure 2.1.31). The following can be observed in the figure below: (1) Two thrust faults formed during the inversion phase (forethrust - R1 and backthrust - R2). The first thrust fault (R1) formed above the mobile plate instead of above the immobile plate as in previous experiments. (2) The strike-slip component was more extensive than in this experiments compared to experiments with shallower angles of inversion. The total strike-slip displacement magnitude equates to 4.3 cm (71.6% of the total displacement). (3) The normal faults have been reactivated both by vertical and horizontal slip, as can be observed by the sharper topography created by the faults blocks that exhumed to the surface, this reactivation occurred mainly in the hanging wall above the mobile plate. Most of the reactivation occurred by strike-slip displacement. (4) The displacement magnitude of the graben in the direction of the foreland is much less extensive compared to previous experiments. (5) The maximum uplift that developed is considerably less compared experiments with $\alpha < 45$ °. (6) the faults tend to rotate clockwise towards the direction of shortening to align with the principal strain axis. (7) The throw of the thrust fault is significantly lower due to the increased strike-slip component. (8) The reactivation above the

mobile plate is much more extensive compared to that above the fixed plate, resulting in a greater maximum uplift. (9) The width of the deformation zone is much narrower compared to experiments with α < 45 °. The throw of the thrust faults tends to decreases as the inversion angle increases, while the lateral slip in the direction of (δv = δ2) of the Andersonian fault-classification tends to increase. The geometry of the thrusted fault zones shows very different characteristics compared to previous experiments.

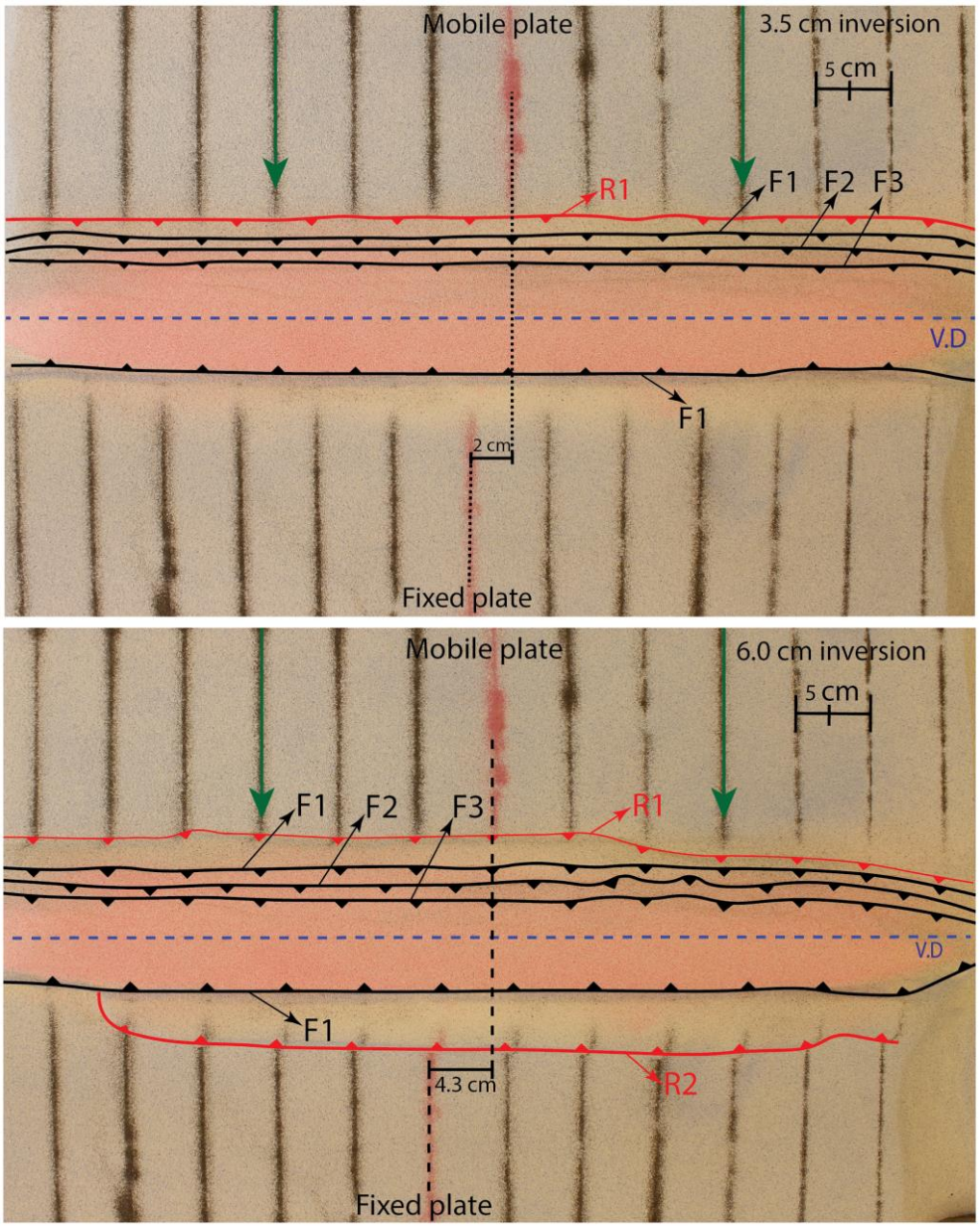

Figure 2.1.32. Top view of the experiment at 3.5 and 6.0 cm of inversion. The green arrows indicate the direction of inversion. Two thrust faults formed because of the inversion (R1 and R2). A large strike-slip component is present in the system.

PIV analysis

PIV vector and vector magnitude analysis was carried out, of which the results are illustrated below in figures 2.1.34 and 2.1.35. Each figure contains 12x frames, of which each frame represents a 0.5 cm inversion steps. The following can be observed in the these figures: (1) The displacement velocity and magnitude decrease from the hinterland to the foreland. (2) The vectors diverge outwards from the graben, pointing to lateral spreading as a result of the strike-slip displacement. (3) New vector fields form after the formation of thrust faults or the reactivation of normal faults, also, the formation of new thrust faults prevents the movement of the foreland as the displacement is accommodated vertically. (4) After the formation of thrust faults (R1) and (R2) the vector magnitudes in the rift basin infill decreases because of the out of plane vertical displacement along the thrust faults. (5) The inversion produces a vector field not only above the entire moving plate, but also above the entire graben, which indicates that the entire rift zone is displaced horizontally during inversion. (6) The highest amount of displacement and formation of maximum uplift occurred along forethrust (R1). (7) Most of the transpression displacement also occurs along (R1). The strike-slip component is much greater compared to that in the previous experiment due to the increasingly orientation of the vectors parallel to the V.D. (8) The strike slip components decreases towards the foreland (the vectors tend to increasingly align perpendicular to the V.D.), this points to the successive filtering of the strike-slip displacement as the movement propagates through the graben towards the foreland, so the overall strike-slip displacement has to be a summation of the strike-slip displacement along each of the individual faults. Care should be taken with the fixation of the immobile plate; some vector fields are present in some of the frames above the 'immobile' plate due to insufficient fixation. From the Histogram (Figure 2.1.33), three main zones with peaks of highest vector magnitudes can be observed at 10-15 pixels/frame ('immobile plate'), 20-25 pixels/frame (graben) and 30-34 pixels/frame (mobile plate). From this plot, it can be concluded that the velocity decoupling between the graben and both plates was less compared to experiments with shallower angles of inversion, which suggests that there was less displacement along the graben border thrust faults. The scatterplot illustrates the orientation of the vectors at 3.0 cm of inversion. There is a large variation in shape of the data cloud., the vectors demonstrate a larger change in orientation due to the increase of the strike-slip components of the system (s-shaped cloud).

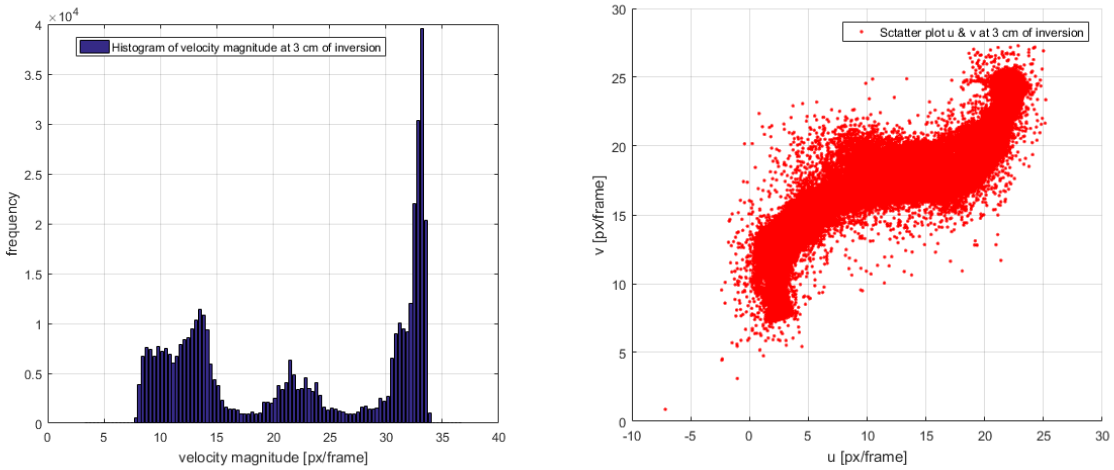

Figure 2.1.33. Histogram and scatter plots of the PIV analysis at 3.0 cm of inversion.

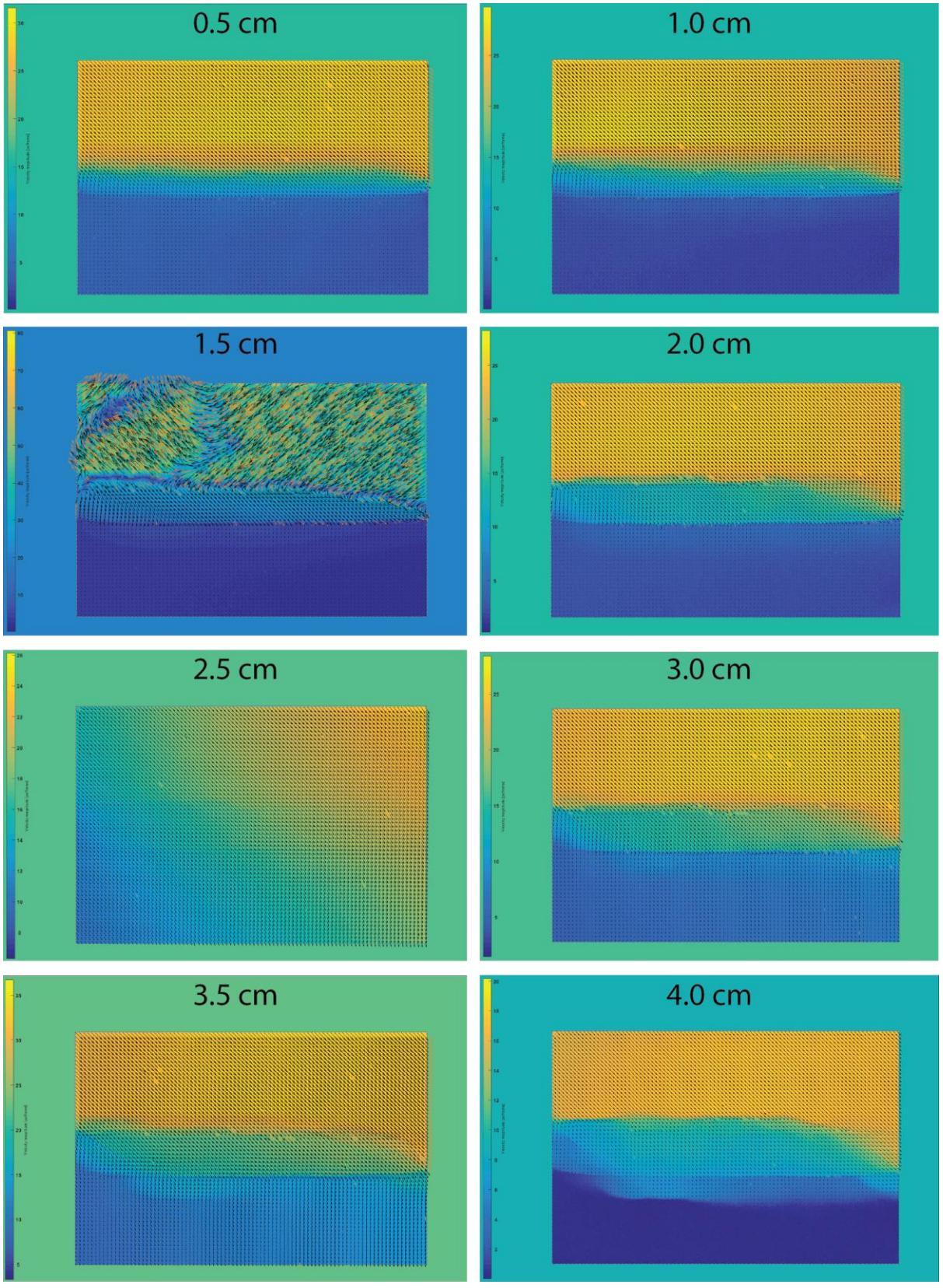
0.5 cm
1.0 cm
1.5 cm
2.0 cm
2.5 cm
3.0 cm
3.5 cm
4.0 cm

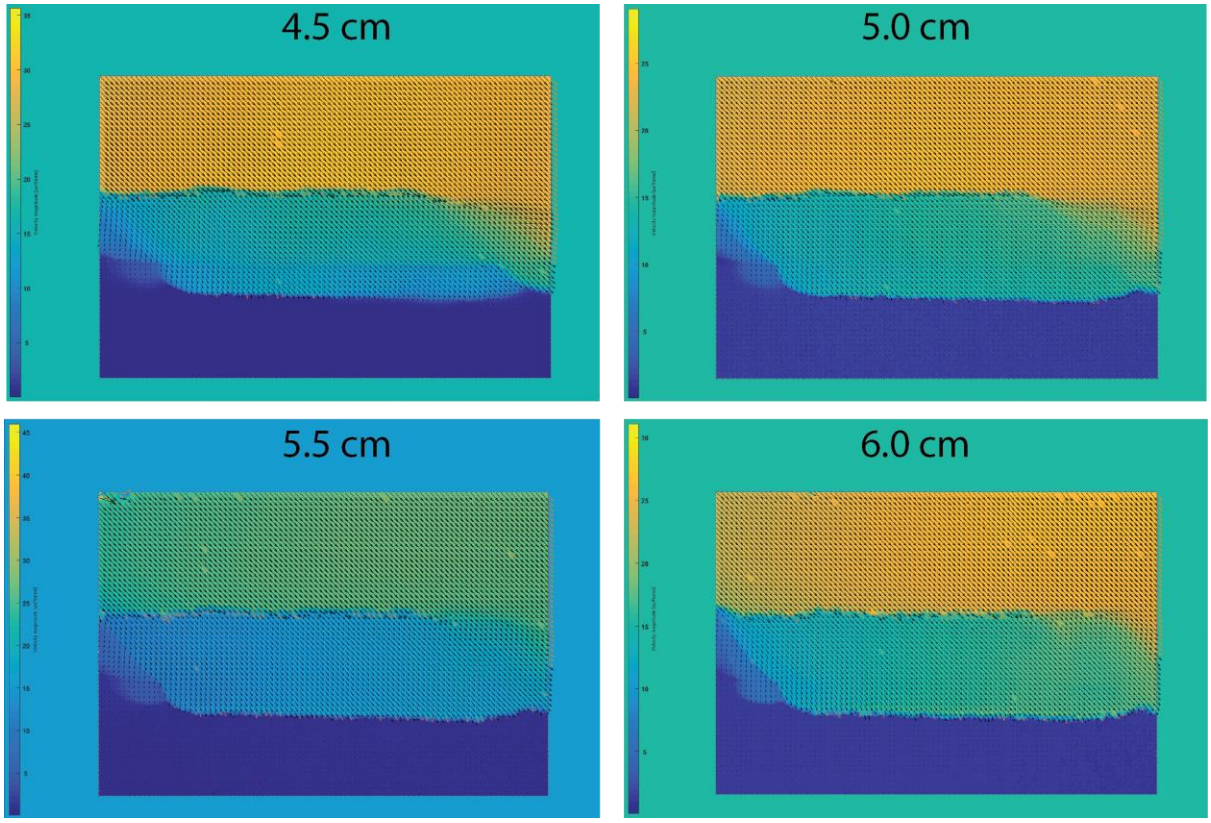

Figure 2.1.34. PIV analysis of the vector magnitude (pixels/frame) of the inversion phase, each diagram represents a 0.5 cm step in the inversion process.

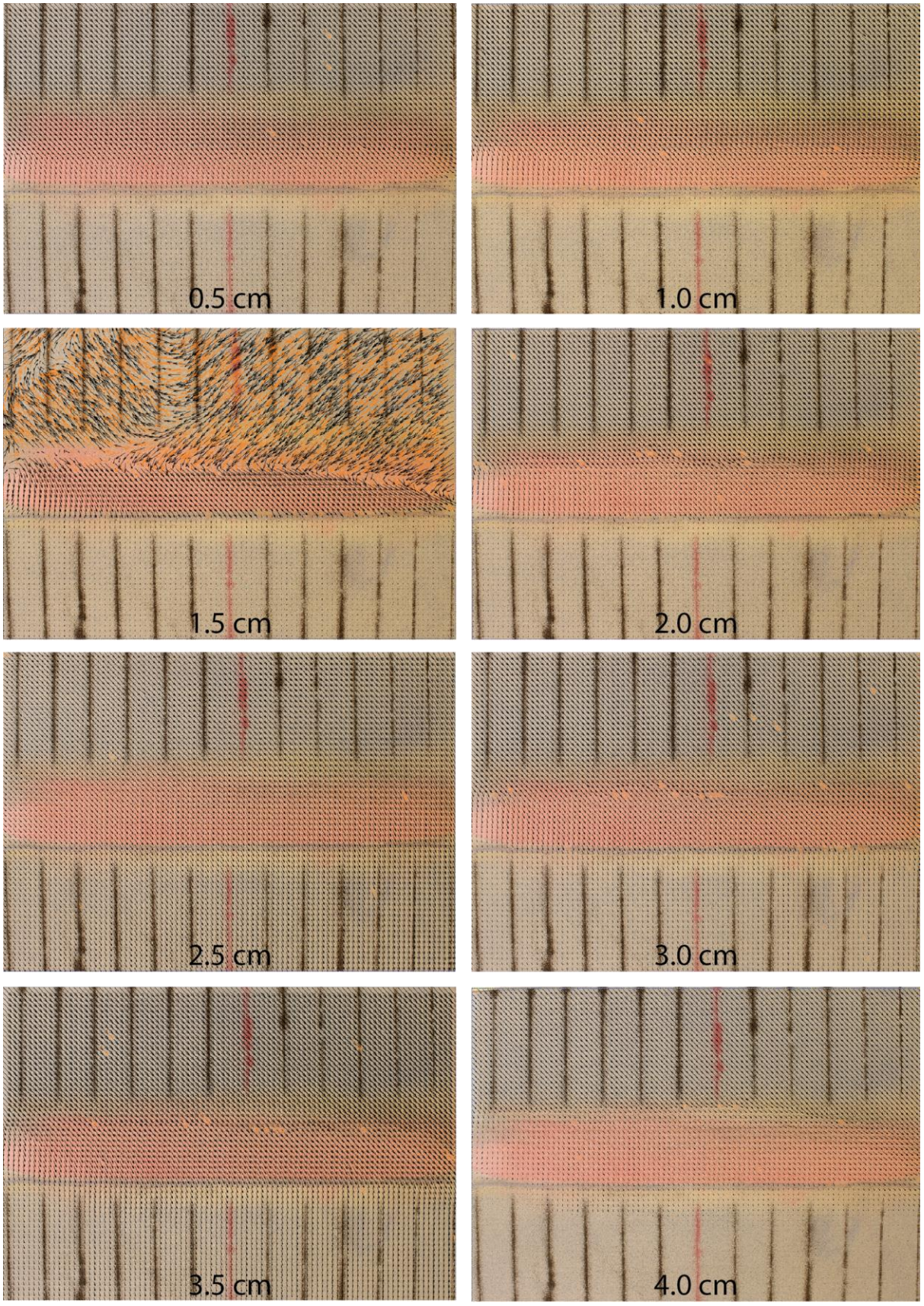
0.5 cm
1.0 cm
1.5 cm
2.0 cm
2.5 cm
3.0 cm
3.5 cm
4.0 cm

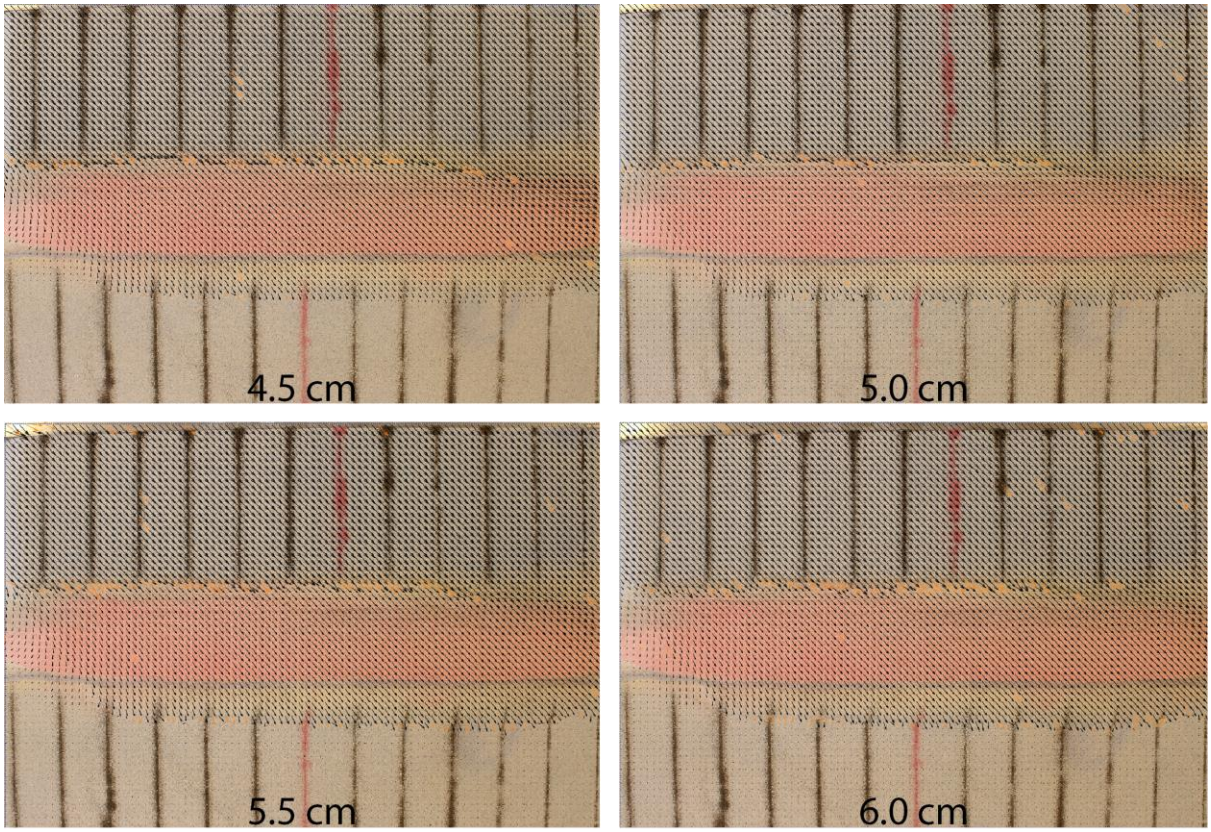

Figure 2.1.35. PIV vector analysis of the inversion phase, each frame represents a 0.5cm displacement step of the inversion phase. There is some vector filed disturbance present in the frame at 1.5 cm of inversion due to accidental camera motion.

Cross-section analysis

The cross section illustrated below in figure 2.1.36 is taken at a 45-degree angle to the V.D at the end of the experiment after 6.0 cm of inversion. The cross section contains five normal faults (2x F1, F2, F3 and F4) and two thrust faults (forethrust R1 and backthrust R2). The following can be observed in this section: (1) All faults are steeper than 60°. (2) The normal faults formed at a higher angle than the thrust faults. (3) The angle of the thrust faults decreases towards the cover, while the angle of the normal faults increases towards the cover. (4) The largest thrust fault with the largest throw formed above the immobile plate in the footwall wall – backthrust (R2). (6) The displacement along thrust faults (R1) and (R2) causes a slight uplift of the graben, although most shortening is accommodated by strike-slip, and thus the maximum topographic uplift is much less compared to experiments with shallower angles of inversion. (7) No shortcut thrust faults formed during the inversion. (8) There are some signs of the vertical reactivation of the normal faults, namely the reverse drag features (e.g. F3) that folds some of the sand layers into synclinal shaped structures. (9) The normal faults inside of the graben are synthetic to F1 in the hanging wall and antithetic to F1 in the footwall. (10) Al thrust faults are basement rooted. The throw of the thrust faults is smaller compared to that of experiments with shallower angles of inversion, pointing to more reactivation of the normal faults.

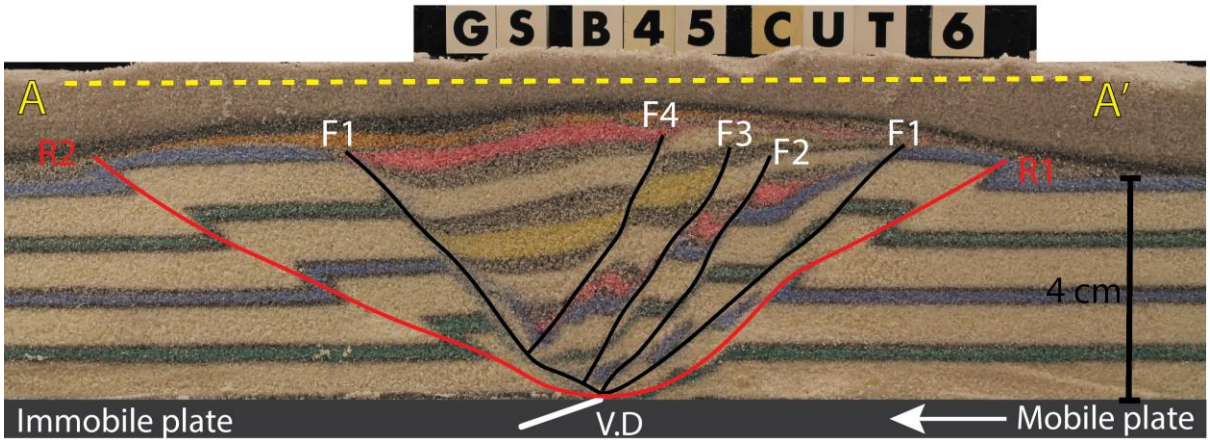

Figure 2.1.36. Cross section taken after 6.0 cm of inversion of the analogue model. Five normal faults (2xF1, F2, F3 and f4) and two thrust faults (R1 and R2) are present in this section

2.1.5 GS-B75: Brittle, Extension and sedimentation followed by 75° inversion

The textured 3D model compiled at the end of the extension phase can be visualized here: https://sketchfab.com/models/b85cdab3e4fe46e89c965db348ff3f4b

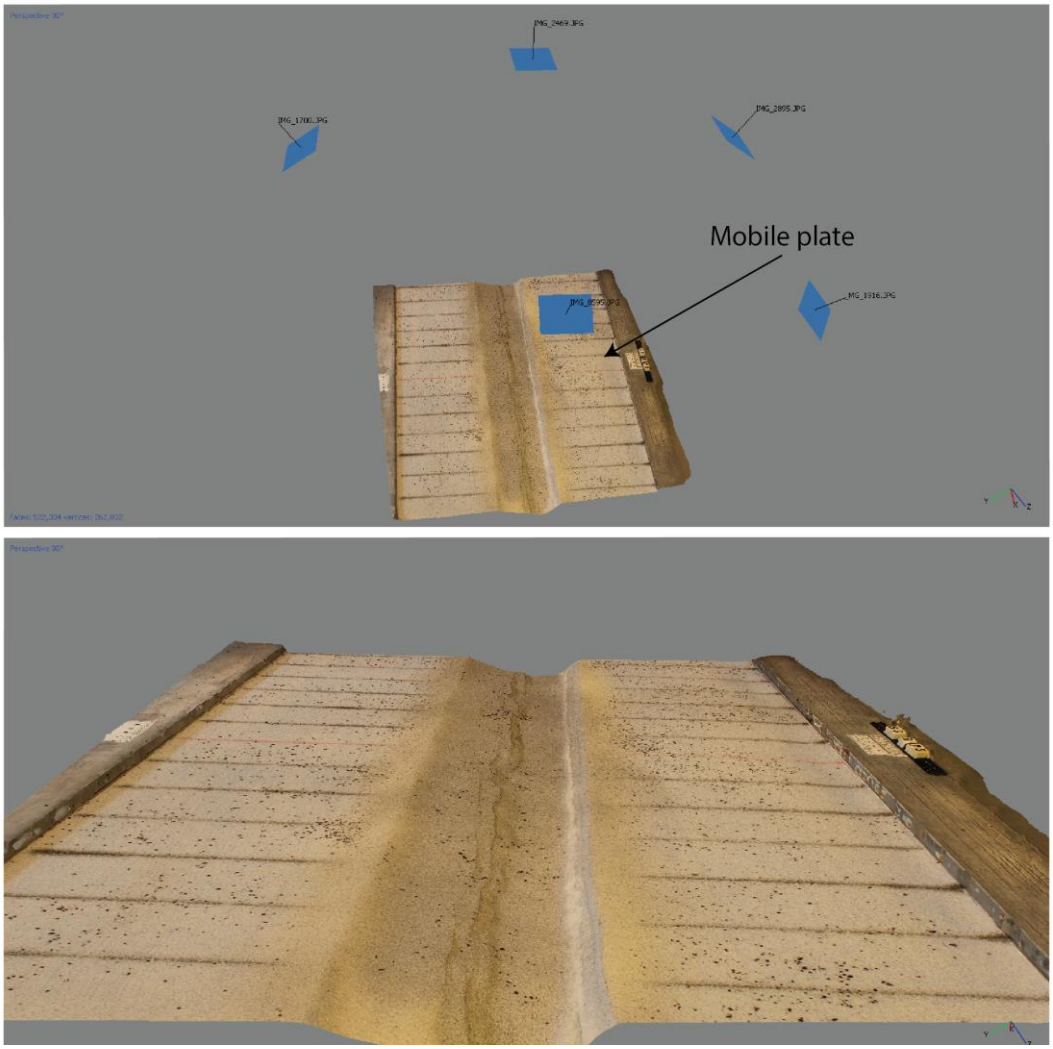

Figure 2.1.37. Screenshot of the 3D model in Agisoft Photoscan at 5.0 cm of extension. Sparse cloud (27.357 points), Dense cloud (2,657,966 points), Mesh (522,334 faces). The distance between each two gridlines is 5.0 cm.

During the initial rifting phase a graben developed as the result of the growth and movement of two large offset bounding faults (F1). The graben topography is asymmetrical along strike. There are two main topography zones inside of the graben which are separated by a small ridge (Figure 2.1.37 and 2.1.39). Progressive extension of the analogue model led to the development of normal faults (F2) and (F3) in the hanging-wall above static plate (Figure 2.1.38). After the completion of the extension phase the faults at the graben surface are not clearly visible due to the syn-tectonic sedimentation and collapse of the fault topography.

Other faults that may have developed within the graben can only be inferred using cross-sections, DEM's or PIV analysis.

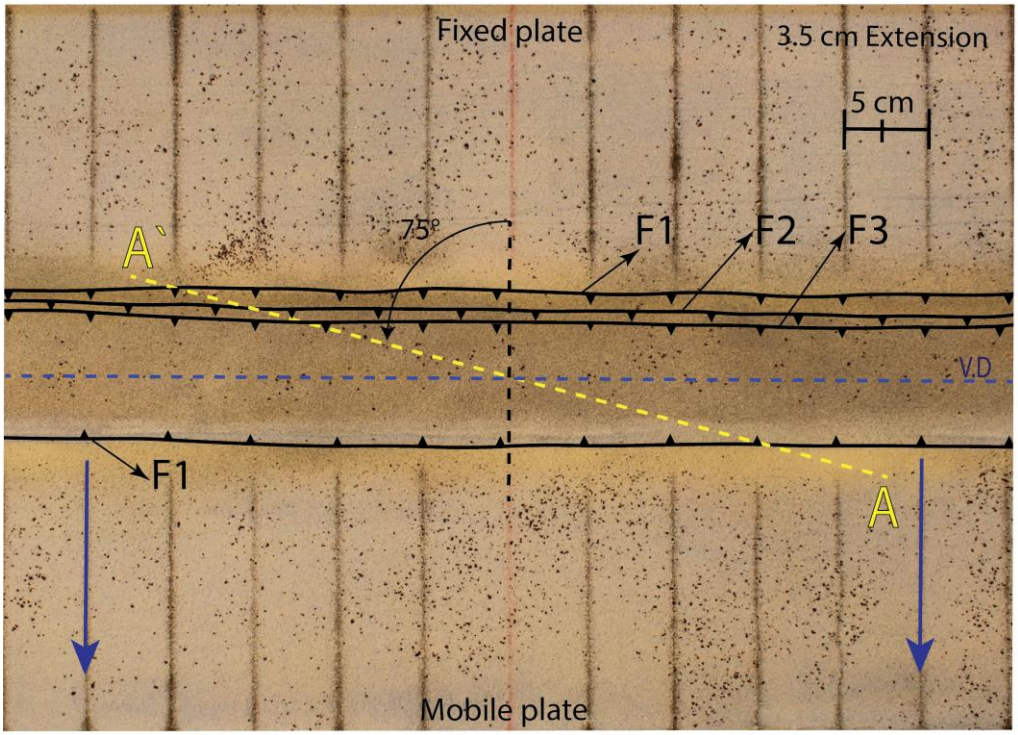

Figure 2.1.38. Top-view of the experiment at 3.5cm of extension (Orthomosaic image exported from Photoscan). Two new faults form in the hanging wall. The blue arrows indicate the direction of extension.

Figure 2.1.39. 3D perspective view of the extension graben.

In figure 2.1.39 relay structures are visible along strike of the faults formed above the V.D. Multiple ramps are visible that include branched relay ramps. These structures are not visible using top-view 2D images. These structures are also visible in figure 2.1.47. Which are the result of the formation of the normal faults F3, F4 and F5 that extrude to the surface.

In some previous experiments these structures are not clearly visible at the surface due to the different degrees of syn-tectonic sedimentation that might or might not covers these structures. After the rifting phase, inversion is applied to the system (Figures 2.1.40 and 2.1.41).

The textured 3D model compiled at the end of the inversion phase can be visualized here: https://sketchfab.com/models/d8d9dccbaabb401d8186171e2deef0b8

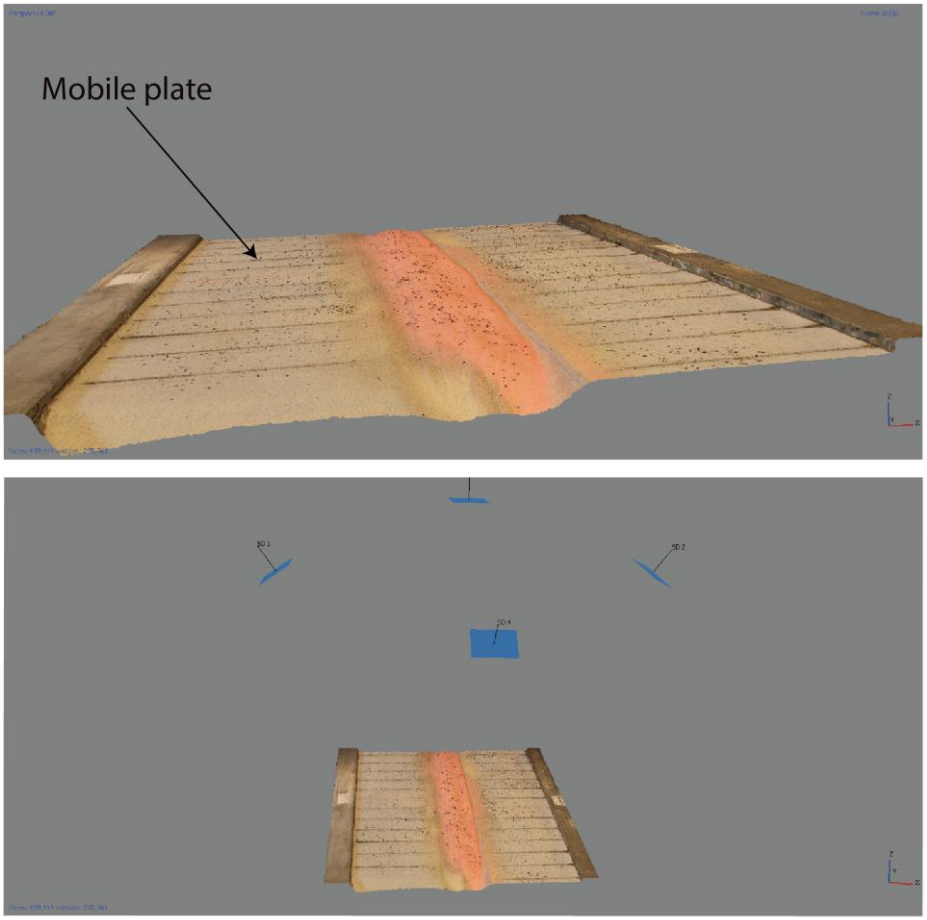

Figure 2.1.40. Screenshot of the 3D model in Agisoft Photoscan at 6.0 cm of inversion. The graben infill is slightly uplifted

The inversion process slowly closes the graben which forces the normal faults formed during the rifting phase to reactivate, both by creation of topography (vertical displacement) and by lateral displacement (strike-slip). In contrast to the previous experiments the following can be observed in figure 2.1.41 below: (1) There is no sign of the formation of thrust faults to accommodate the displacement so all displacement is accommodated by reversing the faults formed during the extension phase. (2) The strike-slip component is more extensive (+δv = δ2), which is clearly indicated by the displacement of the grid lines on both sides of the V.D. The total strike-slip displacement at the end of the experiment is approximately 5.1 cm parallel to the V.D (85% of all displacement). (3) The maximum uplift that formed due to the inversion was much less compared to experiments with shallower angles of inversion. (4) The vertical throw of the faults was much lower due to increased strike-slip component. (5) The reactivation above the moving plate is much more extensive than above the fixed plate, as most of the normal faults are located above the mobile plate during inversion. The topography produced because of the reactivation of the normal faults is much more

significant, which is represented in the 3D model as parallel ridges running along the strike of the graben. (6) Most strike-slip was accommodated by fault (F1) in the hanging wall above the mobile plate. (7) The foreland transport velocity magnitude of the graben is the lowest compared to experiments with shallower angles of inversion.

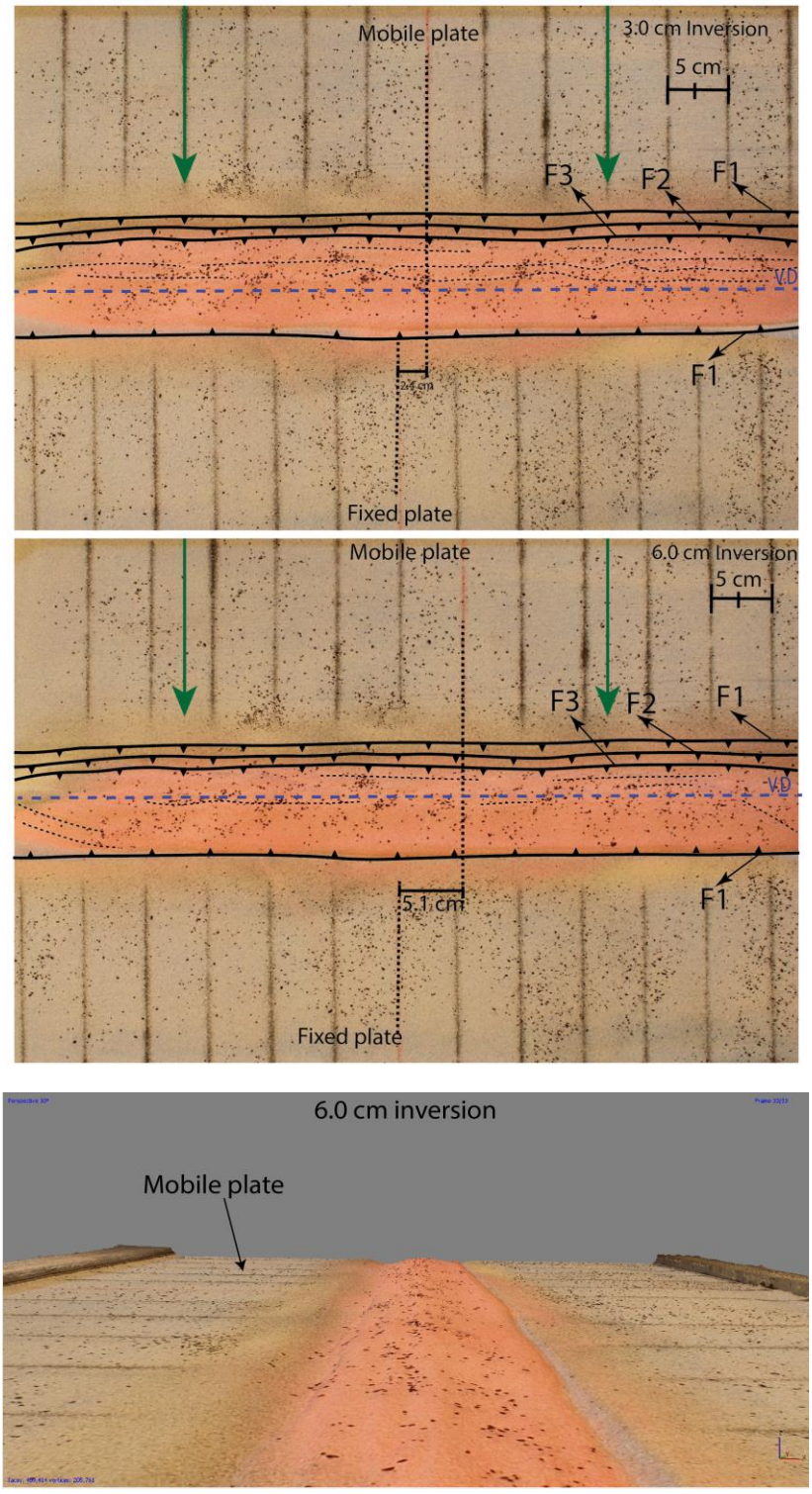

Figure 2.1.41. 3D view at 6.0 cm of inversion and Orthomosaic top-views of the experiment at 3.0 cm and 6.0 cm of inversion. The green arrows indicate the direction of inversion. The black dotted black lines are sections of possible normal faults. No thrust faults formed during the inversion.

PIV analysis

PIV vector and vector magnitude analysis was carried out using undistorted images exported from Agisoft Photoscan, the analysis using these photographs yielded much higher quality results due to the correction for lens distortion and camera tilt. Each of the analysis techniques contains a diagram with 12x frames for each deformation step of 0.5 cm (Figures 2.1.43 and 2.1.44). The following can be observed in these diagrams: (1) The displacement velocity and magnitude decrease from the hinterland to the foreland. (2) Almost all displacement was lateral (strike-slip) and occurred mostly by the reactivation of master normal fault (F1) in the hanging wall above the moving plate. (3) The foreland was much less strained compared to experiments with shallower inversion angles as all movement was accommodated along the normal faults within the graben and no displacement was transferred outside of the graben border faults. (4) Transpressional structures can be inferred from the wave-like movement of the vectors (Figure 2.1.44). (5) No new vector fields formed throughout the inversion phase, which indicates that there was no thrust faults formation. (6) The width of the deformation zone along which movement and strain occurs is much narrower compared to previous experiments with shallower inversion angles. From the Histogram in figure 2.1.42, two main zones with peaks of highest vector magnitudes can be observed at 0-2 pixels/frame (immobile plate) and 23 pixels/frame (mobile plate and graben). Compared to previous experiments there is no a large separation between the vector magnitudes above the moving plate and that of the graben, this suggests that little resistance to displacement occurred (continuous movement). The scatterplot illustrates the orientation of the vectors at 3.0 cm of inversion, this pattern has large similarities with the previous experiments, however, the data cloud is more rotated compared to previous experiments which points to increased strike-slip movement.

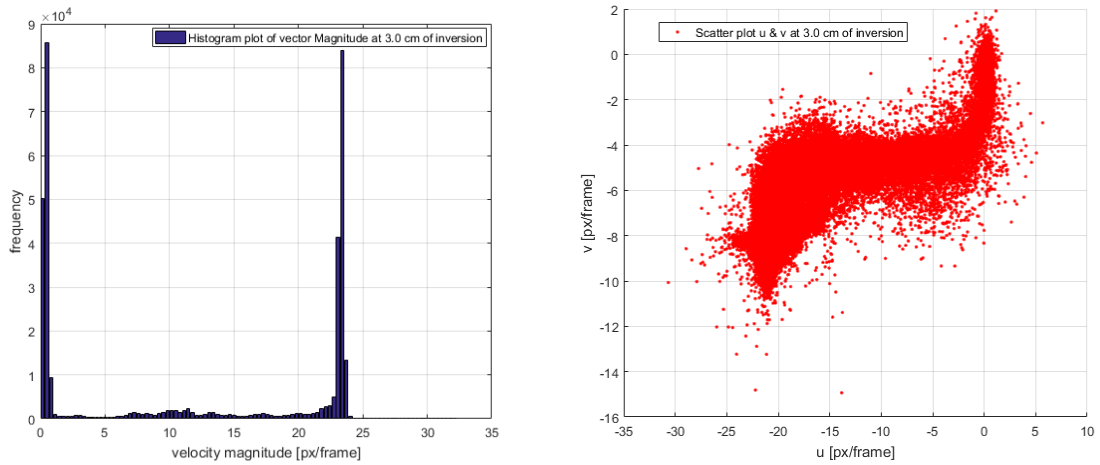

Figure 2.1.42. Histogram and scatter plots of the PIV analysis at 3.0 cm of inversion. There are only two peeks with the highest frequency, indicating that the graben did not resist the movement and that slip required a low activation energy.

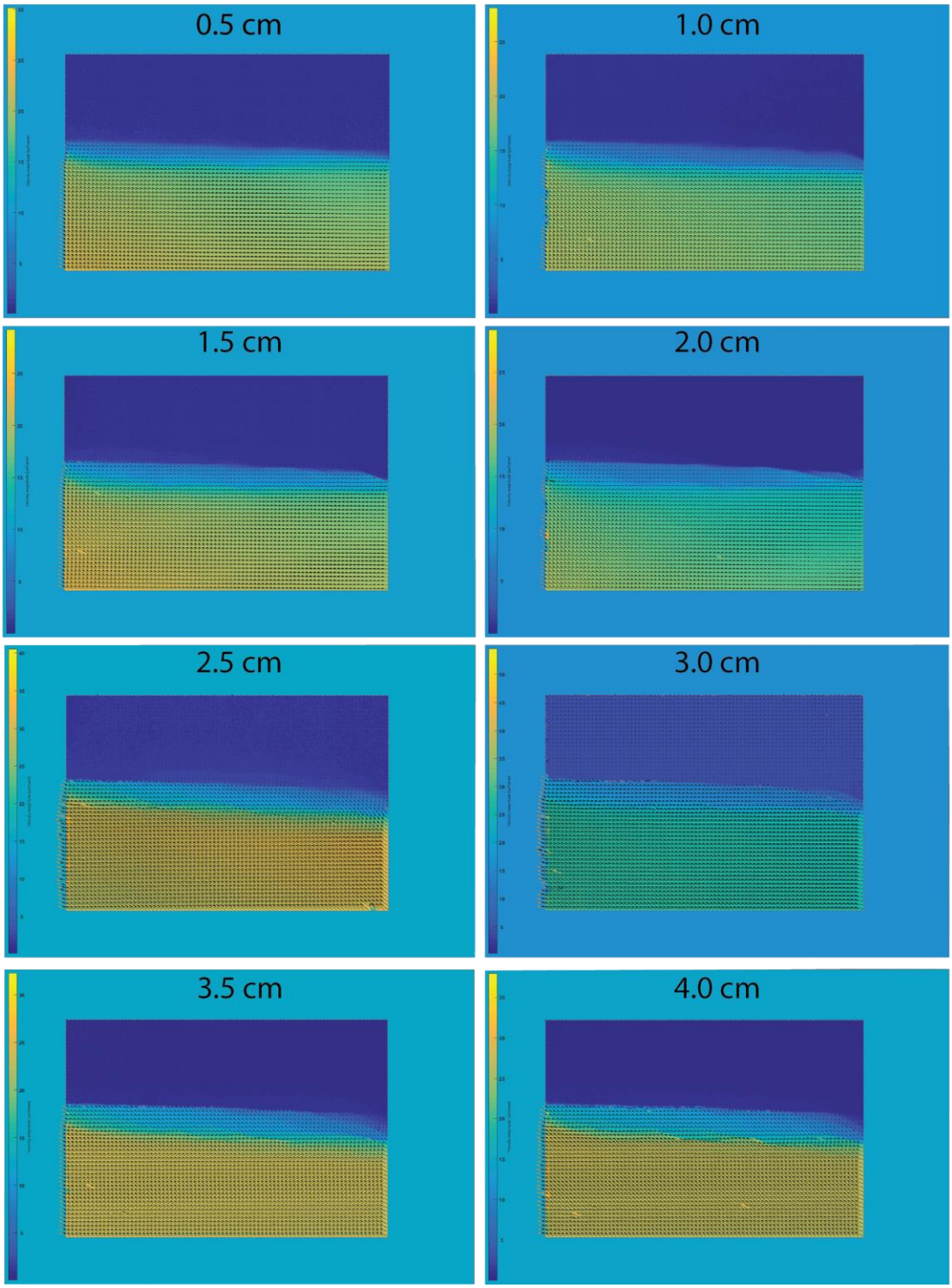
0.5 cm
1.0 cm
1.5 cm
2.0 cm
2.5 cm
3.0 cm
3.5 cm
4.0 cm

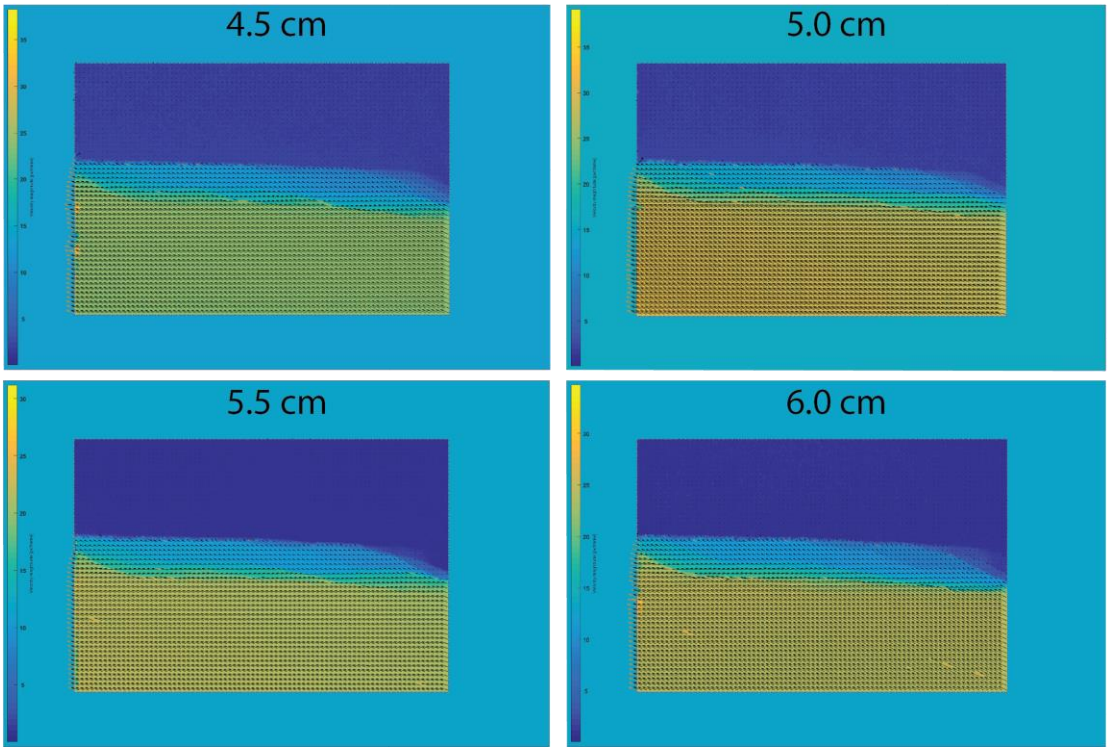

Figure 2.1.43. PIV analysis of the vector magnitude (pixels/frame) of the inversion, each diagram represents a 0.5 cm step of the inversion process.

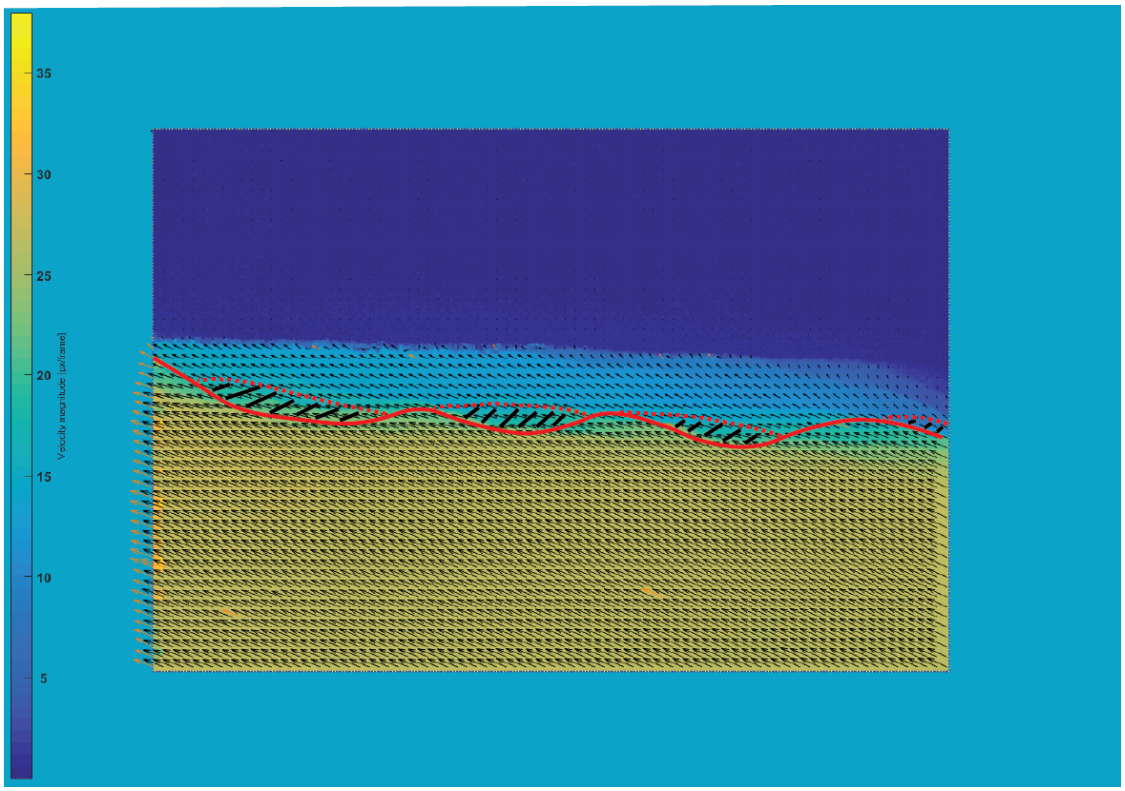

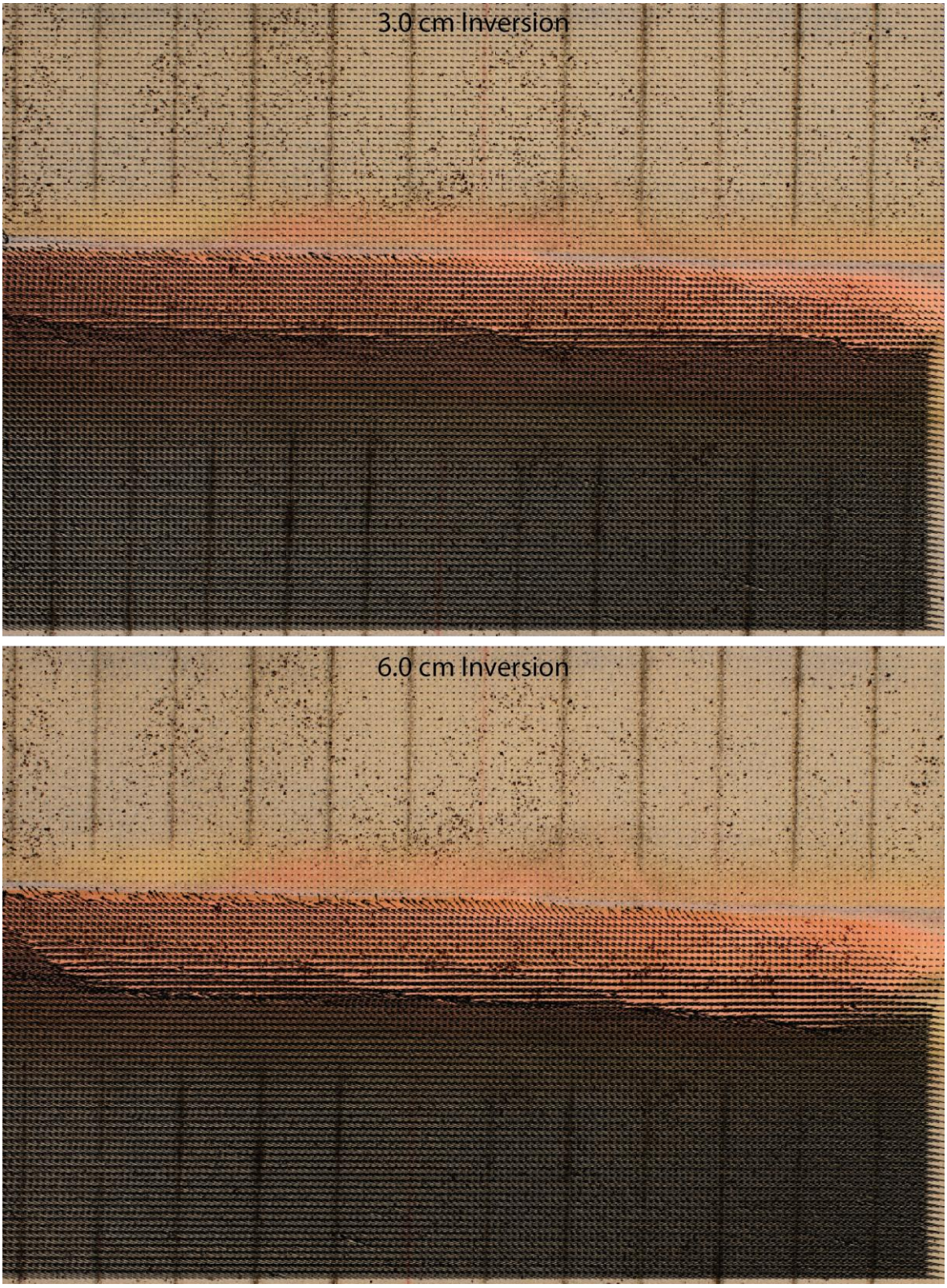

Figure 2.1.44. Wave-like velocity fields points to the formation transpressional structures which led to the formation of restraining and releasing bends which yields different vector field orientations.

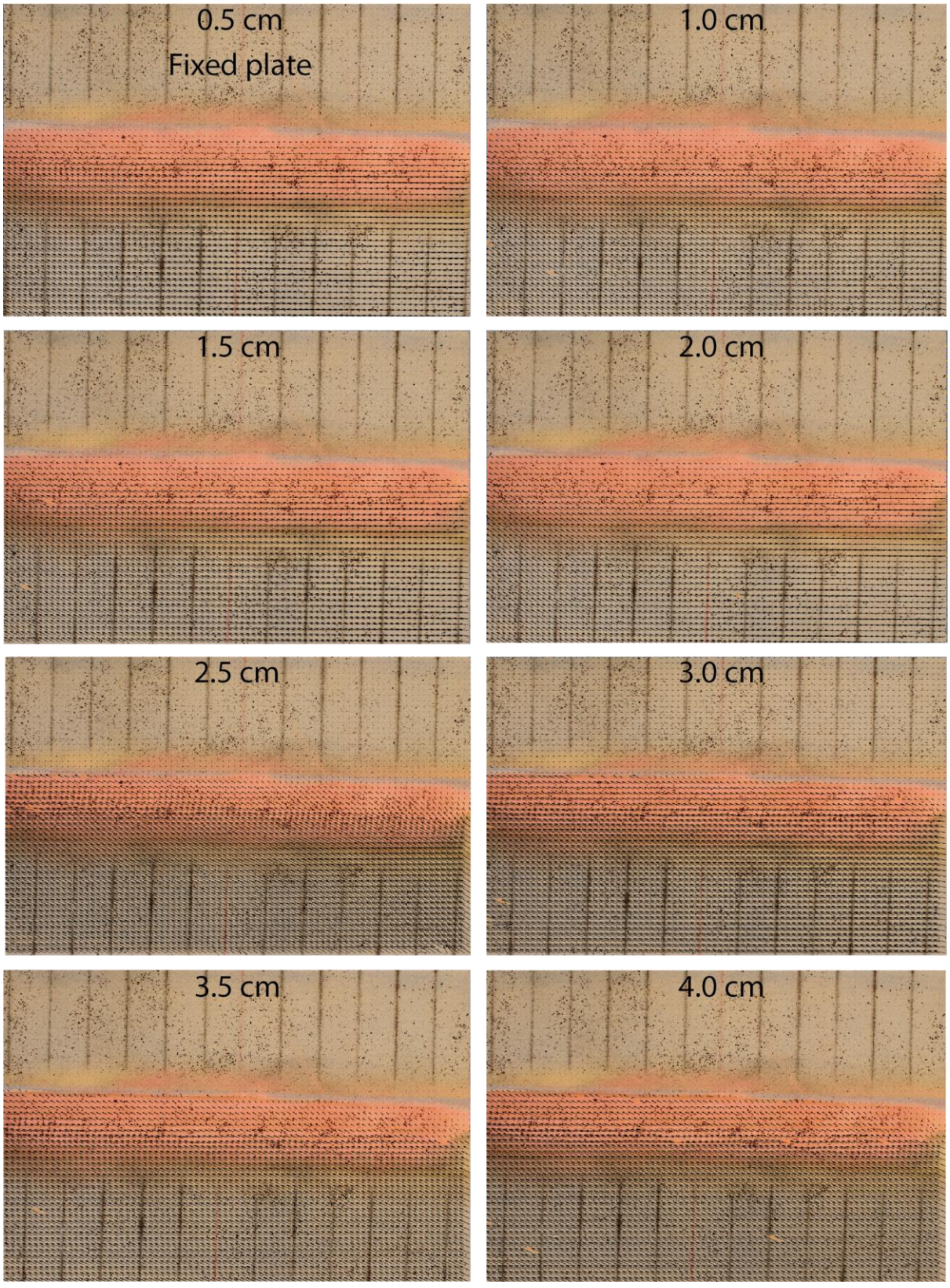
0.5 cm
Fixed plate
1.0 cm
1.5 cm
2.0 cm
2.5 cm
3.0 cm
3.5 cm
4.0 cm

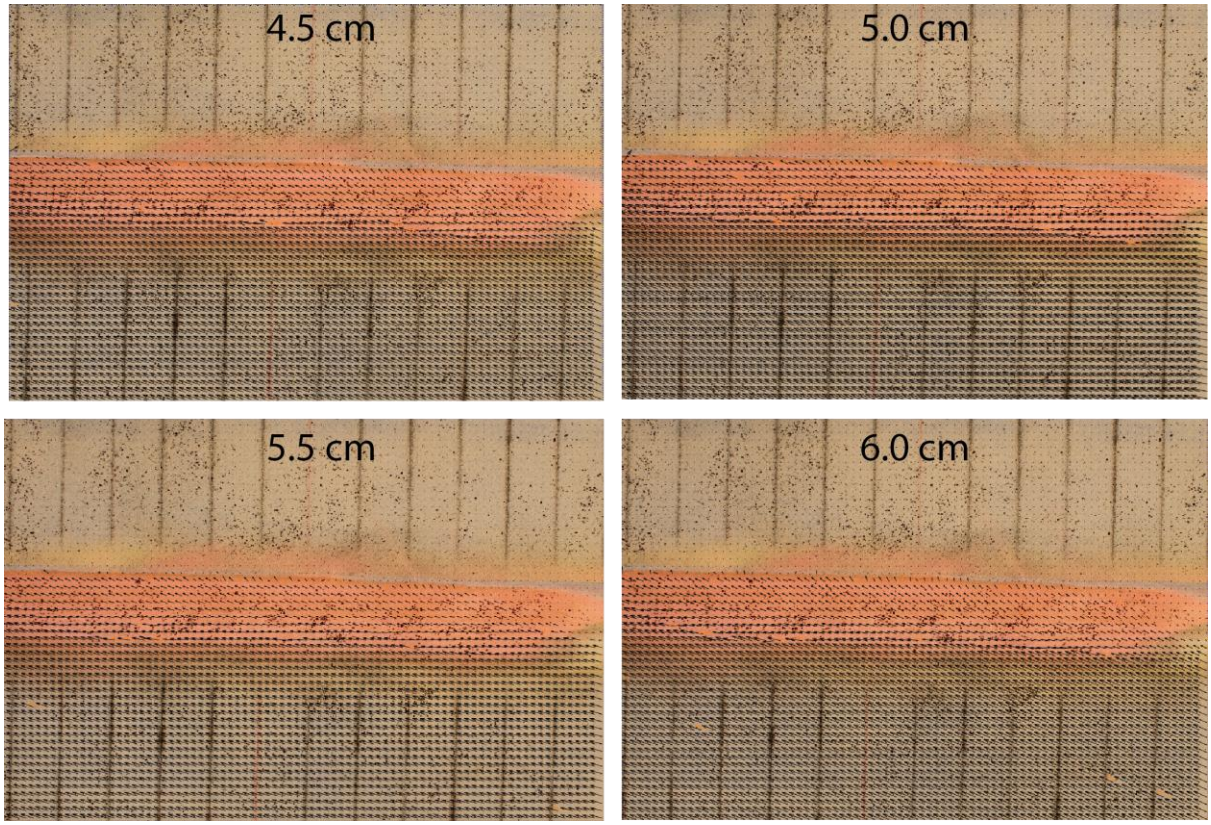

Figure 2.1.45. PIV vector analysis of the inversion phase, each diagram represents a 0.5 cm displacement frame of the inversion phase. No new vector fields formed throughout the inversion, which indicates that the slip was only accommodated by reactivation of existing normal faults.

Only a very small vector density is present close to faults (F1) in the footwall, which indicates that most displacement was already accommodated by slip along the first few faults in the hanging-wall (F1, F2, F3 and F4).

Inversion phase DEM analysis

In the figures below digital elevation models (DEM's) of the inversion phase are presented. Three analysis techniques were applied: Color ramp, Slope analysis and color ramp + Hillshade.

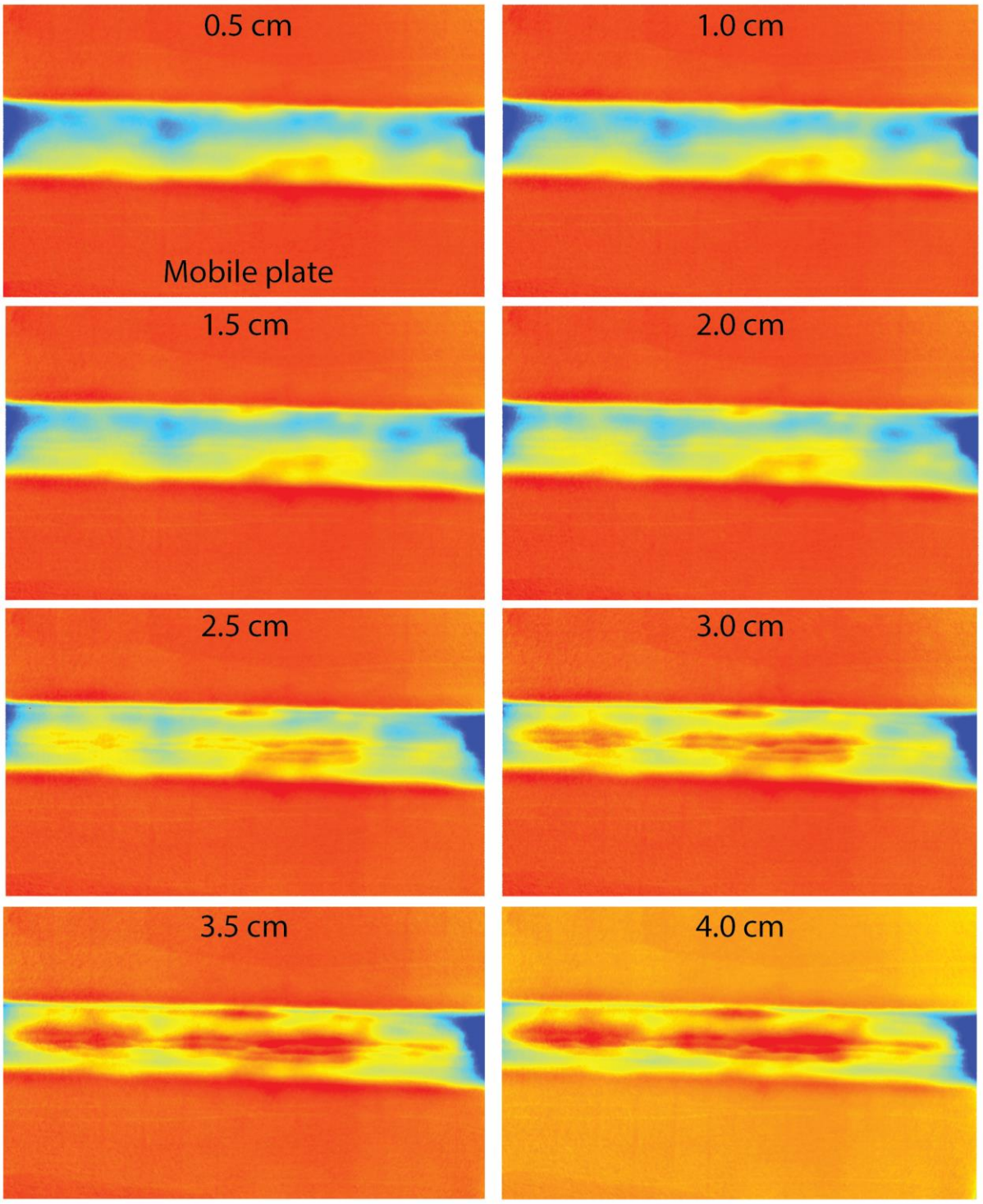
0.5 cm
Mobile plate
1.0 cm
1.5 cm
2.0 cm
2.5 cm
3.0 cm
3.5 cm
4.0 cm

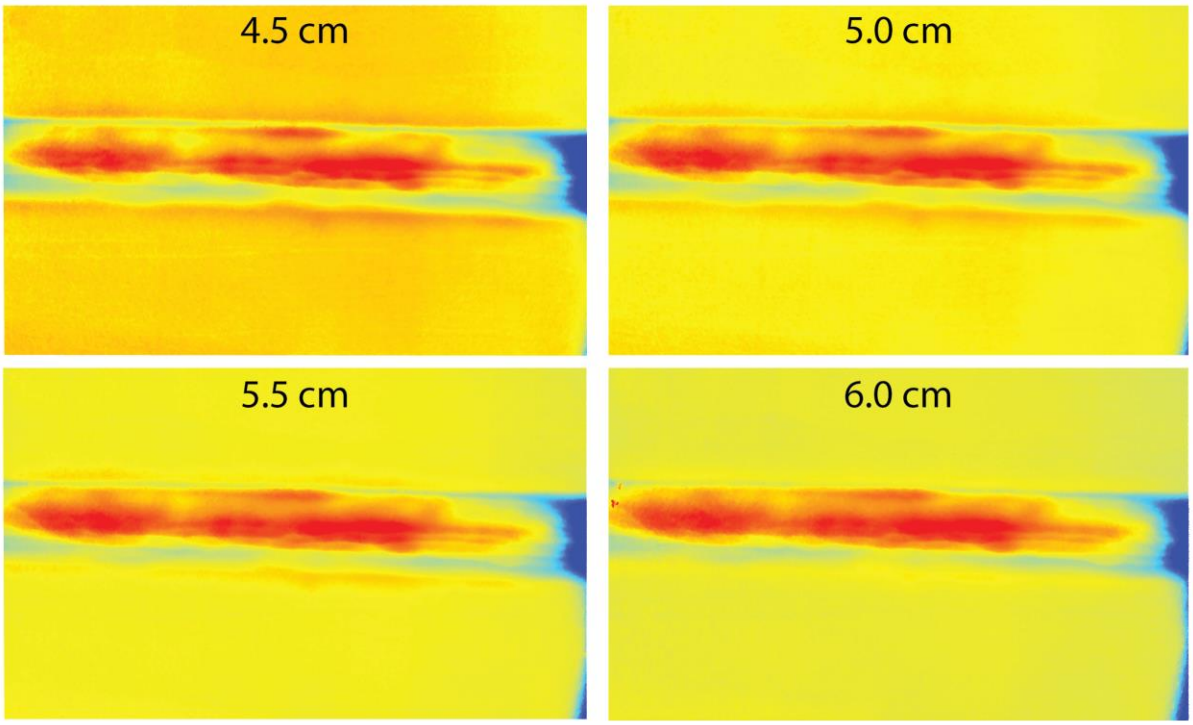

Figure 2.1.46. Inversion phase DEM's as frames (0.5 cm steps), no Hillshade. The graben infill is slowly uplifted, which leads to a more intense red color, indicating that the topography is higher. The slight color change of the model flanks between each frame is the result of the individual processing of each frame in Agisoft, which changes the color ramp range. Only qualitative analysis was performed.

In the DEM's above in figure 2.1.46 it is clearly visible that the topography is displaced towards the fixed plate, however, the maximum uplift that formed close to (F1) above the mobile plate is less compared to the topography formed in the footwall above the immobile plate, this could be related to the fact that the faults that are reactivated in the footwall dip towards the hanging-wall and thus most of the topography that forms as a result of the reverse vertical slip occurs in the direction of the footwall. This also indicates that very little vertical slip occurred at the master normal fault (F1) in the hanging-wall. This thus indicates that there is a partitioning between where strike-slip reactivation occurs and where vertical reactivation occurs.

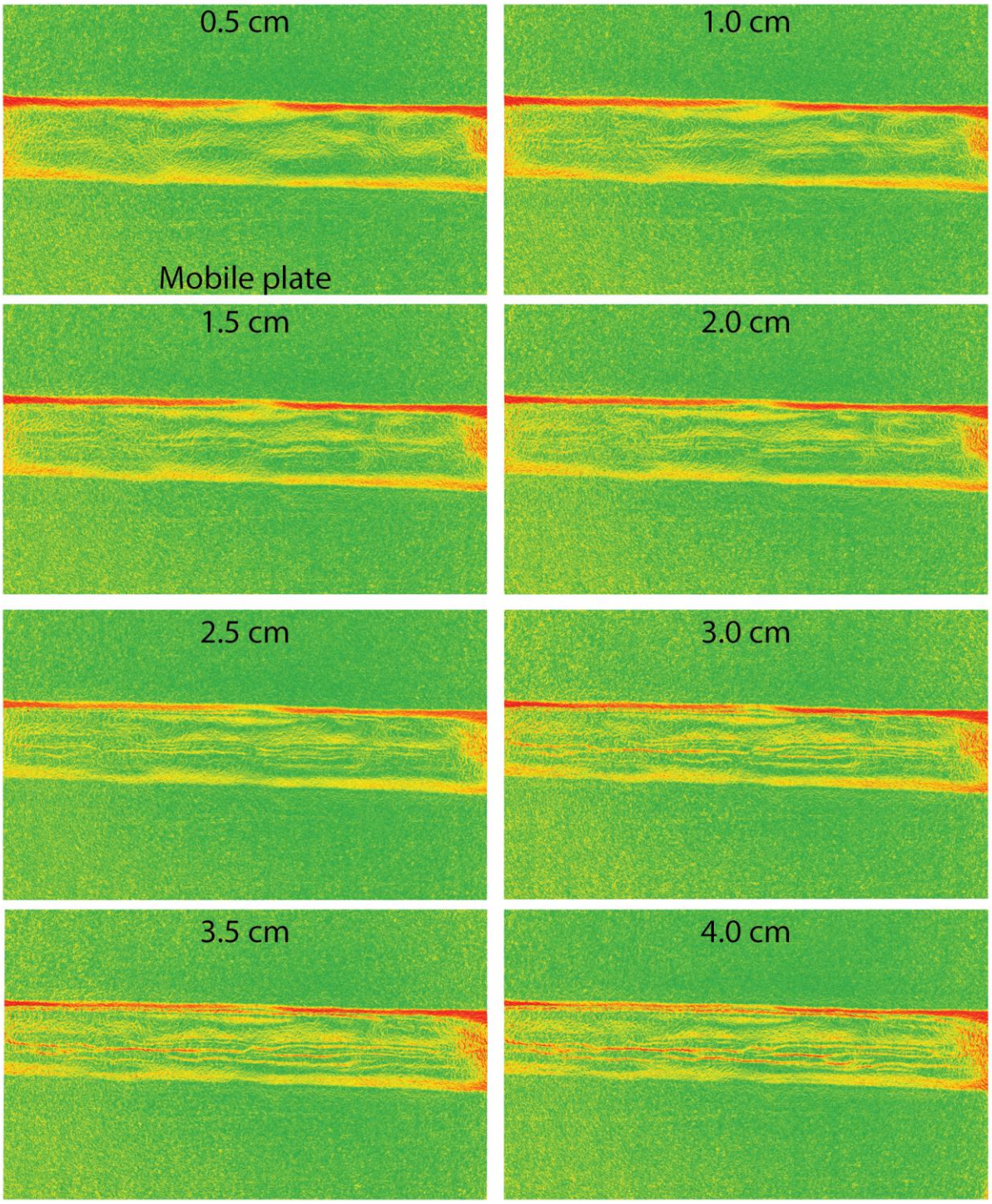
0.5 cm
1.0 cm
Mobile plate
1.5 cm
2.0 cm
2.5 cm
3.0 cm
3.5 cm
4.0 cm

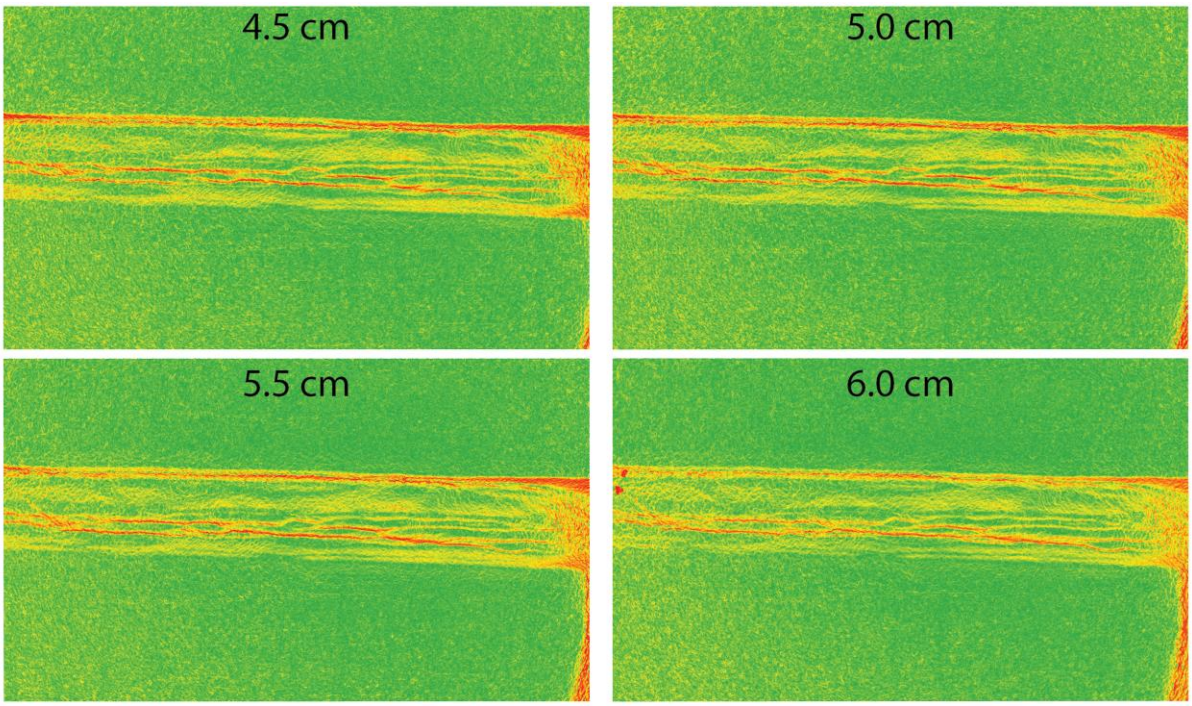

Figure 2.1.47. Spatial slope analysis of the DEM's in ArcMap of each frame of the inversion phase (0.5 cm steps). (0-90 degrees). The red colored bands represent ridges with steep slopes, while the green zones represent the flat model flanks.

From the figure above the following can be observed: (1) As the inversion initiates the larges slopes are located above the fixed plate. (2) As the deformation proceeds, many very small parallel ridges with steep slopes form at the surface of the graben infill. (3) These ridges nucleate above the mobile plate and slowly propagate towards the fixed plate. (4) They have steeper slopes than those closer to the footwall. (5) After 4.0 cm of inversion these ridges bifurcate into (y) shaped structures. (5) The structures with the steepest slopes are located at the center of the graben. (6) As inversion progresses these ridges become increasingly asymmetrical and their wave-like pattern increases. These ridges are related to the vertical reactivation of the normal faults which led to the exhumation to the surface of the model.

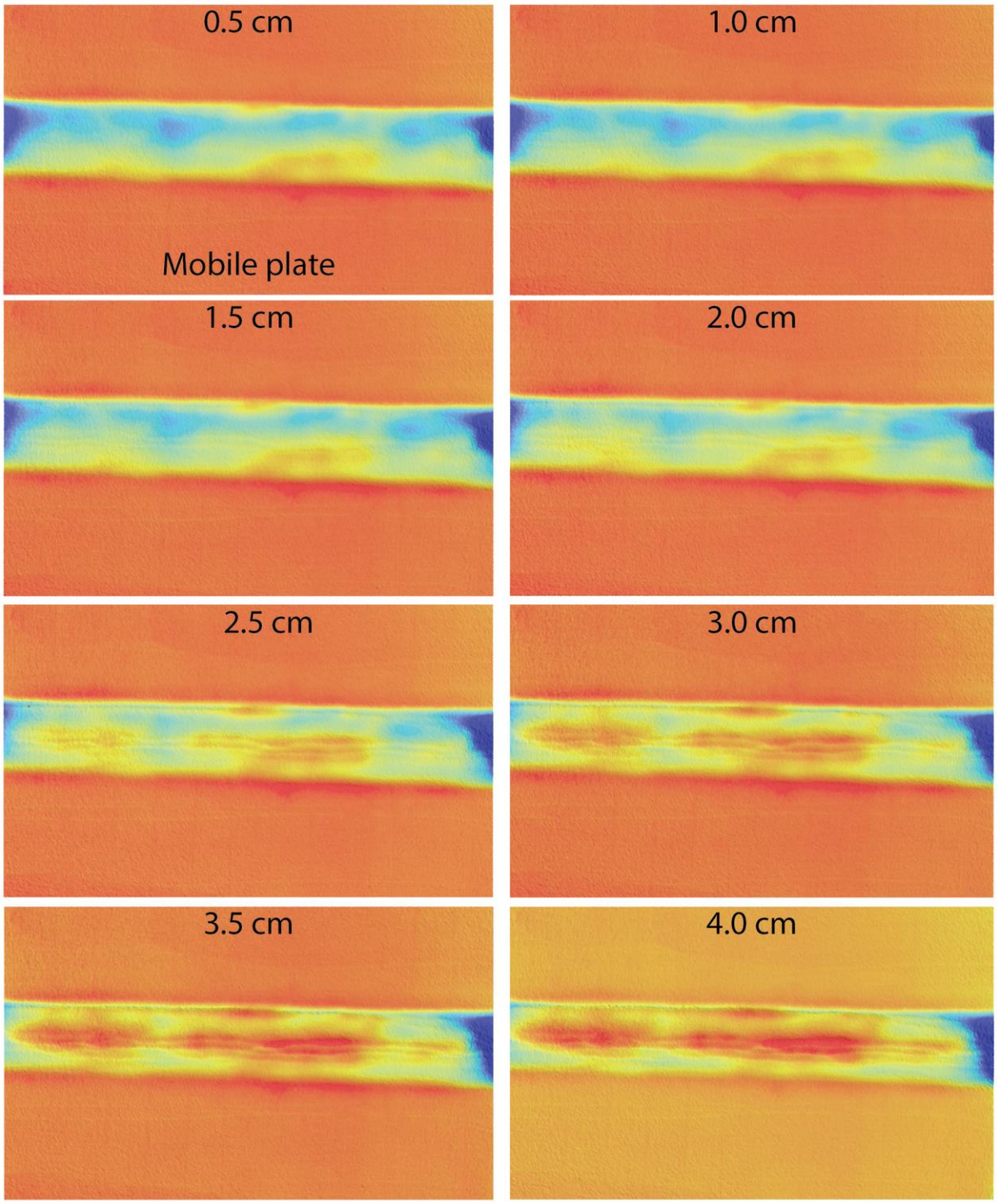
0.5 cm
Mobile plate
1.0 cm
1.5 cm
2.0 cm
2.5 cm
3.0 cm
3.5 cm
4.0 cm

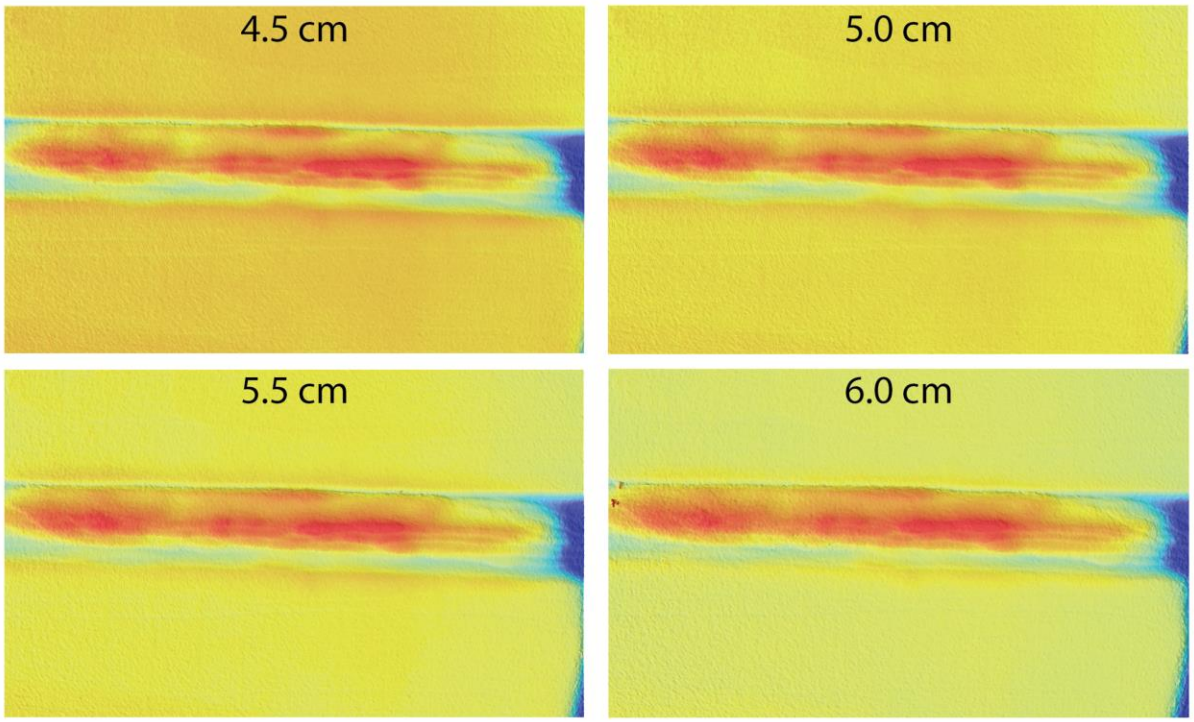

Figure 2.1.48. Spatial Hillshade analysis of the DEM's in ArcMap of each frame of the inversion frames (0.5 cm steps). The graben infill is slowly uplifted, which leads to a more intense red color, indicating that the topography is higher. The slight color change of the model flanks between each frame is the result of the individual processing of each frame in Agisoft, which changes the color ramp range. Only qualitative analysis was performed.

In figure 2.1.48 above the following can be observed: (1) The initial positive topography formed in the center of the graben as two parallel running ridges that run across the whole length of the graben (reactivated normal faults). (2) At 2.0 cm of inversion fault (F1) above the immobile plate was reactivated (ridge formation). (3) Successive shortening mainly produced topography at the two ridges in the center of the model, these ridges are uplifted more extensively compared to the rest of the surrounding graben. (4) After 4.5 cm of inversion almost no new positive topography was produced. (5) Throughout the deformation, the graben was slowly transported in the direction of S1.

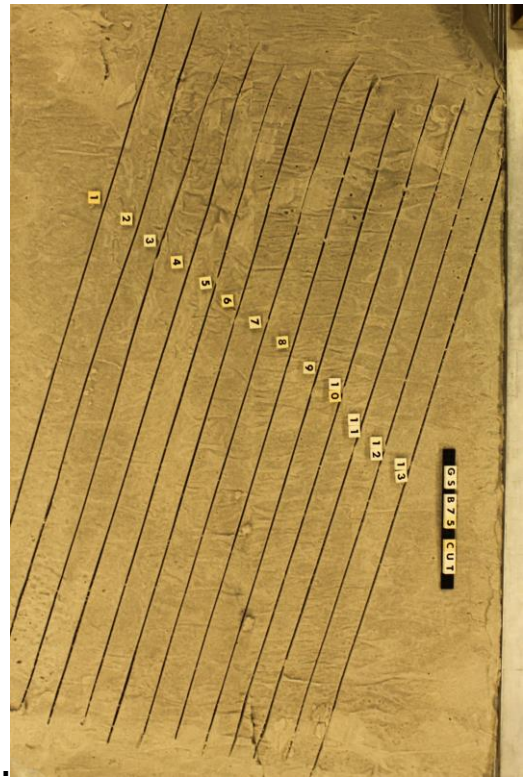

Figure 2.1.49. Cross-section numbering of the analogue model and their relative positions.

The cross section below is taken at a 75° angle to the velocity discontinuity at the end of the experiment after 6.0 cm of inversion is applied to the system. The following can be observed in this cross-section: (1) It contains six normal faults (2x F1, F2, F3, F4 and F5). (2) No thrust fault formation occurred during the inversion. (3) Accommodation of the displacement mainly occurred by vertical and horizontal reactivation of the normal faults. (4) All faults are steeper than 60°. (5) The maximum uplift produced is significantly less compared to experiments with shallower inversion angles. (7) Reverse faulting of F1, F2, F3, F4 and F5 above the mobile plate accommodated almost all the displacement perpendicular to the velocity discontinuity, while only faults F1 and F2 above the mobile plate accommodated most of the displacement parallel to the V.D (with support from PIV analysis).

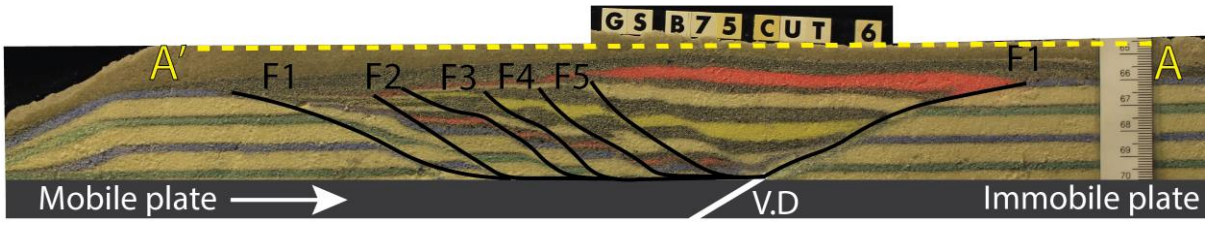

Figure 2.1.50. Cross section taken after 6.0 cm of inversion of the model GS-B75°.

2.2 Brittle-Ductile models

2.2.1 GS-D90: Brittle-Ductile, Extension and sedimentation followed by oblique inversion.

Photographs taken from the top-view camera during the deformation of the analogue model were compiled into a time-lapse that can be visualized here:
https://www.youtube.com/watch?v=hfK3gyEFtPQ
The textured 3D model compiled at the end of the rifting phase can be visualized here:
https://sketchfab.com/models/81dcddb25be140fdbd41a45b25a76f61

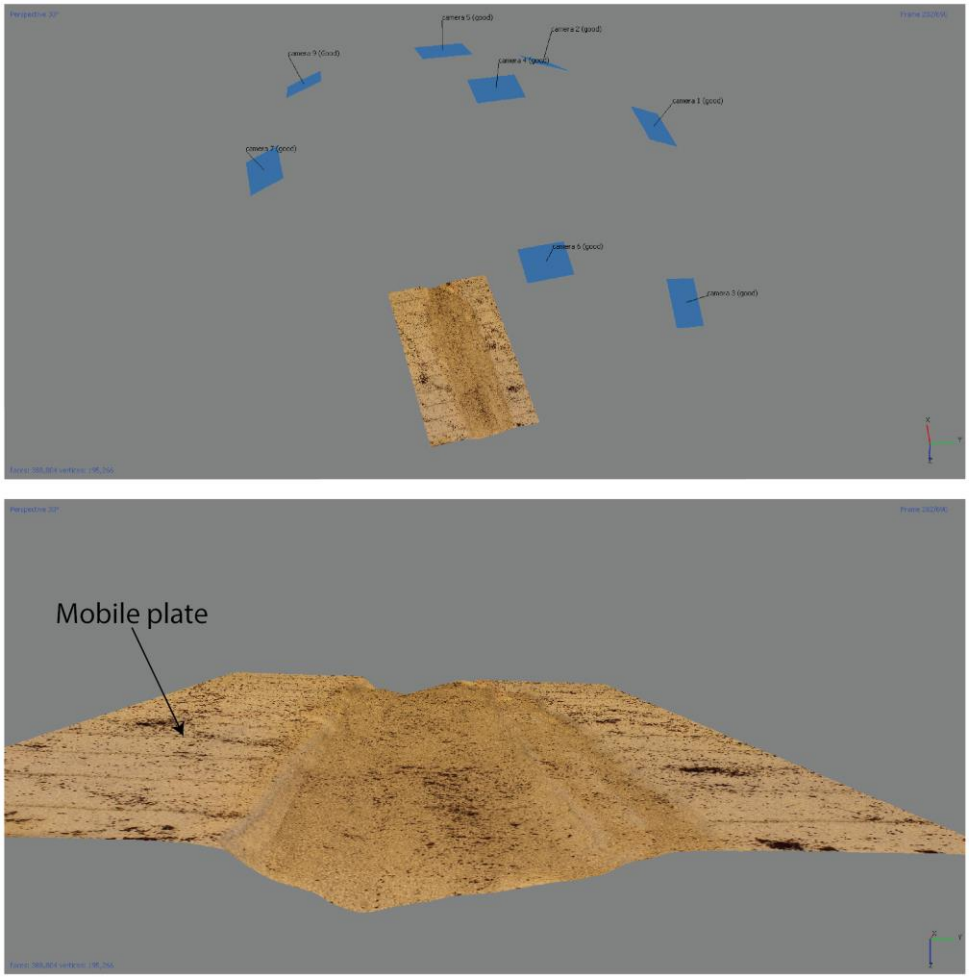

Figure 2.2.1. 0 Screenshot of the 3D model in Agisoft Photoscan at 5.0 cm of extension (8x cameras). Sparse cloud (19,890 points), Dense cloud (1,944,207 points), Mesh (388,804 faces, 195.266 vertices).

The following observations can be made after analyzing the 3D model and the surface top views (Figures 2.2.1 and 2.2.2): (1) The graben geometry and topography is asymmetrical along strike. (2) Smaller grabens formed at the flanks of the main basin. (3) The ridge separating the lowland and highland inside of the graben is not clearly visible. (4) The surface area and volume of the extended 3D model was measured, which equates to a surface area of 0.4341 m2 and a volume of -225,113 cm3. The negative sign is because the volume is a depression, indicating that 225,113 cm3 of water would fill the entire graben up to the model flanks. Extension of the analogue model led to the formation and growth of a graben bounded by two large offsetting master faults (F1). Progressive extension led to the formation of a small graben above the fixed plate bounded by faults (F2). A similar graben formed above the mobile plate, however, this structure is not well visible from the top views. In comparison to previous purely brittle experiments no faults are clearly visible inside of the main rift. Other faults that may develop within the graben can only be identified using cross-sections or inferred using DEM's or PIV analysis.

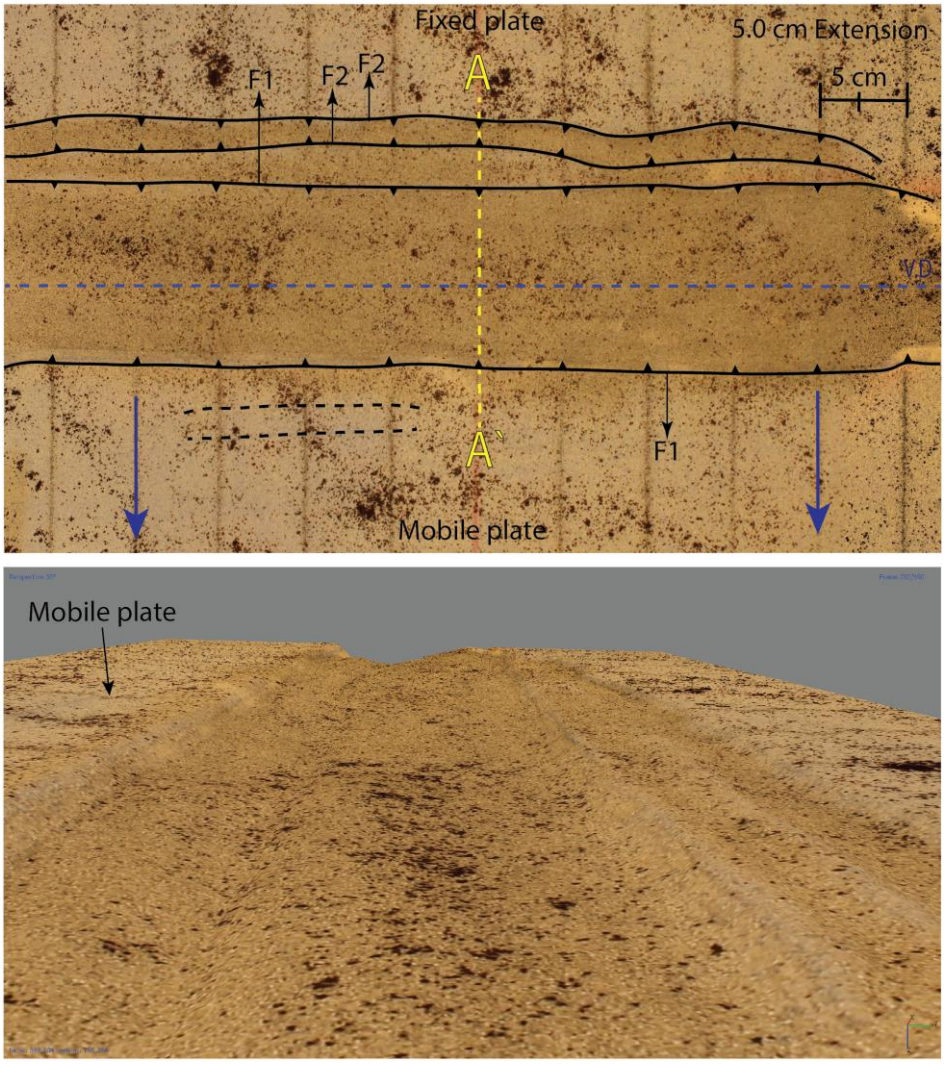

Figure 2.2.2. Top view of the experiment at 5.0 cm of extension (Orthomosaic image from Photoscan, 3796x2566, 0.173mm/pix) and perspective view of the graben at 35°. Four normal faults are visible (2x F1 and 2x F2).

Extension phase DEM analysis

A DEM from the fully extended analogue model (5.0 cm extension) was constructed from the dense point cloud in Agisoft Photoscan. The DEM was exported from Photoscan and processed in ArcMap which yielded the maps below in figures 2.2.3 and 2.2.4.
Most of the micro-topography formed during the extension phase is not well visible in the top view photographs. DEM's of the extension phase can reveal this micro-topography with very high detail and precision. The following can be observed in these DEM maps: (1) The deepest formed depression has a depth -1.203 cm below the surface of the analogue model. (2) A small graben formed above the immobile plate which was not visible with the naked eye during the experiment and is also not visible in the top-view photographs. This graben runs parallel to the graben below delineated by faults (F2). (3) The asymmetry along strike of both these small grabens is significant, which is characterized by their wave-like longitudinal pattern. (4) A small horst separates fault F2 from master fault F1 of the main rift basin. (5) Inside of this basin a small trench runs across its entire length. (6) A small graben also formed above the mobile plate, however, this graben is not continuous and shows significant horizontal displacement, which could point to strike-slip faulting in the sedimentary cover, this structure is not visible in the top-views. (7) The largest and steepest faults formed above the mobile plate (Figure 2.2.4). (7) The faults that formed above the mobile plate during extension have a Southward dipping slope direction, while the faults above the immobile plate have a northward slope direction (Figure 2.2.4). (8) The small platform grabens nucleated at the flanks of the model attached to master faults (F1) and slowly migrated inwards, which led to a 'n' shaped structure in the immobile plate and a 'u' shaped structure above the mobile plate.

Aspect analysis identifies the downslope direction of the maximum rate of change in value from each cell to its neighbors. It can be thought of as the slope direction.

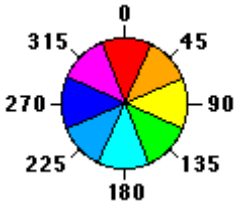

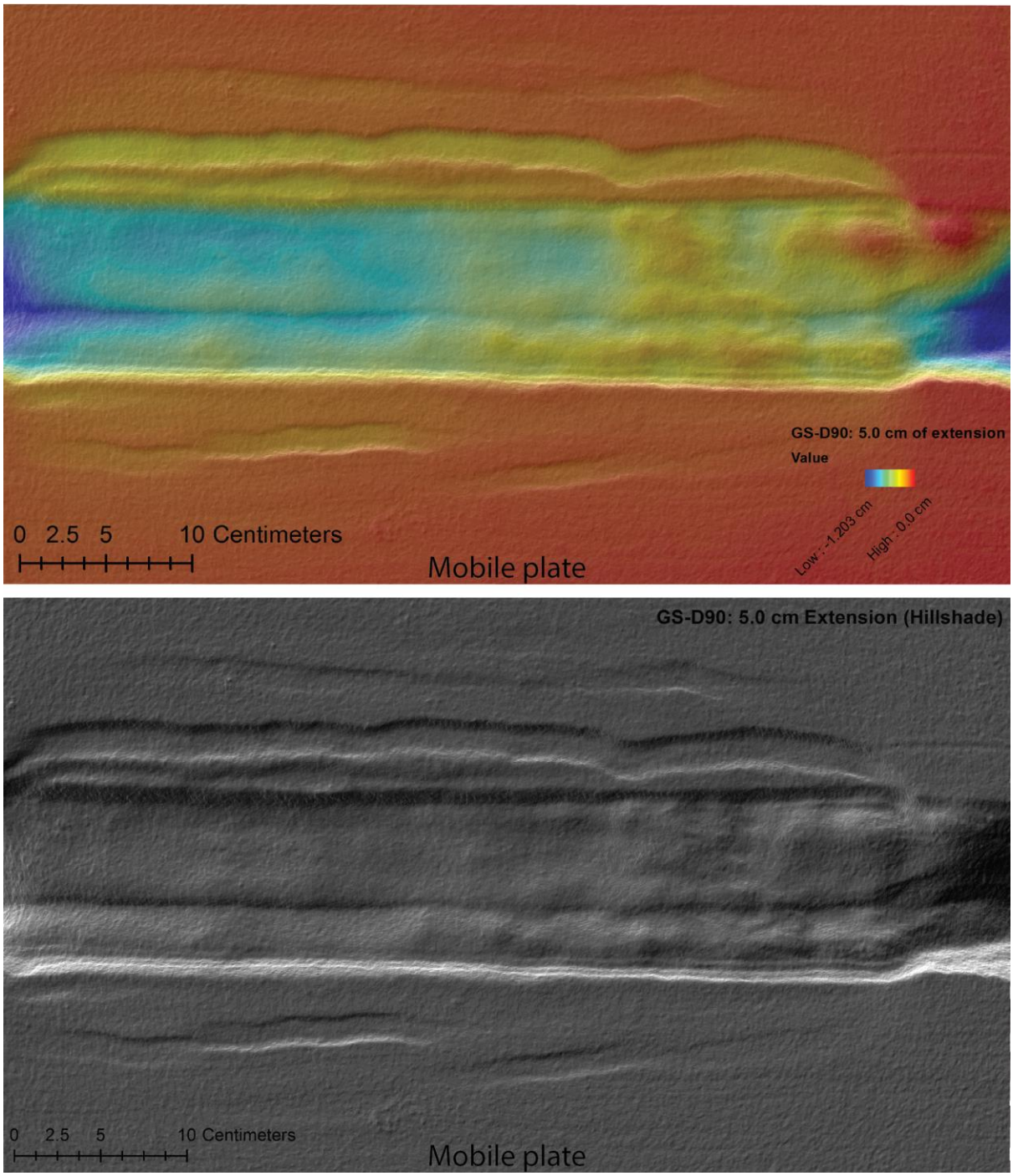

Figure 2.2.3. Color ramp and Hillshade analysis of the DEM in ArcMap (950x643, 0.692 mm/pix). The top image consists of a color ramp combined with a 40% transparent overlay of the Hillshade image. The grey image consists of a Hillshade spatial analysis map (no transparency). 5.0 cm of extension.

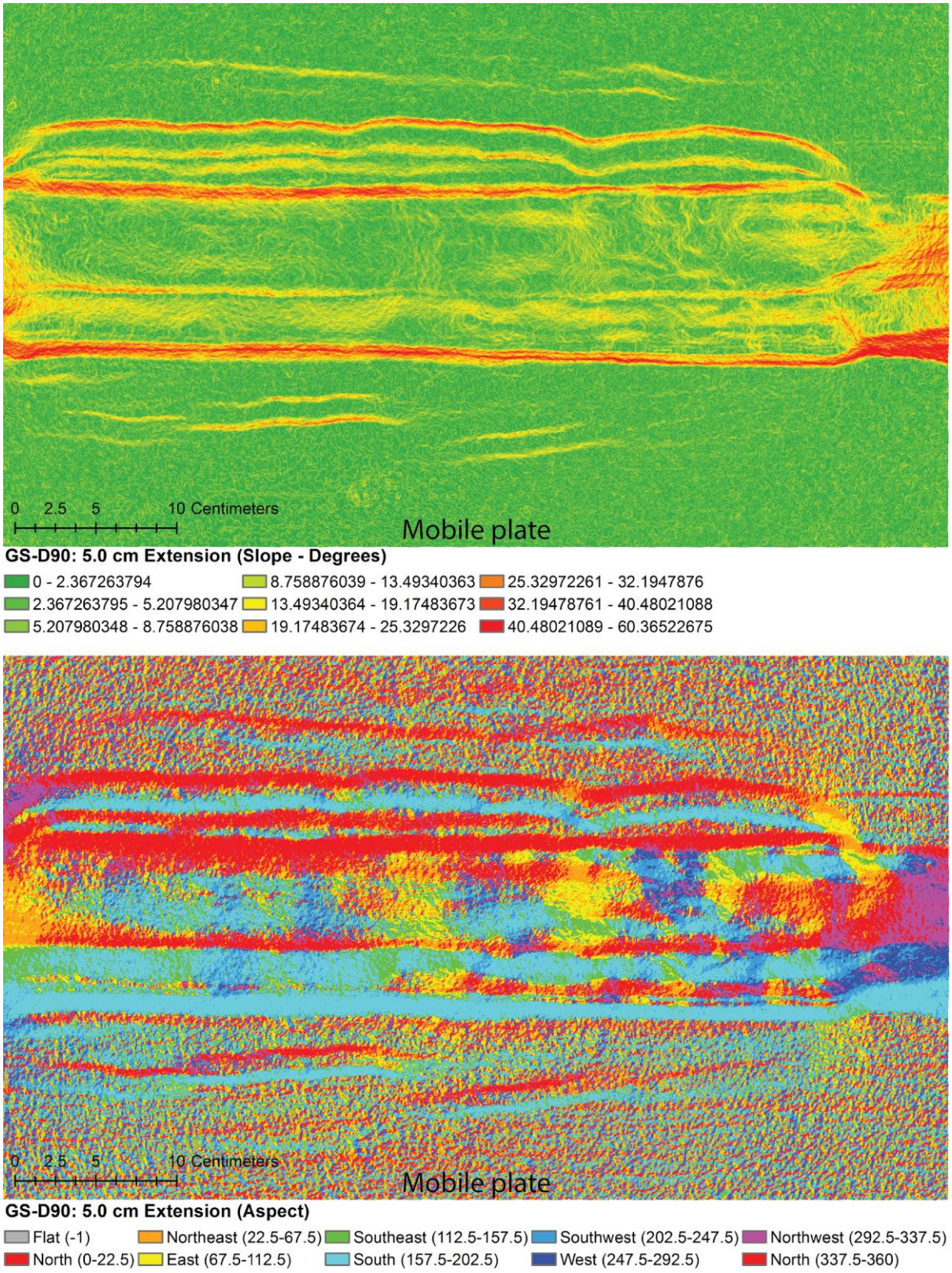

Figure 2.2.4. Slope and Aspect spatial analysis of the DEM in ArcMap (5.0 cm of Extension). The aspect analysis represents the slope direction. The top of the Aspect images is the North direction. The bottom of the image is the South direction. 5.0 cm of extension.

After the extensional phase inversion is applied to the system (Figures 2.2.5 and 2.2.6). The textured 3D model compiled at the end of the inversion phase can be visualized here: https://sketchfab.com/models/75f9d7c08f1b4309b1d494619f984727

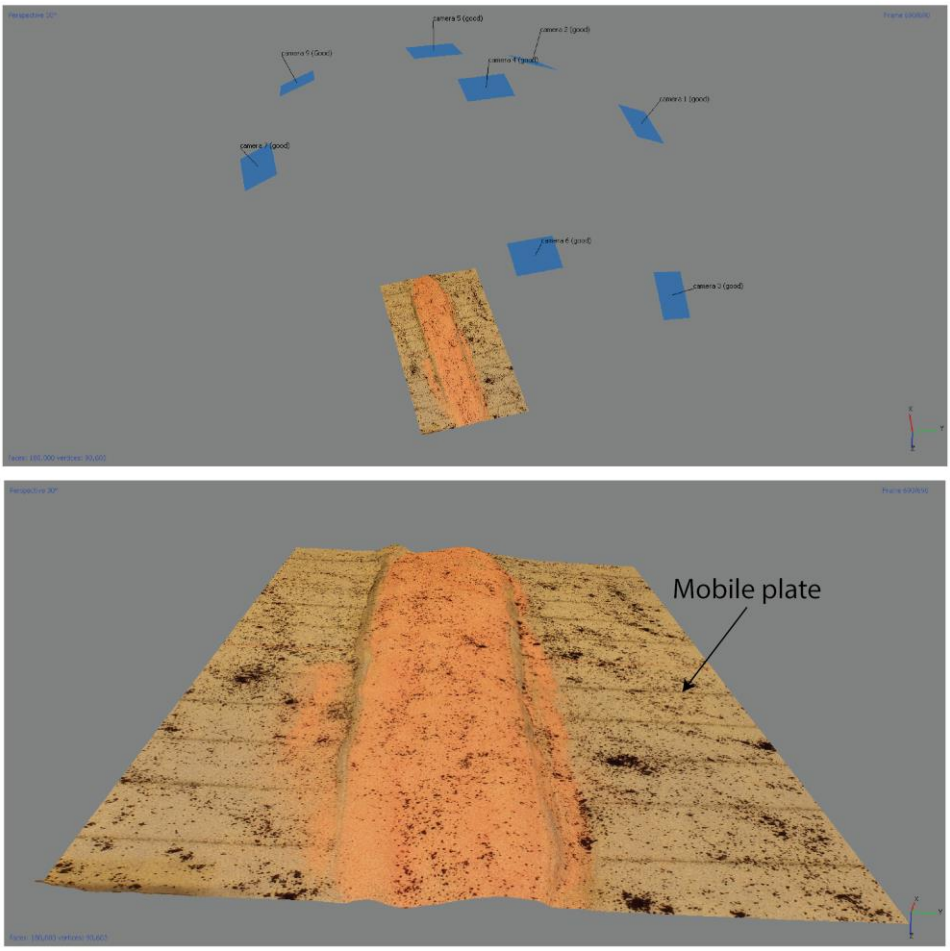

Figure 2.2.5. Screenshots of the 3D model in Agisoft Photoscan at 6.0 cm of inversion. 8x cameras, Sparse Cloud (7,992 points), dense cloud (487,676 points), Mesh (189,00 faces. 90,603 vertices).

The inversion phase slowly closes the graben orthogonally to the velocity discontinuity. The following observations can be made after analyzing the 3D model and the surface top (Figures 2.2.4 and 2.2.6): (1) Two shortcut thrust faults formed on either side of the graben (forethrust R1 and backthrust R2). (2) From deformation observations and PIV analysis in the next section it was found that shortcut fault (R1) was the first thrust fault to form, followed by shortcut fault R2. (3) There is no displacement of the purple central grid line running through the center of the model which suggest that almost no strike-slip components was present in the system during inversion, indicating that the movement was primarily accommodated by the formation of thrust faults that produced positive topography by uplifting the graben. This brittle-ductile model displays the following differences from its purely brittle counterpart: (1) The Amount of uplift that was produced in the brittle-ductile model was less compared to the purely brittle model. (2) The asymmetry along strike of the thrust faults is also less in this model. (3) The topography produced in the brittle-ductile

model was more uniform. The ductile layer clearly influences the system to a very large degree, it controls the way strain develops and is transferred in rift basin during both extension and inversion. The ductile layer prevents the propagation of the faults in the brittle basement to the sedimentary cover and it thus detaches basement and cover which will lower the throw of the cover faults, producing less uplift. The ductile layer also acts as a brake to limit the amount of displacement both vertical and horizontal that can occur in the graben as the ductile layer can flow away (diverge) from regions of highest stress (becomes thinner) which counteracts the displacement, and thus the topography development would have been more significant if no ductile layer was present, this matches the observations above. Throughout the inversion process most of the highest uplift occurred above the mobile plate by the migration of material towards the graben borders followed by uplift once it reaches the bounding faults. This causes the extensional grabens above the mobile plate to be slowly transported in the direction of the rift basin, eventually the graben delineated by faults F2 is rotated and partially thrusted upwards is a in a “inverse subduction” type mechanism.

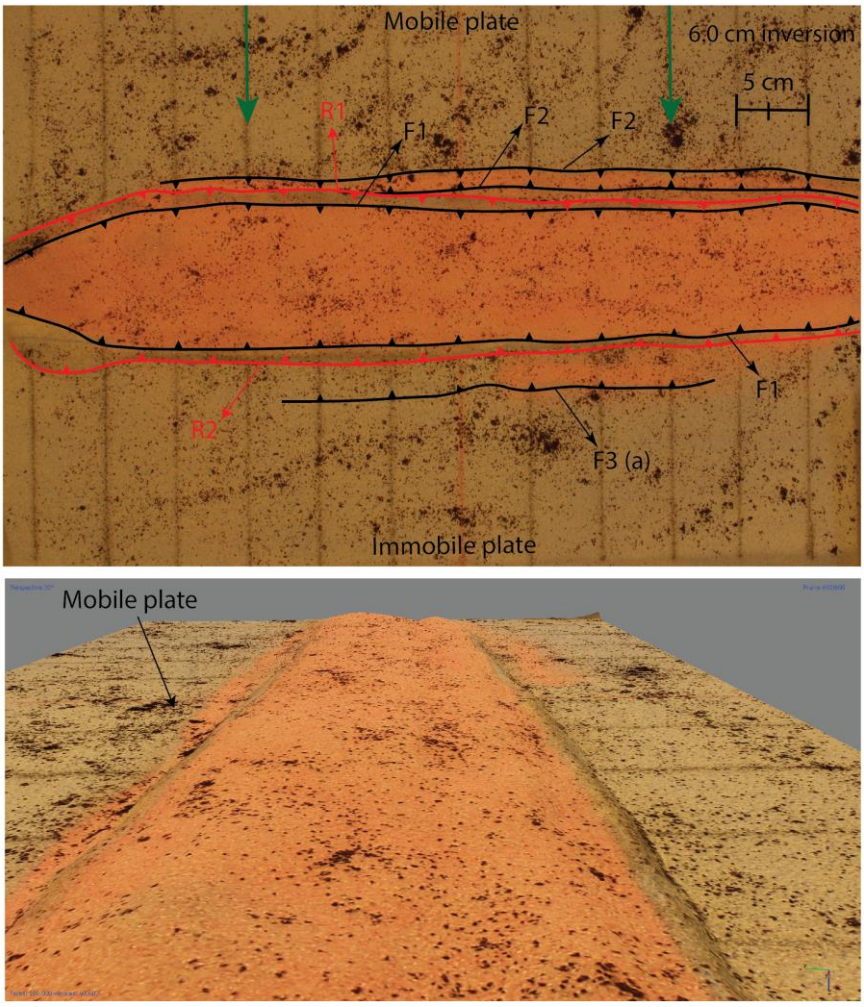

Figure 2.2.6. 3D view and Ortho-mosaic (3796x2568, 0.173mm/pix) top-view of the experiment at 6.0 cm of inversion.

The volume and surface area of the model were measured after 6.0 cm of inversion using Agisoft Photoscan, which yielded the following results:

Surface area: $0.402054\ m^2$
Volume: $160.12800\ cm^3$

Although the surface area of the extension and inversion phases remained largely the same the volume of the graben after the inversion is greater due to the higher magnitude of displacement that produced more extensive uplift.

Inversion phase DEM analysis

Photographs from 8x cameras were processed in Agisoft Photoscan, which yielded a 4D sequence of 690x 3D frames for the entire deformation of the analogue model. For each frame a Sparse and Dense point cloud was compiled. For Each frame a DEM was exported and processed in ArcMap. Due to the large number of DEM's, the process of information extraction (Hillshade) was automated using ArcPy for ArcMap that allows python scripting using the ArcMap functions. A time-lapse of the analysis was compiled and can be observed here: https://www.youtube.com/watch?v=KOdrXSEMRD0
Manual DEM maps were compiled in ArcMap from the last frame (6.0 cm inversion) and are illustrated below in figures 2.2.7 and 2.2.8. Different types of spatial analysis tools were used for the DEM processing that allows both the qualitative and quantitative analysis of the topography produced. In total 1.565 cm of maximum uplift formed because of the inversion. The following can be observed in the digital elevation map figures below: (1) Two small grabens are present above the mobile plate during inversion (fixed during extension) that run parallel to the master graben. Two small grabens are also visible above the immobile plate; however, these are not continuous across the entire length of the model. (2) Shortcut thrust faults (R1 and R2) that delineate the graben are clearly represented as steep ridges (red bands of the slope analysis in figure 2.2.8). (3) Three main ridges are visible inside of the rift basin in the footwall that run across its entire length of the rift basin along strike, the formation of these ridges is most likely linked to the deformation and faulting of the sedimentary cover. (4) The steepest ridges (highest slope angle) formed above the mobile plate. (5) The positive uplift distribution is not uniform across the rift basin and the highest amount of positive uplift that formed is localized to specific patches of the model. (6) The extra amount of topography that is not produced by the formation of the shortcut faults which is clearly visible in the Hillshade analysis represented by the staircase pattern must either be the result of reactivation of the normal faults or due to deformation of the sedimentary cover, which would also explain the ridges running across the uplifted graben. (7) The strain distribution throughout the model deformation was not uniform. At locations where the highest amount of normal faulting occurred (left side of the DEM) the smallest amount of topography was produced during the inversion. As the inversion angle is the same as the extension angle the only possible explanation would include the heterogeneous strain distribution in the ductile layer that strains the sedimentary cover to different degrees. (8) Most of the analogue model ridges have a Southward dipping slope, except for a small zone above the mobile plate (Aspect spatial analysis). (9) The deformation is localized on the graben borders (e.g. Brun and Nalpas, 1996).

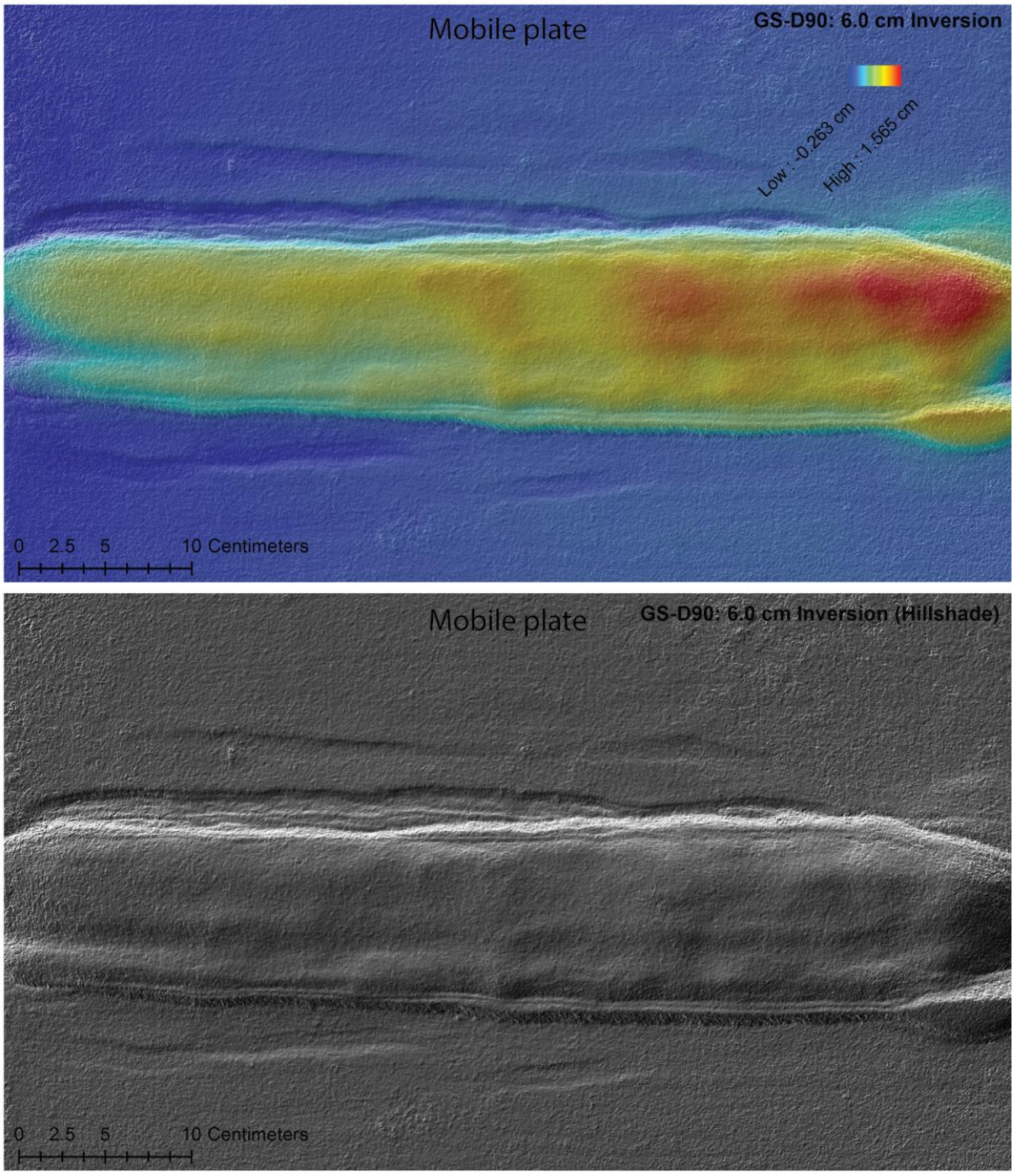

Figure 2.2.7. Color ramp and Hillshade analysis of the DEM in ArcMap (3751x2658, 0.157 mm/pix). The top image consists of a color ramp combined with a 40% transparent overlay of the Hillshade image. The grey image consists of a Hillshade spatial analysis map (no transparency). 6.0 cm of inversion.

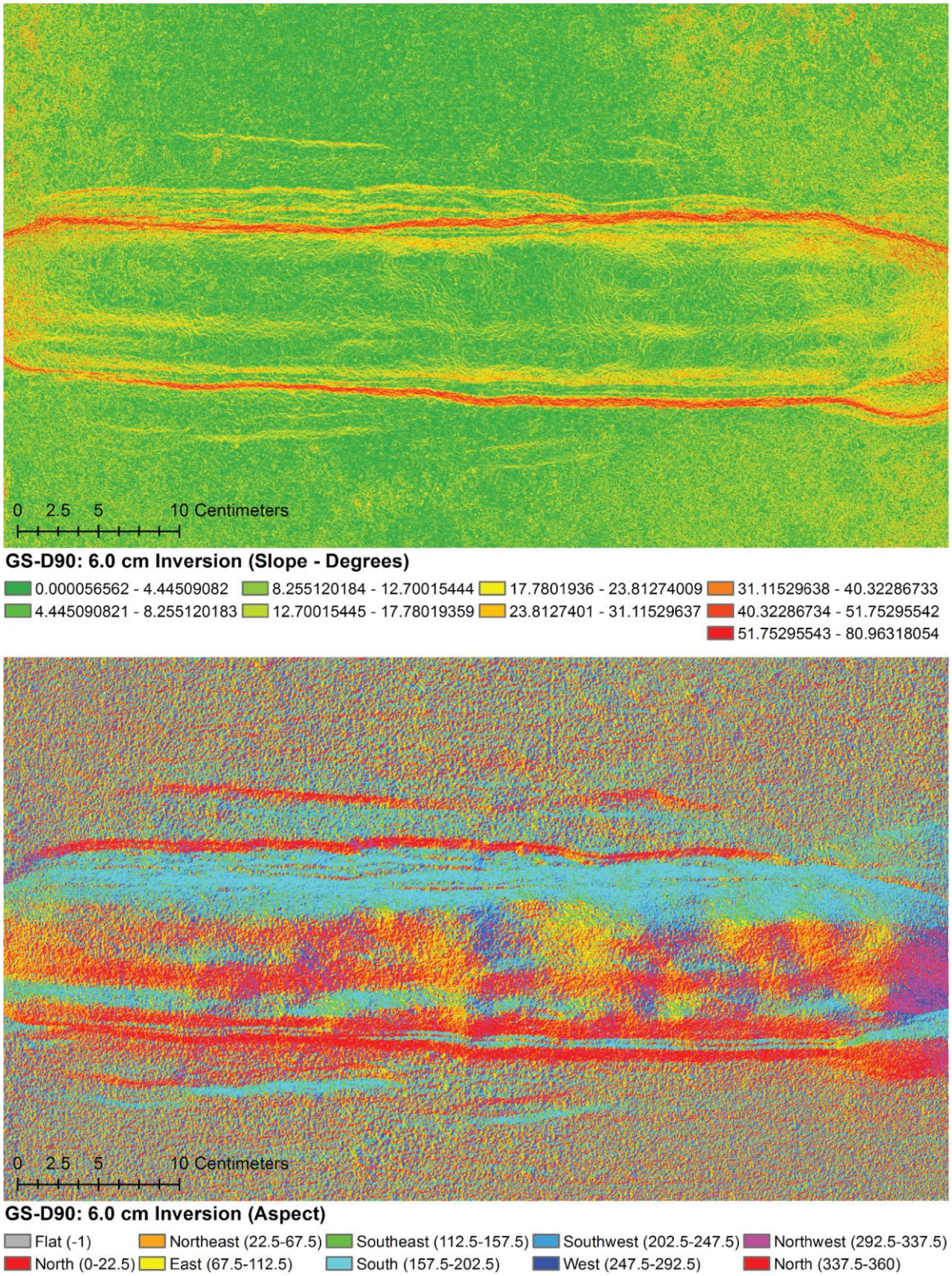

Figure 2.2.8. Slope and Aspect spatial analysis of the DEM in ArcMap. The aspect analysis represents the slope direction. The top of the Aspect images is the North direction. The bottom of the image is the South direction. 6.0 cm of inversion.

PIV analysis

PIV vector and vector magnitude analysis was carried using undistorted images of the inversion phase exported from Agisoft Photoscan. The PIV analysis using these photographs yielded much higher quality results because of the correction for lens distortion and camera tilt. Due to the motor-driven deformation at 6 cm/h and photographs taken every 7 seconds, the displacement between each two frames is very small and thus the magnitude of the vectors is almost zero. For this reason, it was decided to take every 5th image to increase the displacement between each frame but still to keep a high enough resolution for the entire sequence. A batch script was used to copy every fifth file from the photograph directory using the written script below:

```
@echo off
set Counter=0
for %%f in (*.jpg) do call :p "%%f"
goto :eof

:p
   set /a Counter+=1
   set /a X=Counter %% 5
   if %X%==0 copy %1 D:\GS_D90\PIV\copy
goto :eof
```

This yielded a total of 65x frames that were imported into PIVlab for analysis. The image sequence was compiled into a time-lapse at 2 FPS. The time-lapse of the vector analysis can be found here (https://www.youtube.com/watch?v=Y7qZgrBa6bI) and the vector magnitude analysis time-lapse can be found here (https://www.youtube.com/watch?v=3k1PZecPs-w). The figure below illustrates both PIV analysis methods at 3.0 cm (a) and 6.0 cm of inversion (b). The following can be observed in both the time lapses and figure 2.2.9 below: (1) The displacement velocity and magnitude decreases from the hinterland to the foreland. (2) Almost all displacement is perpendicular to the graben and no strike-slip component is visible, which leads to a more circular vector (u & v) component distribution scatter (Figure 2.2.10). (3) The vector field stops after the shortcut fault formation in the footwall above the immobile platen and not much strain is transferred to the foreland as displacement is accommodated along the thrust fault. (4) The vector magnitudes inside of the graben are lower compared to the vector magnitudes above the mobile plate due to the vertical accommodation of displacement which decreases the horizontal in-plane displacement. (5) There was no overall change in velocity magnitude and vector orientation throughout the inversion phase, this stands in contrast to the PIV analysis of the purely brittle model with the same angle of inversion which demonstrated significant changes in vector velocities in different regions of the model throughout the inversion phase. (6) The symmetry of the graben remained consistent along strike throughout the inversion which was not the case with the purely brittle model. (7) The velocity field inside of the graben also remains uniform throughout the inversion phase.

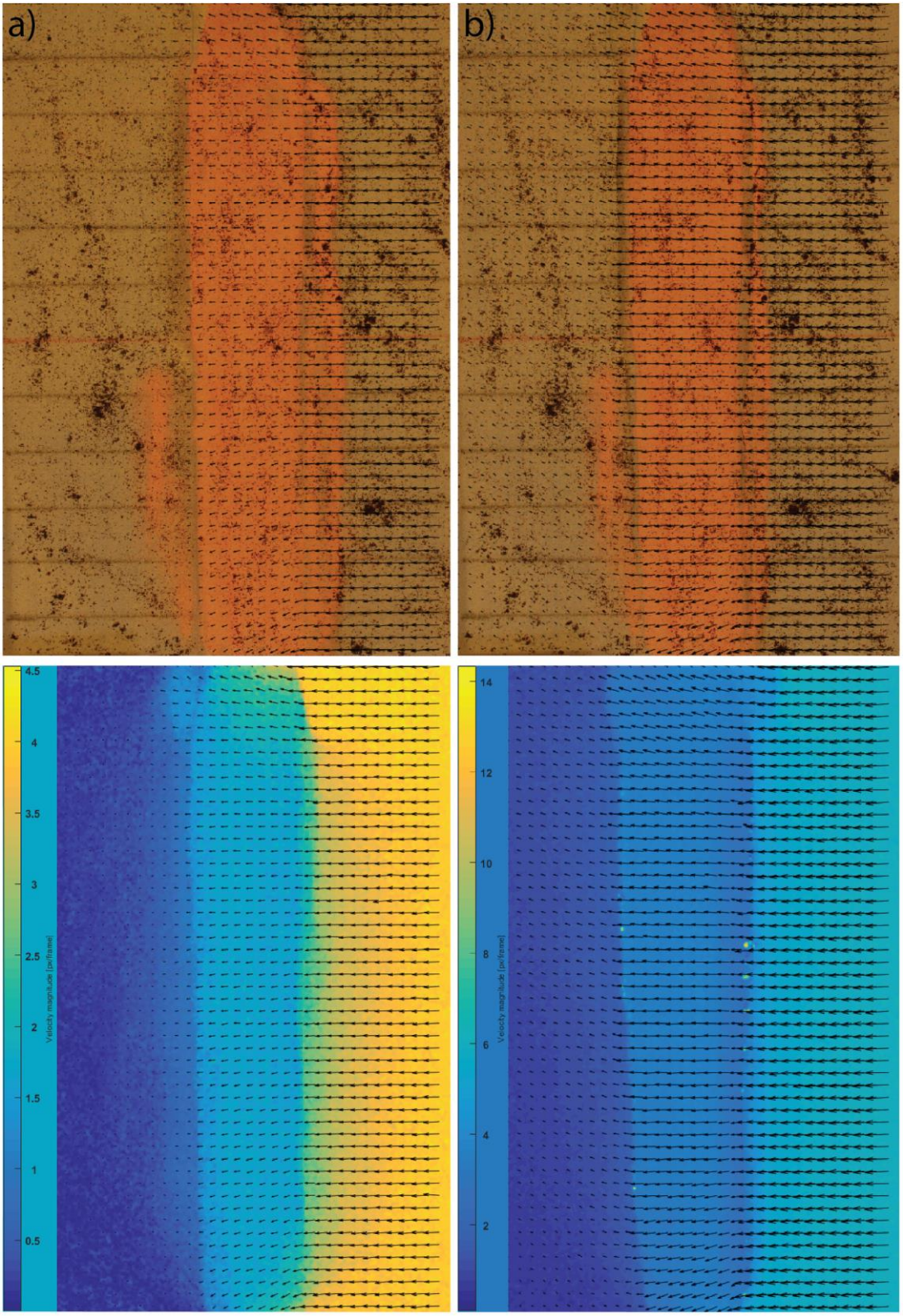

Figure 2.2.9. Vector and Vector magnitude analysis (pixels/frame) at 3.0 cm - (a) and 6.0 cm - (b) of inversion.

Histogram plots in (a) - figure 2.2.10 illustrates three main zones with peaks of highest vector magnitude at 0-0.5 pixels/frame (‘immobile’ plate), 1.5-2.0 pixels/frame (graben) and 3.5-4.0 pixels/frame (mobile plate). These values vary slightly compared to the histogram in (b), however, the pattern remains the same. From these plots, it can be observed that the there is a velocity decoupling between the graben and both plates, which suggest that there is extensive displacement along the graben border thrust faults or along the border normal faults by reactivation due to the upward pressure imposed by the ductile layer which could lower the reactivation barrier. Also, important to note is the difference in size of the gap between each of the three vector fields, the gap between the graben and the mobile plate is the largest which suggests that the highest velocity decoupling and accommodation magnitude of displacement occurred in the hanging-wall above the moving plate. The scatter plot illustrates the orientation of the vectors at both 3.0 cm and 6.0 cm of inversion, this pattern stands in contrast relative to other scatter plots of experiments with shallower angles of inversion where the scatter cloud has a (s) form. This suggests that most vectors have the same orientation and thus there is almost no strike-slip component is present in the system. The overall shape of the scatter plot is similar to that of the purely brittle model with the same angle of inversion, which indicates that the ductile layer does not change the overall vector field heading.

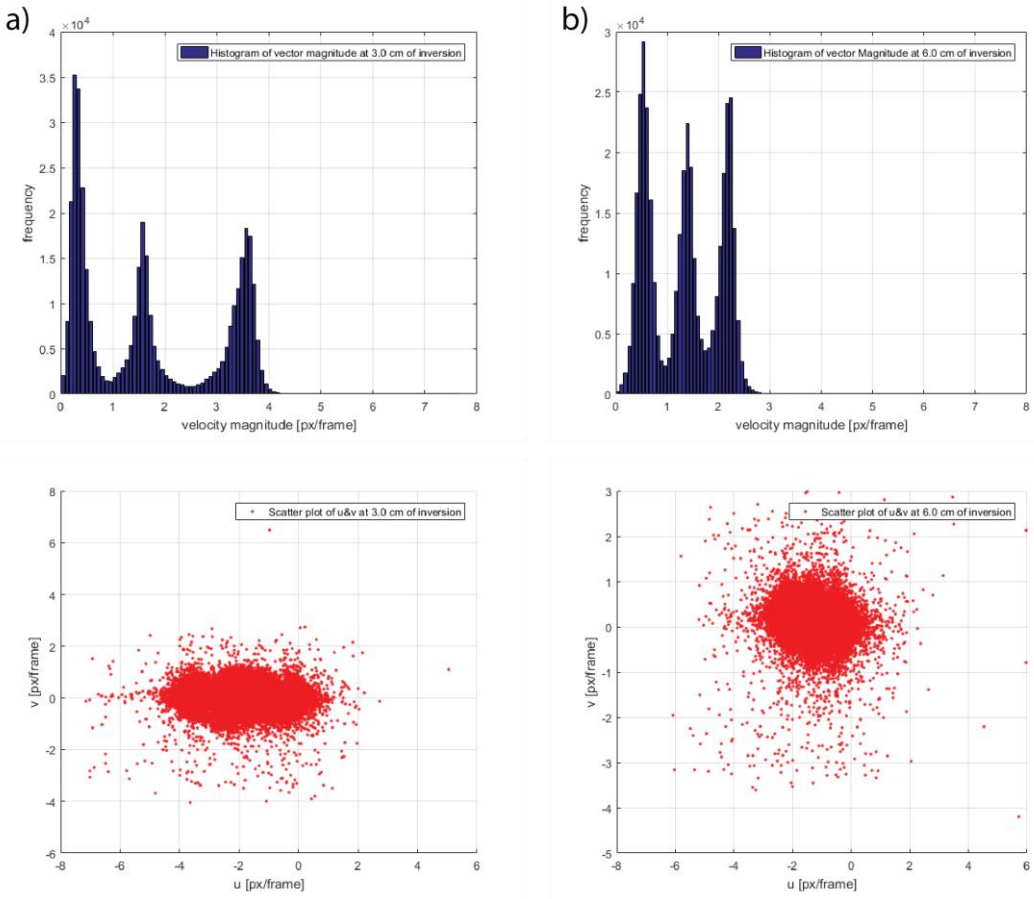

Figure 2.2.10. Histogram and scatter plots of the PIV analysis at 3.0 cm (a) and 6.0 cm (b) of inversion.

Cross-section analysis

The cross sections illustrated below in figures 2.2.11 and 2.6.12 are taken at the end of the experiment after 6.0 cm of inversion in the center of the model (CUT 6 - (b)) and close to it (CUT 9 - (a)). The following can be observed in the cross sections: (1) The silicon layer acts as a decollement, decoupling the sedimentary cover from the sedimentary basement. (2) The sedimentary cover is characterized by extension which extends on both sides outside of the graben (Brun and Nalpas., 1996). (3) The décollement transfers the extension horizontally by thinning of the silicone layer diverging from the graben axis. (4) The most extensive normal faulting occurred in the sediment cover above the immobile plate during the extension phase (mobile during inversion), which lead to the formation of small rift grabens delineated by faults (F3) in (a) and (F2) in (b). (4) The décollement is thicker above the mobile plate after the inversion and thinner above mobile plate during the extension phase. The thickening of the ductile layer at the graben borders during inversion can be related to the divergent flow of the ductile layer away from the hinterland. This led to the formation of silicone walls at the rift borders. (5) Both sections contain a large number of faults, section (a) contains the following normal faults: 2x F1, 3x F2, 2x F3, F4, F5, it also contains two shortcut thrust faults (R1 and R2). Section (b) contains the following normal faults: 2x F1, 2x F2, F3, F4 and F5. This section also includes two thrust faults (R1 and R2). (6) The extension phase caused the graben master faults to propagate from the basement to the sedimentary cover which is linked to the excessive thinning of the ductile layer due to the shearing as a result of movement along the offsetting bounding faults. Initially both rift master normal faults were soft-linked. The excessive thinning of the silicone layer in the footwall during extension eventually causes the ductile layer to rupture and hard-linking the master fault in the sedimentary cover and basement. This thinning was less in the hanging-wall and thus the cover master fault was not allowed to become hard-linked with the master basement faults. (7) simple shearing of the décollement was extensive during the rifting phase as can be seen by the drag present in the ductile layer. (8) Extensive structural collapse occurred within the graben sedimentary cover which resulted in extensive faulting and the formation of a synclinal structure above the décollement. (9) Faults (F5) in both sections (a) and (b) show a reverse slip components. (10) Sedimentation through time increased the sediment loading, which not only further promoted divergent flow and thinning of the ductile layer closest to the graben, it also forced the ductile section bounded by the brittle basement faults to sink towards the V.D as no sediment can penetrate the ductile layer to fill the newly created space by rifting, allowing only downward and minor lateral spreading movement. (11) On the flanks of the graben the ductile layer is much thicker compared to the overall thickness of the layer across the whole section, it also shows upward drag and the layer is significantly deformed. (12) The deformation is localized on the graben borders (e.g. Brun and Nalpas, 1996). (13) The rift border faults were reactivated during the initial stages of inversion. The highest reverse slip magnitude occurred at the master fault in the hanging-wall. This slip was also coupled with very minor diapir formation. Little reverse-slip occurred within the rift basin sedimentary cover.

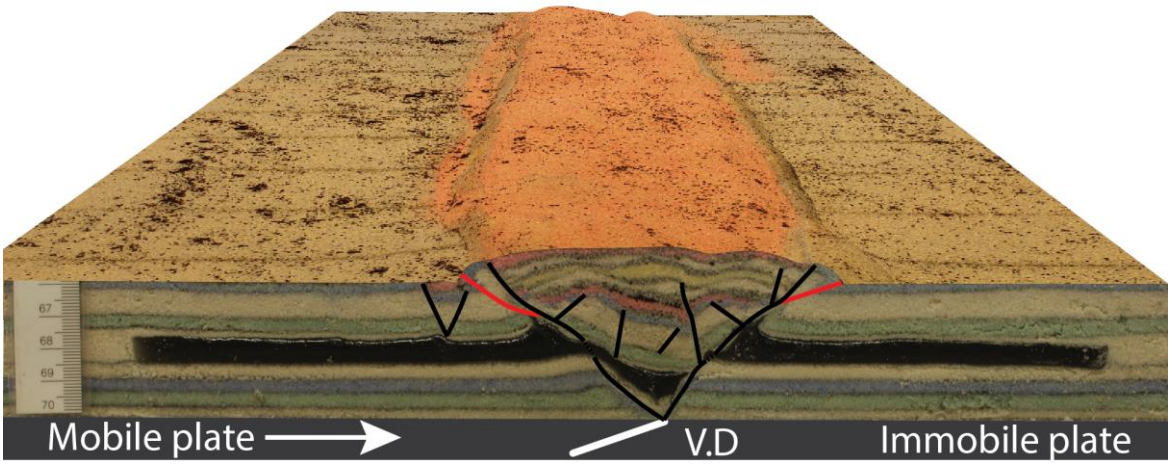

Figure 2.2.11. Combination between the cross-sections in figure 2.2.12 and the 3D surface model in figure 2.2.5.

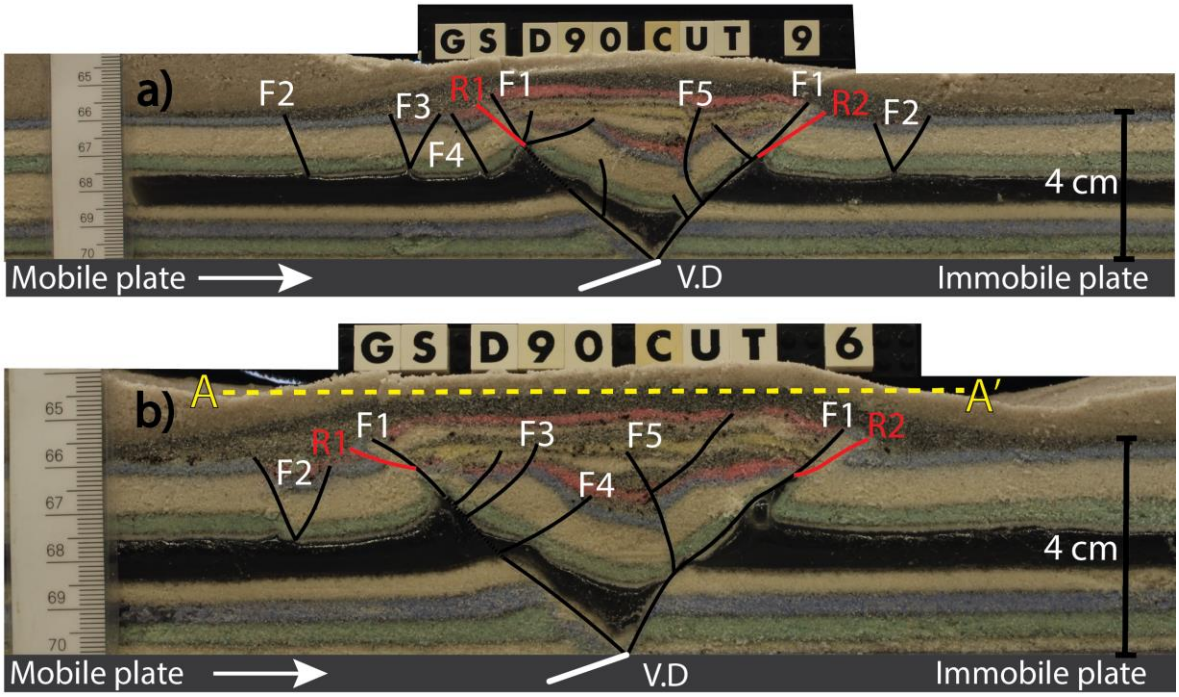

Figure 2.2.12. Cross sections taken after 6.0 cm of inversion. Sections (a) and (b) are taken at two different positions and show slightly different structures and thus slightly different descriptions of the fault patterns. The black lines represent the normal faults. The red lines represent the thrust faults.

2.2.2 GS-D15: Brittle-Ductile, Extension and sedimentation followed by 15° inversion

Photographs taken from the top-view camera during the deformation of the analogue model were compiled into a time-lapse and can be visualized here:
https://www.youtube.com/watch?v=hVFN9Gezh3w
The textured 3D model compiled at the end of the rifting phase can be visualized here:
https://sketchfab.com/models/2c192a6cc01b4985b943d8ce0d336003

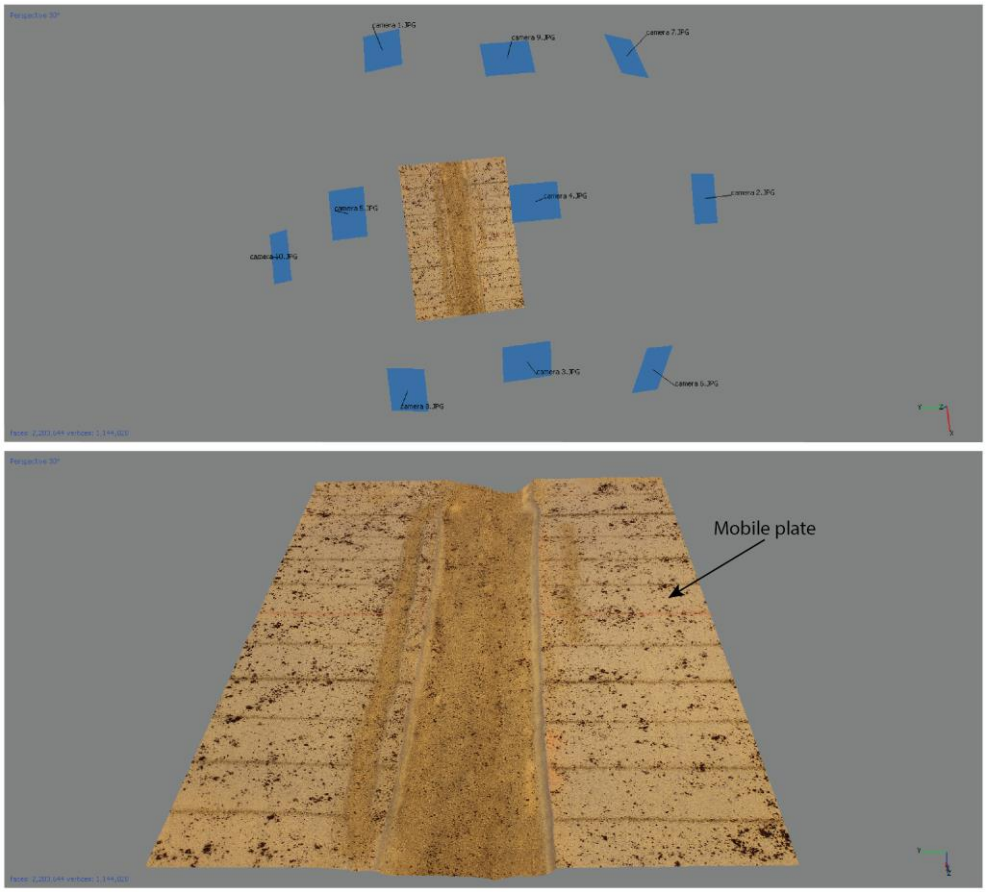

Figure 2.2.13. Screenshot of the 3D model in Agisoft Photoscan at 5.0 cm of extension (10x cameras). Sparse cloud (210,314 points), Dense cloud (12,758,861 points), Mesh (2,283,644 faces; 1,440,028 vertices).

The following observations can be made after analyzing the 3D model and the surface top-views of the analogue model (Figures 2.2.13 and 2.2.14): (1) The rift basin topography is asymmetrical. (2) Extension of the model led to the formation and growth of a rift basin delineated by two large offset border master faults (F1). Progressive extension led to the formation of a small graben above the fixed plate followed by the development of a graben above the mobile plate. (3) A small graben developed above the immobile plate during the extension which runs parallel to the main rift zone and is delineated by two opposing normal faults (F2). A similar depression also formed above the mobile plate which is delineated by faults (F3), however, this structure is less well visible and does not run across the entire length of the model. (4) The surface area and volume of the fully extended 3D reconstructed model was measured, which equated to a volume of $-384.3\ cm^3$ and a surface area of $0.494146\ m^2$. The volume represents the volume of the depressions formed below the surface of the model. (5) The grabens that formed at the flanks of the model are also asymmetrical along strike. Other faults and structures that may have developed can only be identified using cross-sections, DEM's or PIV analysis.

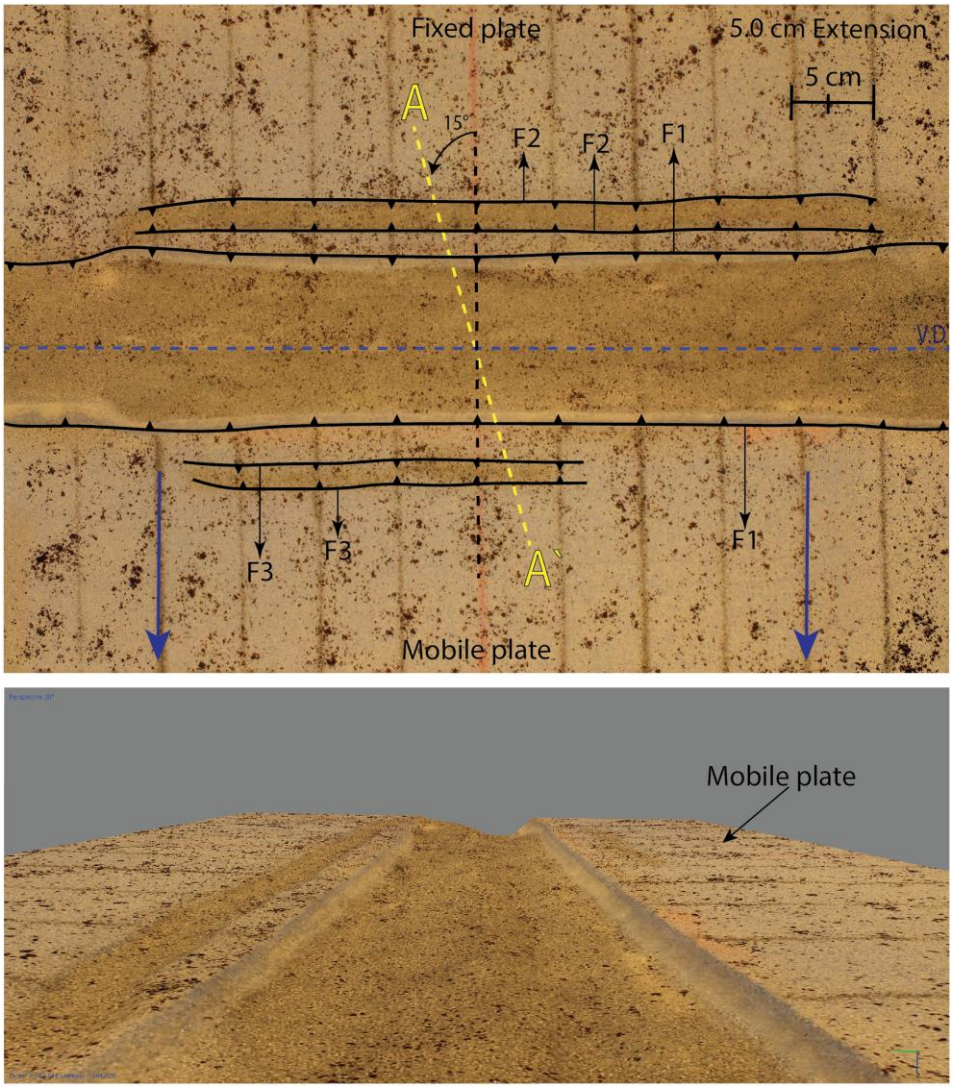

Figure 2.2.14. Top view of the experiment at 5.0 cm of extension (Orthomosaic image from Photoscan, 3750x2656, 0.157 mm/pix) and perspective view of the graben at 35°.

Extension phase DEM analysis

A DEM from the fully extended analogue model (5.0 cm extension) was constructed from the dense point cloud in Agisoft Photoscan. The DEM was exported from Photoscan and processed in ArcMap which yielded the maps below in figures 2.2.15 and 2.2.16.
Most of the micro-topography that formed during the extension is not well visible in the top view photographs. Digital elevation models of the extension phase can reveal this micro-topography with very high detail and precision. The following can be observed in these digital elevation maps: (1) The deepest depression formed equates to *-1.92 cm* below the surface of the analogue model. (2) Two very small depression are present above the immobile plate which are not visible with the naked eye during the experiments and is also not visible in the top view photographs, these depressions most likely formed as the result of the birth of new small grabens. (3) Two grabens also formed above the mobile plate which are better developed than those above the immobile plate, however they are not continuous along strike. These structures are larger than was inferred from the top view photograph analysis. (4) A small trench formed inside of the master graben that runs along its entire length along strike. (5) A horst separates fault (F2) from bounding fault (F1). (6) The largest slopes formed above the mobile plate (Figure 2.2.16). (8) The slopes that formed above the mobile plate during extension are Southward dipping, while the slopes above the immobile plate have a Northward dipping direction (Figure 2.2.16). (9) The grabens that formed at the model flanks nucleate attached to the border master faults (F1) and slowly migrate inwards, which led to a ‘n’ shaped structure in the immobile plate and a ‘u’ shaped structure above the mobile plate. Compared to the previous ductile experiment, the symmetry of all formed grabens is significantly greater in this experiment. Also, above the mobile plate the two formed micro grabens are larger and more well developed. The trench inside of the main graben has a greater depth in this experiment compared to the previous experiment. This difference in micro-topography clearly indicates that however the extension parameters of both experiments were identical, the produced result still show some degree of variation.

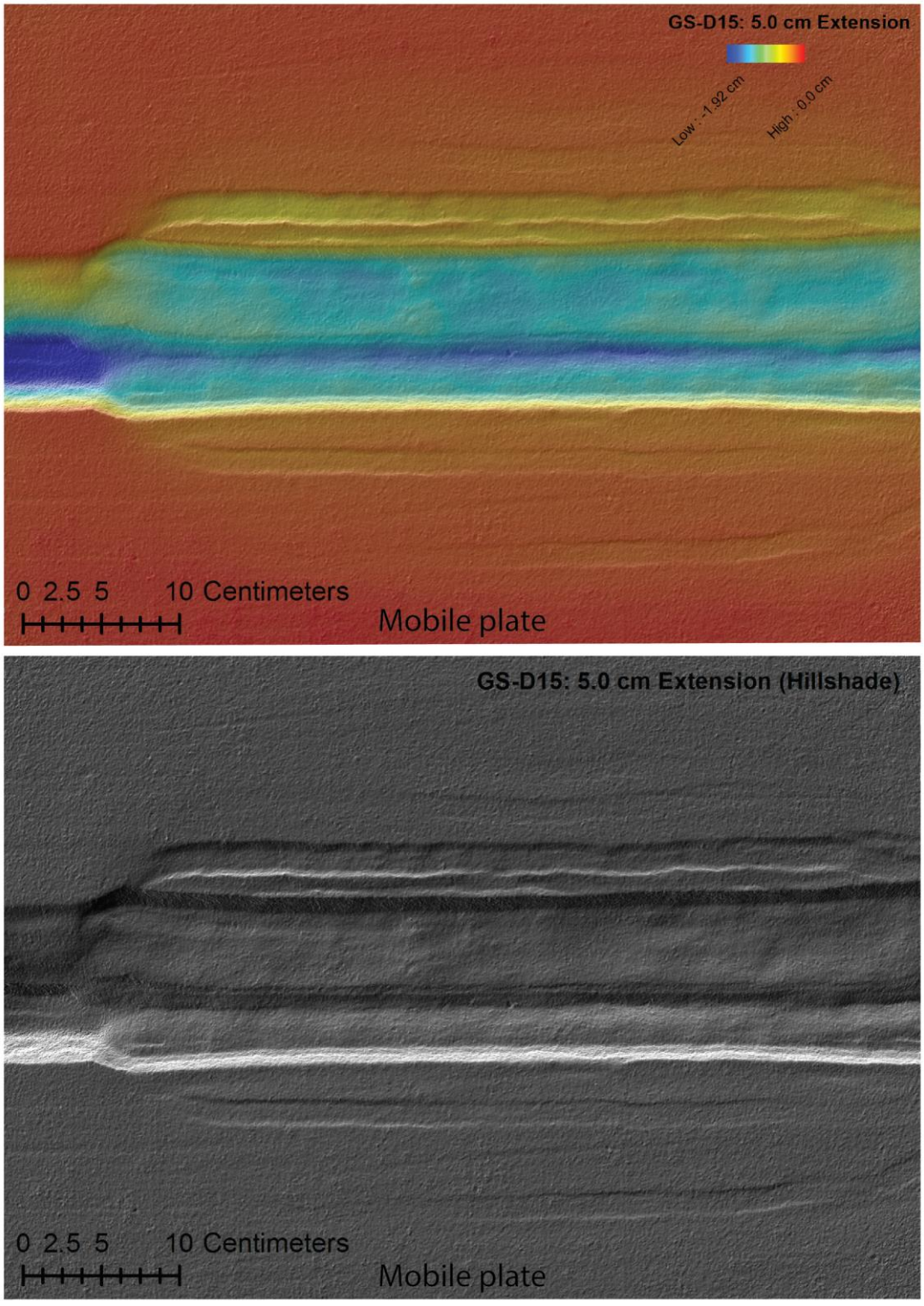

Figure 2.2.15. Color ramp and Hillshade analysis of the DEM in ArcMap (3751x2658, 0.157 mm/pix). The top image consists of a color ramp combined with a 40% transparent overlay of the Hillshade image. The grey image consists of a Hillshade spatial analysis map (no transparency). 5.0 cm of extension.

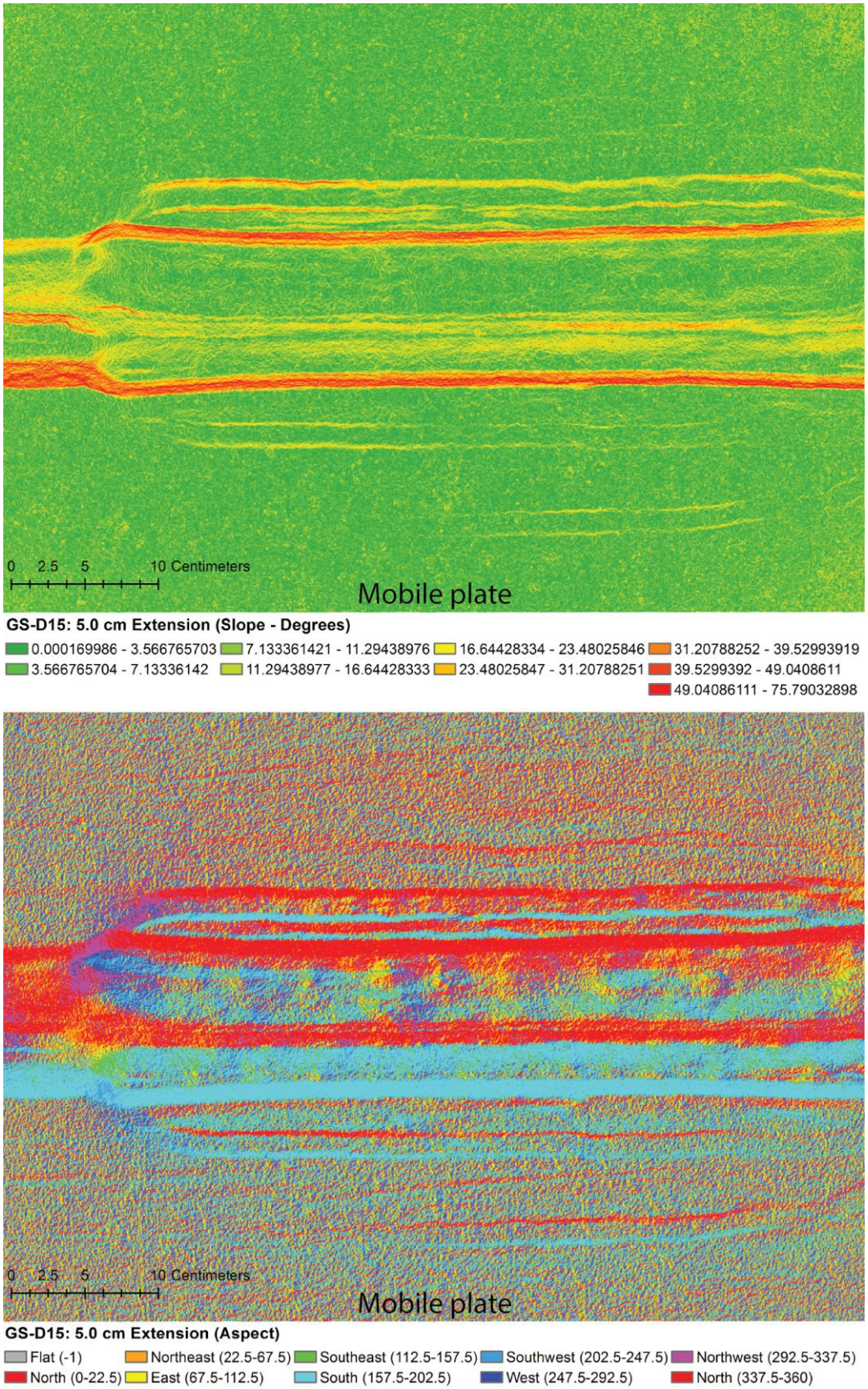

Figure 2.2.16. Slope and Aspect spatial analysis of the DEM in ArcMap. The aspect analysis represents the slope direction. The top of the Aspect images is the North direction. The bottom of the image is the South direction. 5.0 cm of extension.

After the extensional phase inversion is applied to the system (Figures 2.2.17 and 2.2.18). The textured 3D model compiled at the end of the inversion phase can be visualized here: https://sketchfab.com/models/4973bd9475524242b40f745cfd605914

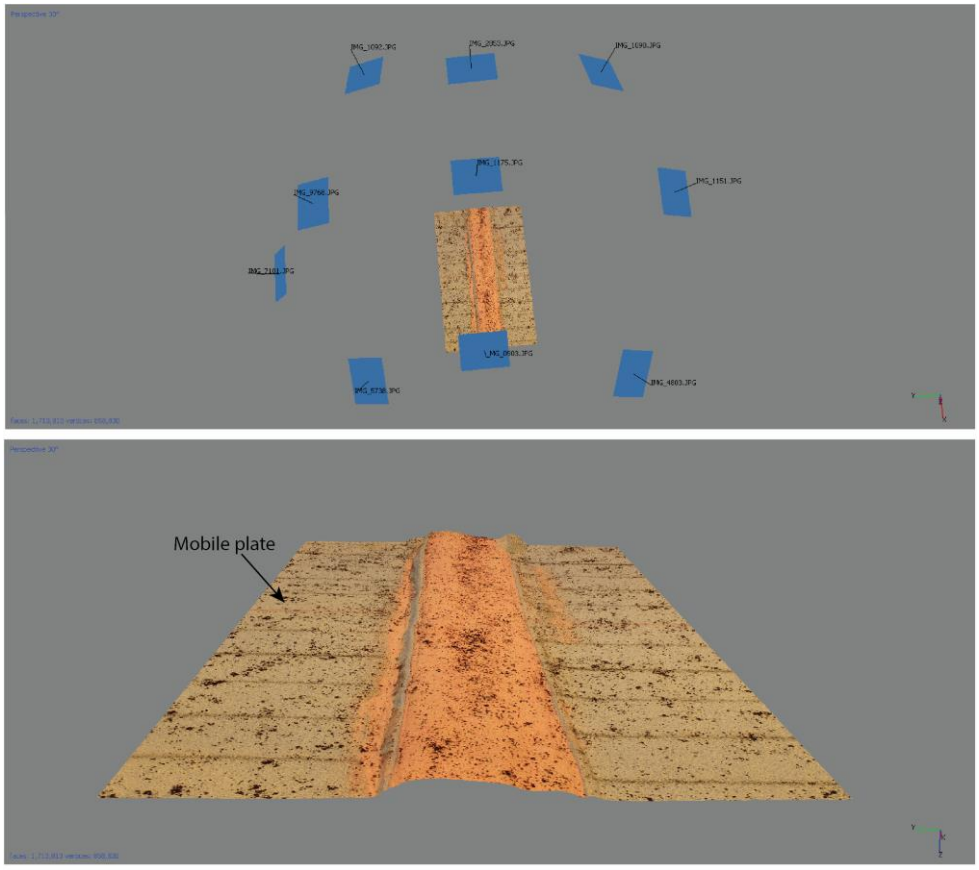

Figure 2.2.17. Screenshots of the 3D model in Agisoft Photoscan at 6.0 cm of inversion. 10x cameras, Sparse Cloud (802,991 points), dense cloud (67,830,716 points), Mesh (13,574,422 faces. 6,787,219 vertices).

The following observations can be made after analyzing the 3D model and the top views of the surface (Figures 2.2.17 and 2.2.18): (1) A forethrust shortcut fault (R1) formed above the mobile plate. (2) The central grid-line is displaced laterally with a total magnitude of *1.90 cm* as a result of the inversion, which indicates that a strike-slip component is present in the system. Interesting to note is that this displacement magnitude is smaller compared to the purely brittle model with the same angle of inversion. The accommodation of the displacement by strike-slip decreased the maximum positive uplift created as a result of the inversion. (3) The displacement magnitude of the graben in the direction of the foreland decreases as the result of the formation of thrust fault (R1) which breaks down the purely horizontal displacement component of the graben into both a vertical and horizontal component. Although no other thrust faults are clearly visible, analysis of the cross-sections must be carried out to rule out the formation of other thrust faults. Throughout the inversion phase most of the positive topography developed above the mobile plate by the migration of material towards the main graben followed by uplift once it reaches the bounding faults. This caused the extensional grabens at the flanks of the model above the mobile plate to be

slowly transported in the direction of the main graben, eventually the graben delineated by faults F2 is partially rotated and thrusted upwards is a in a “inverse subduction” type mechanism.

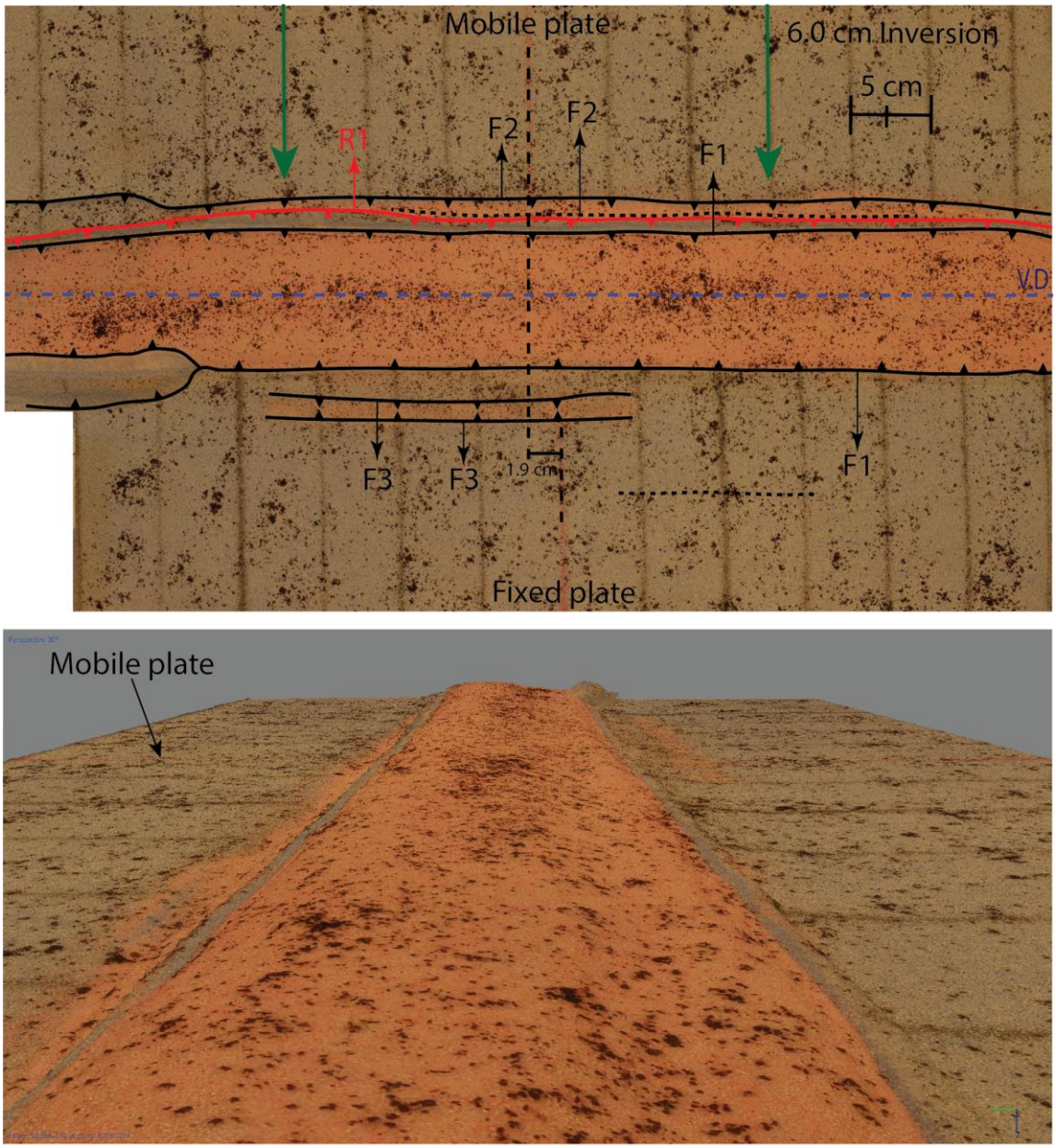

Figure 2.2.18. Orthomosaic top-view of the analogue model at the end of the experiment after 6.0 cm of inversion (9832x5997, 0.0682 mm/pix) and perspective view of the inversion graben at 35°. Orthomosaic and 3D model were reconstructed from 61 images.

The volume and surface area of the 3D model after 6.0 cm of inversion was measured using Agisoft Photoscan, which yielded the following results:

Surface area: $0.536755\ m^2$

Volume: $48.1373\ cm^3$

Although the surface area of the extension and inversion phases remained largely the same, the volume of the graben after the inversion is now positive, however this amount is lower compared to the brittle-ductile model with an oblique angle of inversion. This can be attributed to the strike-slip component of the system which prevents the formation of increasing positive uplift, which will lower the volume.

Inversion phase DEM analysis

Photographs taken across all 10x cameras were processed in Photoscan, which yielded a 4D sequence of 3D frames for the entire inversion phase. For each frame a Sparse and Dense point cloud was compiled. For each frame a DEM was exported and processed in ArcMap. Due to the large number of DEM's, the process of information extraction (Hillshade) was automated using ArcPy for ArcMap that allows python scripting using the ArcMap functions. A time-lapse for the Hillshade analysis was produced and can be visualized here: https://www.youtube.com/watch?v=3tCAYVRcDE8

The two scripts are as follows:

Hillshade:

```
import arcpy
from arcpy import env
from arcpy import sa
from arcpy.sa import *

arcpy.CheckOutExtension("Spatial")

env.workspace = r"<path to folder containing .tif files, input>"

lstRasters = arcpy.ListRasters("*")

for raster in lstRasters:
   outHillshade = Hillshade(raster, 315, 45, "SHADOWS", 2)
   outHillshade.save(r"<output path>" + "\\" + str(raster) + "_hillshade.tif")
```

Slope:

```
import arcpy
from arcpy import env
from arcpy import sa
from arcpy.sa import *
```

```
arcpy.CheckOutExtension("Spatial")

env.workspace = r"<path to folder containing .tif files>"

lstRasters = arcpy.ListRasters("*")

for raster in lstRasters:
   outSlope = Slope(raster, "DEGREE", .3043)
   outSlope.save(r"<output path>" + "\\" + str(raster) + "_slope.tif")
```

Manual DEM maps were produced in ArcMap from the last frame (6.0 cm inversion) and are illustrated below in figures 2.2.19 and 2.2.20. Different types of spatial analysis tools were used for the DEM processing that allows both the qualitative and quantitative analysis of the topography produced. In total, the maximum uplift that was produced at the end of the inversion of the analogue model equates to *1.511 cm*. This amount is lower compared to ductile experiment with smaller angles of inversion, which is to be expected. It should be noted that most of the maximum uplift was produced outside of the ductile zone as the ductile layer is positioned 10.0 cm inwards from all four directions. The following can be observed in the digital elevation model analysis maps below: (1) Two small grabens are present above the mobile plate during inversion (fixed during extension) that run parallel to the master graben. Two small depressions are also visible above the immobile plate which are more mature and more continuous. (2) Shortcut thrust fault (R1) above the mobile plate that delineates the graben is represented as a steep ridge (red band of slope analysis in figure 2.2.20). (3) A very small shortcut fault appears to have formed above the immobile plate as well. (4) A ridge is visible inside of the graben above the immobile plate in the footwall that runs along the strike of the graben, the formation of this ridges is most likely linked to the deformation and faulting of the sedimentary cover. (5) The steepest ridges (highest slope angle) formed above the mobile plate. (6) The amount of topography produced is not uniform across the graben, the highest amount of topography that formed tends to be localized to certain areas. (7) The strain distribution throughout the model deformation was not uniform. (8) Most of the ridges of the model have a Southward and Northward dipping slope direction (Aspect spatial analysis). Compared to the purely brittle counterpart experiment the symmetry of the formed ridges is significantly greater in this ductile experiment.

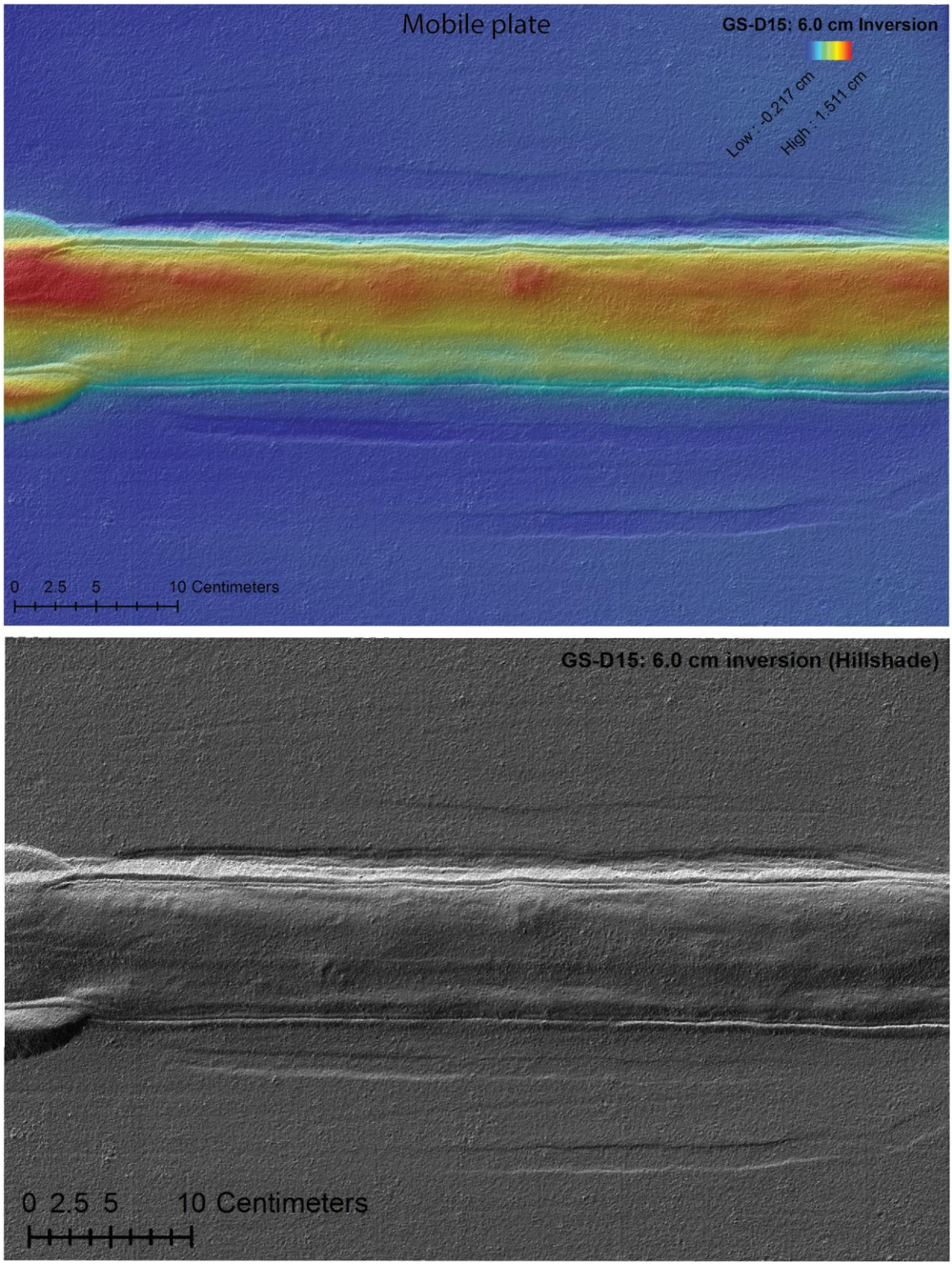

Figure 2.2.19. Spatial Hillshade analysis of the DEM in ArcMap. Top image consists of a color ramp combined with a 40% transparent overlay of the pure Hillshade grey image. The grey image is a pure Hillshade spatial analysis map (no transparency). 6.0 cm of inversion.

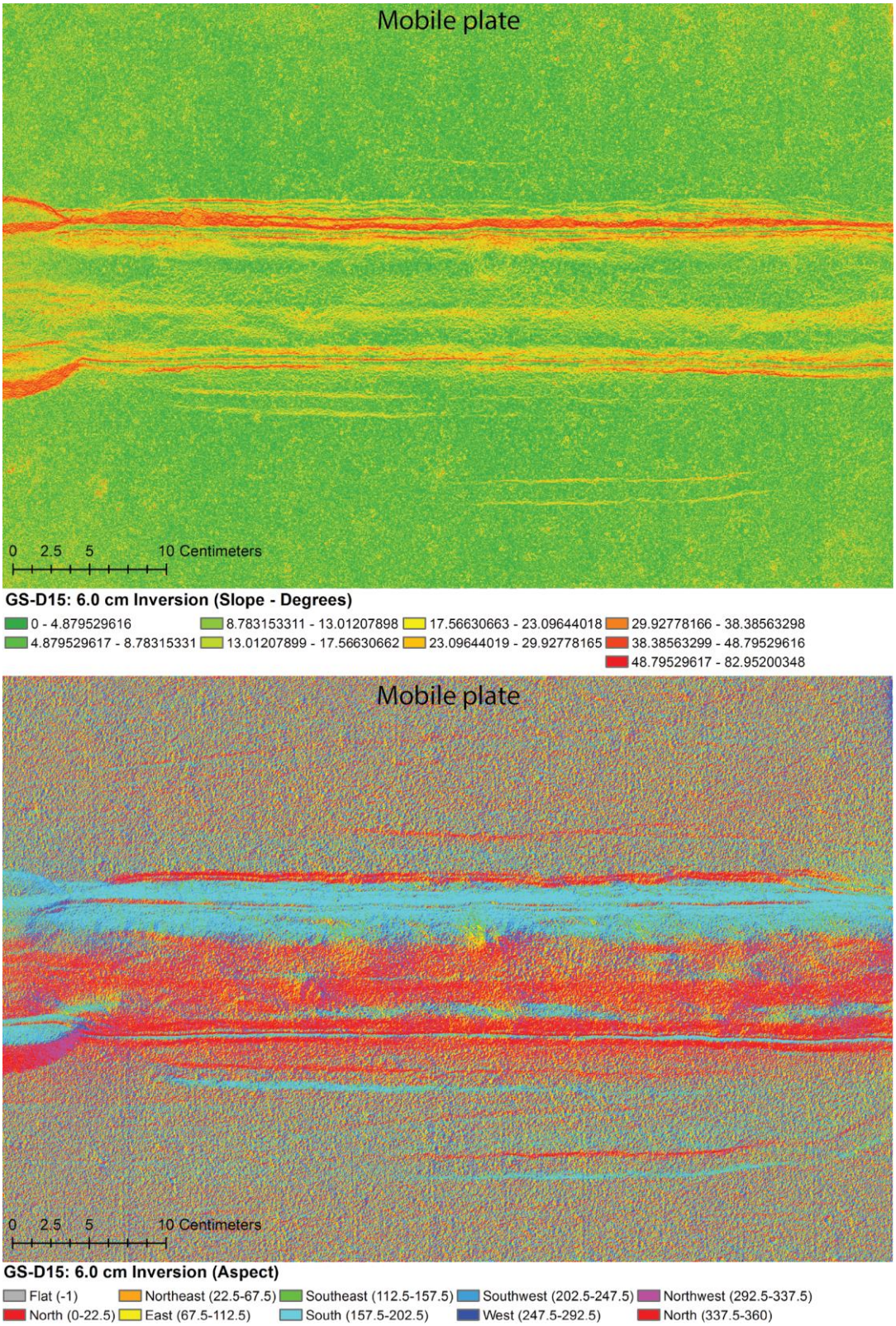

Figure 2.2.20. Slope and Aspect spatial analysis of the DEM in ArcMap. The aspect analysis represents the slope direction. The top of the Aspect image is the North direction. The bottom of the image is the South direction. 6.0 cm of inversion.

PIV analysis

PIV vector and vector magnitude analysis was carried out of the inversion phase using undistorted images exported from Photoscan, the analysis using these photographs yielded much higher quality results due to the correction for lens distortion and camera tilt. Due to the motor-driven deformation at *6 cm/h* and photographs taken every *7 seconds*, the displacement between each two frames is very small and thus the magnitude of the vectors is almost zero. For this reason, it was decided to take every 5th image to increase the displacement between each frame but still to keep a high enough resolution. This resulted in a frame sequence that was imported into PIVlab for analysis. The image sequence was compiled into a time-lapse at 2 FPS. The time-lapse of the vector analysis can be found here (https://www.youtube.com/watch?v=cWmlFyqKYq4) and the vector magnitude analysis can be found here (https://www.youtube.com/watch?v=KoJLxgdTA_U). The figure below illustrates both PIV analysis techniques at 3.0 cm - (a) and 6.0 cm of inversion - (b). The following can be visualized in both the time-lapses and figure 2.2.21 below: (1) The displacement velocity and magnitude decreases from the hinterland to the foreland. (2) The vectors above the mobile plate have a 15° angle relative to the extension direction, which corresponds to the inversion angle (α). (3) The vector fields weaken significantly after the formation of the shortcut fault in the footwall above the immobile platen and not much strain is transferred to the foreland beyond the fault tip. (4) The vector magnitudes inside of the graben are lower compared to the vector magnitudes above the mobile plate due to the vertical accommodation of displacement which decreases the horizontal in-plane displacement. This led to the decoupling of the rift basin from the rest of the analogue model. (5) The vector field tends to align perpendicularly to the velocity discontinuity towards the immobile plate, thus the strike-slip displacement magnitude is lower in the backthrust and footwall master normal fault as most of it is dissipated in the forethrust and hanging wall normal faults. (6) The vectors above the immobile plate display a slightly clockwise rotation. (7) The graben remains overall symmetrical throughout the inversion phase and no large vector field fluctuations occurred. (8) There are two zones inside of the graben which move at different speeds, these two zones are separated into two distinct bands (Figure 2.2.22). The band with the lowest velocity is delineated by forethrust (R1) and a secondary fault inside of the graben. As observed in the digital elevation models, the maximum topographic uplift produced throughout the inversion phase occurred at the interface between the mobile plate and the rift basin delineated by master normal fault (F1). The extensive vertical displacement in the low velocity zone decreased the overall horizontal displacement velocity. This uplift must be paired with counterclockwise rotation of not only the low velocity zone but also of the faults that delineate these two zones inside of the graben. This explains why the high velocity zone is located closer to the foreland, as it does not have this extensive uplift and rotation component. The rotation led to tearing faults, which steepened the fault angles and increased the coefficient of internal friction for reverse faulting to occur, which led to the formation of a high velocity band inside of the graben. The analysis of the cross-sections will be able to indicate the exact kinematic mechanism behind this process. The velocity decoupling is also clearly visible in the Histogram in figure 2.2.23.

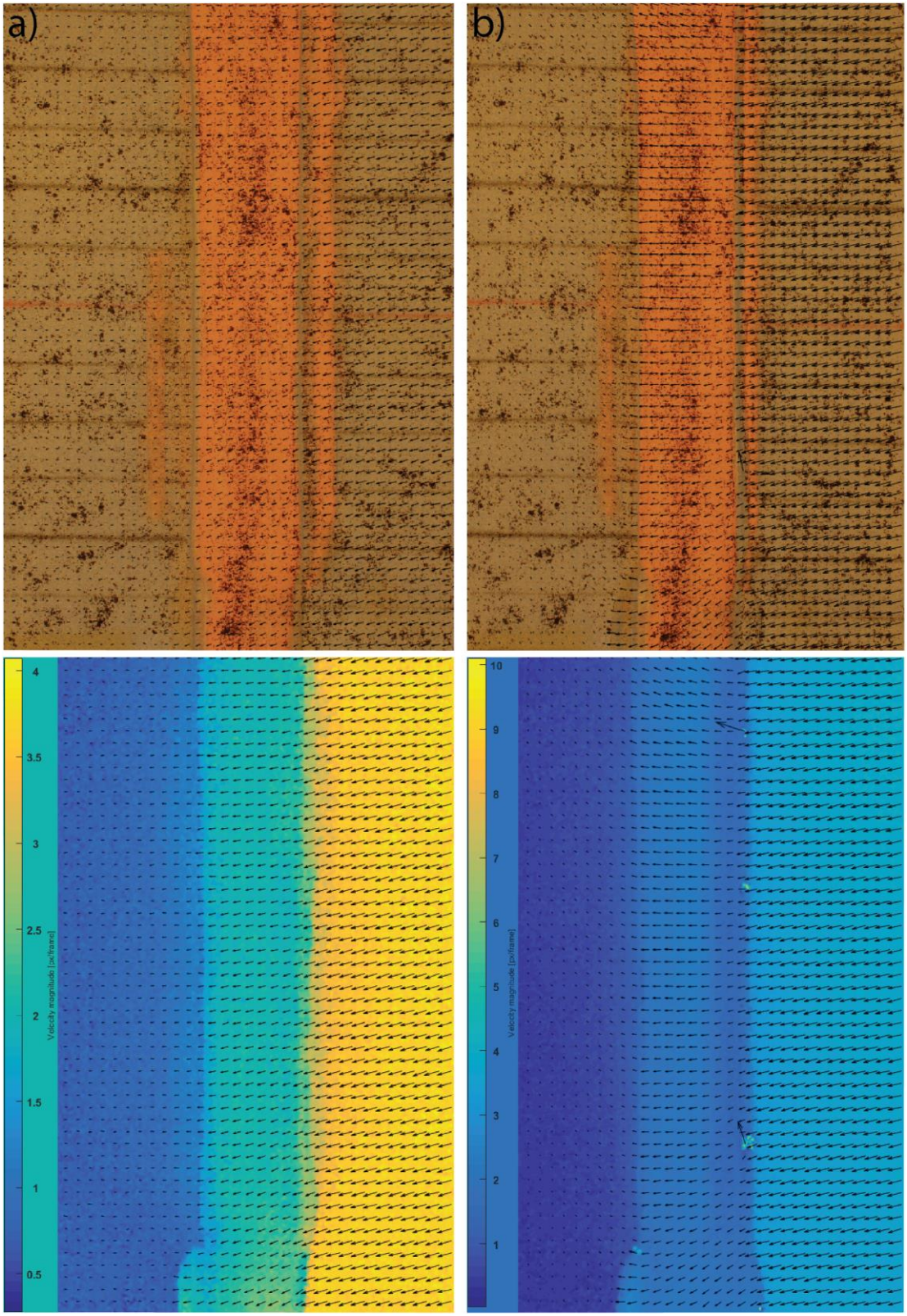

Figure 2.2.21. Vector and Vector magnitude analysis (pixels/frame) at 3.0 cm - (a) and 6.0 cm - (b) of inversion.

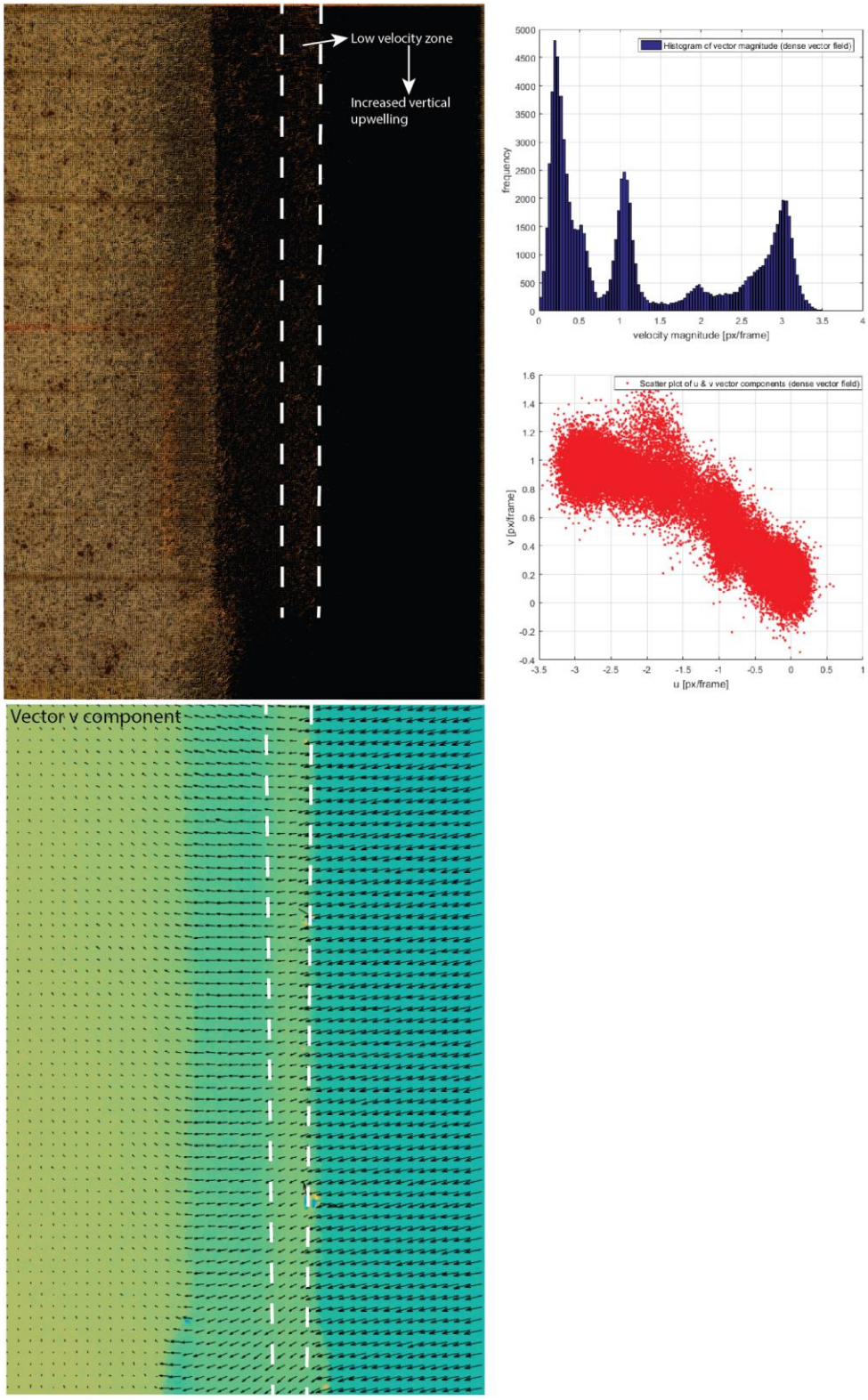

Figure 2.2.22. Two distinct velocity zones are present inside of the graben. The top image consists of very densely packed vectors with the attached statistical diagrams, while the bottom image was compiled from the vector (v) component.

In the histogram plots in (b) - figure 2.2.23, three main zones with peaks of highest vector magnitude can be observed at 0-0.6 pixels/frame (‘immobile’ plate), 1.0-2.1 pixels/frame (graben) and 3.5-4.0 pixels/frame (mobile plate). These values vary slightly between the histogram in (a), however the pattern remains the same. From these plots, it can be observed that the there is a velocity decoupling between the graben and both plates, which suggest that there is extensive displacement along the graben border thrust faults or along the master normal faults by reactivation. Also, important to note is the difference in size of the gap between each of the three vector fields, the gap between the graben and the mobile plate is the largest which suggests that the highest amount of accommodation of displacement occurs in the hanging-wall above the moving plate. The scatter plot illustrates the orientation of the vectors at both 3.0 cm and 6.0 cm of inversion, this pattern has a different shape compared to its purely brittle counterpart, the scatter plot of the ductile model appears to consist of three separate zones. This suggests that there are significant changes in vector orientations.

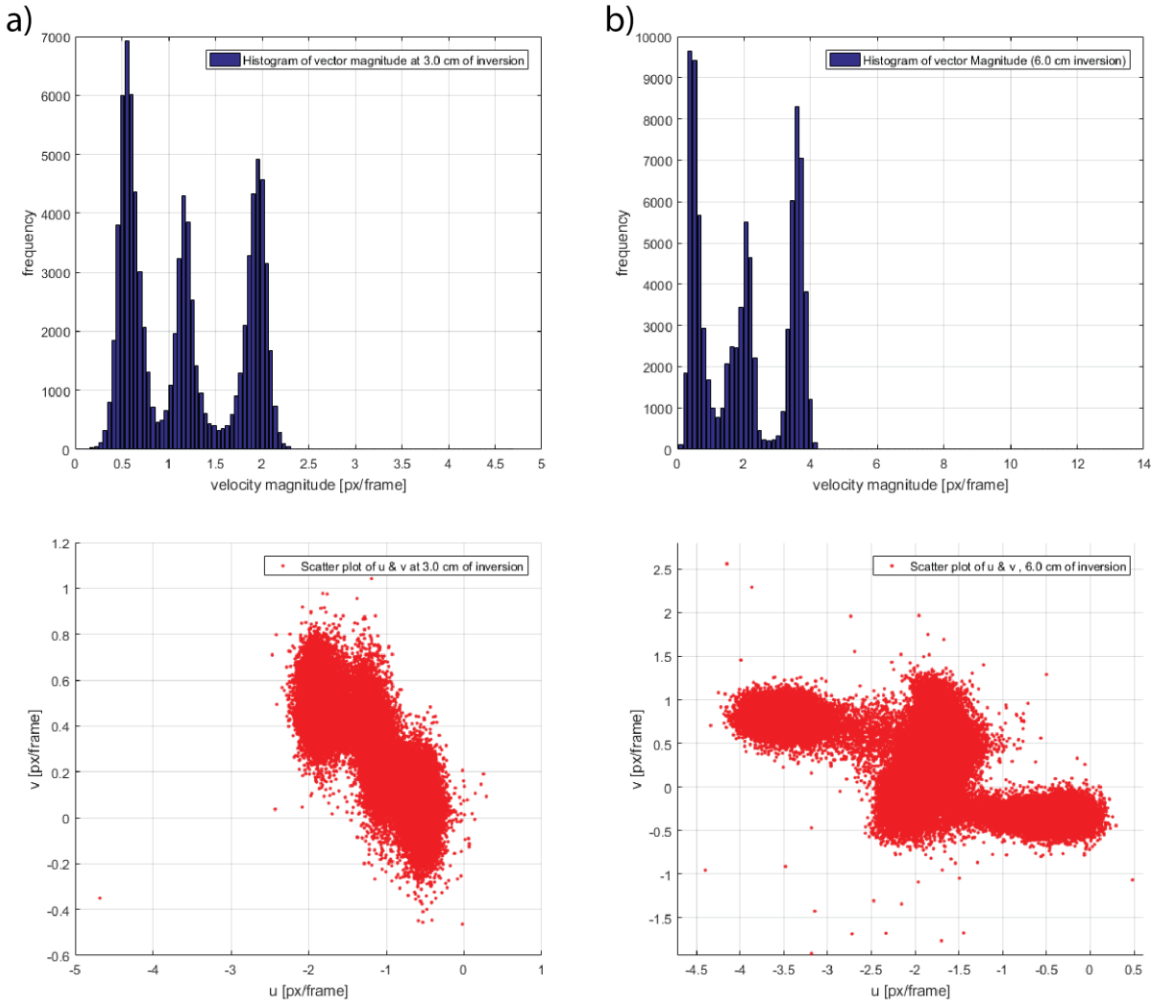

Figure 2.2.23. Histogram and scatter plots of the PIV analysis at 3.0 cm (a) and 6.0 cm (b) of inversion.

Cross-section analysis

The cross sections illustrated below in figure 2.2.24 are taken at the end of the experiment after 6.0 cm of inversion in the center of the model (CUT 6 - (b)) and close to it (CUT 10 - (a)). The following can be observed in these cross sections: (1) The silicon layer acts as a decollement, decoupling the sedimentary cover from the sedimentary basement. (2) The sedimentary cover is characterized by extension during the rifting phase which extends on both sides outside of the graben (Brun and Nalpas., 1996). (3) The décollement transfers the extension horizontally by thinning of the silicone layer. (4) The most extensive amount of normal faulting occurred in the sedimentary cover above the immobile plate during the extension phase (mobile during inversion), which led to the formation of small grabens at the main rift flanks delineated by faults F3 in (a) and F2 in (b). (5) At the end of the deformation the décollement is thicker above the mobile plate during inversion and thinner above mobile plate during extension. This is related to the flow of the ductile layer away from the hinterland which led to the formation of silicone walls at the border master faults. (6) Both sections contain a large number of faults, section (a) contains the following normal faults: 2x F1, F2, 2x F3 and F4, it also contains two shortcut thrust faults (R1 and R2), shortcut fault (R1) is larger than (R2). Section (b) contains the following normal faults: 2x F1, F2, 2xF3 and F4. The section also includes two thrust faults (R1 and R2), of which R1 is also larger than R2. (7) The extension phase caused the graben master faults to propagate from the basement to the sedimentary cover which is linked to the excessive thinning of the ductile layer due to the shearing as a result of movement along the offsetting bounding faults. Initially both rift master normal faults were soft-linked. The excessive thinning of the silicone layer in the footwall during extension eventually causes the ductile layer to rupture and in turn hard-linking the master fault in the sedimentary cover and basement. This thinning was less in the hanging-wall and thus the cover master fault was not allowed to become hard-linked with the master basement faults. (8) simple shearing of the décollement was extensive during the rifting phase as can be seen by the drag present in the ductile layer. (9) Extensive structural collapse occurred inside of the graben sedimentary cover that resulted in extensive faulting and rotation of the faults, which in turn led to the formation of a synclinal structure above the décollement. This rotation steepens the normal faults and plays a crucial role in the velocity decoupling inside of the graben as described in the PIV analysis above. (10) Normal fault (F4) in both sections (a) and (b) show a reverse faulting components. (11) Sedimentation inside of the graben through time increased the sediment loading, which not only further promoted lateral flow and thinning of the ductile layer, it also forced the ductile section bounded by the brittle basement faults to sink towards the V.D as no new sediment can penetrate the ductile layer to fill the newly created space by rifting due to its sealing capability, allowing only downward and minor lateral spreading movement. (12) The silicone inside of the graben is significantly deformed and displays upward drag features. The thickening of the décollement at the graben borders pushes the sediments upward.

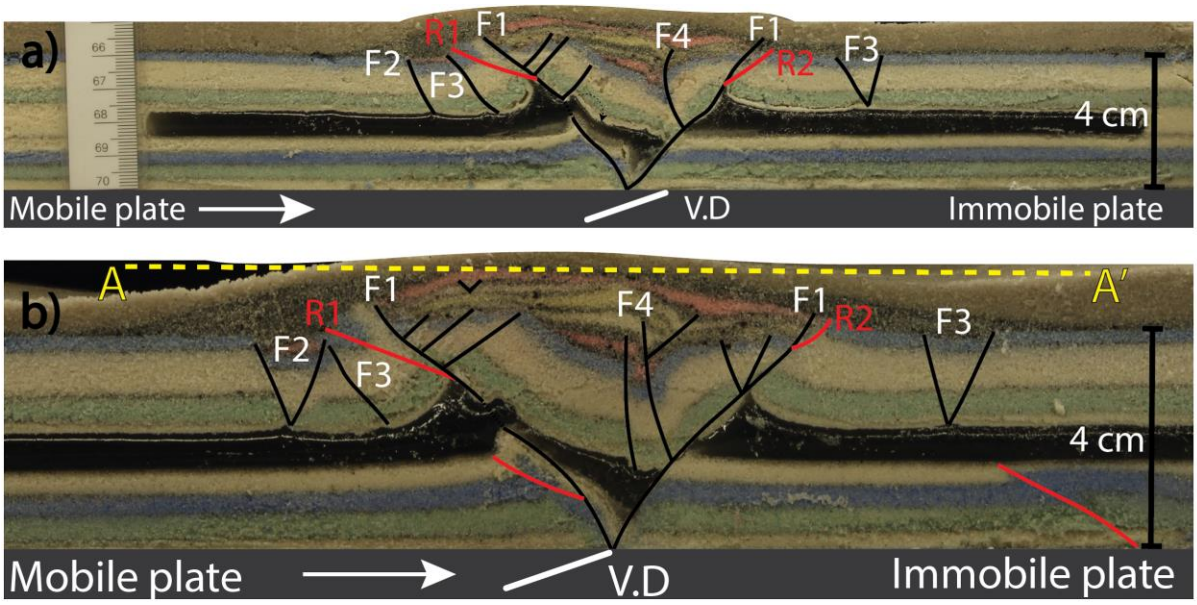

Figure 2.2.24. Cross sections taken after 6.0 cm of inversion. Sections (a) and (b) are taken at two different positions and show slightly different structures and thus slightly different descriptions of the fault patterns. The black lines represent the normal faults. The red lines represent the thrust faults.

2.2.3 GS-D45: Brittle-Ductile, Extension and sedimentation followed by 45° inversion

Photographs taken from the top-view camera during the deformation of the analogue model were compiled into a time-lapse and can be visualized here:
https://www.youtube.com/watch?v=G4QXSDAYgIA
The textured 3D model compiled at the end of the extension phase can be visualized here:
https://sketchfab.com/models/34488572494c421693d308dc7a511b54

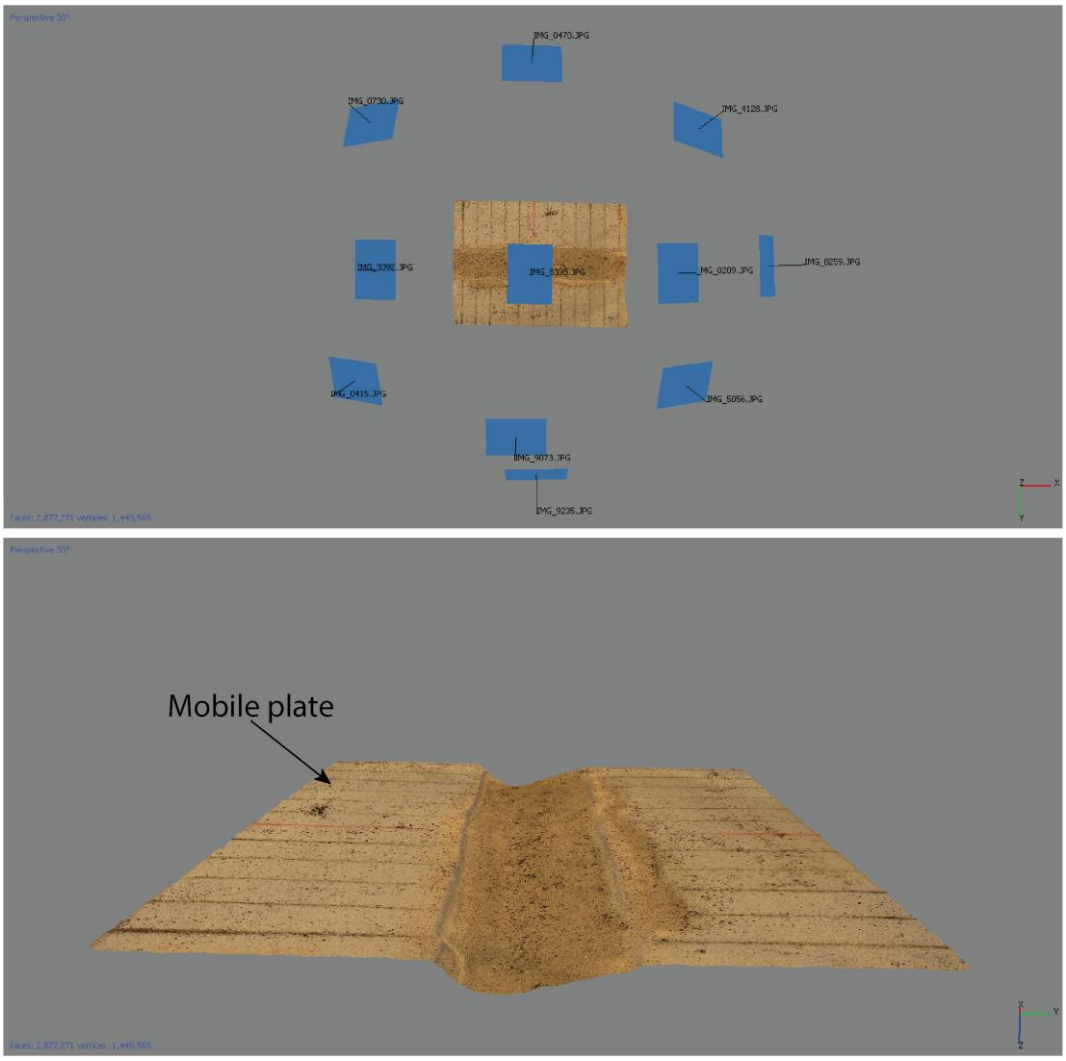

Figure 2.2.25. Screenshot of the 3D model in Agisoft Photoscan at 5.0 cm of extension (11x cameras). Sparse cloud (163,430 points), Dense cloud (24,386,360 points), Mesh (2,877,271 faces; 1,440,565 vertices).

The following observations can be made after analyzing the 3D model and the analogue model surface top-views (Figures 2.2.25 and 2.2.26): (1) Extension of the analogue model led to the formation and growth of a rift basin delineated by two large border master faults (F1). Progressive extension led to the formation of a small graben above the fixed plate bounded by faults (F2). (2) A small ridge is visible that separates the lowland from the highland inside of the rift basin. (3) The surface area and volume of the extended 3D model was measured, which equated to a volume of $-276.2\ cm^3$ and a surface area of $0.553\ m^2$. (4) The geometry of the formed graben is asymmetrical both in 2D and 3D along strike. Other faults and structures that may have developed during the extension phase can only be identified using cross-sections, DEM's or PIV analysis.

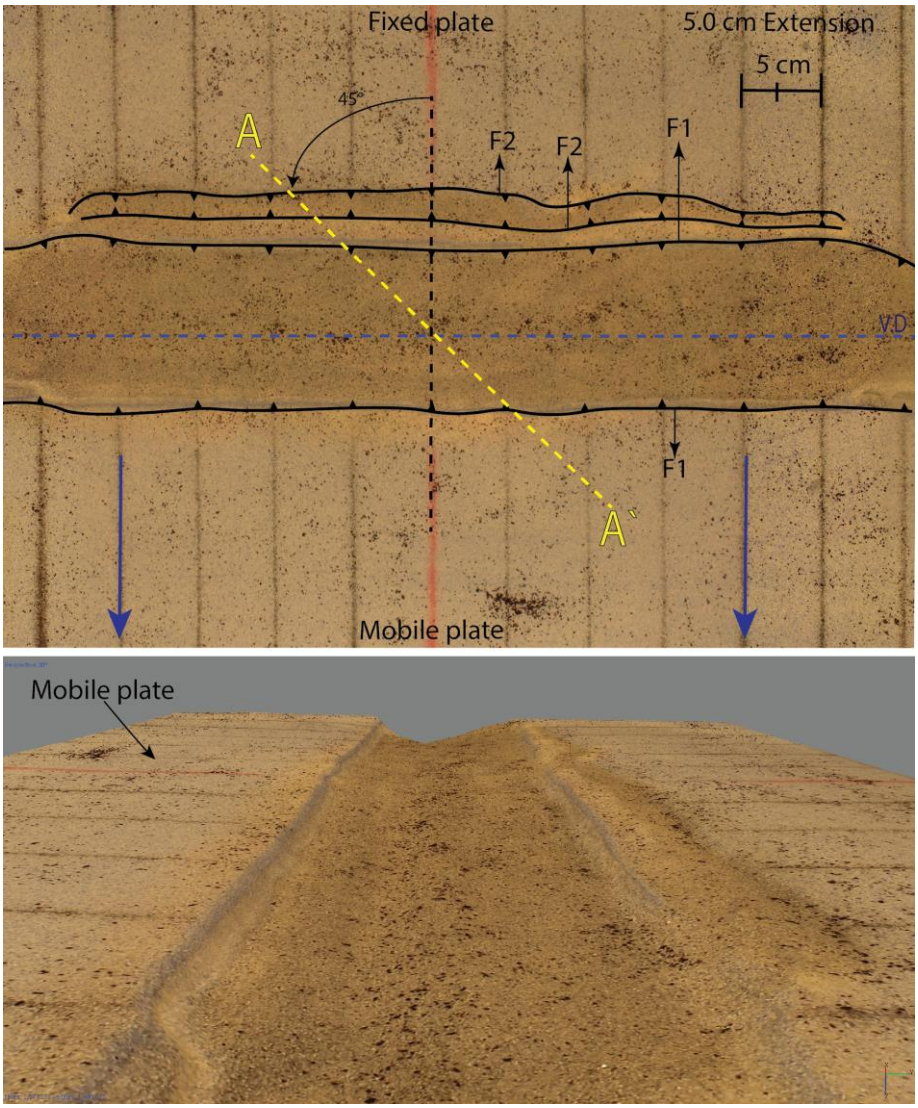

Figure 2.2.26. Top view of the experiment at 5.0 cm of extension constructed from Orthomosaic image exported from Photoscan (4213x3047, 0.149 mm/pix) and perspective view of the graben at 35°.

Extension phase DEM analysis

DEM maps of the fully extended analogue model (5.0 cm extension) were constructed from the dense point cloud in Agisoft Photoscan. The DEM was exported from Photoscan and processed in ArcMap which yielded the maps below in figures 2.2.27, 2.2.28 and 2.2.29. Most of the micro-topography formed during the extension phase is not well visible in the top view photographs. DEM's of the extension phase can reveal the micro-topography that developed during the extension phase with very high detail and precision. The following can be observed in these digital elevation maps: (1) The deepest formed depression has a depth of *-2.23 cm* below the surface of the analogue model. (2) Two very small graben nucleation zones are present above the immobile plate which are not visible with the naked eye during the experiment and are also not visible in the top view photographs. These depressions are not continuous along strike of the rift basin. (3) The graben delineated by faults (F2) is more irregularly shaped and less continuous compared to previous ductile experiments. (4) A small graben also nucleated above the mobile plate, however it is not continuous along strike. This small graben shows significant horizontal displacement which could point to strike-slip faulting in the sedimentary cover parallel to S1. (5) Inside of the main graben a small trench runs across its entire length, which most likely formed as a result of movement along the velocity discontinuity. (5) The largest slopes formed above the immobile plate (Figure 2.2.28). (6) The deformation zone above the immobile plate is larger than that above the mobile plate. (7) The faults that formed in the footwall have a Southward dipping slope direction, while the faults formed in the hanging-wall have a Northward slope dip direction (Figure 2.2.28). (8) The small grabens in the flanks of the model nucleated attached to master border faults (F1) and slowly migrate inwards along strike, which led to a 'n' shaped structure above the immobile plate and a 'u' shaped structure above the mobile plate. Compared to the previous ductile experiment, the symmetry of all formed grabens is significantly lower in this experiment. Also, above the mobile plate the two formed micro grabens are smaller and less well developed in this experiment.

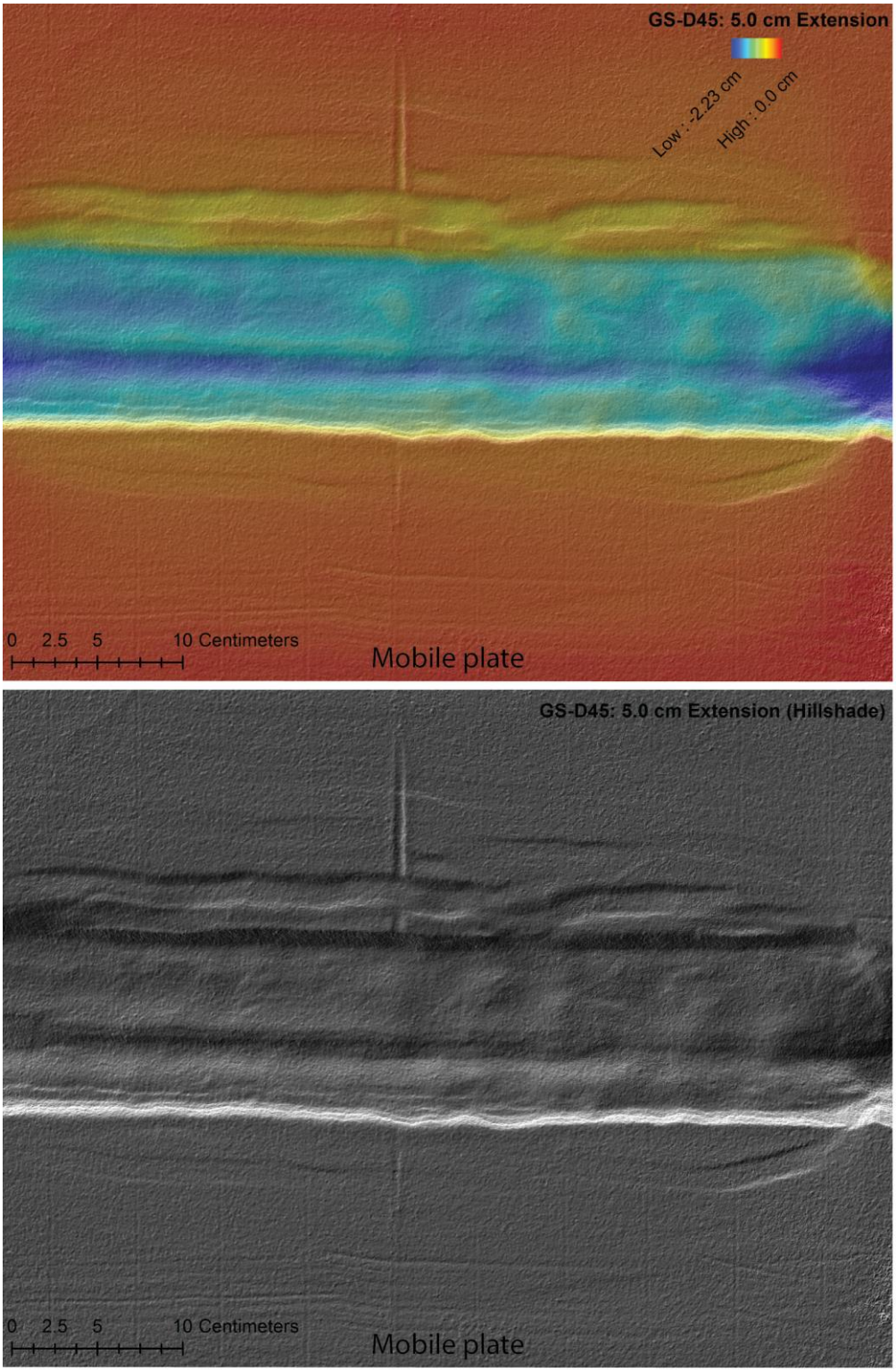

Figure 2.2.27. Color ramp and Hillshade analysis of the DEM in ArcMap (3564x2745, 0.149 mm/pix). The top image consists of a color ramp combined with a 40% transparent overlay of the Hillshade image. The grey image consists of a Hillshade spatial analysis map (no transparency). 5.0 cm of extension.

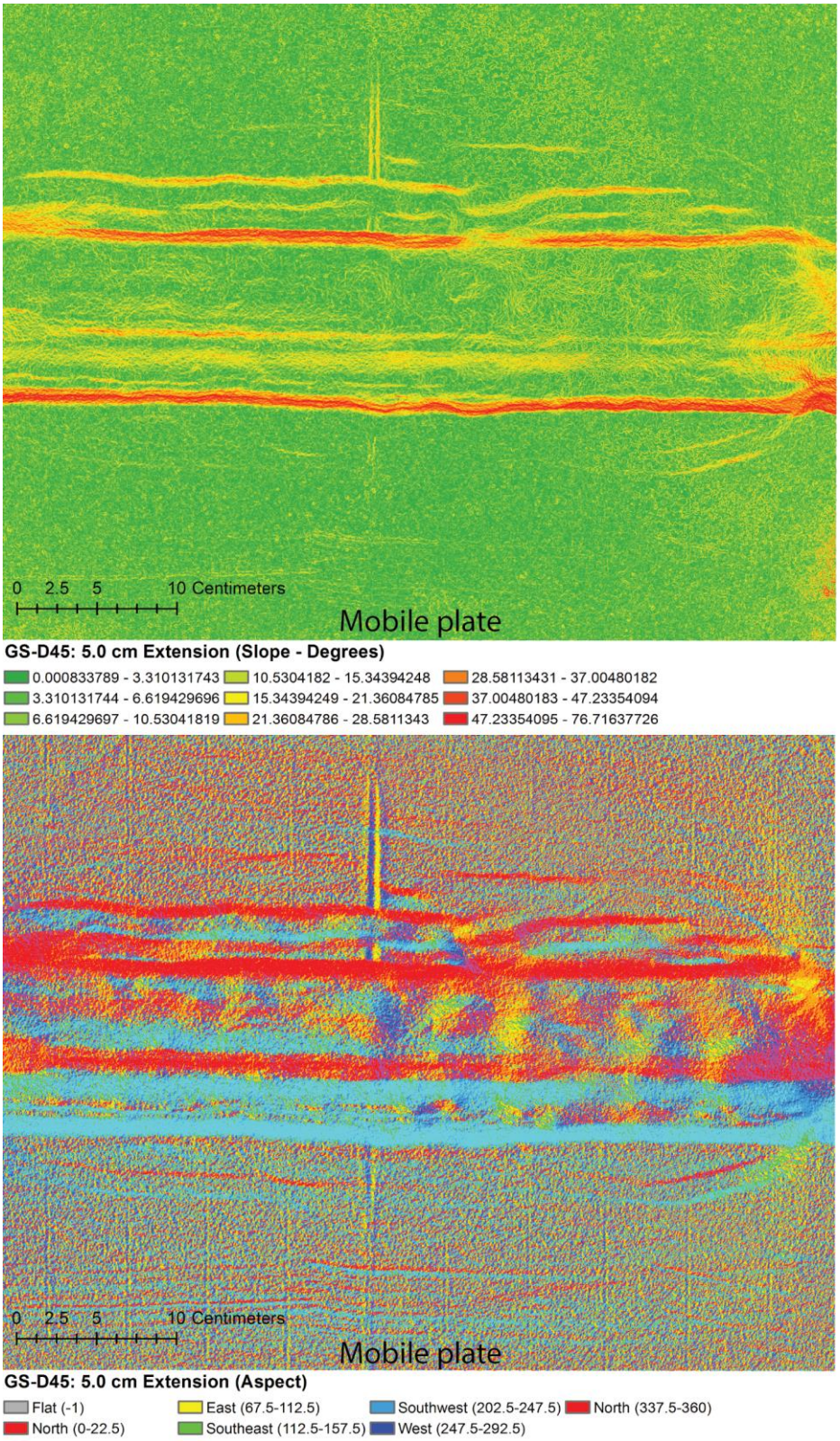

Figure 2.2.28. Spatial Slope and Aspect analysis of the DEM in ArcMap. The aspect analysis represents the slope direction. The top of the Aspect images is the North direction. The bottom of the image is the South direction. 5.0 cm of extension.

The exact width of the deformation zone is best visualized by looking at the raw DEM illustrated below in figure 2.2.29. The deformation zone is much wider compared to the purely brittle models and ranges over almost the entire sedimentary cover. The thinning of the décollement clearly lowered the entire sedimentary cover above décollement even so slightly.

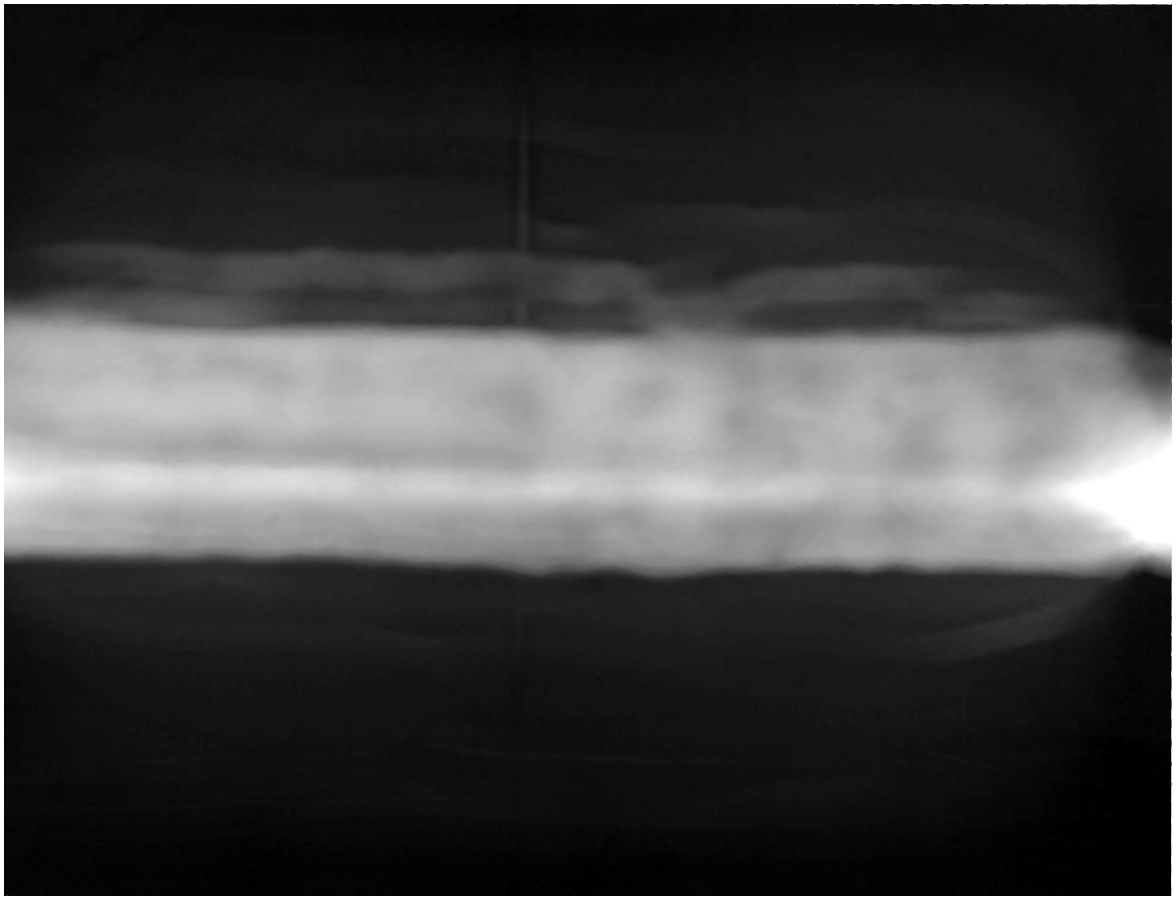

Figure 2.2.29. Raw DEM compiled at the end of the extension phase and exported from Agisoft Photoscan.

After the extensional phase inversion is applied to the system (Figures 2.8.4 and 2.8.5). The textured 3D model compiled at the end of the inversion phase can be visualized here: https://sketchfab.com/models/f3439f38aa054a53b77c211d251b4c71

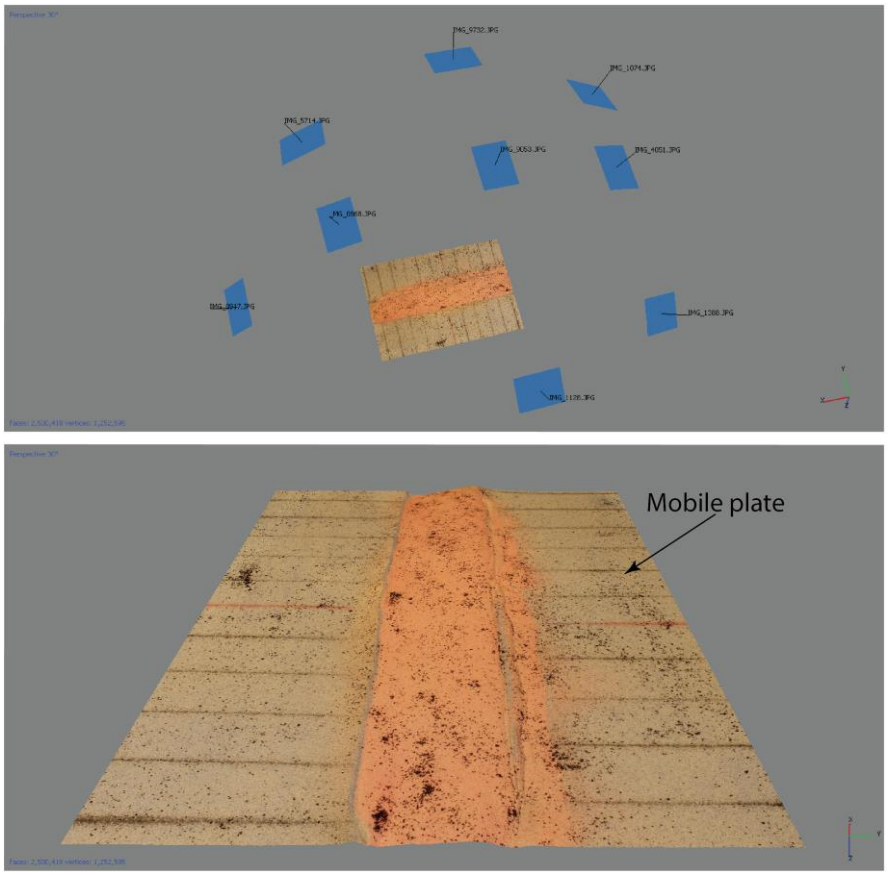

Figure 2.2.30. Screenshots of the 3D model in Agisoft Photoscan at 6.0 cm of inversion. x9 cameras, Sparse Cloud (127,866 points), dense cloud (14,245,577 points), Mesh (2,500,577 faces; 1,252,595 vertices).

The following observations can be made after analyzing the 3D model and the surface top views (Figures 2.2.30 and 2.2.31): (1) A forethrust shortcut fault (R1) developed above the mobile plate. (2) The central grid-line is displaced laterally *2.88 cm*, which indicates that a significant strike-slip component was present in the system during inversion. Interesting to note is that this displacement magnitude is smaller compared to the purely brittle model with the same angle of inversion. The accommodation of displacement by strike-slip decreased the amount of positive topography that developed. (3) The displacement magnitude of the graben in the direction of the foreland decreases as the result of the formation of thrust fault (R1) which converts the purely horizontal displacement component of the graben into a vertical and horizontal component. Although no other thrust faults are clearly visible in the top-view photographs, analysis of the cross-sections must be carried out to rule out the formation of other thrusts. Throughout the inversion phase maximum uplift occurred at the hanging-wall by the migration of material towards the rift basin followed by uplift once it reached the border faults. This caused the secondary extensional graben at the model flanks above the mobile plate to be slowly transported in the direction of the graben margin,

eventually this secondary graben delineated by faults (F2) is partially rotated and thrusted upwards is a in a “inverse subduction” type mechanism. The amount of topography and maximum uplift that was produced during the inversion is lower compared to the previous ductile experiments with lower (α) values. Backthrust formation appears to have been absent.

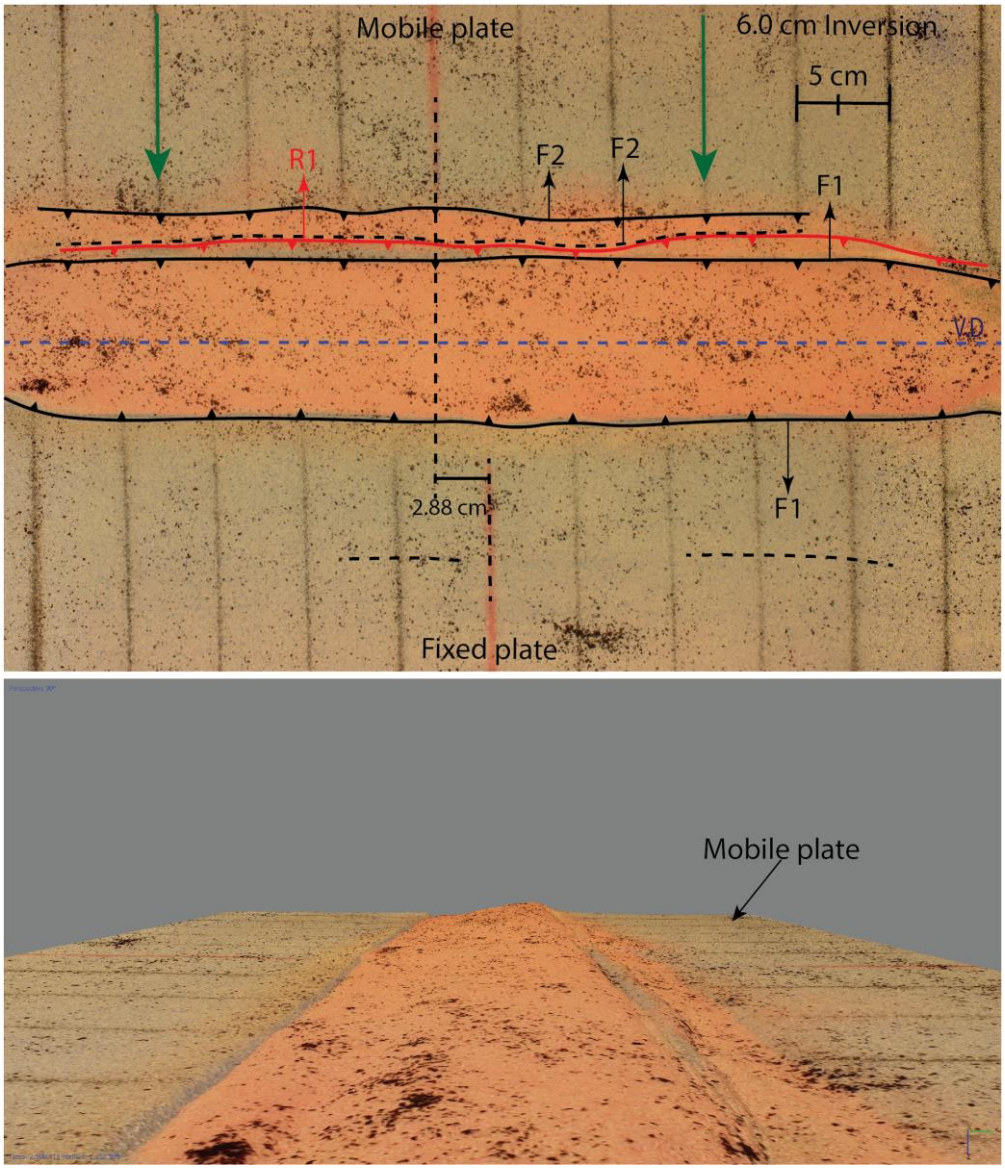

Figure 2.2.31. Orthomosaic top view of the analogue model at the end of the experiment after 6.0 cm of inversion (3666x2530, 0.145 mm/pix) and perspective view of the inversion graben at 35°. Orthomosaic and 3D model constructed from 9x images.

The volume and surface area of the reconstructed 3D model after 6.0 cm of inversion were measured using Agisoft Photoscan, which yielded the following results:

Surface area: $0.4137\ m^2$
Volume: $19.7587\ cm^3$

The measured volume at the end of the inversion phase is lower compared to previous experiments (α< 45°), which is to be expected due to the lower amount of positive topography that formed during the inversion phase because of the increased strike-slip component.

Inversion phase DEM analysis

In total 5,922 photographs from 9x cameras were processed in Agisoft Photoscan, which yielded a 4D sequence of 658x 3D frames for the entire inversion phase. For each frame a Sparse and Dense point cloud was compiled. For Each frame a DEM was exported and processed in ArcMap. Due to the large number of DEM's, the process of information extraction (Slope and Hillshade) was automated using ArcPy for ArcMap. A time-lapse for each of the analysis was produced and can be observed here:
https://www.youtube.com/watch?v=ziqB__OZyzk
Manual DEM maps were compiled in ArcMap from the last frame (6.0 cm inversion), which are illustrated below in figures 2.2.32 and 2.2.33. Different types of spatial analysis tools were used for the DEM processing that allows both the qualitative and quantitative analysis of the topography produced. In total *1.014 cm* of maximum uplift formed at the end of the inversion of the analogue model. This amount is lower compared to ductile experiment with smaller angles of inversion, which is to be expected. It should be noted that most of the highest topography was produced outside of the ductile zone as the ductile layer is positioned 10.0 cm inwards from all four directions. The following can be observed in the digital elevation model analysis figures below: (1) A small grabens is present above the mobile plate during inversion (fixed during extension) that run parallel to the master grabens, this small graben is bordered by shortcut fault (F1). Comparing the DEM of the inversion phase to the DEM of the extension phase it appears that this small graben migrated a significant distance towards the foreland, more however it also appears that sections of this stall graben have been subducted underneath the thrust fault (R1). A single less developed graben is also visible above the immobile plate. (2) The shortcut thrust fault (R1) above the mobile plate that delineates the graben is clearly represented as a steep ridge (red band of slope analysis in figure 2.2.33). This shortcut fault has a high asymmetry compared to the same structure in previous ductile experiments. (3) No shortcut fault formation occurred above the immobile plate. (4) A ridge is present in the footwall that runs across the entire length of the graben, the formation of this structure is most likely linked to the deformation and faulting of the sedimentary cover. (5) The steepest ridges (highest slope angle) formed above the mobile plate. (6) The amount of topography that was produced is not uniform across the graben and the highest amount of topography that formed tends to be localized to certain areas. (7) The strain distribution throughout the model deformation was not uniform. (8) Most of the ridges formed during the inversion phase have a Southward or Northward dipping slope direction (Aspect spatial analysis).

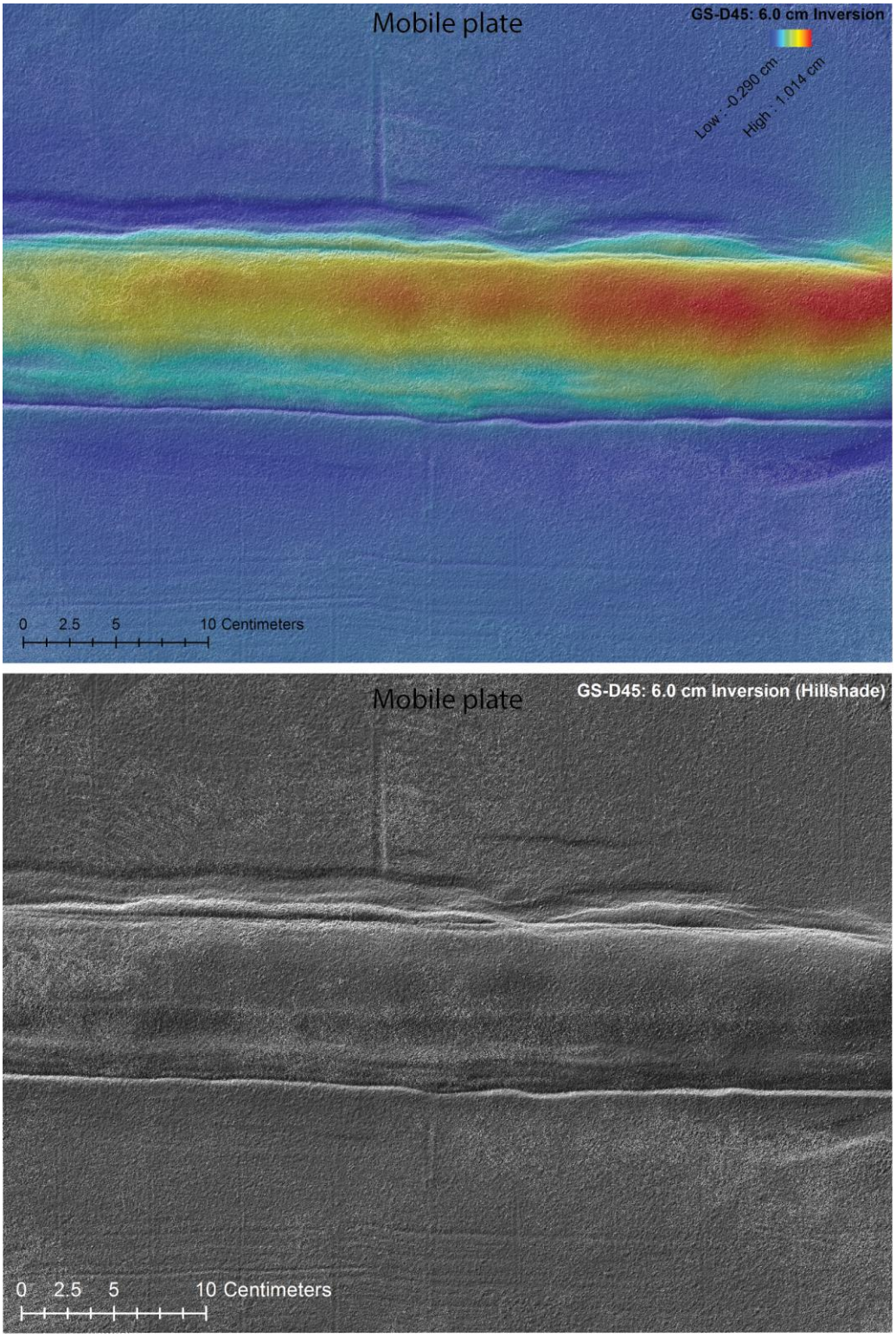

Figure 2.2.32. Spatial Hillshade analysis of the DEM in ArcMap (12810x9644. 0.0382mm/pix). Top image consists of a color ramp combined with a 40% transparent overlay of the pure Hillshade grey image. The grey image is a pure Hillshade spatial analysis map (no transparency). 6.0 cm of inversion

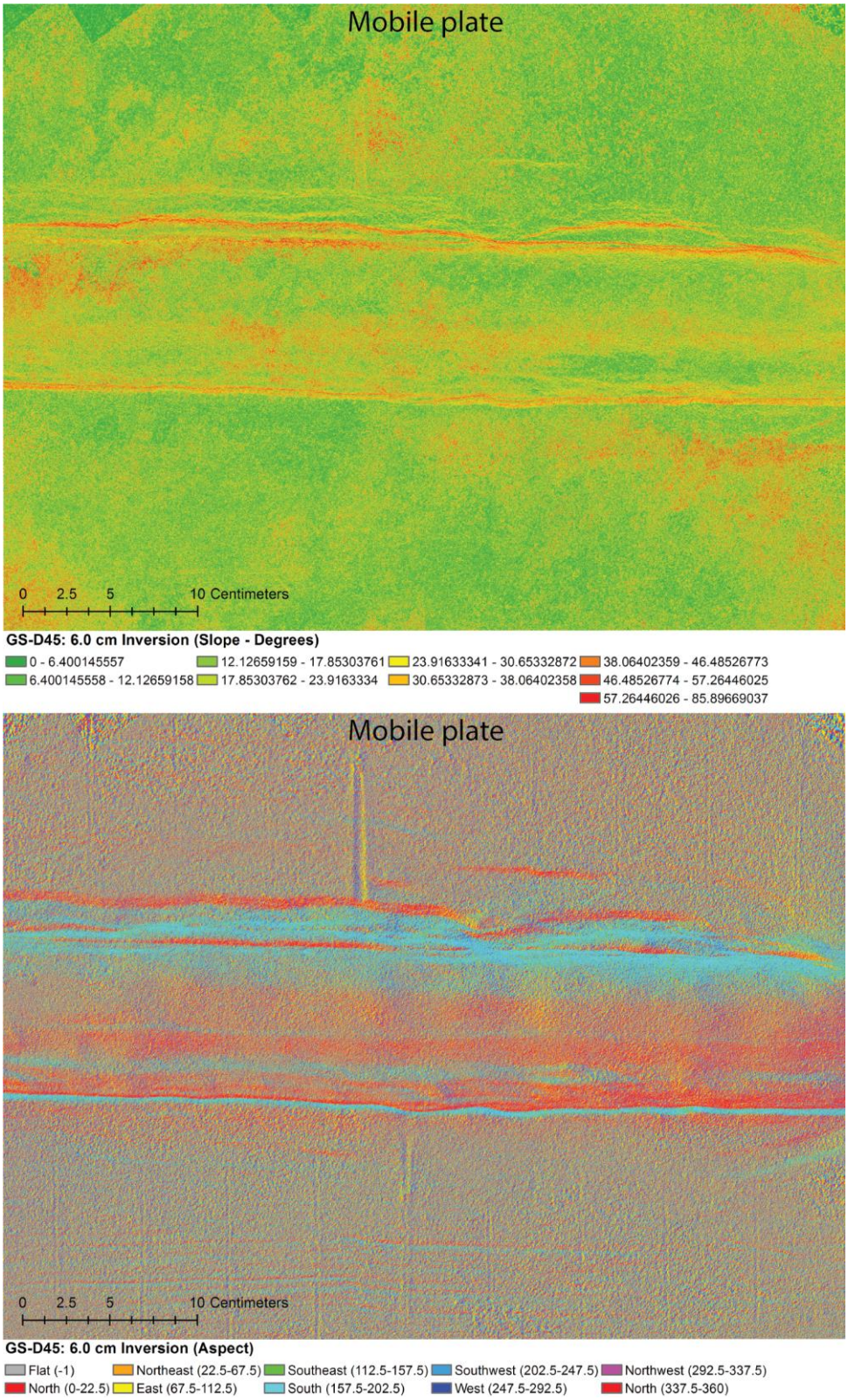

Figure 2.2.33. Spatial Slope and Aspect analysis of the DEM in ArcMap. The aspect analysis represents the slope direction. The top of the Aspect images is the North direction. The bottom of the image is the South direction. 6.0 cm of inversion.

Depth and Height profiles

Computed height profiles measured at the center of the analogue model are illustrated below in figure 2.2.34. Graph (a) corresponds to the completed extension phase, while graph (b) corresponds to the completed inversion phase. The formation of the trench above the mobile plate is clearly visible in graph (a) as a sharp depression at 15.0 cm. Fault (F1) above the immobile plate appears to have a steeper slope than F1 above the mobile plate. The exact opposite is true for the inversion phase in (b). The formed graben delineated by normal faults (F2) is represented as a small depression at 5.0 cm in (a) and at 1.0-2.0 cm in (b).

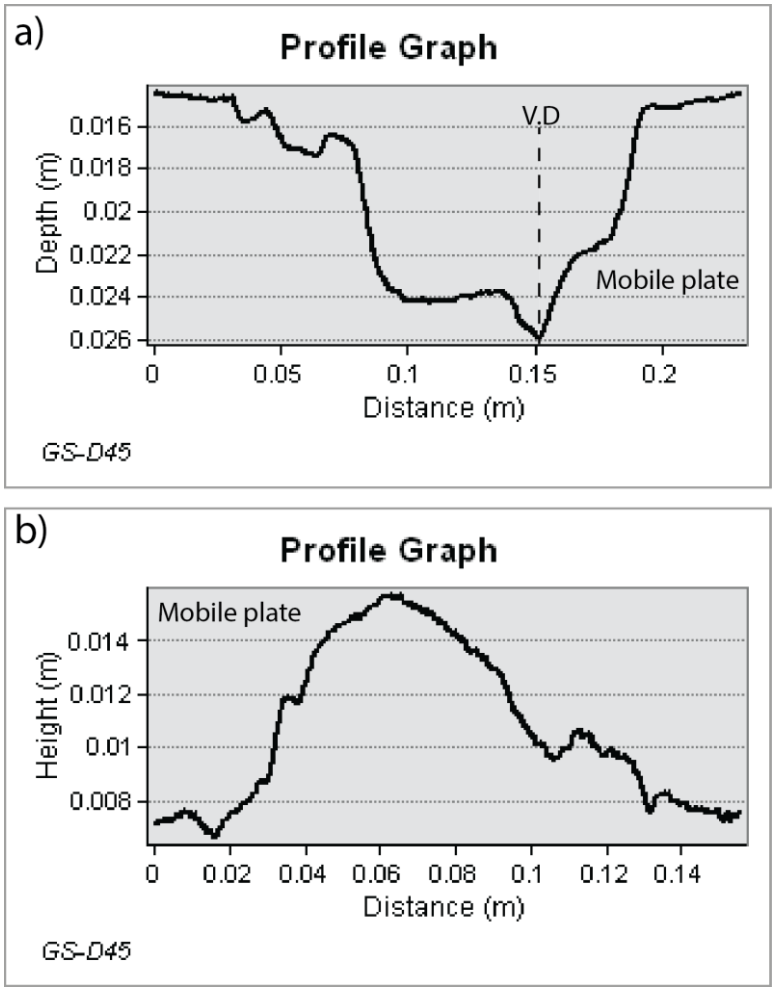

Figure 2.2.34. Computed height profiles measured at the center of the analogue model (same orientation as cross-sections) at 5.0 cm of Extension (a) and 6.0 cm of inversion (b).

PIV analysis

PIV vector and vector magnitude analysis was carried out of the inversion phase using undistorted images exported from Photoscan, the analysis using these photographs yielded much higher quality results due to the correction for lens distortion and camera tilt. Due to the extensive stick-slip component during the inversion it was not possible to compile a time-lapse due to the lack of frames. The figure below illustrates both PIV analysis techniques at 3.0 cm - (a) and 6.0 cm of inversion - (b). The following can be visualized in both the time-lapses and figure 2.2.35 below: (1) The displacement velocity and magnitude decreases from the hinterland to the foreland. (2) The vectors above the mobile plate have a 45° angle relative to the extension direction, which corresponds to the inversion angle (α). (3) The vector magnitudes inside of the graben are lower compared to the vector magnitudes above the mobile plate due to the horizontal accommodation of displacement by strike-slip at master fault (F1) in the hanging-wall. This led to the decoupling of the rift basin from the rest of the analogue model. The decoupling magnitude was almost identical in both normal master faults. (4) The vector field tends to align parallel to the velocity discontinuity. (5) The vectors above the immobile plate display a slightly clockwise rotation. (6) The graben remained overall symmetrical throughout the inversion phase and no large vector field fluctuations occurred. (7) The vector magnitude of the rift basin remains uniform throughout the inversion phase, indicating that there was little preference to reactivate specific faults within the graben. As observed in the digital elevation models, the maximum topographic uplift produced throughout the inversion phase occurred at the interface between the mobile plate and the rift basin delineated by master normal fault (F1). Histogram plots in (a) - figure 2.2.35 illustrates three main zones with peaks of highest vector magnitude at 0-0.5 pixels/frame (‘immobile’ plate), 1.2-2.0 pixels/frame (graben) and 2.3-3.0 pixels/frame (mobile plate). These values vary slightly compared to the histogram in (b), however, the pattern remains the same. From these plots, it can be observed that the there is a velocity decoupling between the graben and both plates, which suggest that there was extensive displacement along the graben border master normal faults by horizontal reactivation. The overall high symmetry of the three zones indicates that reactivation mainly occurred at border normal faults (F1), where both faults accommodated almost the same amount of displacement. The scatter plot illustrates the orientation of the vectors at both 3.0 cm and 6.0 cm of inversion, this pattern stands in contrast relative to other scatter plots of experiments with shallower angles of inversion where the scatter cloud has a (s) form. This suggests that there was a significant strike-slip component present in the system.

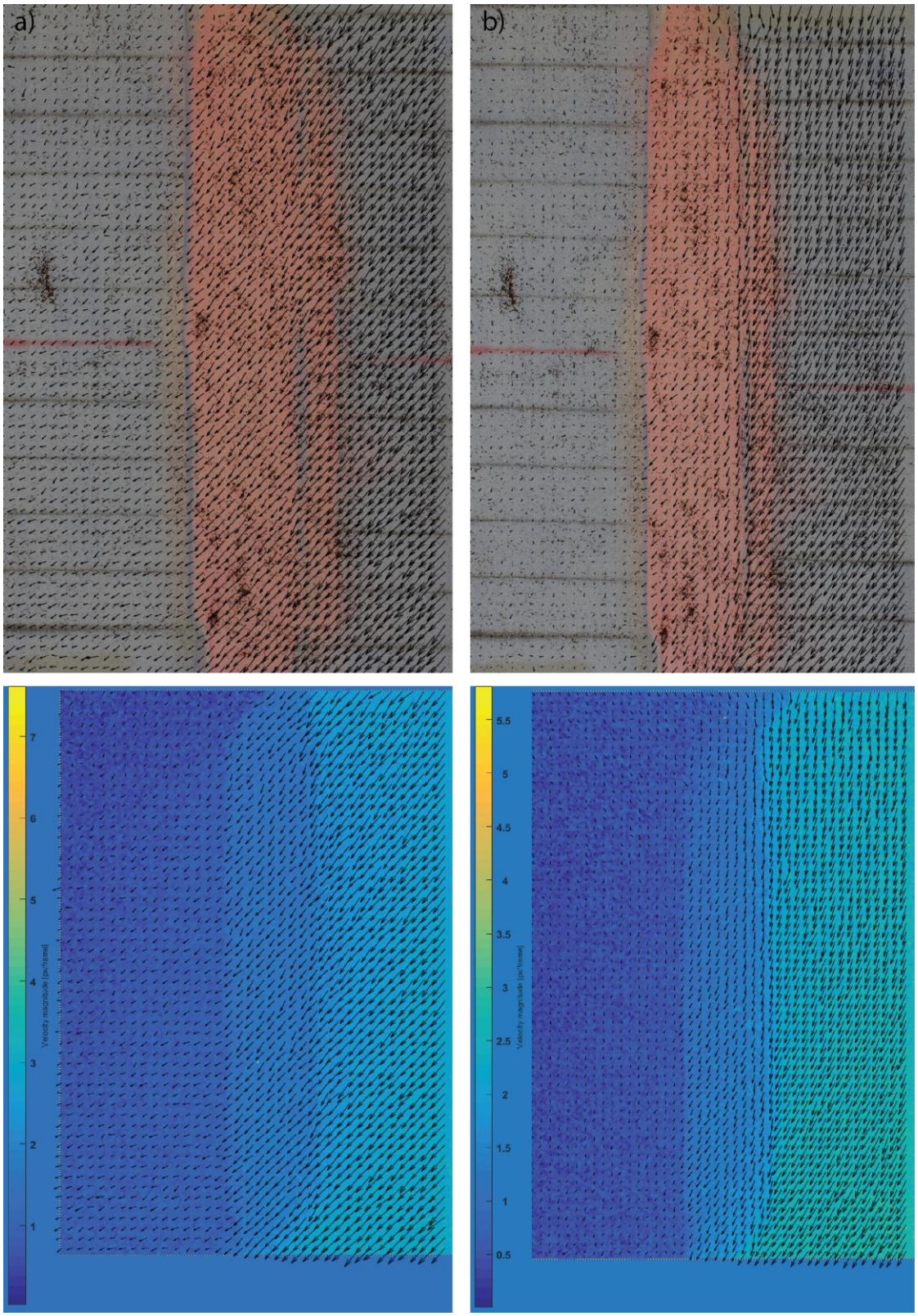

Figure 2.2.35. Vector and Vector magnitude analysis (pixels/frame) at 3.0 cm - (a) and 6.0 cm - (b) of inversion.

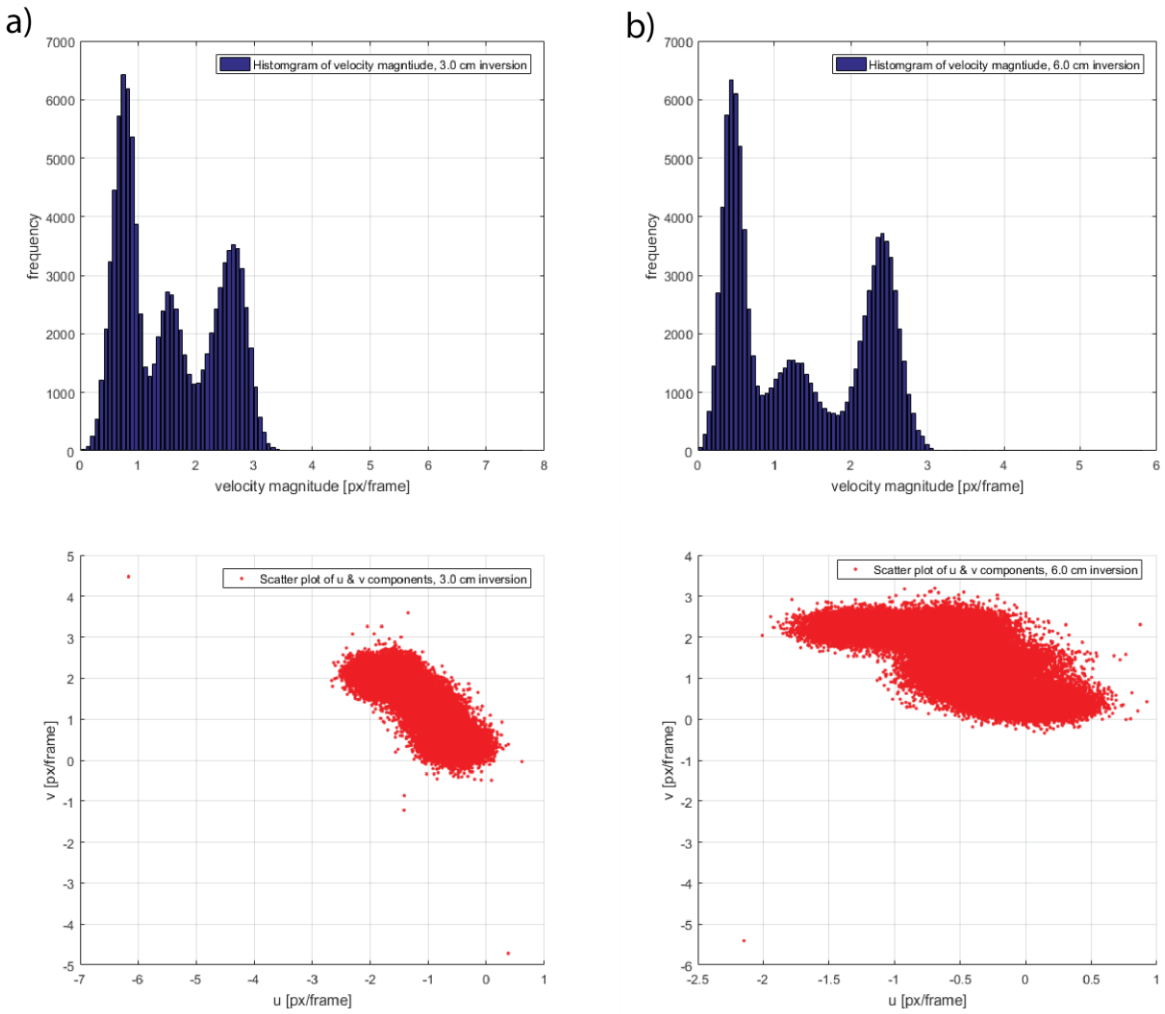

Figure 2.2.36. Histogram and scatter plots of the PIV analysis at 3.0 cm (a) and 6.0 cm (b) of inversion.

Cross-section analysis

The cross sections illustrated below in figure 2.2.37 were taken at the end of the experiment after 6.0 cm of inversion in the center of the model (CUT 5 - (a) and (b)) and at the upper flank (CUT 10 - (c), CUT 7 - (b)). The following can be observed in these sections: (1) The silicon layer acts as a decollement, decoupling the sedimentary cover from the sedimentary basement. (2) The sedimentary cover is characterized by extension during the rifting phase which extends on both sides outside of the graben (Brun and Nalpas., 1996). (3) The décollement transfers the extension horizontally by thinning of the silicone layer. (4) The most extensive amount of normal faulting occurred in the sedimentary cover above the immobile plate during the extension phase, which led to the formation of a small graben delineated by faults F2. (5) At the end of deformation of the analogue model, the décollement is thicker above the mobile plate during inversion and thinner above mobile plate during the extension phase. this is related to the flow of the ductile layer away from the hinterland. (5) The sections contain many faults, including the following main normal faults: 2x F1, F2, F3, and one shortcut thrust faults (R1). (6) The extension phase caused the graben master normal faults to propagate from the basement to the sedimentary cover which is linked to the excessive thinning of the ductile layer due to the shearing as a result of movement along the offsetting bounding faults above and below the décollement. Normal fault (F1) in the footwall was only allowed to become hard-linked linked due to the excessive stretching and thinning and eventual rupture of the ductile layer. This thinning was less in the hanging-wall during the extension and thus the cover border fault was not allowed to become hard-linked with the basement fault, this indicates that there was more displacement along (F1) in the footwall during extension relative to (F1) in the hanging wall. (7) simple shearing of the décollement was extensive during the rifting phase as can be seen by the drag features present in the ductile layer. (8) Extensive brittle structural collapse occurred inside of the graben sedimentary cover that led to extensive faulting and rotation, which in turn led to the formation of a synclinal structure above the décollement. This rotation steepens the normal faults. (9) Fault (F3) displays a reverse-slip component. (10) Sedimentation through time increased the sediment loading, which not only further promoted lateral flow and thinning of the ductile layer, it also forced the ductile section within the graben infill to sink towards the V.D as no new sediment can penetrate the ductile layer to fill the newly created space by rifting due to its sealing capability, allowing only downward and minor lateral spreading movement. Interesting to note is that the sedimentary basement accommodated most of the strike slip displacement and less strike-slip is transferred to the sedimentary cover as the décollement decouples the cover from the basement and absorbed most of the movement by lateral flow. The silicone layer cannot be sheared, which implies that it can't transfer shear strain to the sedimentary cover. The only places where shear strain can be transferred is at fault (F1) in the footwall where the silicone layer is very thin to nonexistent and the master fault is hard-linked. This explains the lower amount of strike-slip displacement that was observed compared to purely brittle models. Most of the strike-slip is accommodated by the rift border fault in the hanging-wall. At $\alpha = 45°$ significant vertical and horizontal reactivation of the rift master faults occurred during the inversion. Salt walls developed at these borders which facilitated the reactivation of the master normal faults, it also led to small scale diapirism which grew into these faults. These intrusions led to the formation of pop-up structures which rotate clockwise. The reactivation was less in the footwall than in the hanging-wall. Small scale flame structures formed in the ductile layer above the velocity discontinuity. Only a very small degree of reactivation occurred within the graben. The most extensive reactivation within the graben occurred at fault (F3) where the fault block was both rotated counter-clockwise and inverted at the same time, which led to

the formation of a steeper reverse fault. During inversion, a thrust fault developed in the hanging-wall of the sedimentary basement that produced a ridge which forced the silicone above it upwards. Upward flow of the brittle material along the reactivated hanging-wall border fault due to inversion and strike-slip motion also greatly assisted the formation of the ridge. Significant clockwise rotation of this structure occurred which caused the silicone above it to also rotated clockwise. At the same time the silicone outside of the graben rotated anti-clockwise due to flow away from the hinterland. These opposite forces produced small-scale diapirs with opposite orientations. The resulting force vector is vertical, which greatly assisted in the reactivation of the shallow border master fault.

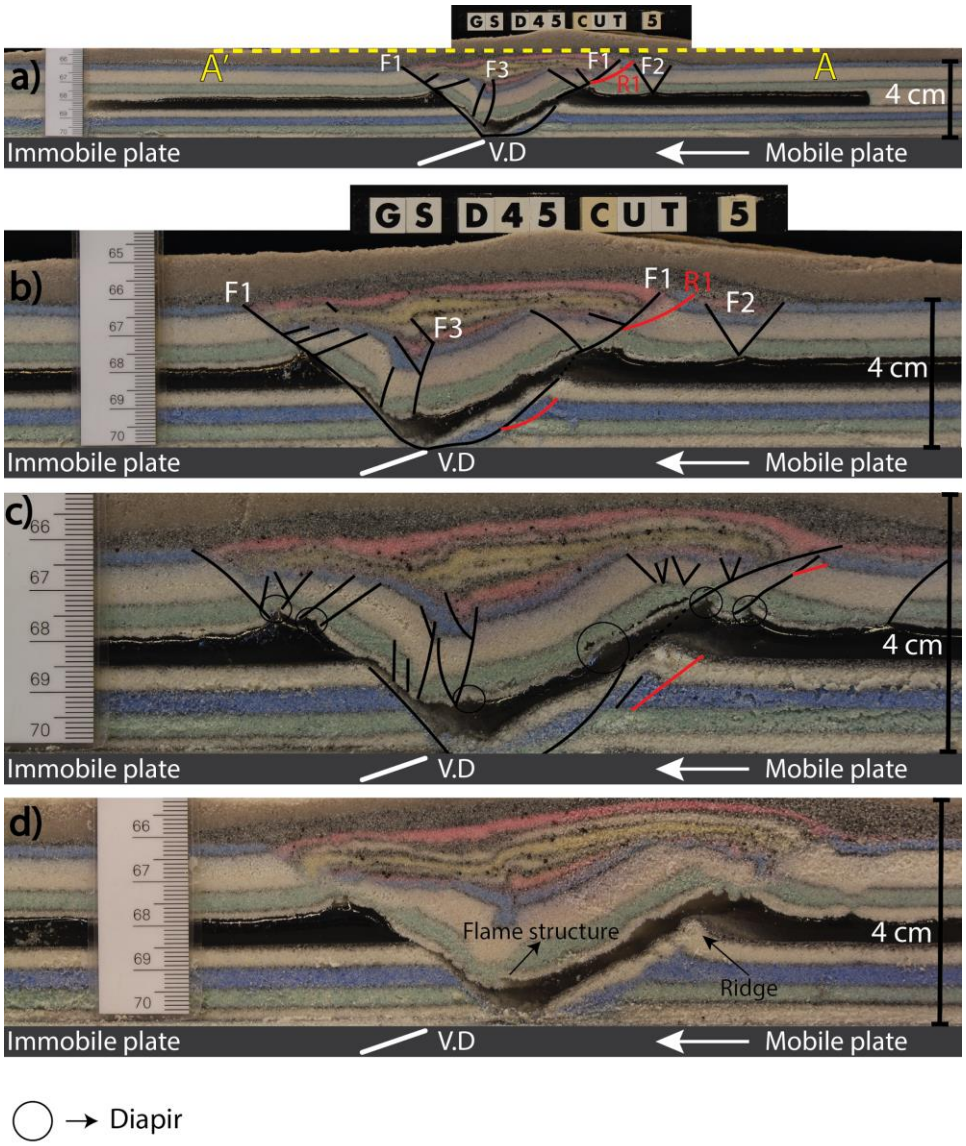

Figure 2.2.37. Cross sections taken after 6.0 cm of inversion. The graben border faults are reactivated which is paired with thickening of the ductile wall and extensive small-scale diapir formation. A ridge develops in the basement of the hanging-wall which facilitates the reactivation of the graben border fault of the sedimentary cover above. The black lines represent the normal faults. The red lines represent the thrust faults.

2.2.4 GS-D75: Brittle-Ductile, Extension and sedimentation followed by 75° inversion

Photographs taken from the top-view camera during the deformation of the analogue model were compiled into a time-lapse and can be visualized here:
https://www.youtube.com/watch?v=pXvSXIwbvvM
The textured 3D model compiled at the end of the extension phase can be visualized here:
https://sketchfab.com/models/02e61193e40f4f71958a78e4171a8938

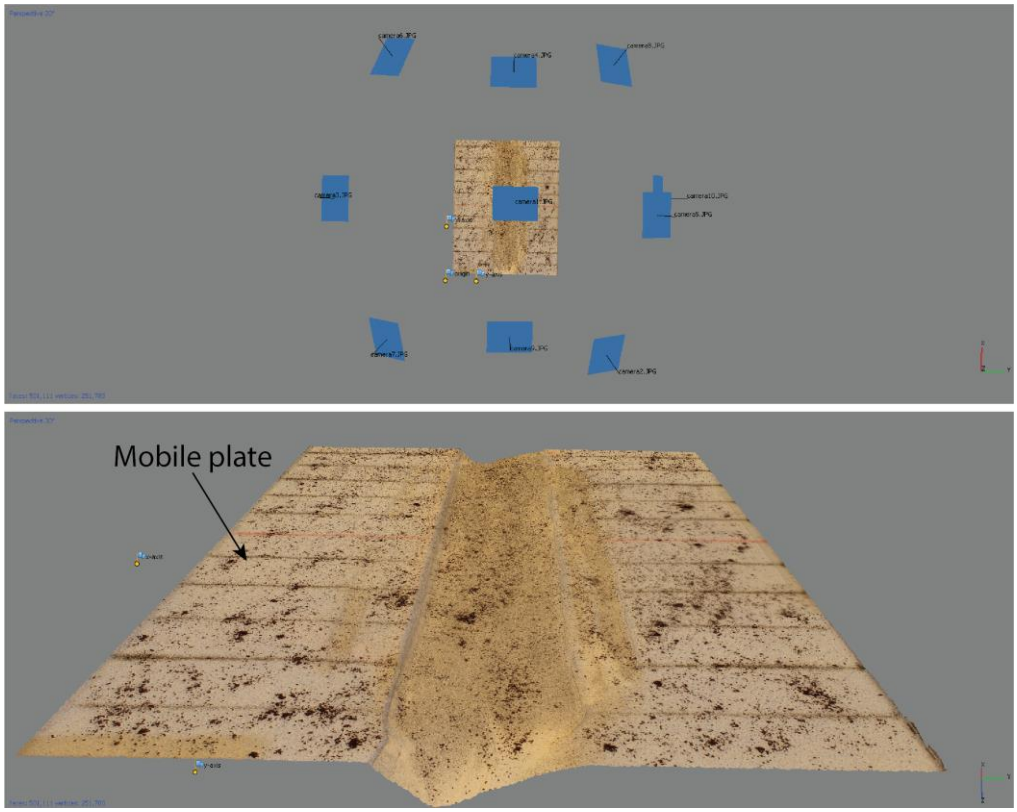

Figure 2.2.38. Screenshot of the 3D model in Agisoft Photoscan at 5.0 cm of extension (11x cameras). Sparse cloud (233,613 points), Dense cloud (4,090,646 points), Mesh (501,111 faces, 251,780 vertices).

The following observations can be made after analyzing the 3D model and the top-views of the surface of the analogue model (Figures 2.2.38 and 2.2.39): (1) Extension of the analogue model led to the formation and growth of a graben delineated by two large offsetting border faults (F1). (2) The geometry of the formed graben is asymmetrical along strike in both 2D and 3D. (3) Two normal faults developed above the immobile plate during the extension which runs parallel to the main graben and are delineated by faults (F2) and (F3). A small graben formed above the mobile plate which is delineated by faults (F4), however, this structure is less well visible and is not continuous along the length of the model, further DEM analysis can reveal more information concerning micro-topography that is not well visible in top-view photographs. (4) There is no clear indication of a ridge formation inside of the graben that separates the lowland from the highland. (5) The surface

area and volume of the extended 3D model was measured, which equated to a volume of $-174.78\ cm^3$ and a surface area of $0.523291\ m^2$.The volume represents the volume of the depressions formed below the surface of the model. Other faults and structures that may have developed can only be inferred using cross-sections, DEM's or PIV analysis.

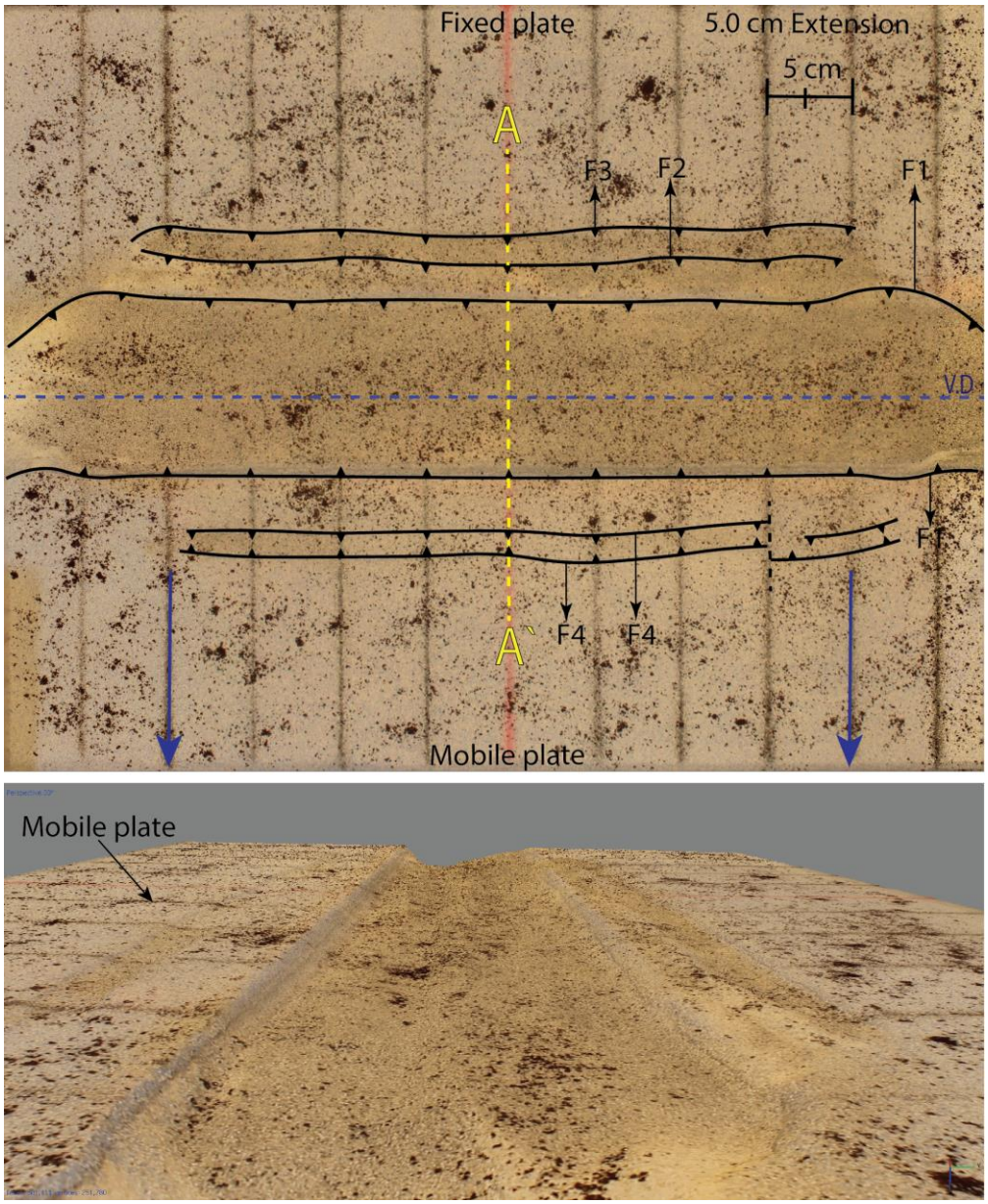

Figure 2.2.39. Top view of the experiment at 5.0 cm of extension (Orthomosaic image from Photoscan, 3827x2986, 0.151 mm/pix) and perspective view of the graben at 35°.

Extension phase DEM analysis

A DEM from the fully extended analogue model (5.0 cm extension) was constructed from the dense point cloud in Agisoft Photoscan. The DEM was exported from Photoscan and processed in ArcMap which yielded the maps below in figures 2.2.40 and 2.2.41. Most of the micro-topography that formed during the extension is not well visible in the top view photographs. Digital elevation models of the extension phase can reveal this micro-topography with very high detail and precision. The following can be observed in these digital elevation maps: (1) The deepest depression that formed has a depth of *-1.934 cm* below the surface of the analogue model. (2) Two very small depression are present above the immobile plate which are not visible with the naked eye during the experiments and is also not visible in the top view photographs. (3) Although Faults (F2) and (F3) are clearly visible above the immobile plate, it appears that both faults transform from two synthetic normal fault to a graben bounded by two antithetic normal faults in some parts of the model along strike, which is indicated by the presence of a horst (red colored ridge). Eventually the horst becomes very thin and disappears, which suggest there is a transformation back to a normal fault, this process repeats itself across the entire length of the model. (4) A small graben formed above the mobile plate delineated by (F4), followed by what appears to be a normal fault which is not visible in the top views. Most of these structures are larger than was inferred from the top view photograph analysis. (4) A small trench is present inside of the main graben and runs across its entire length. (5) The steepest faults formed above the immobile plate (Figure 2.2.41). (6) The slopes that formed above the mobile plate during extension are Southward dipping, while the slopes above the immobile plate have a northward dipping direction (Figure 2.2.41). (7) The small graben above the mobile plate nucleates at the flanks of the model attached to master faults (F1) and slowly migrates inwards, which leads to a ‘n’ shaped structure in the immobile plate and a ‘u’ shaped structure above the mobile plate.

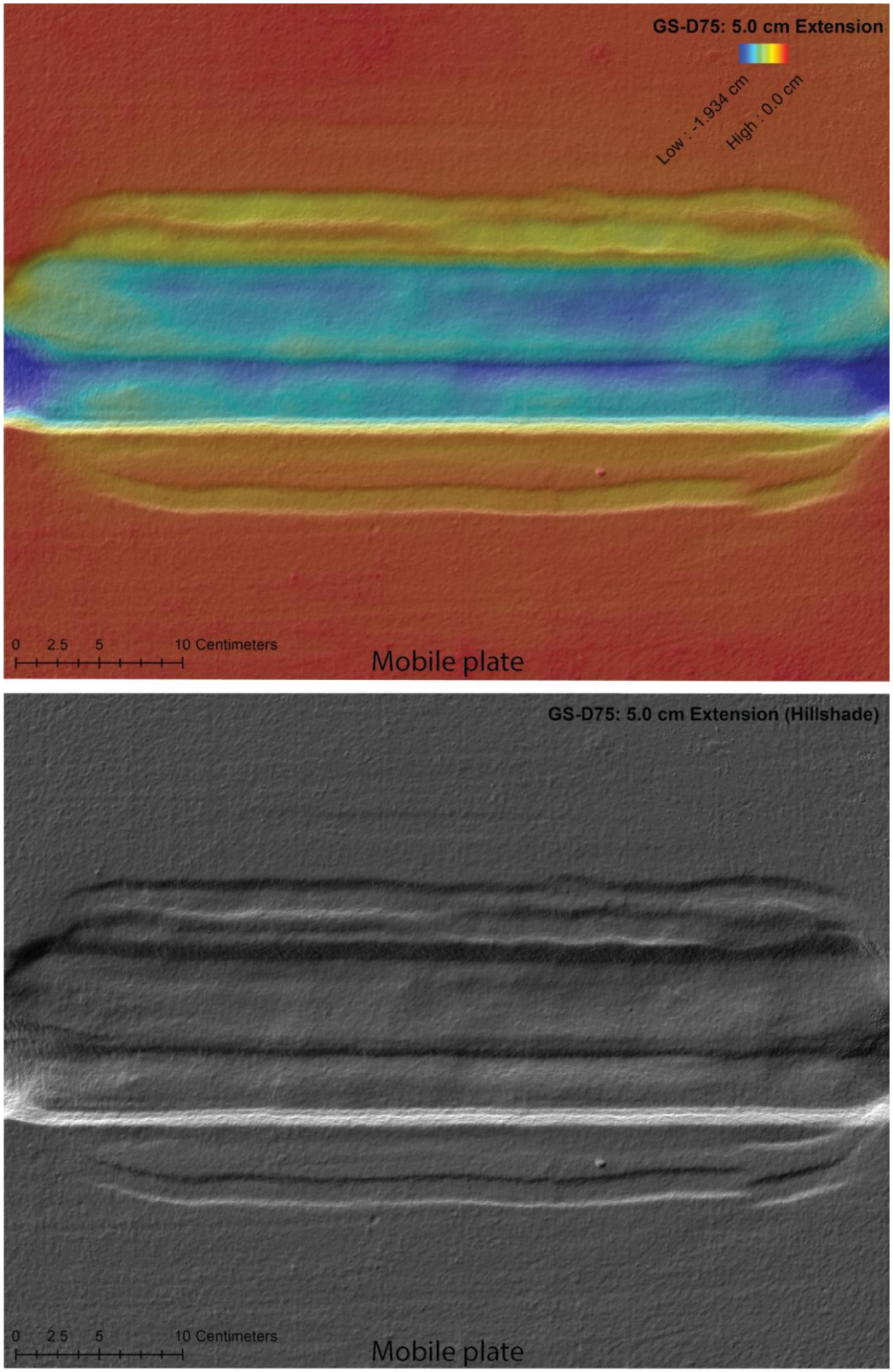

Figure 2.2.40. Digital elevation model and Hillshade analysis of the DEM produced at the end of the extension phase after 5.0 cm of extension (1777x1375, 0.302 mm/pix).

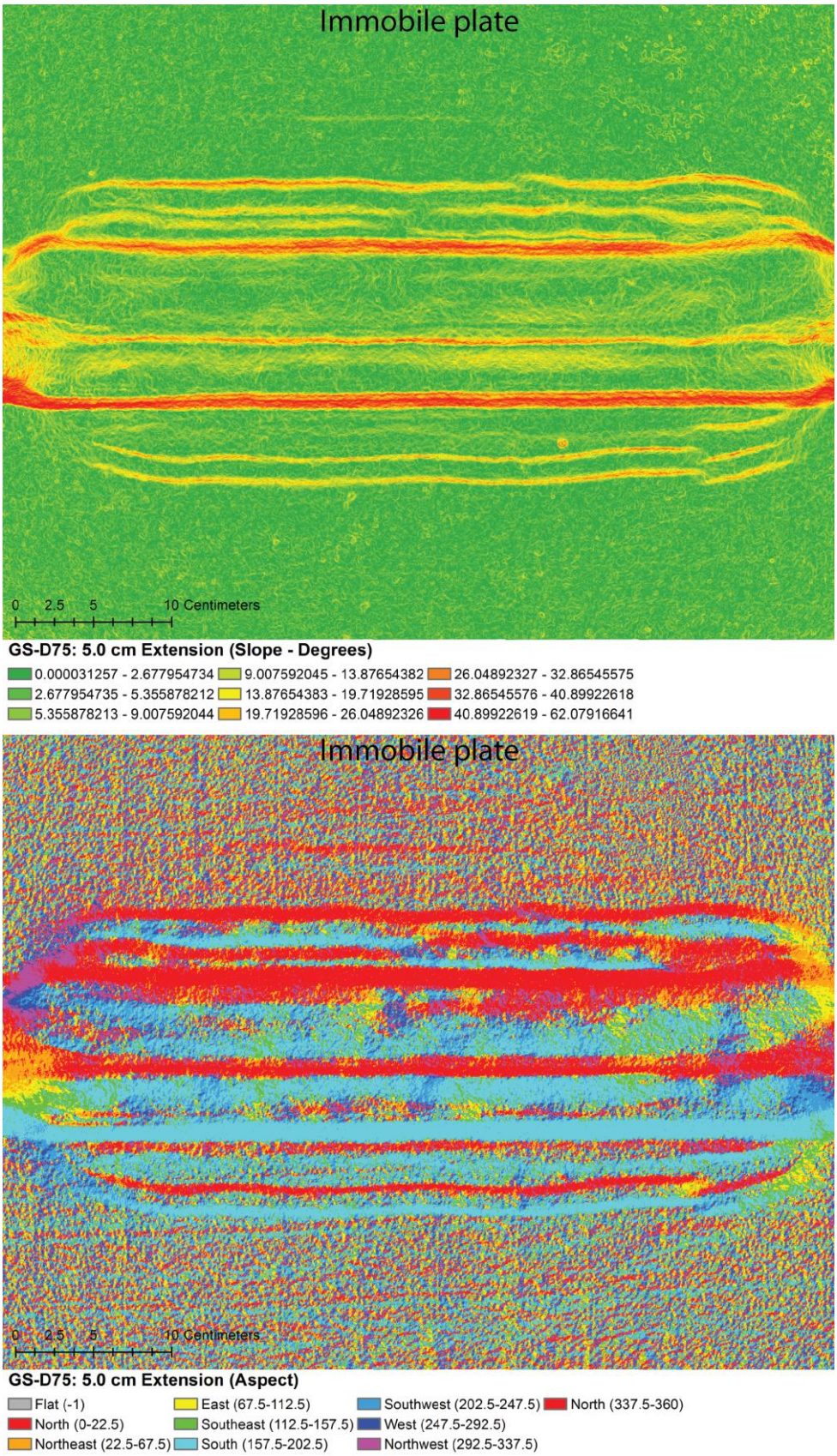

Figure 2.2.41. Spatial Slope and Aspect analysis of the DEM in ArcMap. 5.0 cm of Extension The aspect analysis represents the slope direction. The top of the Aspect images is the North direction. The bottom of the image is the South direction. 5.0 cm of extension.

After the extensional phase inversion is applied to the system (Figures 2.2.42 and 2.2.43). The textured 3D model compiled at the end of the extension phase can be visualized here: https://sketchfab.com/models/8a779230a1b8487fbb4649cd72e0cbbe

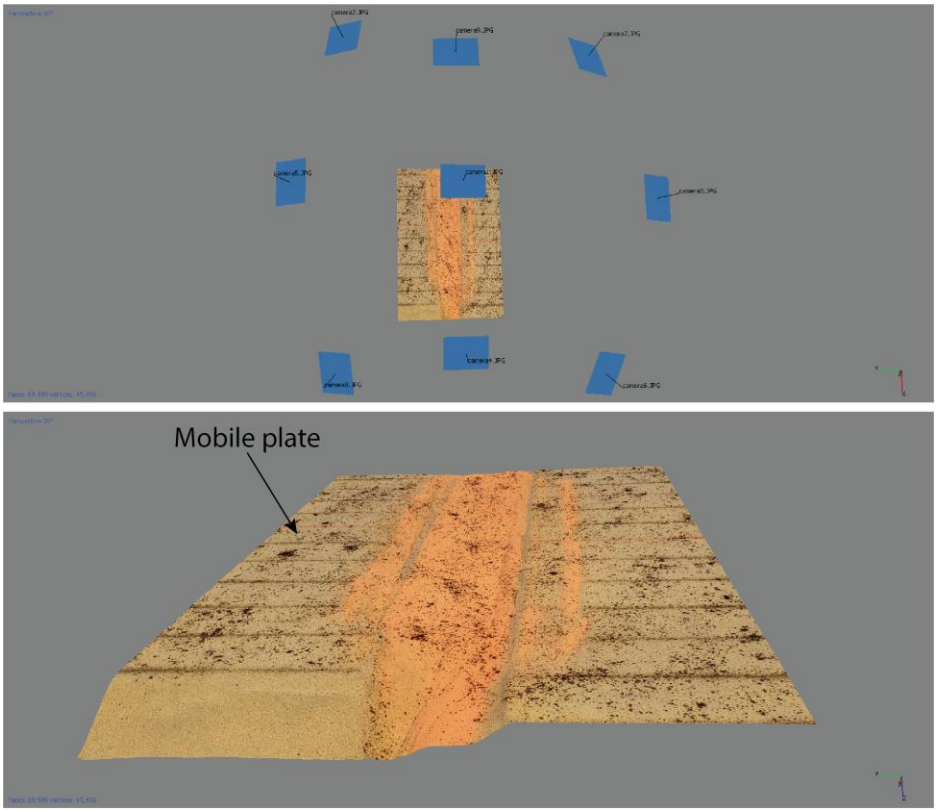

Figure 2.2.42. Screenshots of the 3D model in Agisoft Photoscan at 6.0 cm of inversion. 9x cameras, Sparse Cloud (190,450 points), dense cloud (10,212,950 points), Mesh (11,548,661 faces; 776,352 vertices).

The following observations can be made after analyzing the 3D model and the surface top views (Figures 2.2.42 and 2.2.43): (1) No thrust fault formation occurred, all displacement was accommodated by slip along the existing normal faults. (2) The central grid-line is displaced laterally *5.45 cm*, which indicates that most of the displacement was accommodated by strike-slip. Interesting to note is that this displacement magnitude is lower compared to the purely brittle model with the same angle of inversion, this stands in contrast to the previous ductile experiments. The accommodation of the displacement by strike-slip decreased the amount of positive topography produced at the end of the experiment. (3) Most of the topography formed above the mobile plate due to the inversion of fault (F1) in the hanging wall. The volume and surface area of the model were measured after 6.0 cm of inversion using Agisoft Photoscan, which yielded the following results:

Surface area: $0.364781\ m^2$
Volume: $-121.66\ cm^3$

Although the surface area of extension and inversion phases remained largely the same the volume of the graben after the inversion decreased slightly as the result of some positive

uplift. The volume remained “negative” as the graben is still a depression, in all other ductile experiments the volume remained positive.

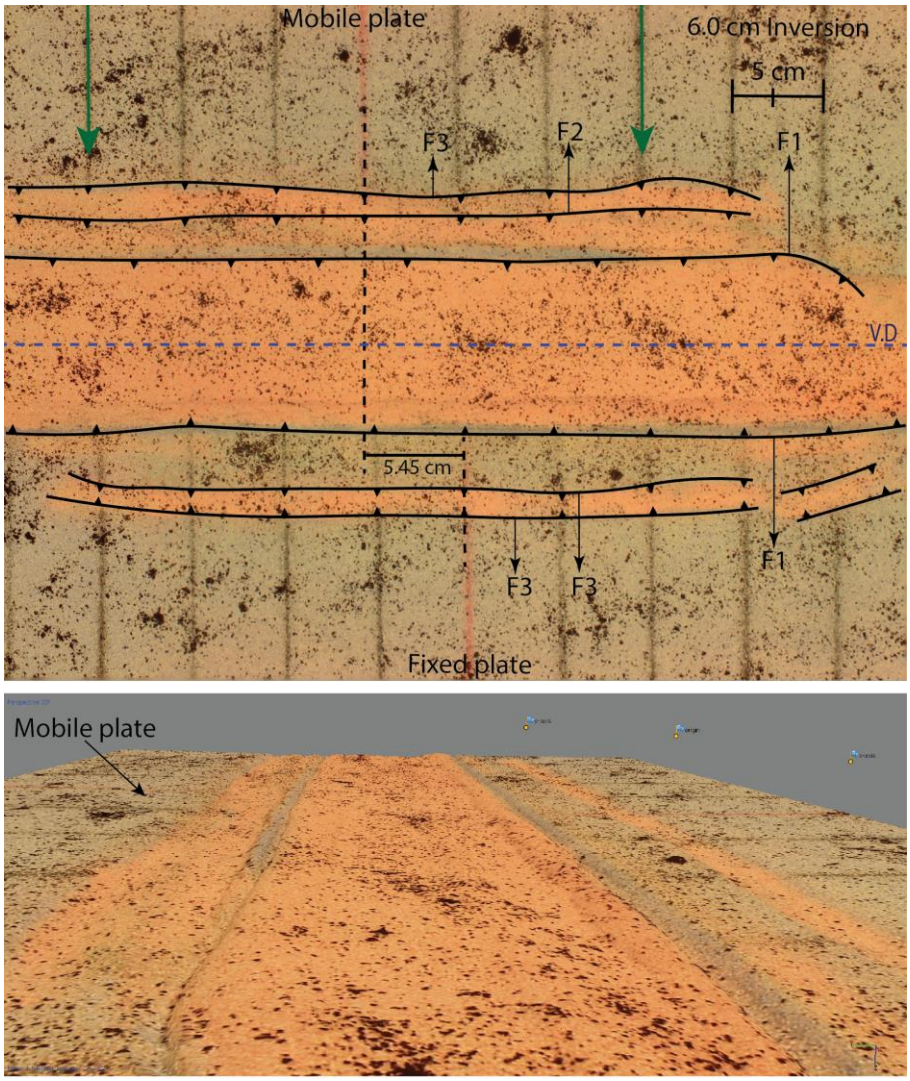

Figure 2.2.43. Orthomosaic top view of the analogue model at the end of the experiment after 6.0 cm of inversion (3500x2411, 0167 mm/pix) and perspective view of the inversion graben at 35°. Orthomosaic and 3D model constructed from 9x images.

Inversion phase DEM analysis

Photographs from 9x cameras were processed in Agisoft Photoscan, which yielded a 4D sequence of 1160x 3D frames for the entire deformation of the analogue model. For each frame a Sparse and Dense point cloud was compiled. For every dense cloud a DEM was exported and processed in ArcMap. Due to the large number of DEM's, the process of information extraction (Hillshade) was automated using ArcPy. A time-lapse for the analysis was produced and can be observed here: https://www.youtube.com/watch?v=_8UczF90rPc

Manual DEM maps were produced in ArcMap from the last frame (6.0 cm inversion) and are illustrated below in figures 2.2.43 and 2.2.44. Different types of spatial analysis tools were used for the DEM processing to allow both the qualitative and quantitative analysis of the topography produced. In total *0.202 cm* of maximum positive topography formed at the end of the inversion of the analogue model. This amount is much lower compared to ductile experiment with shallower angles of inversion, which is to be expected as the strike-slip component increases with increasing angles of inversion. It should be noted that most of the highest topography is produced outside of the ductile zone. The following can be observed in the digital elevation model analysis figures below: (1) A complex low-lying zone is present above the moving plate (discussed in the extension DEM's) which is characterized by an exchange between two synthetic normal faults and a graben delineated by two antithetic faults. Comparing the DEM of the inversion phase to the DEM of the extension phase it appears that this zone suffered a large lateral migration due to the extensive strike-slip component. A single small graben is also visible above the immobile plate which is less well visible to the naked eye. (2) No shortcut faults formed during the inversion phase. (3) A ridge is present inside of the main graben and runs across its entire length, the formation of this ridges is most likely linked to the deformation and faulting of the sedimentary cover. (4) The steepest ridges (highest slope angle) formed above the mobile plate (Figure 2.2.44). (5) The strain distribution throughout the model deformation was not uniform. (8) Most of the ridges of the model have a Southward or Northward dipping slope direction (Aspect spatial analysis).

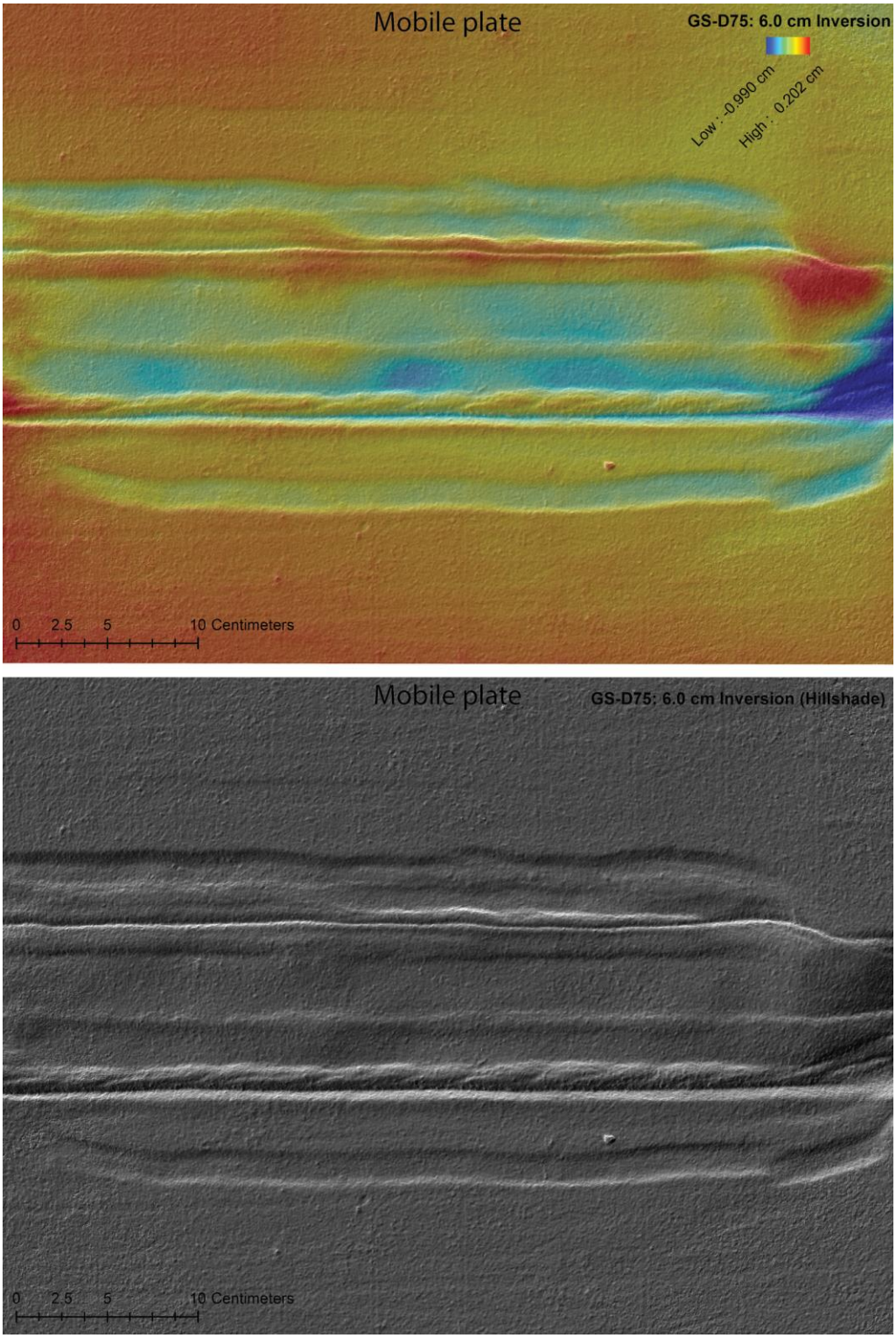

Figure 2.2.44. Spatial Hillshade analysis of the DEM (2998x2230, 0.166 mm/pix) in ArcMap. Top image consists of a color ramp combined with a 40% transparent overlay of the pure Hillshade grey image. The grey image is a pure Hillshade spatial analysis map (no transparency). 6.0 cm of inversion.

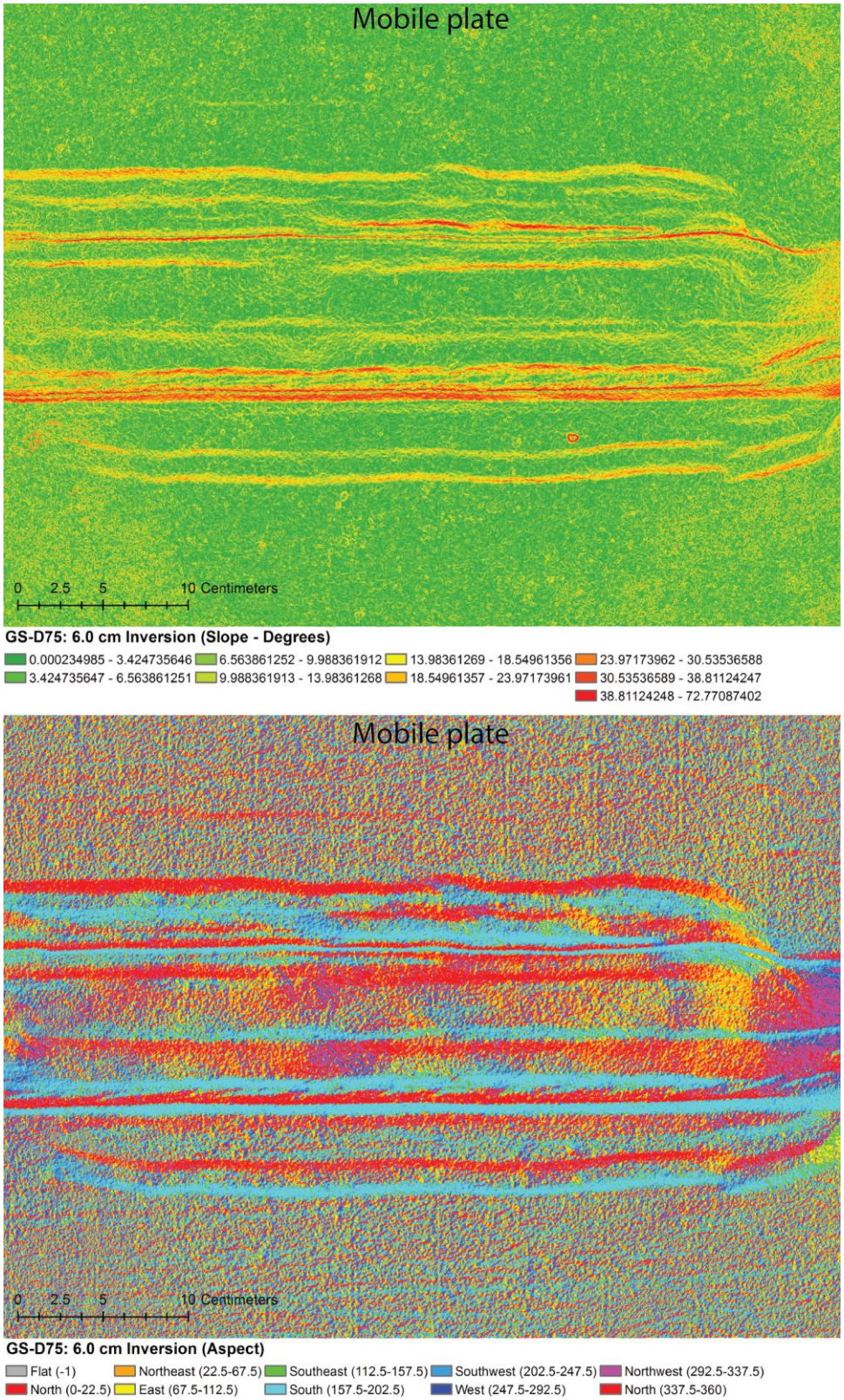

Figure 2.2.45. Spatial Slope and Aspect analysis of the DEM in ArcMap. 6.0 cm of inversion. The aspect analysis represents the slope direction. The top of the Aspect images is the North direction. The bottom of the image is the South direction.

Depth and Height profiles

Computed Depth profiles measured in the center of the analogue model are illustrated below in figure 2.2.46. The depth starts at *1.4 cm* as this is the distance from the markers to the surface of the analogue model. Graph (a) corresponds to the completed extension phase while graph (b) corresponds to the completed inversion phase. The formation of the trench is clearly visible in graph (a) as a sharp depression at *15.0 cm*, this trench corresponds to the V.D. At *5.0 cm* in (a) we have the depression between fault (F3) and (F1). At *22.0-25.0 cm*, we have the graben delineated by faults (F4). The total depth of the graben after the inversion is now only about *0.4 cm* and thus the scale of the topography increases compared to (a). Both depressions on each of the plates is visible as in (a), however, now a secondary peak is visible in the depression above the mobile plate. After this depression, a large peak *(0.3 cm height)* is present which corresponds to the reactivation of Fault *F1* in the hanging wall.

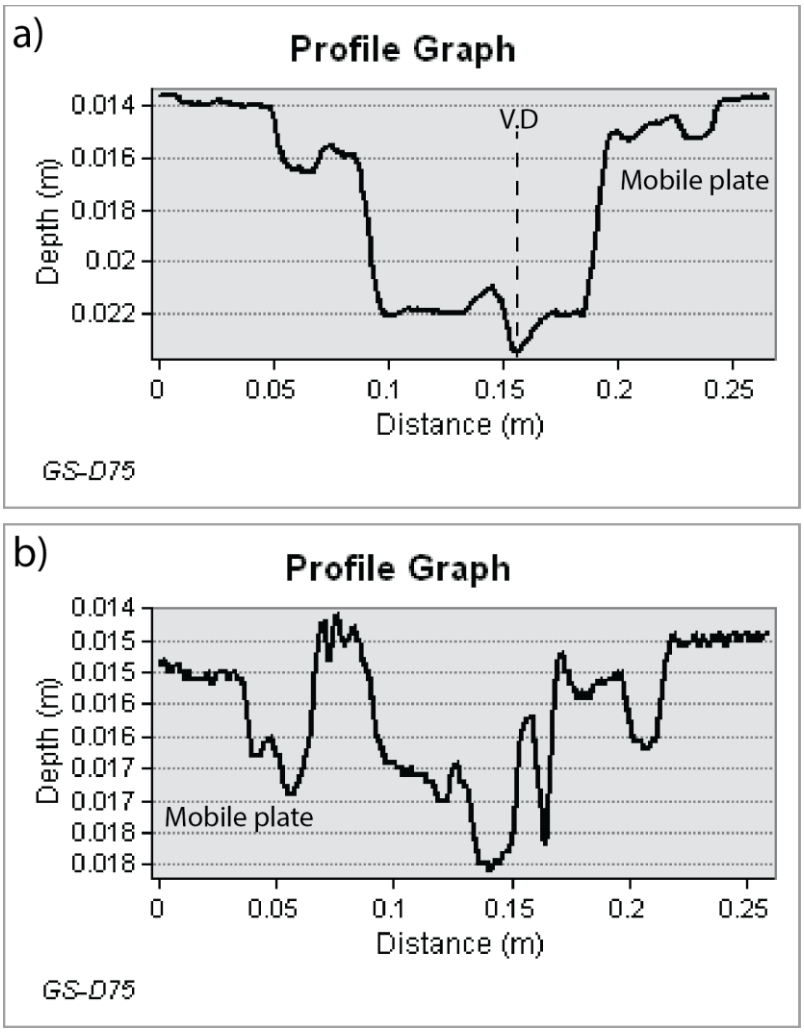

Figure 2.2.46.Computed height profiles measured at the center of the analogue model (same orientation as cross-sections) at 5.0 cm of Extension (a) and 6.0 cm of inversion (b).

PIV analysis

PIV vector and vector magnitude analysis was carried out of the inversion phase using undistorted images exported from Photoscan, the analysis using these photographs yielded much higher quality results due to the correction for lens distortion and camera tilt. Due to the motor-driven deformation at *6 cm/h* and photographs taken every 7 seconds, the displacement between each two frames is very small and thus the magnitude of the vectors is almost zero. For this reason, it was decided to take every 5th image to increase the displacement between each frame but still to keep a high enough resolution.
This resulted in a frame sequence that was imported into PIVlab for analysis. The image sequence was compiled into a time-lapse at 2 FPS. The time-lapse of the vector analysis can be found here (https://www.youtube.com/watch?v=nXXo9kRX3Ic) and the vector magnitude analysis can be found here (https://www.youtube.com/watch?v=ae_Jv9dovUA).
The figure below illustrates both PIV analysis techniques at 3.0 cm - (a) and 6.0 cm of inversion - (b). The following can be visualized in both the time-lapses and figure 2.2.47 below: (1) The displacement velocity and magnitude decreases from the hinterland to the foreland. (2) The vectors above the mobile plate have a 75° angle relative to the extension direction, which corresponds to the inversion angle (α). (3) The vector magnitudes inside of the graben are just slightly lower compared to the vector magnitudes above the mobile plate, which indicates that little strike-slip accommodation accrued in the gaming-wall. Almost all strike-slip displacement was accommodated at border fault (F1) in the footwall (Figure 2.2.49). Indicating that the velocity decoupling was maximum between the graben and the immobile plate. (4) The vector field tends to align parallel to the velocity discontinuity. (5) The vectors above the immobile plate display a slightly clockwise rotation. (6) The graben remained overall symmetrical throughout the inversion phase and no large vector field fluctuations occurred. (7) The vector magnitude of the rift basin remains uniform throughout the inversion phase, indicating that there was little preference to reactivate specific faults within the graben infill.

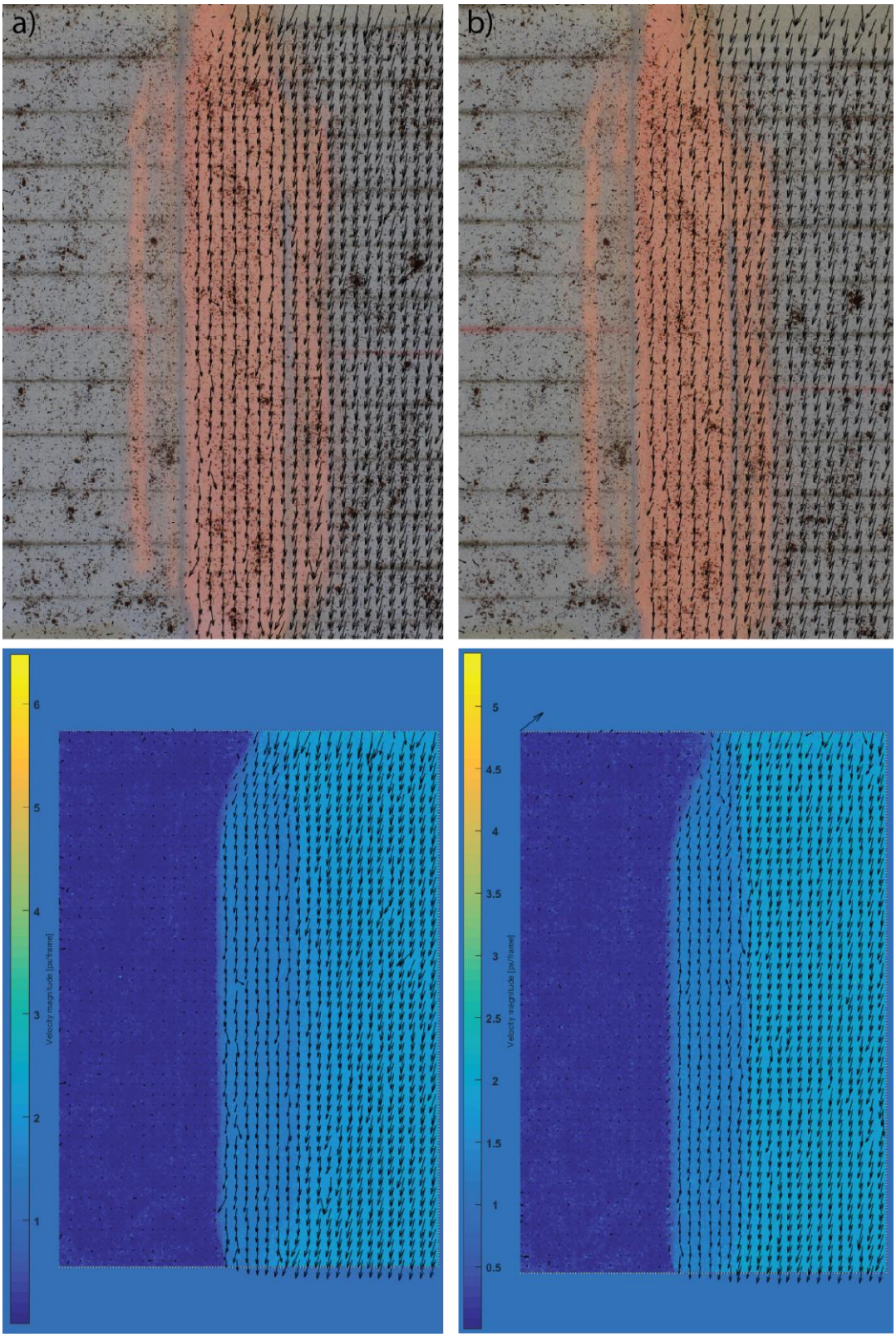

Figure 2.2.47. Vector and Vector magnitude analysis (pixels/frame) at 3.0 cm - (a) and 6.0 cm - (b) of inversion.

Histogram plots in (a) - figure 2.2.48 illustrates three main zones with peaks of highest vector magnitude at 0-0.3 pixels/frame (‘immobile’ plate), 1.3-1.5 pixels/frame (graben) and 1.7-2.2 pixels/frame (mobile plate). These values vary slightly compared to the histogram in (b), however, the pattern remains similar. From these plots, it can be observed that the there was a velocity decoupling between the graben and both plates, which suggest that extensive displacement occurred along the master fault (F1) in the footwall. The largest gap between the two peaks is present between the immobile plate and the graben, which indicates that the velocity decoupling was maximum, this supports the statement above that the highest strike-slip displacement occurred at master fault (F1) in the footwall. The scatter plot illustrates the orientation of the vectors at both 3.0 cm and 6.0 cm of inversion. The scatter plot also proves that almost all strike-slip was accommodated at fault (F1) in the footwall as the patters remains relatively circular. This also indicates that almost no strike-slip occurred at (F1) in the hanging-wall.

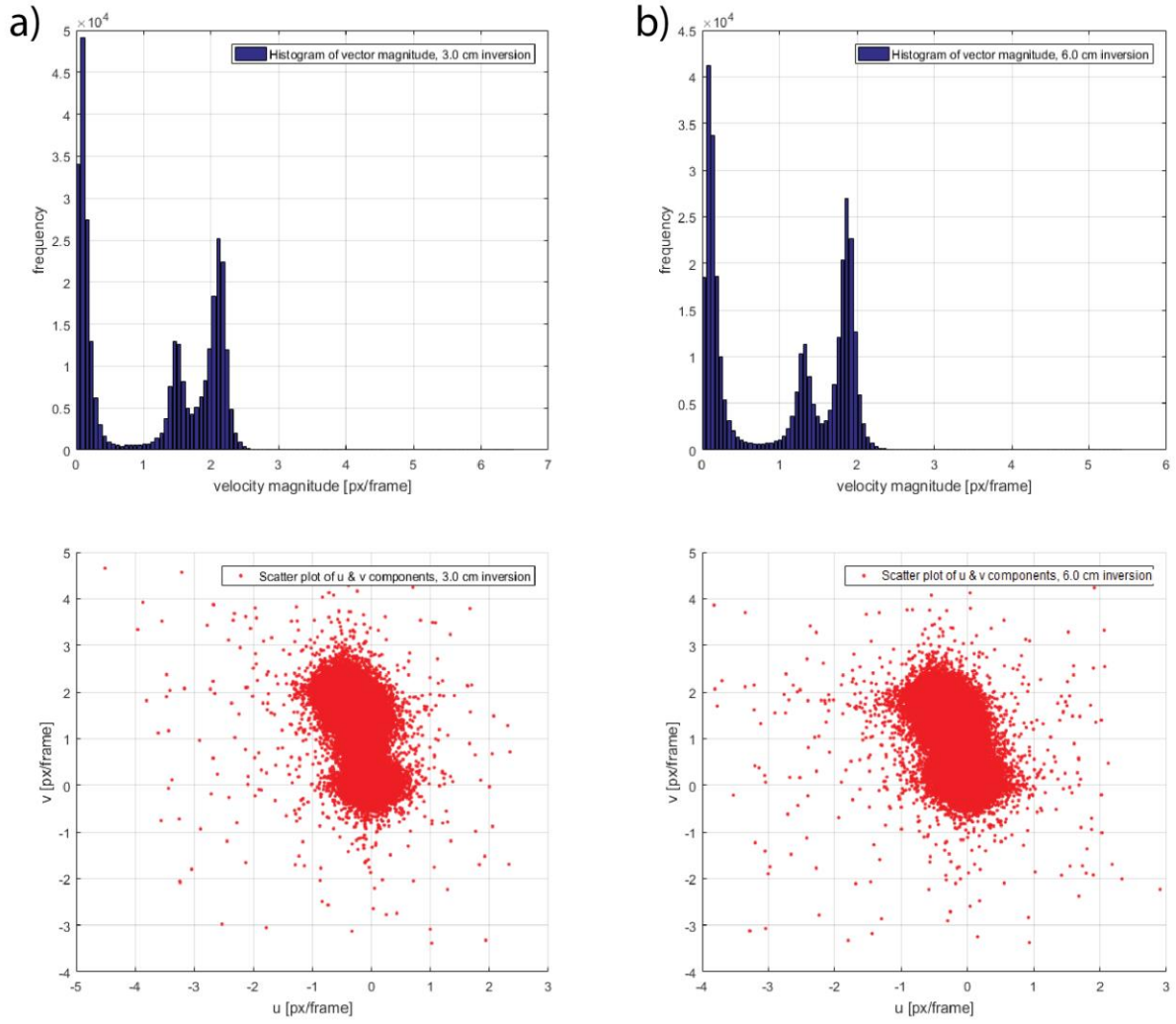

Figure 2.2.48. Histogram and scatter plots of the PIV analysis at 3.0 cm (a) and 6.0 cm (b) of inversion.

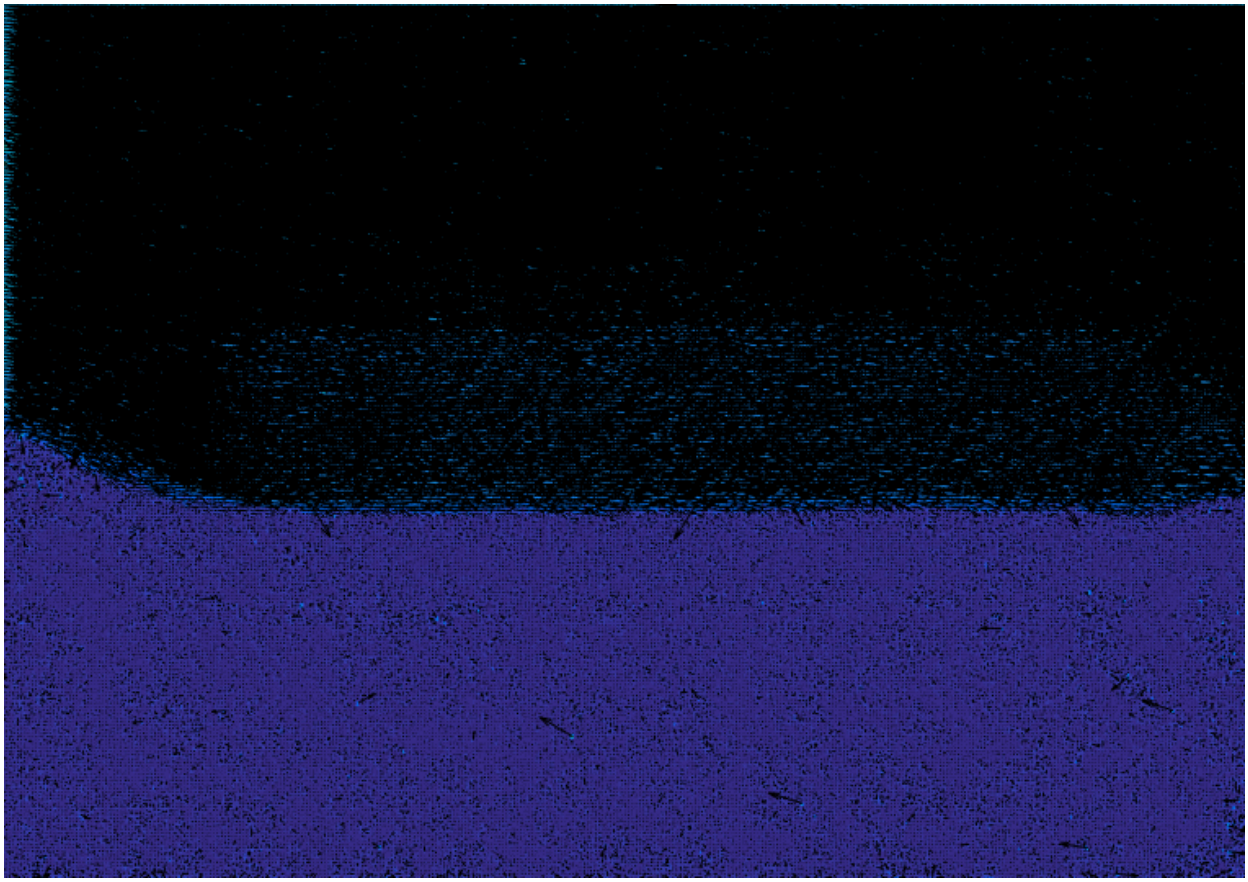

Figure 2.2.49. Densely packed vector field from the velocity magnitude analysis at 6.0 cm of inversion. No displacement is transferred to the immobile plate, most displacement is accommodated by (F1) in the footwall.

Cross-section analysis

The cross sections illustrated below in figures 2.2.42 and 2.2.43 are taken at the end of the experiment after 6.0 cm of inversion. The cross sections are taken oblique to the graben. CUT 13 - (a) was taken close to the end of the ductile layer, CUT 2 - (b) was taken at the beginning of the analogue model, CUT 6 - (c) was taken in the center of the analogue model (A - A'). The following can be observed in these cross sections: (1) The silicon layer acts as a decollement, decoupling the sedimentary cover from the sedimentary basement. (2) The sedimentary cover is characterized by extension which extends on both sides outside of the graben (Brun and Nalpas., 1996). (3) The décollement transfers the extension horizontally by thinning of the silicone layer. (4) Master normal faults (F1) were the first faults to form, they nucleated in the basement and propagated to the sedimentary cover, however, both faults (F1) in the basement and in the sedimentary cover were not allowed to become hard-linked during the initial phase of growth due to the presence of the décollement. The most extensive amount of normal faulting occurred in the sedimentary cover, which led to the formation of normal faults (F2) and (F3) above the mobile plate in (b), a graben delineated by faults (F2) and a normal fault (F3) in (c). Above the immobile plate normal fault (F4) and a graben delineated by (F5) formed in (b), in (c) only a graben developed above the immobile plate bounded by faults (F4). (4) The décollement is thicker above the mobile during inversion and thinner above mobile plate during the extension phase, this can be related to the flow of the ductile layer away from regions of highest stress. (5) Excessive extension

caused the décollement in the footwall to rupture which resulted in the hard-linking of the master fault. This thinning was less in the hanging-wall during the extension and only soft-linkage occurred. (7) simple shearing of the décollement was extensive during the rifting phase as can be seen by the drag features present in the ductile layer. (8) The rupture of the décollement and linkage of Fault (F1) started below the ductile layer in the vertical center of the analogue model (9) Extensive structural collapse is present inside of the brittle graben sedimentary cover that led to extensive faulting and the formation of a synclinal structure above the décollement. (10) Fault (F1) in the hanging wall in all sections shows a vertical reverse slip components. (11) Sedimentation through time increased the sediment loading, which not only further promoted lateral flow and thinning of the ductile layer, it also forces the ductile section bounded by the brittle basement faults to sink towards the V.D as no new sediment can penetrate the ductile layer to fill the newly created space by rifting, allowing only downward and minor lateral spreading movement. (12) On both sides of the graben the ductile layer is much thicker compared to the overall thickness of the layer across the whole section, this thickening led to the formation of ‘salt walls` and minor diapirism. No thrust fault formation occurred during the deformation phase, all deformation was accommodated by strike slip, inversion and rotation of normal faults. It must be noted that less vertical reverse slip occurred compared to the experiment with α = 45 °.

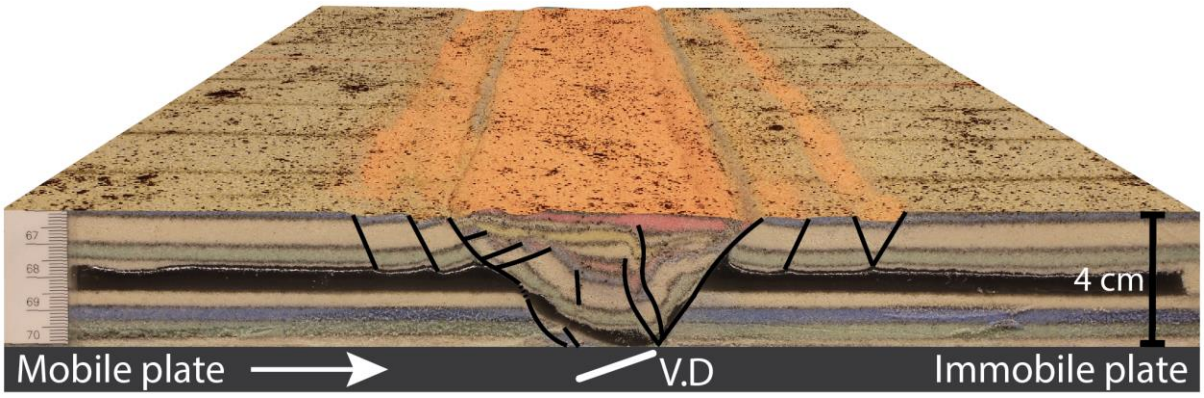

Figure 2.2.50. Combination between the cross-sections in figure 2.2.51 and the 3D surface model in figure 2.2.42.

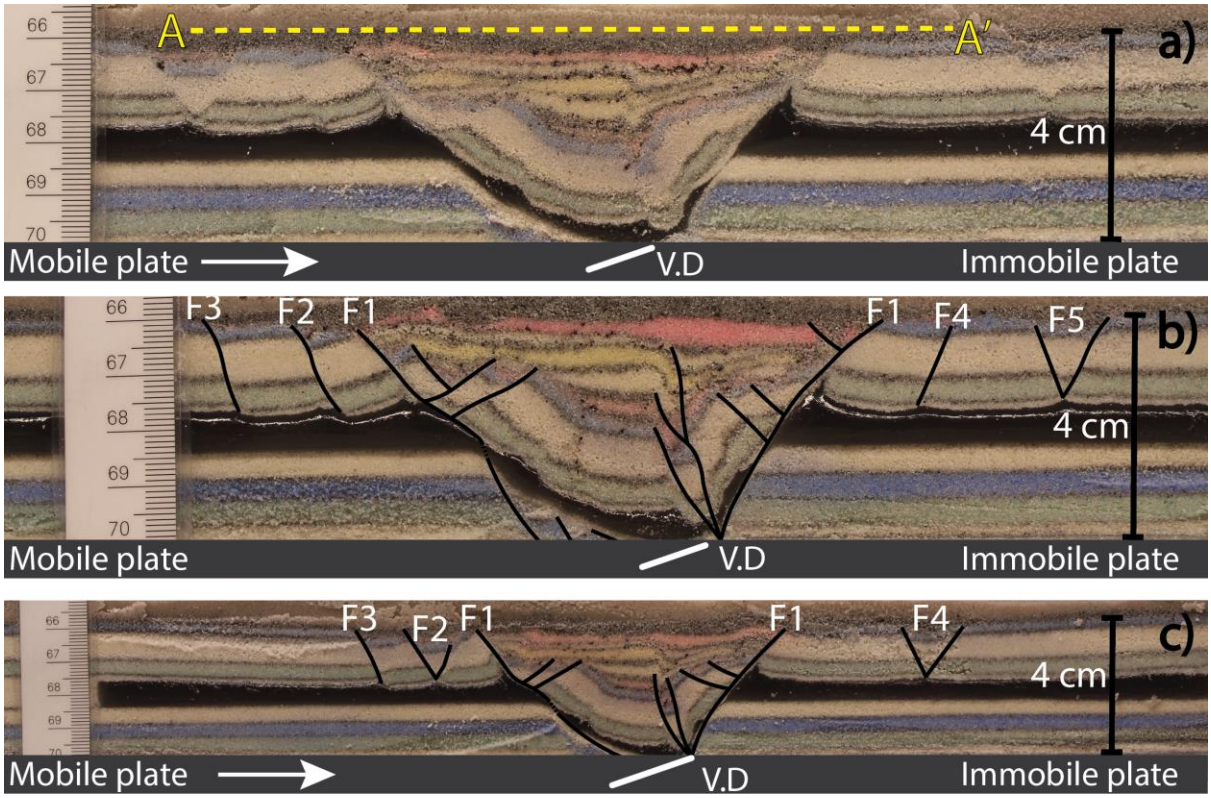

Figure 2.2.51. Cross sections taken after 6.0 cm of inversion. Sections (a) and (b) are taken at two different positions and show slightly different structures and thus slightly different descriptions of the fault patterns. The black lines represent the normal faults. The red lines represent the thrust faults.

Inversion phase DEM interpretation

Below in figure 2.2.52 an interpreted DEM is illustrated that was constructed with the information extracted from the cross-sections. A shear band with a “en échelon” pattern is present above in the footwall bounded by normal fault (F1) and a secondary fault within the graben infill. The shear band zone is continuous across the entire length of the fault. This band is not present above the mobile plate in the hanging wall. From previous experiments, it was found that the ductile layer ruptured during the extension phase because of the extensive movement along fault (F1) in the footwall, which allowed the hard-linkage of the two fault sections in both the cover and the basement. This linkage increases the coefficient of internal friction as now shear stain can be transferred from the basement to the sedimentary cover. The formation of the shear bands is most likely linked to the shear strain transfer from the basement to the sedimentary cover. The fault system that formed above the immobile plate during the extension phase is more complicated than was expected, multiple fault systems are present inside of this small depression and there is a lateral change in structure, which occurs at the zone delineated by the white line.

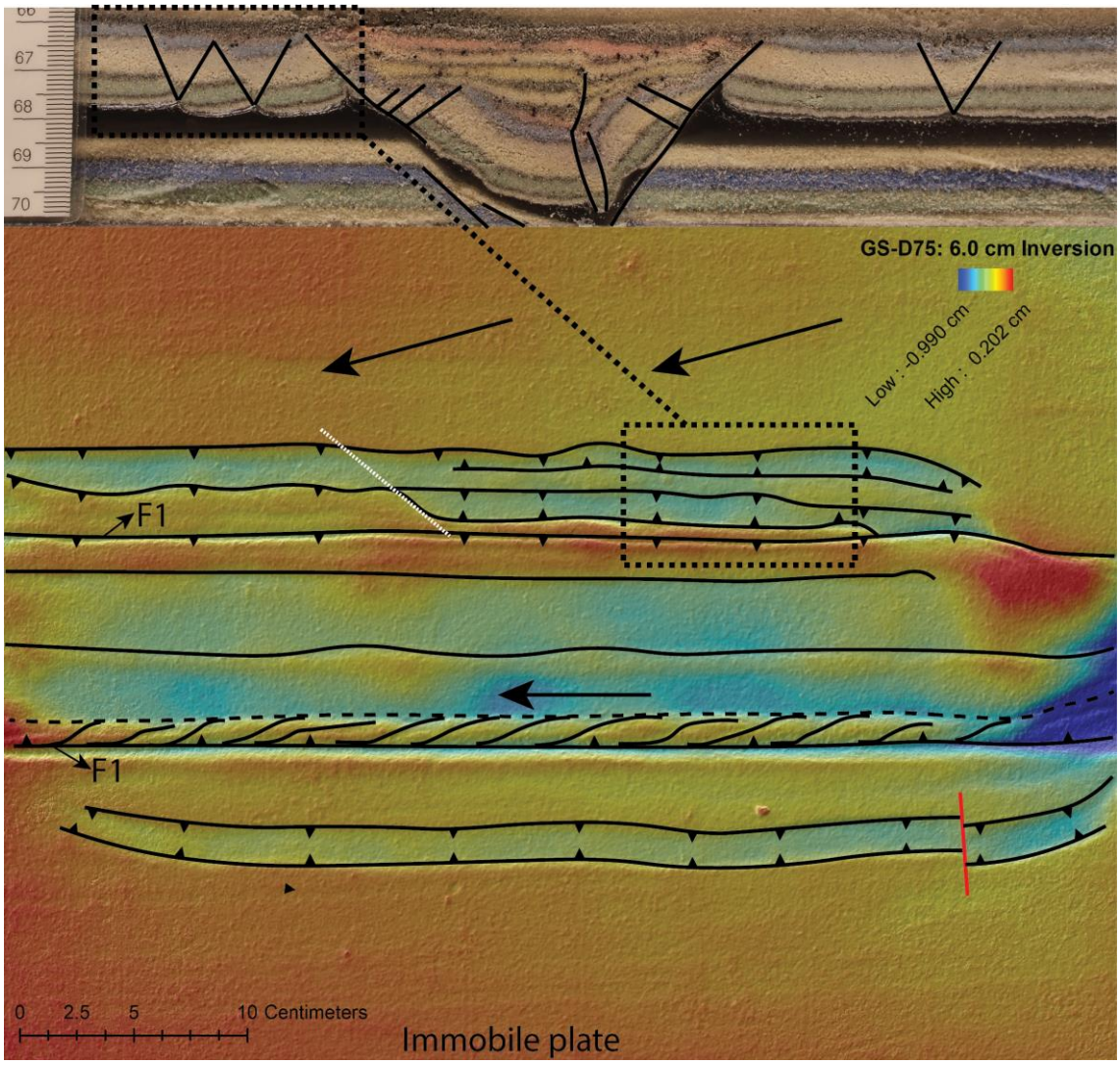

Figure 2.2.52. Interpretation of the inversion DEM (color ramp and Hillshade) at 6.0 cm of inversion.

3 Discussion

In the following section the experimental results will be discussed.

3.1 Brittle models

The basement and cover of the brittle models have the same mechanical properties, which implies that there is no decoupling between the basement and sedimentary cover. The following can be inferred from the result analysis:

Extensional regime

The geometry of the formed rift structures during the extension phase remains largely consistent across all experiments, however, the geometry of the rift master faults illustrates some along-strike variation in fault geometry (see 3D extension models: https://sketchfab.com/TecLab; Gabrielsen et al., 2015). Minor variation in surface geometry is present because of the different degrees of syn-tectonic sedimentation, which influences the stability of the sediments during the extension. Normal faulting during the extension phase occurs 'in-sequence' starting at the hanging-wall and slowly migrates towards the footwall, forming a domino fault system with rotated blocks (Figure 2.1.10; Elena et al., 2007). PIV analysis of the extension phase shows that the sequential normal faulting immobilizes the previously formed normal faults and promotes the formation of new normal fault to accommodate the extension (Figures 2.1.7 and 2.1.8). The surface geometry of this faulting pattern is characterized by *ramp-flat-ramp* systems with relay ramps and transfer faults (Figures 2.1.3 and 2.1.10; Beauchamp, 2004). The relay ramps are of interest as they provide pathways by which sediments can be transported into the graben (Athmer et al., 2010). The geometry and surface morphology of the formed rift basin influences how sediments are transported into the basin and where the largest sediment accumulation occurs. Across all brittle experiments, it was found that the deepest depression formed at the bottom of the footwall (see 3D extension models). As extension progresses and the graben widens, it is in this deep zone where new accommodation space is created for sedimentation to occur. More however, it also leads to a greater instability of the steep slope and promotes slumping of sediments into the graben. Important to note is that the extension direction remained the same during the extension phase, in natural experiments however there can be fluctuations in the extension angle which will largely alter the geometry and morphology of the rift system and will ultimately influence the degree and mechanism of sediment intake

Effect of variable angles of inversion on reverse dip-slip

Variable angles of inversion have a large effect on the deformation style of the analogue models.
As the inversion angle (α) decreases, the width of the deformation zone, the amount of maximum uplift and the number of thrust faults increases. At low angles of inversion ($0° \leq \alpha \leq 15°$), only the rift master normal faults show slight dip-slip reactivated due to bulk

horizontal shortening (e.g. Figures 2.1.18 and 2.1.19). Only during the first stages of shortening doe reactivation of the steep graben master normal faults occur (e.g. Elena et al., 2007). Most of this shortening is accommodated by the master the graben border fault in the hanging-wall. Examples of the reactivation of steep normal faults bordering the grabens include the eastern Sunda shelf (Letouzey et al., 1990).
No reactivation occurs within the rift basin at these low inversion angles (Elena et al., 2007). Most of the inversion displacement is accommodated by the formation of thrust faults, both basement rooted and shortcut thrusts which are non-basement rooted (e.g. Brun and Nalpas, 1996; Jagger and McClay, 2016; Coward et al., 1991). All newly formed thrusts formed outside of the inverted graben and rotate to become flatter throughout the inversion phase (Figures 2.1.19 and 2.1.29; e.g. Elena et al., 2007; Mitra, 1993; Panien et al., 2005; Eisenstadt and Withjack, 1995). These thrusts cut-off pre-existing normal faults during inversion and prevents extensive normal fault reactivation (Panien et al., 2005). Hinterland-dipping normal faults will favor the development of foreland-directed thrusts, while early foreland ward-dipping normal faults would favor the formation of back-thrusts (Cooper et al., 1989). The largest number of thrust faults formed as forethrusts, the throw of each individual forethrust is lower compared to the throw of each individual backthrust. However, the total throw magnitude of all forethrusts combined is still greater. This indicates that more extensive uplift occurred in the hanging-wall during inversion. PIV analysis supports this as it demonstrates that there is a large velocity decoupling between the graben infill, footwall and hanging-wall (Figures 2.1.16, 2.1.17, 2.1.25, 2.1.26 and 2.1.27). This is the result of variable thrusting magnitudes between both the forethrusts and backthrusts and causes the entire graben to slowly rotate towards the foreland. The asymmetry of the thrust faults also increases significantly as (α) decreases, which leads to branching thrust faults and different throw magnitudes along strike (Figure 2.1.15). Forethrusts tend to be steeper than backthrusts and thus the horizontal vector velocity increases as the thrust fault angle becomes shallower. The largest throw along strike occurred close to the center of the analogue model (purple grid line), decreasing to the extremities of the graben. An imaginary inclined symmetry line passing through the center of the model separates the two model halves by the velocity discontinuity where the largest thrust fault throw occurred (Figures 2.1.14 and 2.1.15). It appears that on the model halve where the throw was largest, the throw was smallest on the opposite half, which is then mirrored downwards. This indicates that there is a large stick-slip component present in the system along strike. The master fault detachment from the basement exerts the primary control on both the lateral variation of hanging wall deformation and related along-strike component of material transfer (Yamada and McClay, 2003b).
As (α) increases, the formation of basement rooted thrust faults gives way to forethrust shortcut faults which produce significantly less uplift.
For $\alpha \geq 45°$ significant dip-slip reactivation occurs. Although most of the reverse dip-slip occurs at the experiment with $\alpha = 75°$, the experiment with $\alpha = 45°$ does demonstrate some reactivation of the domino-block fault system, however, the border faults do not appear to have been significantly reactivated (Figure 2.1.36). For $\alpha = 75°$, the largest reactivation magnitude mainly occurs along the rift border normal faults (Figure 2.1.50) and along the normal faults inside of the graben (Figures 2.1.48 and 2.1.50) where the cover is thick (high confining pressure), which gives rise to moderate to high angle reverse faults (Nalpas et al., 1994; Letouzey et al., 1990). These faults rotate to become oblique to the principal strain axis, which eventually locks the faults. Thus far, fault reactivation was mainly a function of

the steepness of the normal faults and the confining pressure. Although there has been significant debate regarding the influence of steepness of the normal faults on reactivation potential, it was shown that reverse dip-slip can occur at both high-and-low angle normal faults, indicating that the factors influencing reactivation potential are more complex, for example fault weakening and fault length (e.g. Mandl, 2000; Koopman et al., 1987; Marques and Nogueira, 2008). The brittle experiments carried out in this study contained normal faults that fit the *steep* normal fault category (50-75°). The advantage of steep normal faults is the fact that less cohesion of the material is necessary, as cohesion is created artificially due to the downward gravitational pull that naturally causes fault block to stay intact. The disadvantage however is that the fault plane is rotated away from the principal stress axis which gives high angle normal faults a lower reactivation potential and lifespan. Some studies showed that the Inversion of normal faults depends on their initial geometry and orientation with respect to the direction of contraction (Etheridge, 1986; McClay, 1989; Holdsworth et al., 1997; Walsh et al., 2001). Etheridge (1986) showed with theoretical studies that the primary parameters controlling fault reactivation include the contrast in cohesive and frictional strengths between intact and previously faulted rocks. Analogue model experiments were later carried out to confirm the theoretical results (e.g. Cooke and Harris, 1987; Buchanan and McClay, 1991; Yamada and McClay, 2004). Dubois et al. (2002) showed that another important factor influencing reactivation is the age of the normal faults, it was shown that older faults were less likely to reactivate due to the internal cohesion loss throughout deformation of the analogue model.

Effect of variable angles of inversion on reverse strike-slip

Due to the existence of strike-slip faults within the graben which are *oblique* to the rift borders, the rift boundary master thrust faults developed with different patterns and display different throw degrees along strike (GS-B90, GS-B15; Brun and Nalpas, 1996), the result of this phenomena is discussed in the section above. As the inversion angle increases, so does the strike-slip magnitude parallel to the rift borders. For experiments with $\alpha \geq 75°$ Riedel shear bands form that are characteristic for dextral strike-slip during graben inversion (Figures 2.1.43 and 2.1.44; Sylvester, 1988; Nalpas et al., 1994). A large strike-slip fault also develops in the center of the graben for $\alpha = 75°$ (Nalpas et al., 1994). Compared to reverse dip-slip, detection and quantification of strike-slip along individual faults is a difficult task as it is not easily detected in cross section analysis. Surface observations and PIV analysis played a large role in extrapolating the along strike movement of the formed faults. As the inversion angle increases, most strike-slip tends to be accommodated by the master normal fault in the hanging-wall above the mobile plate (Figure 2.1.45), and less displacement is accommodated along the faults towards the footwall. This indicates that the strike-slip displacement is progressively filtered out and thus very little displacement along strike is transferred to the footwall. This indicates that significant less activation energy is present to kick-start the reactivation process.

3.2 Brittle-Ductile models

Many of the factors influencing thrust fault formation and normal fault reactivation described above also apply to the ductile models, below are some points that were only observed in the ductile models.

Extensional regime

The rift-bounding normal faults formed by along-strike propagation and linkage of originally shorter, similarly dipping segments (e.g. Cowie et al., 2001). The rift master normal faults below and above the décollement in the footwall are firm-linked to hard-linked across all experiments (e.g. Figure 2.2.12). By continued extension, these normal faults transform from soft-linked to hard-linked. The border faults in the hanging-wall across all experiments remain soft-linked throughout the extension phase (Gabrielsen et al., 2015). Faults in the sedimentary cover most commonly nucleate close to the silicone polymer layer and grow up-section. Faults that formed in the sedimentary basement nucleated at the velocity discontinuity and also grew up section. Significant variances in the surface morphology of the rift basin exist between the different models (see 3D extension models). This phenomenon was most likely induced as a result of slight variances in thickness of the silicone layer and variances in the placement of the layer in the model construction. Significant less negative topography was produced in the brittle-ductile experiments compared to the purely brittle models as more displacement was transferred outside of the main rift zone towards the model flanks. Although less maximum negative topography was produced in the ductile models, the displacement was accommodated by a larger number of normal faults across a wider zone. This indicates that the presence of a décollement can significantly increase the number of normal faults that develop during extension compared to purely brittle models.

Effect of variable angles of inversion on reverse dip-slip

As was the case in the extension phase, the magnitude of maximum positive topography that formed is also lower compared to the purely brittle experiments (e.g. Figure 2.2.7). The cover thrust faults in these experiments also show significant less variation in throw along strike compared to the purely brittle experiments (e.g. Figures 2.2.5 and 2.2.6).
At $\alpha = 0°$ the deformation is localized at the graben borders by the formation of two cover thrust faults (R1 and R2; Figure 2.2.12). The same applies for the experiment with $\alpha = 15°$ (Figure 2.2.24). The most extensive dip-slip reactivation of the rift normal faults occurs at $\alpha = 45°$, which is also paired with extensive diapir formation (Figure 2.2.37; Koopman et al., 1987). More extensive reactivation occurs at the hanging-wall rift border fault which is also paired with a thicker ‘salt wall’ and more extensive diapirism. The reactivation is paired with upward brittle displacement and accumulation of material from the fault zone which produces a local positive elevation (sand ridge) in the hanging-wall (Figure 2.2.37). The formation of this local elevation forces the ductile layer upwards and ultimately uplifts the sedimentary cover above it. This mechanism could potentially facilitate fault dip-slip reactivation in the sedimentary cover. Flame structures formed in the ductile layer above the velocity

discontinuity which suggests extensive shearing of the ductile layer. Natural examples of these brittle-ductile environments include the Broad Fourteens basin and the Northern Apennines (Italy).

Effect of variable angles of inversion on reverse strike-slip

The strike-slip displacement magnitude of most ductile experiments is lower than that of the purely brittle experiments, which can be attributed to the decoupling of the cover from the basement and the inefficient transfer of shear strain to the sedimentary cover. The inversion angle and strike-slip magnitude are directly proportional ($0° \leq \alpha \leq 90°$), as the inversion angle increases so does the strike-slip magnitude.
The most extensive strike-slip displacement occurs for $\alpha = 75°$ mainly at the master normal fault in the footwall where the fault is hard-linked and shear strain can easily be transferred from basement to cover (Figures 2.2.47 and 2.2.49). For experiments with $\alpha \geq 75°$ Riedel shear bands form that are characteristic for dextral strike-slip during graben inversion (Figure 2.2.52; Sylvester, 1988; Nalpas et al., 1994).

3.3 Comparison

1. The most extensive dip-slip reactivation of normal faults in the purely brittle experiments ($\alpha = 75°$) occurred at faults inside of the graben where high confining pressure is present. The most extensive dip-slip reactivation in the brittle-ductile experiments ($\alpha = 45°$) occurred at the rift border faults where the thickening and upward pressure of the décollement assisted the reactivation. This indicates that the mechanism of reactivation of normal faults differs between the brittle and ductile experiments. Strike-slip reactivation occurred mainly at the graben master fault in the hanging-wall across both brittle and brittle-ductile experiments. This indicates that the accommodation of strike-slip motion is similar across both experimental model types.
2. Less thrust fault formation occurred in the brittle-ductile experiments compared to the purely brittle experiments because of the low strain rate permeability of the décollement that prevents the propagation of the necessary stresses for thrust fault formation to propagate to the sedimentary cover. Thrust faulting that occurred in the sedimentary cover always initiates in the sedimentary cover.
3. The deformation zone width of the ductile experiments is more extensive than that of the purely brittle models and is formed mainly during the rifting phase because of the formation of multiple small grabens at the flanks of the main graben as a result of décollement stretching. During the inversion phase the deformation zone of the brittle-ductile models is narrowed due to contraction of the extensional structures, while the deformation zone of the purely brittle models is widened as a result of thrust fault formation outside of the graben.
4. On average, less strike slip displacement was produced in the sedimentary cover of brittle-ductile models as a result of the reduction of shear strain transfer by the décollement to the sedimentary cover. Where the basement and cover border faults become hard-linked due to thinning and rupture of the ductile layer, shear strain in the form of strike slip will mostly accumulate which gives rise to Riedel shears at the

model surface. In the purely brittle models no decoupling occurs and all strike-slip displacement is directly transferred from the basement to the sedimentary cover.
5. Antithetic faults dipping away from the compressional stress direction did not reactivate during inversion in both model setups.

3.4 Implications

1. The inversion of syn-rift normal faults is favorable for maturation and trapping of hydrocarbons. Transfer zones, relay ramps and shear structures may influence the process of hydrocarbon migration and trapping (Wheeler, 1980; Morley et al., 1990; Peacock and Sanderson, 1994; Coskun, 1997; Turner and Williams, 2004).
2. Understanding of the surface dynamics of extended and inverted rift basins allows the accurate prediction of sediment pathways and transport mechanisms into the graben.
3. Relay fault systems and transfer fault zones developed over basement structures have been interpreted as controlling a broad variety of mineralization types and styles (e.g. Clendenin and Duane, 1990; Hulbert et al., 1990; White et al., 1995; Henley and Adams, 1992; Sibson and Scott, 1998).
4. The magnitude and extent of fault reactivation and basin inversion exert fundamental controls on hydrocarbon prospectivity (e.g. Macgregor, 1995; Withjack et al., 1998; Davies et al., 2004; Turner & Williams, 2004; Cooper & Warren, 2010; Bevan & Moustafa, 2012).
5. Basin inversion is a very efficient mechanism for producing large fluid overpressuring, the contraction of the sedimentary fill being expected to drive significant reduction of porosity and consequent relevant fluid expulsion (Bonini et al., 2011).

4 Conclusions

1- The main factors governing the reactivation potential of normal faults include: (1) pre-inversion fault steepness, (2) orientation of the fault with respect to the inversion stress, and (3) frictional resistance along the fault plane (e.g. Turner and Williams, 2004). The reactivation mechanisms vary largely between the purely brittle and the brittle-ductile experiments.
2- The silicone décollement simulates a synthetic upward 'fluid pressure' that reduces the frictional resistance for reactivation, which is especially significant in the reactivation of low-angle normal faults.
3- Normal fault reactivation is selective, only a few out of several faults with the same orientation and age have been reactivated. Fault weakness has been demonstrated experimentally to be a key factor in controlling fault reactivation.
4- The results of the experiments presented in this work suggest that dip-slip reactivation of moderate-to-high-angle normal faults can take place with notable up-dip displacement where fault weakness is related solely to sand dilatancy of precursor faults. These processes potentially involve: (1) syn-inversion rotation (to shallower dips) of pre-existing faults accomplished by shearing along the basal décollement, and (2) rotation of the principal stress axes.
5- High definition 4D monitoring of the surface micro-topography with dynamic Photogrammetry in contrary to traditional monitoring techniques can be implemented in the laboratory for a fraction of the cost and delivers much higher quality results, both spatial and temporal.
1. Room-scale Virtual reality (VR) observation of 3D reconstructed analogue models gives new insight into the linkage between the surface and interior of the analogue model, accelerating and increasing the final quality of analogue model analysis.
2. 3D printing of scaled analogue models can be used for a variety of purposes which include the use in secondary experiments, prototyping and educational purposes.

5 Some extra words

- The application of 4D Photogrammetry and Photogrammetry in general for Geological purposes has been scarce, only a few Geology papers used Photogrammetry as a surface monitoring technique and almost none used 4D photogrammetry. Interestingly these papers concluded that Photogrammetry is by far the best and most accurate surface monitoring technique if implemented properly, as it can also be used in the field. The lack of the use of photogrammetry can be attributed to the fact that only in recent years the algorithms and computer technology become powerful to process the results in a timely manner, and only very few labs are prepared to spend money on new technologies in which they have limited expertise. Every year higher resolution consumer cameras hit market that step by step increase the power of 3D photogrammetry reconstruction. I hope that in the near future more Geoscientist around the world will use this amazing technology to reconstruct and monitor a large array of geologic features and experiments.
- Room Scale Virtual reality (VR) and Augmented reality (AR) although in their infancy, will shape the future of 3D and 4D observational techniques in Geosciences, from fieldwork site prospecting to augmented reality experiments by combining reality with digital 3D overlays, the visualization of obtained 3D drone maps to the observation of laboratory experiments in a full immersive and interactive environment. Although costs are still high for true (VR), and (AR) such as the Microsoft Hololens has not hit the consumer market yet, it is imperative that the Geoscience community stays up-to-speed with these technologies and that we develop the necessary knowledge to be able to implement these technologies when and where necessary.
- 3D printing has been around for a long time, it is only recently that modern 3D printers can produce very high quality, resolution, cheap, and full color physical objects in a variety of materials ranging from plastic to steel. This technology is being used more and more by scientists around the globe, the number of application scientific papers and applications have skyrocketed in the last few years, ranging from the 3D printing of tissue, 3D printing of fossils, to the printing of mechanical parts onboard the international space station (ISS). There are countless applications for 3D printing that are being overlooked by almost the entire Geoscience community, ranging from the 3D printing of fossils, Lab equipment and shapes used in experiments, to the full-color 3D printing of lab models or field scanned rock samples. With some R&D existing 3D printing apparatus can be modified to 3D print entire analogue models, which brings down the building process from many hours to mere minutes.

6 Acknowledgements

- I want to thank my supervisors Prof. Dr. Dimitrios Sokoutis and Dr. Ernst Willingshofer for all their countless hours of help and support both on a knowledge level and financial level throughout the making of this work.
- I want to thanks Lucas Giezeman with whom I did parallel research for the great collaboration during the entire process.
- I want to thanks Rob Iseger, ICT Manager of the Geoscience department at Utrecht University for his help and advice on the logistical side.
- I thank Tessa Bosch, lab assistant of the TecLab at the Utrecht University for her support and logistical efforts.
- I want to thank Dr. Wouter Marra for his help and advice during the project and - especially for his advice concerning Agisoft Photoscan.
- Big thanks go out to Dr. Heinrich Mallison for his help with the photogrammetry setup and for his amazing Agisoft tutorials and photogrammetry papers.
- I want to thank Visual Artist Rachel van der Meer for all her modelling, 3D printing and all things Virtual reality help and advice.
- I want to thank my family for all their support through the years.
- Finally, I want to thank the *Sci-Hub* project for providing access to scientific articles that are locked behind paywalls. Scientific knowledge should be available for every person regardless of their income, social status or geographical location.

I hope that my effort in applying these technologies will help bring Geosciences a step closer to its goal and to demonstrate that when technology and Geology move hand-in-hand we can achieve amazing new advances and discoveries, giving us the confidence to tackle the next exciting and complex geologic mystery.

7 Literature

Abdelmalak, M. M., Mourgues, R., Galland O., Bureau, D., 2012. Fracture mode analysis and related surface deformation during dyke intrusion: Results from 2D experimental modelling, Earth Planet. Sci. Lett., 359-360, 93–105.

Adam, J., Klinkmüller, M., Schreurs, G., Wieneke, B., 2013, Quantitative 3D strain analysis in analogue experiments simulating tectonic deformation: Integration of X-ray computed tomography and digital volume correlation techniques, J. Struct. Geol., 55, 127–149.

Adam, J., Urai, J., Wieneke, B., Oncken, O., Pfeiffer, K., Kukowski, N., Lohrmann, J., Hoth, S., van der Zee, W., Schmatz, J., 2005. Shear localization and strain distribution during tectonic faulting—new insights from granular-flow experiments and high-resolution optical image correlation techniques. J. Struct. Geol. 27, 283–301.

Agisoft LLC. Agisoft PhotoScan User Manual Professional Edition Version 1.2., 2016.

Agisoft LLC. PhotoScan Python Reference, Release 1.2.5., 2016.

Albertz, J., HRSC Co-Investigator Team, 24 co-authors, 2005. HRSC on Mars Express – photogrammetric and cartographic. Res. Photogramm. Eng. Rem. Sens. 71 (10), 1153–1166.

Athmer, W., Groenenberg, R. M., Luthi, S. M., Donselaar, R., Sokoutis, D., and Willingshofer, E., 2010, Relay ramps as pathways for turbidity currents: a study combining analogue sandbox experiments and numerical flow simulations: Sedimentology, v. 57, DOI: 10.1111/j.1365-3091.2009.01120.x, p. 806-823.

Babault, J., Bonnet, S., Crave, A., Van Den Driessche, J., 2005. Influence of piedmont sedimentation on erosion dynamics of an uplifting landscape: An experimental approach, Geology, 33(4), 301–304.

Babault, J., Bonnet, S., Van Den Driessche, J., Crave, A., 2007. High elevation of low-relief surfaces in mountain belts: Does it equate to post-orogenic surface uplift? Terra Nova, 19(4), 272–277.

Ballard, J-F., Brun, J-P., et Van Ven Driessche, J., 1987. Propagation des chevauchements au-dessus des zones de décollement: modèles expérimentaux. Comptes Rendus de l'Académie des Sciences, Paris, 11, 305, 1249-1253.

Bally, A.W., 1984. Tectogénèse et sismique réflexion. Bull. Soc. Geol. France, 7(2), 279–285.

Bay, H., Tuytelaars, T., Van Gool, L., 2006. SURF: Speeded Up Robust Features, in Computer Vision—ECCV 2006, edited by A. Leonardis, H. Bischof, and A. Pinz, pp. 404–417, Springer, Berlin Heidelberg.

Bevan, T.G., Moustafa, A.R. 2012. Inverted rift-basins of northern Egypt. In: Roberts, D.G. & Bally, A.W. (eds) Phanerozoic Rift Systems and Sedimentary Basins. Elsevier, 483–507.

Bio, A., Bastos, L., Granja, H., Pinho, J.L.S., Gonçalves, J.A., Henriques, R., Madeira, S., Magalhães, A., Rodrigues, D., 2015. Methods for coastal monitoring and erosion risk assessment: two Portuguese case studies. Revista de Gestão Costeira Integrada / Journal of Integrated Coastal Zone Management, 15(1):47-63 (2015).

Bonini, M., 1998. Chronology of deformation and analogue modelling of the Plio-Pleistocene 'Tiber Basin': implications for the evolution of the Northern Apennines (Italy). Tectonophysics 285, 147–165.

Bonini, M., Sani, F. Antonielli, B., 2011. Basin inversion and contractional reactivation of inherited normal faults: A review based on previous and new experimental models. Tectonophysics 522–523 (2012) 55–88

Bonini, M., Sani, F., Antonielli, B., 2012. Basin inversion and contractional reactivation of inherited normal faults: a review based on previous and new experimental models. Tectonophysics, 522–523, 55–88.

Boutelier, D., 2016. TecPIV—A MATLAB-based application for PIV-analysis of experimental tectonics. Computers & Geosciences 89 (2016) 186–199.

Breque, C., Dupre, J-C., Bremand, F., 2004. Calibration of a system of projection moiré for relief measuring: biomechanical applications. Opt Laser Eng 2004; 41: 241–60.

Brun, J.-P. 1999. Narrow rifts versus wide rifts: inferences for the mechanics of rifting from laboratory experiments. Phil. Trans. R. Soc. Lond. A (1999) 357, 695–712.

Brun, J.P., Nalpas, T., 1996. Graben inversion in nature and experiments. Tectonics 15, 677–687.

Buchanan, J.G., Buchanan, P.G. (Eds.)., 1995. Basin Inversion, 88. Geological Society, Special Publication. 596 pp.

Buchanan, P.G., McClay, K.R., 1991. Sandbox experiments of inverted listric and planar fault systems. Tectonophysics, Volume 188, Issues 1–2, 10 March 1991, Pages 97-115.

Burchardt, S., Walter, T. R., 2010. Propagation, linkage, and interaction of caldera ring-faults: Comparison between analogue experiments and caldera collapse at Miyakejima, Japan, in 2000, Bull. Volcanol. 72(3), 297–308.

Burton, D. & Wood, L.J., 2010. Seismic geomorphology and tectonostratigraphic fill of half grabens, West Natuna Basin, Indonesia. AAPG Bull., 94, 1695–1712.

Byerlee, J., 1978. Friction of rocks. Pure and applied geophysics, vol 116 pp. 615- 626.

Calignano, E., Sokoutis, D., Willingshofer, E., Gueydan, F., Cloetingh, S., 2015. Strain localization at the margins of strong lithospheric domains: Insights from analog models, Tectonics, 34, 396–412.

Carbonell, P.J.T., Guzmán, C., Yagupsky, D., Dimieri, L.V., 2016. Tectonic models for the Patagonian orogenic curve (southernmost Andes): An appraisal based on analog experiments from the Fuegian thrust–fold belt. Tectonophysics 671 (2016) 76–94.

Clendenin, W., and Duane, M.J., 1990. Focused fluid flow and Ozark Mississippi Valley-type deposits. Geology 18, 116-119.

Cobbold, P.R., Jackson, M.P.A., 1992. Gum rosin (colophony): A suitable material for mechanical modelling of the lithosphere. Tectonophysics 210, 255–271.

Collettini, C., Sibson, R.H., 2001. Normal faults, normal friction? Geology 29, 927–930. Collyer, A.A., 1973. Time independent fluids. Physics Education 8, 333–338.

Cooke, A., Harris, L.B., 1987. Analogue modelling experiments during normal and oblique extension. Applied extension tectonics. Aust. BMR Rec. 51, 116-124.

Cooper, M., and Warren, M.J., 2010. The geometric characteristics, genesis and petroleum significance of inversion structures. Geological Society, London, Special Publications 2010, v. 335, p. 827-846.

Cooper, M.A., Williams, G.D. (Eds.), 1989. Inversion Tectonics, 44. Geological Society of London Special Publication. 375 pp.

Coskun, B., 1997. Oil and gas fields—transfer zone relationships, Thrace basin, NW Turkey. Marine and Petroleum Geology. Volume 14, Issue 4, June 1997, Pages 401-416.

Coward, M.P., 1994. Inversion tectonics. In: Continental Deformation (Ed. by P.L. Hancock), pp. 289–304. Pergamon Press, Oxford.

Coward, M.P., 1996. Balancing sections through inverted basins. In: Modern Developments in structural Interpretation, Validation and Modelling (Ed. by Buchanan P.G. & Nieuwland D.A.) Geol. Soc. London. Spec. Publ., 99, 51–77.

Cowie, P.A., Roberts, G.P., 2001. Constraining slip rates and spacings for active normal faults. Journal of Structural Geology 23 (2001) 1901 - 1915.

Davies, R., Cloke, I., Cartwright, J., Robinson, A. & Ferrero, C., 2004. Post-breakup compression of a passive margin and its impact on hydrocarbon prospectivity: An example from the Tertiary of the Faeroe-Shetland Basin, United Kingdom. AAPG Bull., 88, 1–20.

Davy, P., Cobbold, P.R., 1988. Indentation tectonics in nature experiment. 1. Experiments scaled for gravity. Bull. 143–166. Geol. Inst. Univ. Uppsala, N.S. 14, 129–141.

Davy, P., Cobbold, P.R., 1991. Experiments on shortening of 4-layer model of the continental lithosphere. In: Cobbold, P.R. (Ed.), Experimental and Numerical Modelling of Continental Deformation: Tectonophysics, 188, pp. 1–25.

De Reu, J., Plets, G., Verhoeven, G., De Smedt, P., Bats, M., Cherretté, B., De Maeyer, W., Deconynck, J., Herremans, D., Laloo, P., Van Meirvenne, M., De Clercq, W., 2013. Towards a three-dimensional cost-effective registration of the archaeological heritage. Journal of Archaeological Science 40 (2013) 1108-1121.

Delcamp, A., van Wyk de Vries, B., James, M. R., 2008. The influence of edifice slope and substrata on volcano spreading, J. Volcanol. Geotherm. Res., 177(4), 925–943.

Deng, C., Zhou, Z., LI, W., Hou, B., 2016. A Panoramic Geology Field Trip System Using Image-Based Rendering. 2016 IEEE 40th Annual Computer Software and Applications Conference.

Donnadieu, F., Kelfoun, K., van Wyk de Vries, B., Cecchi, E., Merle, O., 2003. Digital photogrammetry as a tool in analogue modelling: Applications to volcano instability, J. Volcanol. Geotherm. Res., 123(1-2), 161–180.

Duboisa, A., Odonneb, F., Massonnatc, G., Lebourgd, T., Fabred, R., 2002. Analogue modelling of fault reactivation: tectonic inversion and oblique remobilisation of grabens. Journal of Structural Geology, Volume 24, Issue 11, 1 November 2002, Pages 1741–1752.

Eauchamp, W., 2004. Superposed folding resulting from inversion of a synrift accommodation zone, Atlas Mountains, Morocco, in K. R. McClay, ed., Thrust tectonics and hydrocarbon systems: AAPG Memoir 82, p. 635 – 646.

Eisenstadt, G., Withjack, M.O., 1995. Estimating inversion: results from clay models. Geological Society, London, Special Publications 1995, v. 88, p. 119-136.

Etheridge, M.A., 1986. On the reactivation of extensional fault systems. Philosophical Transactions of the Royal Society of London. Series A-317, 179–194.

Farzipour-Saein, A., Nilfouroushan, F., Koyi, H., 2013. The effect of basement step/topography on the geometry of the Zagros fold and thrust belt (SW Iran): an analog modeling approach. International Journal of Earth Sciences: November 2013, Volume 102, Issue 8, pp 2117–2135.

Fischler, M.A., Bolles, R.C., 1980. Random sample consensus: a paradigm for model fitting with applications to image analysis and automated cartography. SRI International, Technical Note, 213, 1–37.

Gabrielsen, R.H., Sokoutis, D., Willingshofer, E., and Faleide, J.I., 2015. Fault linkage across weak layers during extension: an experimental approach with reference to the Hoop Fault Complex of the SW Barents Sea. PG - Petroleum Geoscience, Vol. 22, 2016, pp. 123–135.

Galland, O., Bertelsen, H.S., Guldstrand, F., Girod, L., Johannessen R.F., Bjugger, F. Burchardt, S., and Mair, K., 2016. Application of open-source photogrammetric software MicMac for monitoring

surface deformation in laboratory models. Journal of Geophysical Research: Solid Earth 10.1002/2015JB012564.

Goetze, C., Evan, B., 1979. Stress and temperature in the bending lithosphere as constrained by experimental rock mechanics. Geophys. J. R. ash. SOC. (1979) 59, 463-478.

Gomes, C.J.S., 2013. Investigating new materials in the context of analog-physical models. J. Struct. Geol. 46, 158e166.

Graveleau, F., Dominguez, S., 2008, Analogue modelling of the interaction between tectonics, erosion and sedimentation in foreland thrust belts, C. R. Geosci., 340(5), 324–333.

Graveleau, F., Malavieille, J., Dominguez, S., 2012. Experimental modelling of orogenic wedges: A review, Tectonophysics, 538-540, 1–66.

Gruen, A., 1997. Fundamentals of videogrammetry — A review. Human Movement Science, Volume 16, Issues 2–3, April 1997, Pages 155–187.

Grujic, D., Walter, T. R., Gärtner, H., 2002. Shape and structure of (analogue models of) refolded layers, J. Struct. Geol., 24(8), 1313–1326.

Gwinner, K., Jaumann, R., Hauber, E., Hoffmann, H., Heipke, C., Oberst, J., Neukum, G., Ansan, V., Bostelmann, J., Dumke, A., Elgner, S., Erkeling, G., Fueten, F., Hiesinger, H., Hoekzema, N.M., Kersten, E., Loizeau, D., Matz, K.-D., McGuire, P.C., Mertens, V., Michael, G., Pasewaldt, A., Pinet, P., Preusker, F., Reiss, D., Roatsch, T., Schmidt, R., Scholten, F., Spiegel, M., Stesky, R., Tirsch, D., van Gasselt, S., Walter, S., Wählisch, M., Willner, K., 2016. The High-Resolution Stereo Camera (HRSC) of Mars Express and its approach to science analysis and mapping for Mars and its satellites. Planetary and Space Science 126 (2016) 93–138.

Harding, T.P., 1985. Seismic characteristics and identification of negative flowers structures, positive flowers structures, and positive structural inversion. AAPG Bulletin 69, 582–600.

Haruyama, J., Hara, S., Hioki, K., Iwasaki, A., Morota, T., Ohtake, M., Matsunaga, T., Araki, H., Matsumoto, K., Ishihara, Y., Noda, H., Sasaki, S., Goossens, S., Iwata, T., 2012. Lunar Global Digital Terrain Model Dataset Produced from Selene (Kaguya) Terrain Camera Stereo Observations. In: Proceedings of the 43rd Lunar and Planetary Science Conference, #1200.

Henley, R. W. and Adams, D.P.M., 1992. Strike-slip fault reactivation as a control on epithermal vein-style gold mineralization. Geology 20, 443-446.

Hodgetts, D., 2013. Laser scanning and digital outcrop geology in the petroleum industry: A review. Marine and Petroleum Geology 46 (2013) 335-354.

Holdsworth, R.E., Butler, C.A., and Roberts, A.M., 1997. The recognition of reactivation during continental deformation. Journal of the Geological Society, 154, 73-78.

Horsfield, W.T., 1977. An experimental approach to basement controlled faulting. Geologie en Mijnbouw 56, 363–370.

Hubbert M.K., 1951, Mechanical basis for certain familiar geologic structures. Bull. of the Geol. Soc. of America vol. 62, pp. 355-372.

Hubbert, M.K., 1937. Theory of scaled models as applied to the study of geological structures. Geological Society of America Bulletin 48, 1459–1520.

Hubbert, M.K., 1951. Mechanical basis for creation geological structures. Bulletin of the Geological Society of America 62, 355–372.

Hulbert, L.J., Carne R.C., Gregoire, D.C., Paktunc, D., 1992. Sedimentary nickel, zinc, and platinum-group-element mineralization in Devonian black shales at the Nick Property, Yukon, Canada; a new deposit type. Expl. Mining Geol. 1, 39-62.

Jagger, L.J., and McClay, K.R., 2016. Analogue modelling of inverted domino-style basement fault systems. Basin Research (2016) 1–19.

Javernick, L., Brasington, J., Caruso, B., 2014. Modelling the topography of shallow braided rivers using Structure from Motion photogrammetry. Geomorphology 213: 166–182.

Kavanagh, J. L., Boutelier, D., Cruden, A. R., 2015. The mechanics of sill inception, propagation and growth: Experimental evidence for rapid reduction in magmatic overpressure, Earth Planet. Sci. Lett., 421, 117–128.

Kearsley, A.T., Burchell, M.J., Graham, G.A., Hörz, F., Wozniakiewicz, P.A., and Cole, M.J. 2007. Cometary dust characteristics: comparison of stardust craters with laboratory impacts. 38th Lunar and Planetary Science Conference, 1562.

Koenderink, J. J., and A. J. van Doorn., 1991. Affine structure from motion, J. Opt. Soc. Am. A, 8(2), 377–385.

Konstantinovskaya E.A., Harris, L.B., Poulin, J., Ivanov, G.M., 2007. Transfer zones and fault reactivation in inverted rift basins: Insights from physical modelling. Tectonophysics, Volume 441, Issues 1–4, 15 August 2007, Pages 1–26.

Koopman, A., Speksnijder, A., Horsfield, W.T., 1987. Sandbox model studies of inversion tectonics. Tectonophysics, Volume 137, Issues 1–4, 1 June 1987, Pages 379-388.

Krantz, R.W., 1991. Measurements of friction coefficients and cohesion for faulting and fault reactivation in laboratory models using sand and sand mixtures. Tectonophysics 202, 319e333.

Krezsec, C., Adam, J. and Grujic, D., 2007. Mechanics of fault and expulsion rollover systems developed on passive margins detached on salt: insights from analogue modelling and optical strain monitoring. In: Structurally Complex Reservoirs (Ed. by Jolley S.J., Barr D., Walsh J.J. & Knipe R.J.) Geol. Soc. London. Spec. Publ., 292, 103–121.

Lague, D., Crave, A., Davy, P., 2003. Laboratory experiments simulating the geomorphic response to tectonic uplift. JOURNAL OF GEOPHYSICAL RESEARCH, VOL. 108, NO. B1, 2008.

Leever, K. A., Gabrielsen, R. H., Sokoutis, D., and Willingshofer, E., 2011. The effect of convergence angle on the kinematic evolution of strain partitioning in transpressional brittle wedges: Insight from analog modeling and high-resolution digital image analysis, Tectonics, 30, TC2013.

Lejot, J., Delacourt, C., Piégay, H., Fournier, T., Trémélo, M-L., Allemand, P., 2007. Very high spatial resolution imagery for channel bathymetry and topography from an unmanned mapping controlled platform. Earth Surf. Process. Landforms 32, 1705–1725 (2007).

Letouzey, J., 1990. Fault reactivation, inversion and fold-thrust belt, in Petroleum and Tectonics in Mobile Belts, edited by J. Letouzey, pp. 101-128, Technip, Paris, 1990.

Lohrmann, J., Kukowski, N., Adam, J., Oncken, O., 2003. The impact of analogue material properties on the geometry, kinematics, and dynamics of convergent sand wedges. J. Struct. Geol. 25, 1691e1711.

Lowe, D. G., 1999. Object recognition from local scale-invariant features. Computer Vision, 1999. The Proceedings of the Seventh IEEE International Conference on (Volume: 2).

Lowe, D. G., 2004. Distinctive image features from scale-invariant keypoints, Int. J. Comput. Vision, 60(2), 91–110.

Lozano, J.F., Sokoutis, D., Willingshofer, E., Cloetingh, S., De Vicente, G., 2011. Cenozoic deformation of Iberia: A model for intraplate mountain building and basin development based on analogue modeling. TECTONICS, VOL. 30, TC1001.

Luth, S., Willingshofer, E., Sokoutis, D., Cloetingh, S., 2009. Analogue modelling of continental collision: Influence of plate coupling on mantle lithosphere subduction, crustal deformation and surface topography. Tectonophysics 484 (2010) 87–102.

Macgregor, D.S., 1995. Hydrocarbon habitat and classification of inverted rift basins. Geol. Soc. London. Spec. Publ., 88, 83–93.

Maillot, B., 2013. A sedimentation device to produce uniform sand packs. Tectonophysics 593, 85e94.

Mallison, H. Wings, O., 2014. Photogrammetry in Paleontology – A Practical Guide. Journal of Paleontological Techniques.

Mandal, G., 2000. Faulting in Brittle Rocks: an introduction to the Mechanics of Tectonic Faults. Springer-Verlag, Berlin. 434pp.

Marques, F.O., Nogueira, C.R., 2008. Normal fault inversion by orthogonal compression: Sandbox experiments with weak faults. Journal of Structural Geology 30, 761–766.

Martinod, J., Davy, P., 1994. Periodic instabilities during compression of the lithosphere 2. Analogue experiments. JOURNAL OF GEOPHYSICAL RESEARCH, VOL. 99, NO. B6, PAGES 12,057-12,069, June 10, 1994.

McClay, K. R., 1989. Analogue models of inversion tectonics. Geological Society, London, Special Publications 1989, v. 44, p. 41-59.

Mikolajczyk, K., Tuytelaars, T., Schmid, C., Zisserman, A., Matas, J., Schaffalitzky, F., Kadir, T., Van Gool, L., 2005. A comparison of affine region detectors. International Journal of Computer Vision 65(1/2): 43–72.

Morel, J.-M., Yu, G., 2009. Asift: A new framework for fully affine invariant image comparison, SIAM J. Imaging Sci., 2(2), 438–469.

Morley, C. K., Nelson, R. A., Patton, T. L., Munn, S. G., 1990. Transfer Zones in the East African Rift System and Their Relevance to Hydrocarbon Exploration in Rifts. AAPG Bulletin. Volume 74, Issue 8, PP. 1234-1253.

Nalpas, T., 1996. Inversion des grabens du Sud de la Mer du Nord. Données de subsurface et modélisation analogique. Thèse d'Université, Mémoires de Géosciences Rennes 71, 245 pp.

Nalpas, T., Le Douaran, S., Brun, J.-P., Unternehr, P., Richert, J.-P., 1994. Inversion of the Broad Fourteens Basin (offshore Netherlands), a small-scale model investigation. Sedimentary Geology, volume 95, Issues 3–4, March 1995, Pages 237-250.

Nalpas, T., Le Douran, S., Brun, J.P., Untrnehr, P., Richert, J.P., 1995. Inversion of the Broad Fourteens Basin (offshore Netherlands), a small-scale model investigation. Sedimentary Geology 95, 237–250.

Nielsen, S.B., Hansen, D.L., 2000. Physical explanation of the formation and evolution of inversion zones and marginal troughs. Geology 28, 875–878.

Panien, M., Schreurs, G., Pfiffner, A., 2005. Sandbox experiments on basin inversion: testing the influence of basin orientation and basin fill. Journal of Structural Geology, volume 27, Issue 3, March 2005, Pages 433–445.

Panien, M., Schreurs, G., Pfiffner, O.A., 2006. Mechanical behaviour of granular materials used in analogue modeling: insights from grain characterisation, ring-shear tests and sandbox tests. J. Struct. Geol. 28, 1710e1724.

Peacock, D. C. P., Sanderson, D. J., 1994. Geometry and Development of Relay Ramps in normal Fault Systems. Volume: 78 (1994), Issue: 2 (February) PP. 147-165.

Pesci, A., Teza, G., Bonali, E., 2011. Terrestrial laser scanner resolution: numerical simulations and experiments on spatial sampling optimization. Remote Sens. 3, 167–184.

Ramberg, H., 1981. Gravity, Deformation and the Earth's Crust, 2nd ed. Academic Press, London. 452 pp.

Ranalli, G., 1995. Rheology of the Earth, 2nd ed. Chapman and Hall, London. 413 pp.

Ranalli, G., 1997. Rheology of the lithosphere in space and time. In: Burg, J.P., Ford, M. (Eds.), Orogeny Through Time, Geol. Soc.London, Spec. Publ., vol. 121, pp. 19–37.

Ranalli, G., Yin, Z.M., 1990. Critical stress difference and orientation of fault in rocks with strength anisotropies: the two-dimensional case. Journal of Structural Geology 12, 1067–1071.

Rosu, A.-M., Assenbaum, M., De la Torre, M., and Deseilligny, M.P., 2015a. Coastal digital surface model on low contrast images, International Archives of the Photogrammetry, Remote Sensing and Spatial Information Sciences, XL-3/W3, pp. 307–312.

Sandiford, M., 1999. Mechanics of basin inversion. Tectonophysics 305, 109–120.

Sassi, W., Colletta, B., Balé, P., Paquereau, T., 1993. Modelling of structural complexity in sedimentary basins: the role of pre-existing faults in thrust tectonics. Tectonophysics 226, 97–112.

Schellart, W.P., 1999. Shear test results for cohesion and friction coefficients for different granular materials: scaling implications for their usage in analogue modelling. Tectonophysics 324 (2000) 1–16.

Schellart, W.P., 2000. Shear test results for cohesion and friction coefficients for different granular materials: scaling implications for their usage in analogue modeling. Tectonophysics 324, 1e16.

Schreurs, G., and B. Colletta., 1998. Analogue modelling of faulting in zones of continental transpression and transtension, Geol. Soc. London, Spec. Publ., 135(1), 59–79.

Schreurs, G., Buiter, S.J.H., Boutelier, J., Burberry, C., Callot, J.P., Cavozzi, C., Cerca, M., Chen, J.H., Cristallini, E., Cruden, A.R., Cruz, L., Daniel, J-M., Da Poian, G., Garcia, V.H., Gomes, C.J.S., Grall, C., Guillot, Y., Guzmán, C., Hidayah, T.N., Hilley, G., Klinkmüller, M., Koyi, H.A., Lu, C.Y., Maillot, B., Meriaux, C., Nilfouroushan, F., Pan, C.C., Pillot, D., Portillo, R., Rosenau, M., Schellart, W.P., Schlische, R.W., Take, A., Vendeville, B., Vergnaud, M., Vettori, M., Wang, S., Withjack, M.O., Yagupsky, D., Yamada, Y., 2016. Benchmarking Analogue Models of Brittle Thrust Wedges. Journal of Structural Geology. Volume 92, November 2016, Pages 116–139.

Schreurs, G., et al., Benchmarking analogue models of brittle thrust wedges, Journal of Structural Geology (2016).

Shankar Mitra., 1993. Geometry and Kinematic Evolution of Inversion Structures. AAPG Bulletin, Volume 77, issue 7, pages 1159-1191.

Sibson, R.H. Scott, J., 1998. Stress/fault controls on the containment and release of overpressured fluids: Examples from gold-quartz vein systems in Juneau, Alaska; Victoria, Australia and Otago, New Zealand. Ore Geology Reviews, Volume 13, Issues 1–5, April 1998, Pages 293–306.

Sibson, R.H., 1985. A note on fault reactivation. Journal of Structural Geology 7, 751–754.

Sibson, R.H., 1995. Selective fault reactivation during basin inversion: potential for fluid redistribution through fault-valve action. In: Buchanan, J.G., Buchanan, P.G. (Eds.), Basin inversion, 88. Geological Society of London Special Publication, pp. 3–19.

Sibson, R.H., Xie, G., 1998. Dip range for intracontinental reverse fault ruptures: truth not stranger than friction? Bulletin of the Seismological Society of America 88, 1014–1022.

Smith, M.W., Carrivick, J.L., Carrivick, J.L., 2016. Structure from motion photogrammetry in physical geography. Progress in Physical Geography 2016, Vol. 40(2) 247–275.

Snavely, N., Seitz, S. M., and Szeliski, R., 2006, Photo tourism: Exploring photo collections in 3D, in ACM SIGGRAPH 2006 Pap. pp. 835–846, ACM, Boston, Mass.

Snavely, N., Seitz, S. M., and Szeliski, R., 2008. Modeling the world from Internet photo collections, Int. J. Comput. Vision, 80(2), 189–210.

Sokoutis, D., Burg, J.P., Bonini, M., Corti, G., Cloetingh, S., 2005. Lithospheric-scale structures from the perspective of analogue continental collision. Tectonophysics 406 (2005) 1–15.

Sveen, J. K., 2004. An introduction to MatPIV v. 1.6. 1 Preprint series. Mechanics and Applied Mathematics.

Sylvester, A.G., 1988. Strike-Slip faults. Geol. Soc. Am. Bull., 100: 1666-1703.

Tavani, S., Granado, P., Corradetti, A., Girundo, M., Iannace, A., Arbués, P., Muñoz, J., Mazzoli, S., 2014. Building a virtual outcrop, extracting geological information from it, and sharing the results in Google Earth via Open Plot and Photoscan: an example from the Khaviz Anticline (Iran). Comput. Geosci. 63, 44–53.

Thielemann J.T., Berge, A., Skotheim, Ø., Kirkhus, T., 2013. Fast High Resolution Laser Scanning by Real-Time Object tracking and Segmentation. SINTEF ICT, PB 124 Blindern, 0314 Oslo, Norway.

Thielicke, W., and Stamhuis, E.J., 2014. PIVlab – Towards User-friendly, Affordable and Accurate Digital Particle Image Velocimetry in MATLAB. Journal of Open Research Software, 2: e30.

Thurmond J.B, Drzewiecki P.A., Xu, X., 2005. Building simple multiscale visualizations of outcrop geology using virtual reality modeling language (VRML). Computers & Geosciences, Volume 31, Issue 7, August 2005, Pages 913–919.

Tinker, S., 1996. Building the 3-D jigsaw puzzle: applications of sequence stratigraphy to 3-D reservoir characterization, Permian Basin. American Association of Petroleum Geologists Bulletin, 80 (4) (1996), pp. 460–485.

Tong, H., Yin, A., 2011. Reactivation tendency analysis: a theory for predicting the temporal evolution of preexisting weakness under uniform stress state. Tectonophysics 503, 195–200.

Tortini, R., Bonali, F. L., Corazzato, C., Carn, S. A., and Tibaldi, A., 2014. An innovative application of the Kinect in Earth sciences: Quantifying deformation in analogue modelling of volcanoes, Terra Nova, 26(4), 273–281.

Trippanera, D., Acocella, V., and Ruch, J., 2014. Dike-induced contraction along oceanic and continental divergent plate boundaries, Geophys. Res. Lett., 40, 1–7.

Turner J.P, Williams, G.A., 2004. Sedimentary basin inversion and intra-plate shortening. Earth-Science Reviews 65 (2004) 277 – 304.

Van Gent, H.W., Holland, M., Urai, J.L. and Loosveld, R., 2010. Evolution of fault zones in carbonates with mechanical stratigraphy – Insights from scale models using layered cohesive powder. J. Struct. Geol., 32, 1375–1391.

Vautier, F., Corenblit, D., Hortobágyi, B., Fafournoux, L., Steiger, J., 2016. Monitoring and reconstructing past biogeomorphic succession within fluvial corridors using stereophotogrammetry. EARTH SURFACE PROCESSES AND LANDFORMS. Earth Surf. Process. Landforms (2016).

Vitek, J.D., Giardino, J.R., Fitzgerald, J.W., 1995. Mapping geomorphology: A journey from paper maps, computer mapping to GIS and Virtual Reality. Geomorphology 16 (1996) 233-249.

Walsh, J.J., Childs, C., Meyer, V., Manzocchi, T., Imber, J., Nicol, A., Tuckwell, G., Bailey, W.R., Bonson, C.G., Watterson, J., Nell, P.A., Strand, J., 2001. Geometric controls on the evolution of normal fault systems. Geological Society, London, Special Publications 2001, v. 186, p. 157-170.

Weijermars, R., Jackson, M.P.A., Vendeville, B., 1993. Rheological and tectonic modelling of salt provinces. Tectonophysics 217, 143–174.

Weijermars, R., Schmeling, H., 1986. Scaling of Newtonian and non-Newtonian fluid dynamics without inertia for quantitative modelling of rock flow due to gravity (including the concept of rheological similarity. Physics of the Earth and Planetary Interiors 43, 316–330.

Wheeler, R.L., 1980. Cross-strike structural discontinuities; possible exploration tool for natural gas in Appalachian Overthrust Belt. AAPG Bull. 64, 2166-2178.

White, S.H., de Boorder, H., Smith, C.B., 1995. Structural controls of kimberlite and lamproite emplacement. Journal of Geochemical Exploration, Volume 53, Issues 1–3, March 1995, Pages 245-264.

Williams, G.D., Powell, C.M. & Cooper, M.A., 1989. Geometry and kinematics of inversion tectonics. In: Inversion Tectonics (Ed. by Cooper M.A. & Williams G.D.) Geol. Soc. London. Spec. Publ., 44, 3–15.

Withjack, M.O., Schlische, R.W. and Olsen, P.E., 1998. Diachronous rifting, drifting, and inversion on the passive margin of central eastern North America: an analog for other passive margins. AAPG Bull., 82, 817–835.

Woods, T.L., Reed, S., Hsi, S., Woods, J.A., and Woods, M.R., 2016. Pilot Study Using the Augmented Reality Sandbox to Teach Topographic Maps and Surficial Processes in Introductory Geology Labs. Journal of Geoscience Education, Volume 64, Issue 3, (August 2016).

Yamada, Y., and K. McClay, 2004, 3-D Analog modeling of inversion thrust structures, in K. R. McClay, ed., Thrust tectonics and hydrocarbon systems: AAPG Memoir 82, p. 276–301.

Yamadaa, Y., and McClay, K., 2003b. Application of geometric models to inverted listric fault systems in sandbox experiments. Paper 2: insights for possible along strike migration of material during 3D hanging wall deformation. Journal of Structural Geology, volume 25, Issue 8, August 2003, Pages 1331–1336.

Yilmaz, H.M., Yakar, M., Gulec, S.A., Dulgerler, O.N., 2007. Importance of digital close-range photogrammetry in documentation of cultural heritage. Journal of Cultural Heritage 8 (2007) 428-433.

Yin, Z.M., Ranalli, G., 1992. Critical stress difference, fault orientation and slip direction in anisotropic rocks under non-Andersonian stress systems. Journal of Structural Geology 14, 237–244.

Ziegler, P.A. (Ed.), 1987. Compressional intra-plate deformations in the Alpine Foreland: Tectonophysics, 137. 420 pp.

Ziegler, P.A., 1982. Geological Atlas of Western and Central Europe. Elsevier, Amsterdam. 130 pp. and enclosures.

Ziegler, P.A., Cloetingh, S., van Wees, J.D., 1995. Dynamics of intra-plate compressional deformation: the alpine foreland and other examples. Tectonophysics 252, 7–59.

Bright minds, better future

Sustainability

Utrecht University